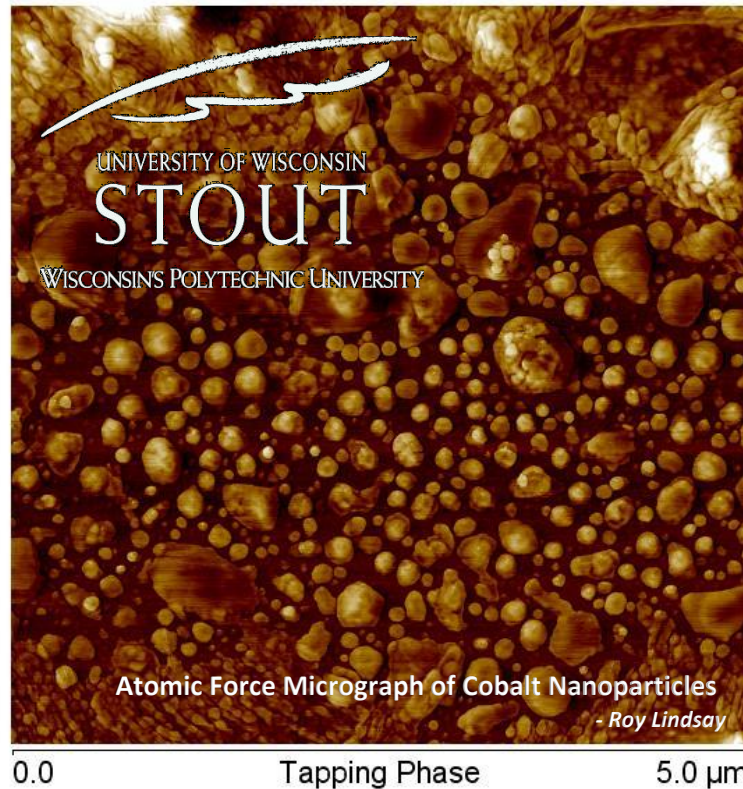


Nanoparticles: Synthesis and Characterization



NANO-401 Nanotechnology Applications University of Wisconsin–Stout Spring 2016

Aaron Forde
Cody Lang
Roy Lindsay
Nicole Moehring

Thomas Palof
Ellie Raethke
Matthew Ray
James Schroder

Table of Contents

Authors	ii
---------------	----

Synthesis

Cobalt	(Lindsay) 1
Copper	(Raethke) 9
Hydroxyapatite	(Palof) 14
Magnetite	(Lang) 17
Titanium Dioxide	(Forde) 26
Tungsten Oxide	(Schroder) 36
Zinc Oxide	(Moehring) 39

Characterization

Zetasizer	(Forde) 45
Disc Centrifuge	(Palof) 47
Sample Preparation	(Raethke) 48
Spin Coater	(Lang) 49
Gold Sputter Coater	(Palof) 50
Carbon Sputter Coater	(Palof) 51
Optical Microscopy	(Forde) 52
Scanning Electron Microscopy (SEM)	(Schroder) 54
Energy Dispersive X-Ray Spectroscopy (EDX)	(Lang) 56
Atomic Force Microscopy (AFM) – Innova	(Moehring) 58
Atomic Force Microscopy (AFM) – Nanosurf	(Schroder) 60
Scanning Tunneling Microscopy (STM)	(Lindsay) 62
Gwyddion	(Lindsay) 64
Image J	(Raethke) 65

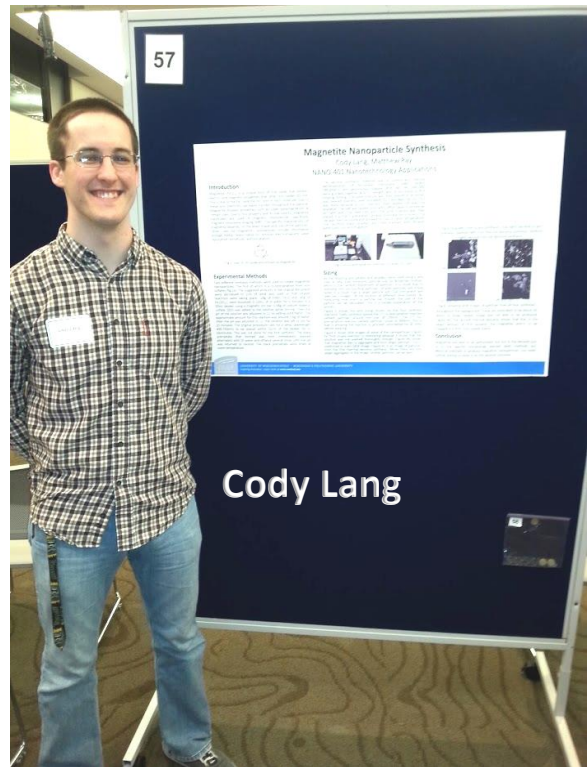
Posters	67
---------------	----

Select References	74
-------------------------	----

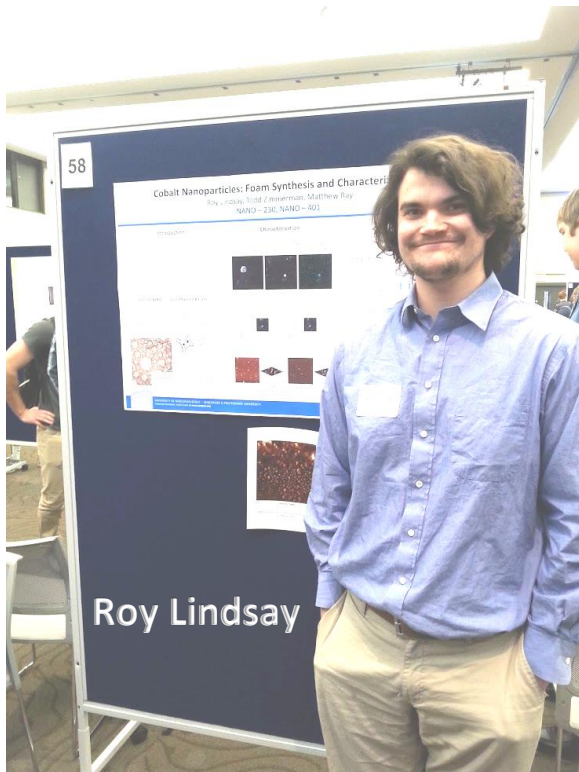
Meet the Authors . . .



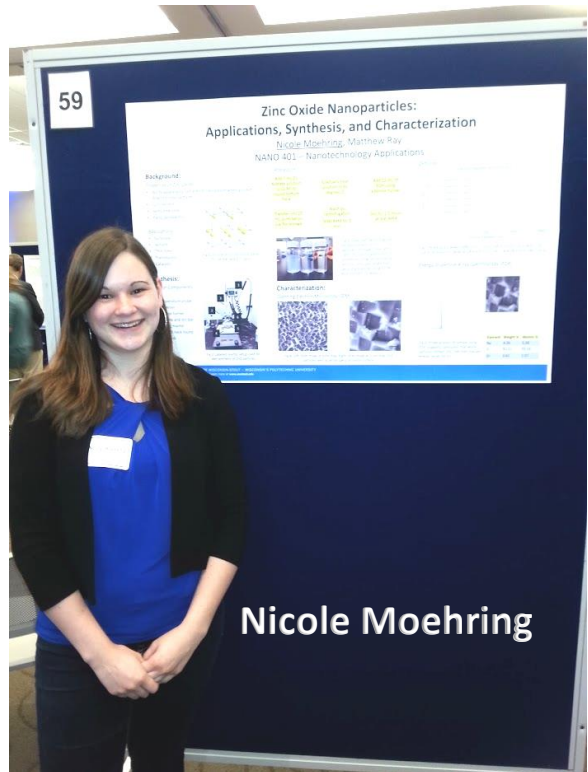
Aaron Forde



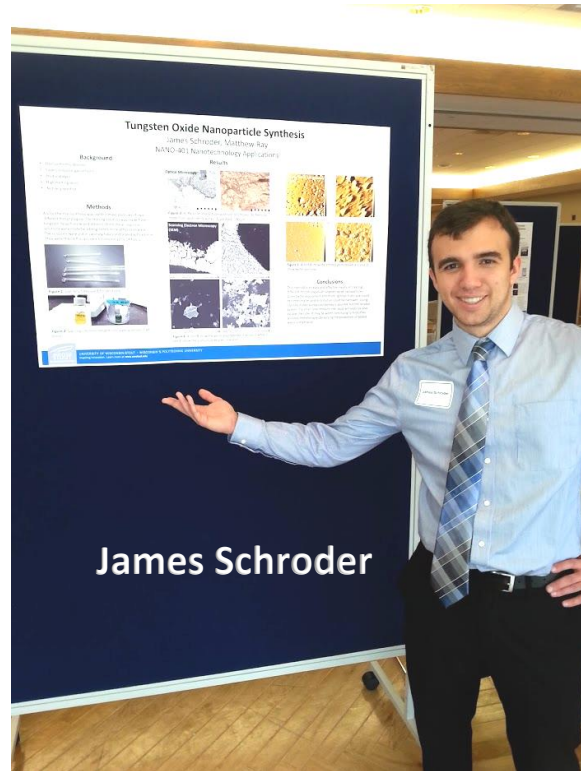
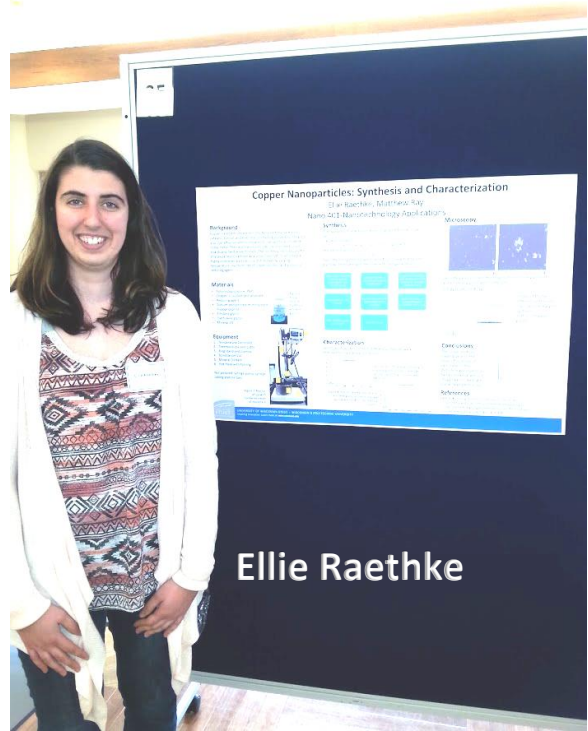
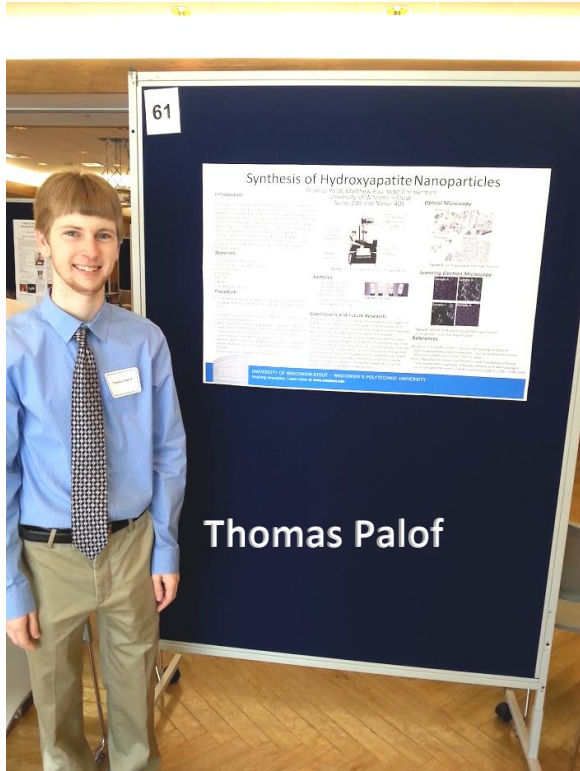
Cody Lang



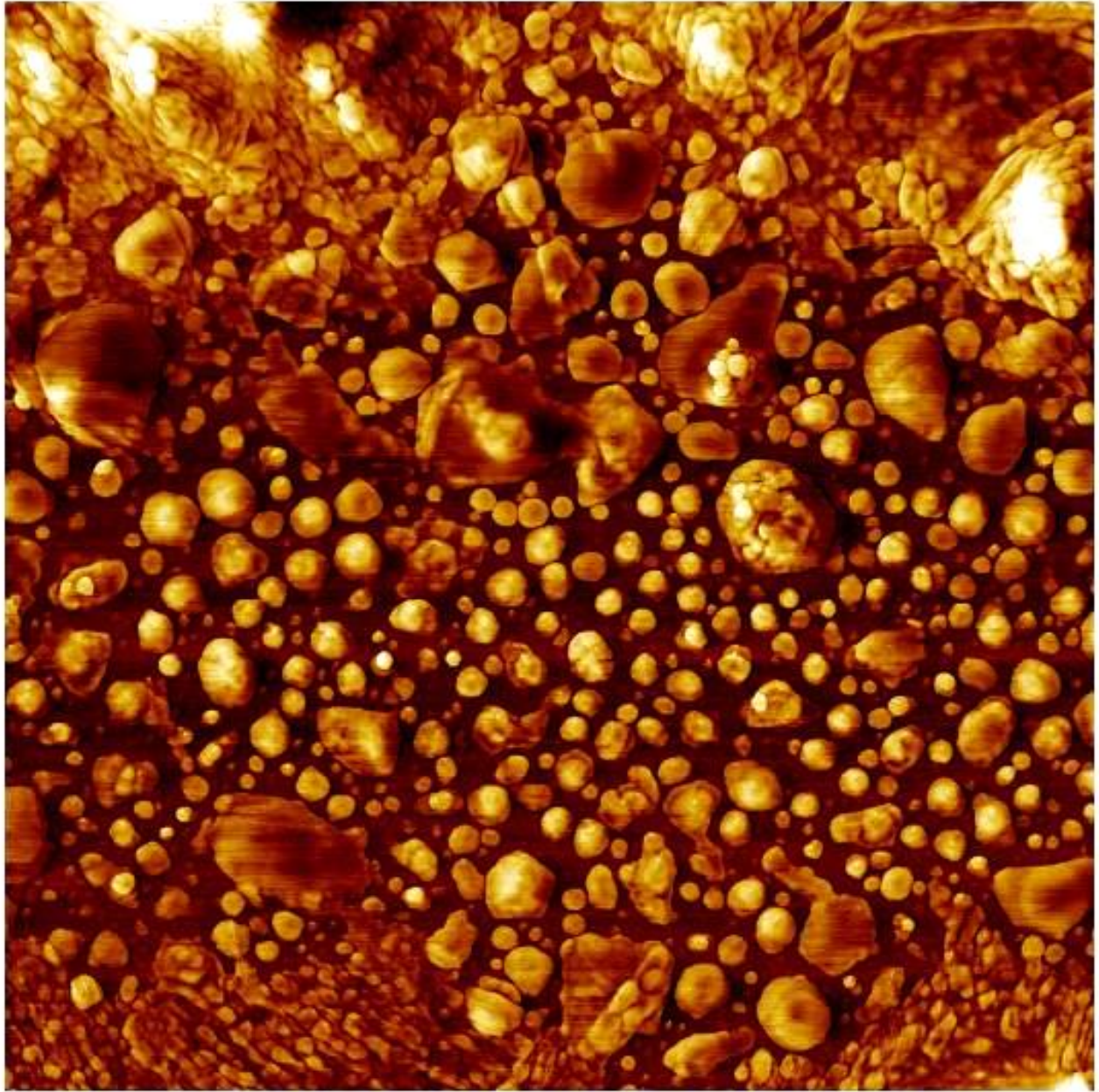
Roy Lindsay



Nicole Moehring



Cobalt Nanoparticle Foam Synthesis



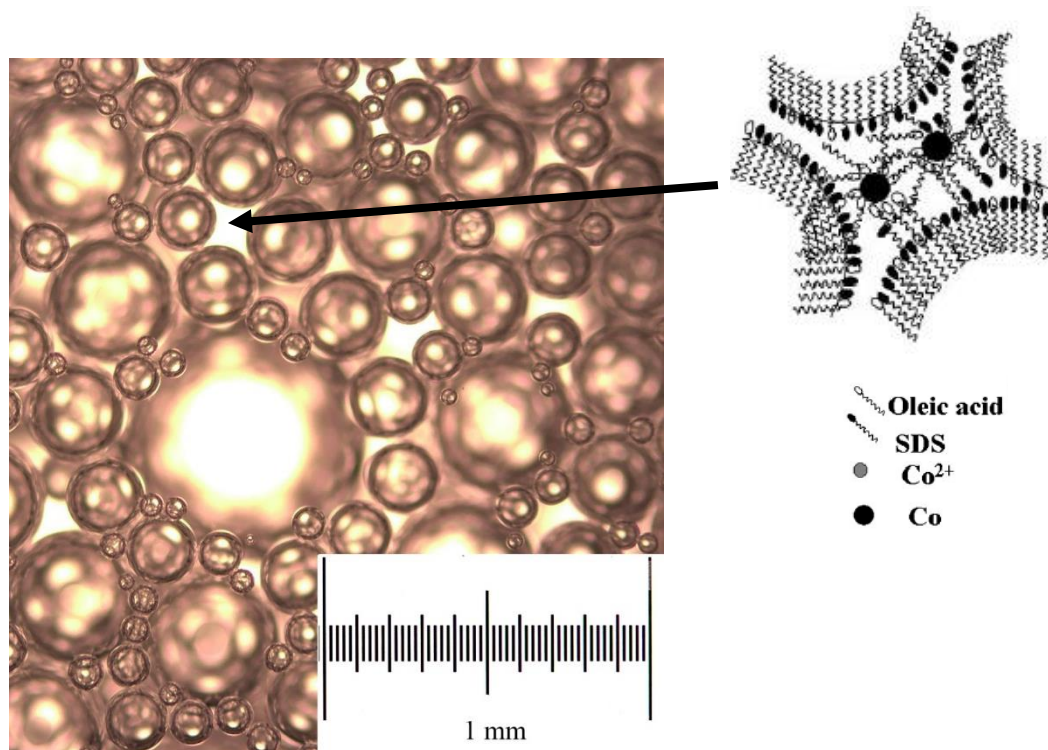
0.0

Tapping Phase

5.0 μm

Introduction:

Cobalt nanoparticles yield interesting electronic, catalytic, optical, and magnetic properties and are – subsequently- an important area of study for applications in magnetic storage, photonics, and electronics.¹ While there are many techniques to produce cobalt nanoparticles such as: co-precipitation, thermal decomposition, micro-emulsion, and hydrothermal synthesis, this guide will focus on the novel foam synthesis method. Much of the content in this manual is directly referenced from Bala et. al's work on ferromagnetic cobalt nanoparticle synthesis using foam. In foam synthesis, the reaction environment is constrained by the interstitial space between micrometer sized bubbles (shown below).



These “micro-reactors” contain the appropriate amount of cobalt oxidizer and organic stabilizer to produce cobalt precipitates in the nano-size regime. Apart from surface passivation, the primary reaction mechanism is a redox reaction between cobalt chloride and sodium borohydride. Cobalt salts are reduced when sodium borohydride micro-droplets are sprayed onto the foam structure, causing individual bubbles to collapse and allowing a redox reaction to take place. The presence of the organic oleic acid stabilizer effects the size and shape of the (by attaching to particle facets and hindering agglomeration).^{2,3}

Safety:

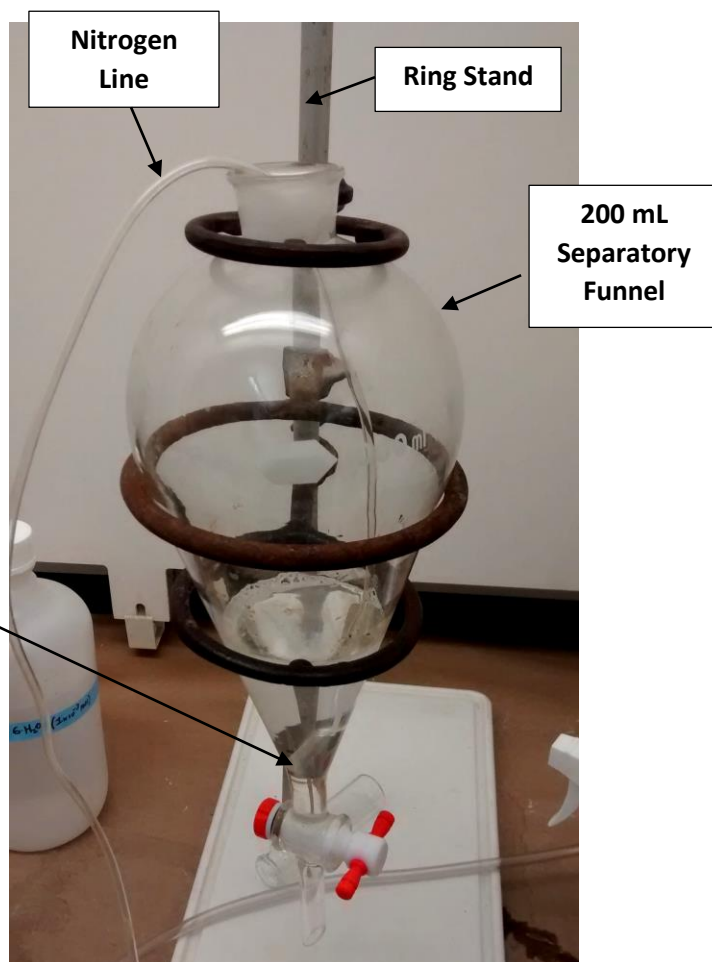
Foam synthesis of cobalt nanoparticles involves toxic, carcinogenic, corrosive, and environmentally hazardous reagents. Conduct all synthesis in a fume hood and always wear protective attire when spraying NaBH₄.

Materials:

1. Reagents:
 - a. Solid Precursor:
 - i. Cobalt(II) chloride
 - b. Reducer:
 - i. Sodium borohydride
 - c. Stabilizer:
 - i. Oleic acid
 - d. Other:
 - i. Methanol
 - ii. Ethanol
 - iii. Sodium dodecyl sulfate (SDS)
2. Equipment:
 - a. 200 mL separatory funnel (with stop-cock)
 - b. Ring stand
 - c. Fume hood
 - d. HPLC frit
 - e. Spray bottle
 - f. Nitrogen gas; gas tubing



HPLC Frit



Synthesis Setup

Synthesis Procedure:

1. Foam synthesis:
 - a. Clean all glassware thoroughly and let dry before synthesis.
 - b. Prepare 25 mL of aqueous CoCl_2 (1mM).
 - c. Prepare 5 mL oleic acid (0.1 M) in methanol.
 - d. Prepare 20 mL of SDS (0.1 M).
 - e. Mix CoCl_2 , oleic acid, and SDS solutions in separatory funnel.
 - f. Prepare 75 mL NaBH_4 (0.1M).
 - g. Dispense NaBH_4 into small spray bottle.
 - h. Connect nitrogen gas to HPLC frit, submerge frit into solution; turn on nitrogen.
 - i. Allow SDS to foam, filling the inside of the separatory funnel.
 - i. Spray foam with NaBH_4
 - i. Foam will begin to collapse.
 - ii. Brownish/black solution will accumulate in the bottom of funnel.
 - j. Drain nanoparticle/ NaBH_4 solution into glassware of appropriate size.
 - i. Try to minimize excess foam from entering glassware.

Wash Procedure:

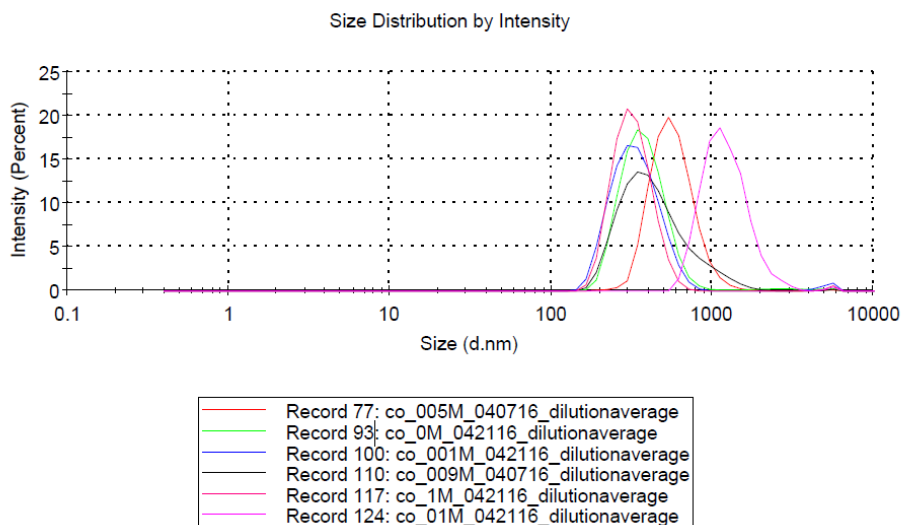
1. Centrifugation:
 - a. Dispense nanoparticle/ NaBH_4 solution into 15mL falcon tubes.
 - b. Centrifuge solution at 6000 RPM for 30 min.
 - c. After first centrifugation, decant NaBH_4 acid solution and replace with ethanol.
 - d. Use probe sonication to disrupt particle aggregation.
 - e. Repeat steps b-d one or two more times.
 - f. Dispense washed particles in glass scintillation vial.

References:

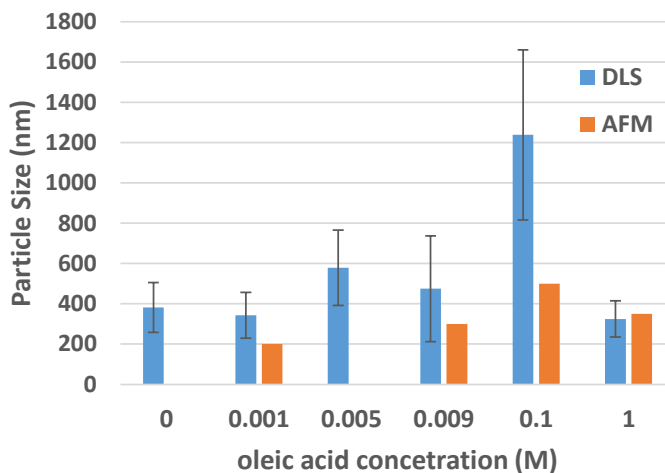
- (1) Brayner, Roberta, Fernand Fiévet, and Thibaud Coradin. *Nanomaterials*. London: Springer, 2013. Print.
- (2) Cha, Seung I. et al. "Ferromagnetic Cobalt Nanodots, Nanorices, Nanowires and Nanoflowers By Polyol Process". *Journal of Materials Research* 20.08 (2005): 2148-2153. Web.
- (3) Bala, T.; Arumugam, S.; Pasricha, R.; Prasad, B.; Sastry, M. Foam-Based Synthesis Of Cobalt Nanoparticles And Their Subsequent Conversion To Cocoreagshell Nanoparticles By A Simple Transmetallation Reaction. *Journal of Materials Chemistry* 2004, 14, 1057.

Particle Size as a function of oleic acid concentration

The concentration of the oleic acid organic stabilizer was found to have very little effect on particle size.

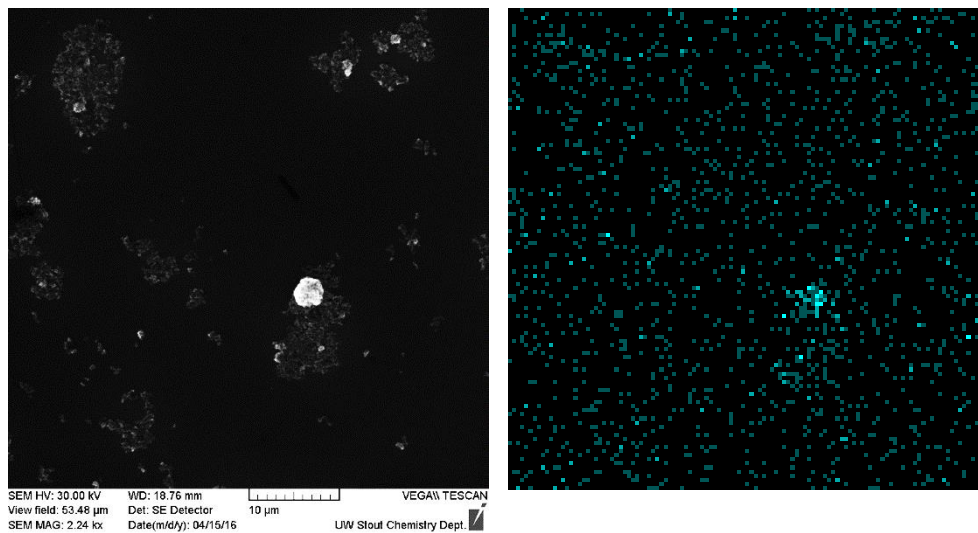
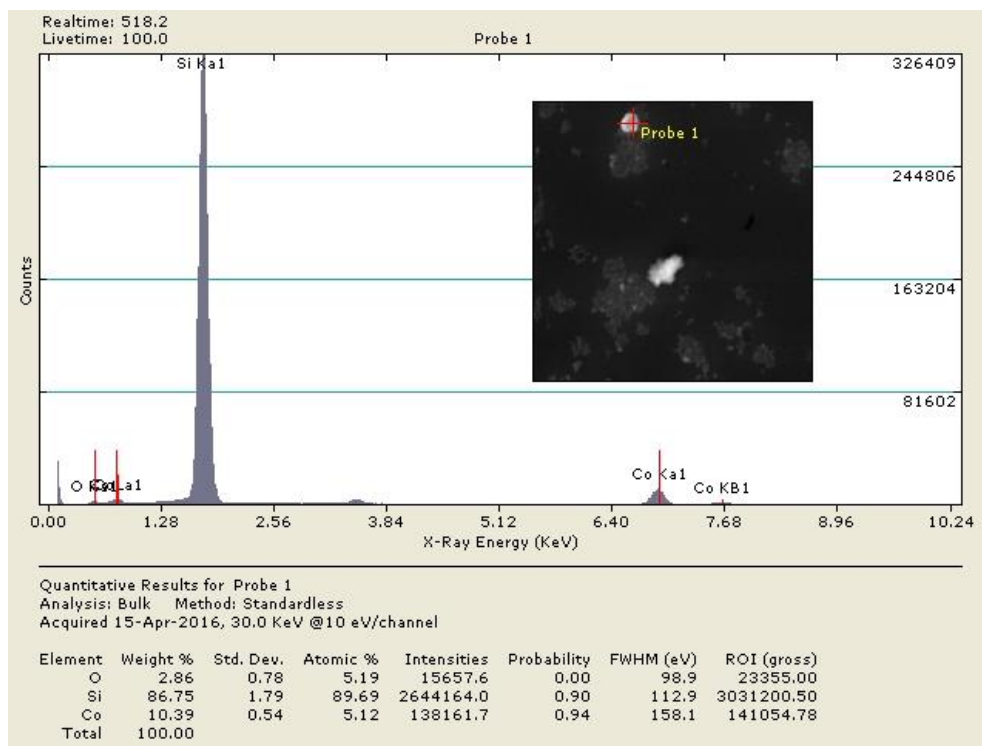


Oleic Acid	DLS		AFM
(M)	(nm)		(nm)
--	AVG	STD	--
0	382	124	--
0.001	343	114	200
0.005	579	187	--
0.009	475	263	300
0.1	1239	422	500
1	325	90	350



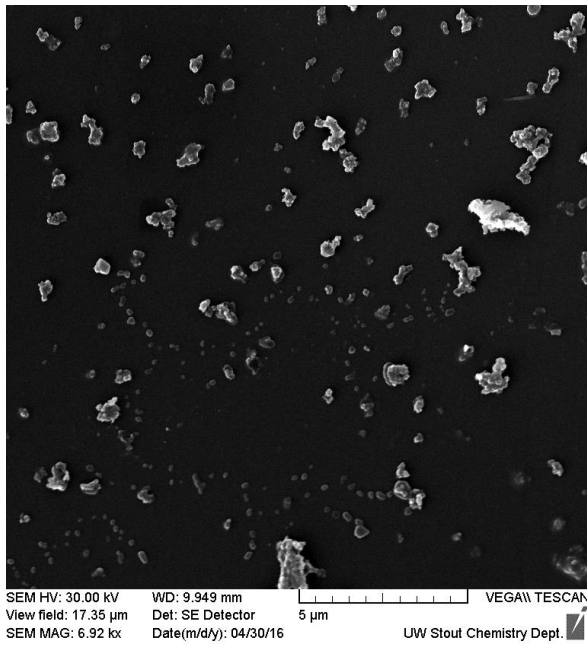
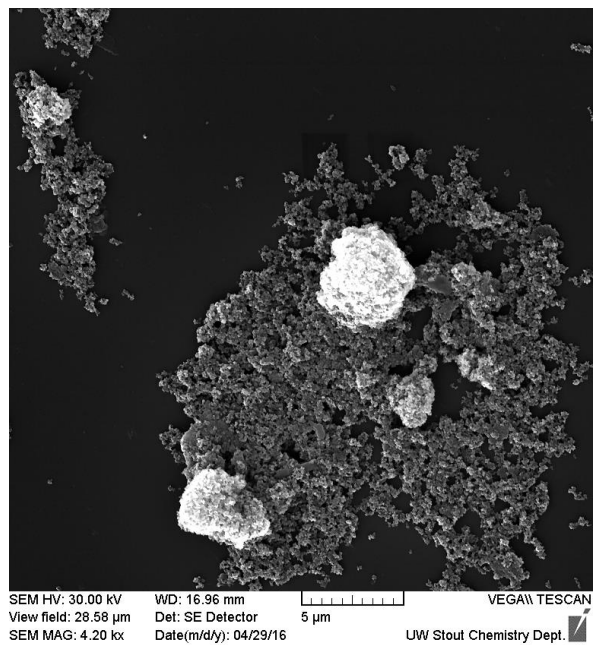
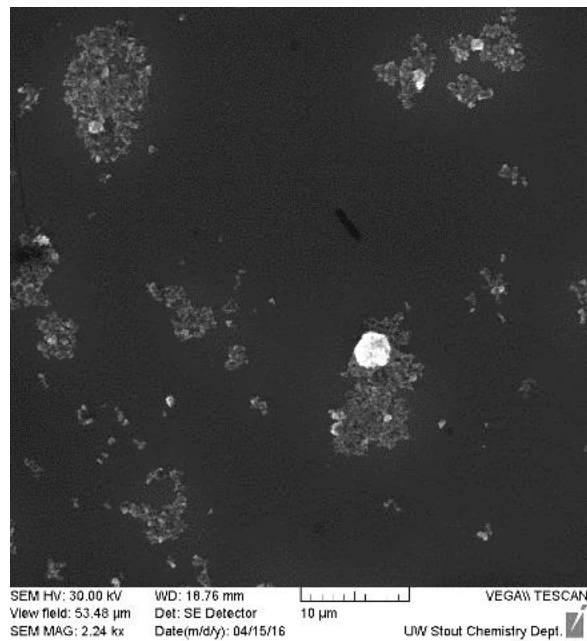
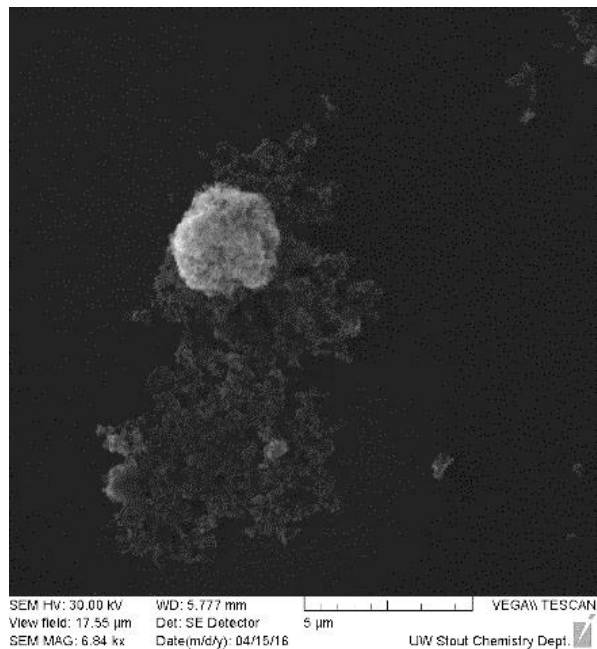
(Top) DLS signal intensity vs particle size. (Left) Nanoparticle size tabulation for various concentrations of oleic acid and (Right) corresponding DLS/AFM data.

EDX Element Characterization



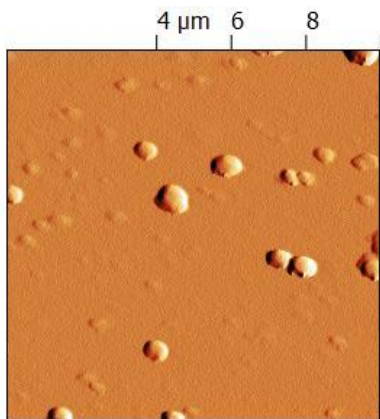
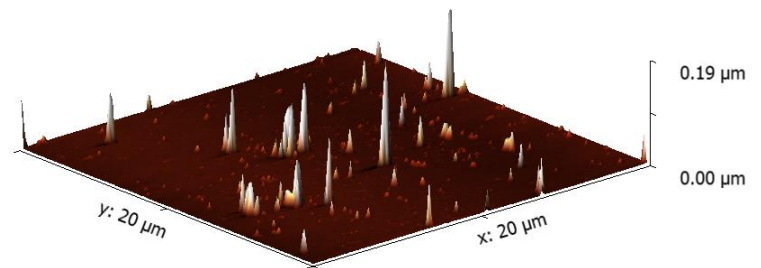
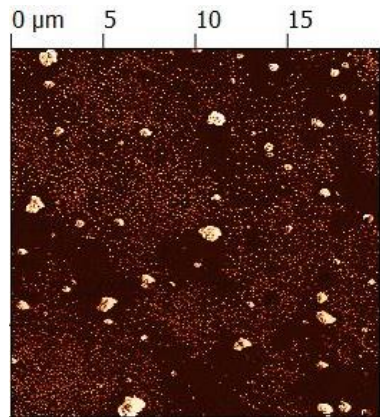
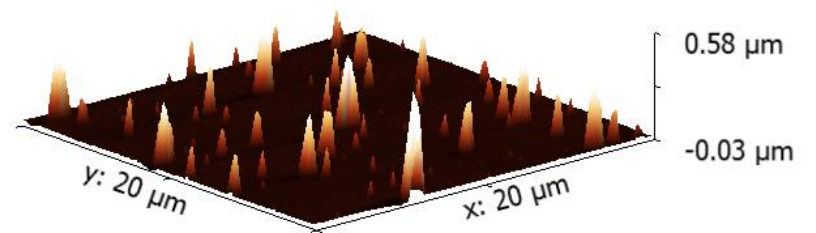
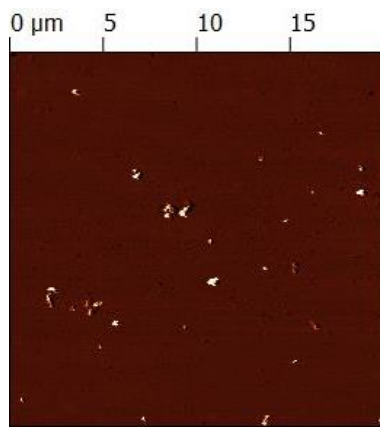
EDX probe scans showing (top) the presence of cobalt in a nanoparticle aggregate and EDX element mapping (bottom left and right), this matches the location of the cobalt aggregate.

SEM Characterization



SEM scan(s) of various oleic capped cobalt nanoparticles

AFM Characterization



Amplitude and topographic AFM scans of various cobalt nanoparticles.

Copper Nanoparticle Synthesis

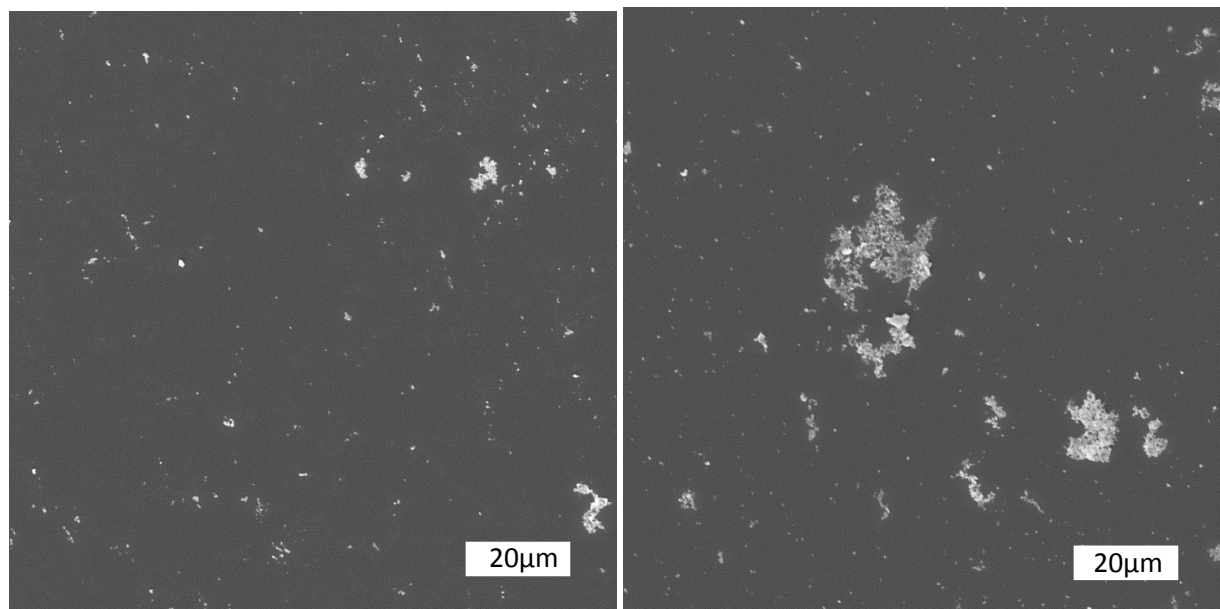


Image on the left is of copper nanoparticles synthesized in ethylene glycol and on the right is the particles synthesized in diethylene glycol.

Introduction:

Metal nanoparticles have a wide range of applications in the catalysis, recording media and electronics fields. These nanoparticles are synthesized with a wide range of methods to control various aspects of their properties. One metal in particular is widely used for a variety of application. It is copper, and its nanoparticles have exciting applications for the electronics field, due to its wide range of particle morphologies.¹ Copper is an ideal choice, because of its low cost and abundance. Additionally, it lends itself to applications for both printed and flexible electronics.² Overall, copper nanoparticles are useful for a range of applications and purposes. The procedure outlined below is for the synthesis of copper nanoparticles and it was adapted from the second resource listed below.

Safety:

Diethylene and ethylene glycol are both an irritant to skin and eyes, and they are also toxic if they are ingested. Polyvinylpyrrolidone can be an irritant if inhaled. Also, the compound copper II sulfate pentahydrate is an irritant to skin, eyes, and if ingested. At high temperature mineral oil is a burn hazard if it comes into contact with skin or if ingested. Gloves should be worn when

handling irritant posing chemicals. Chemical splash goggles should be worn as well, in addition to working in a hood and avoiding ingestion or inhalation of any chemicals.

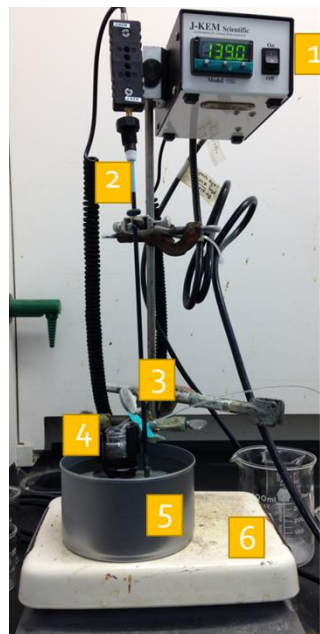
Materials:

- Polyvinylpyrrolidone (PVP), from Sigma Aldrich
- Diethylene glycol, 99% from Alfa Aesar, lot number: 10191456
- Ethylene glycol, from J.T. Baker Chemical Co. lot number: 612611
- Sodium phosphinate monohydrate (Sodium Hypophosphite), from Sigma Aldrich lot number: 24366-3
- Copper II sulfate pentahydrate, 98% extra pure from Acros Organics, lot number: A0297464
- Mineral Oil, from CVS Heath

Equipment:

1. Temperature controller
2. Thermocouple and cable
3. Ring stand and clamps
4. Scintillation vial
5. Mineral oil bath
6. Hot plate with stirring

Not pictured: syringe pump, syringe, tubing and stir bars.



Procedure:

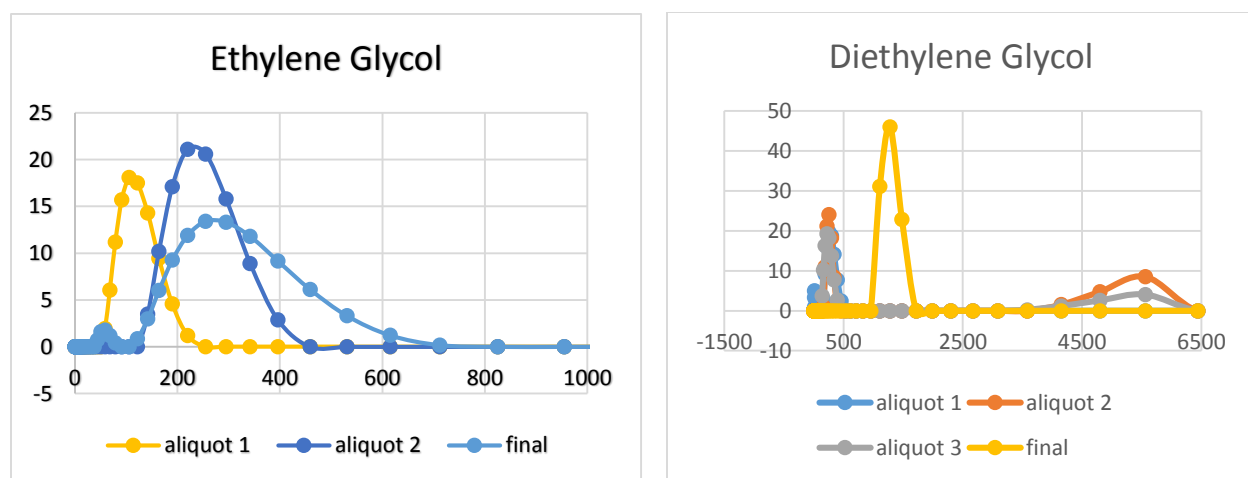
1. Create stock solutions of 1% PVP, 0.2M copper II sulfate pentahydrate, and 0.2M sodium hypophosphite in both ethylene and diethylene glycol. Note: in order for the copper solution to dissolve properly, the stock solutions were heated to a temperature of 100°C until all copper crystal had disappeared and solution was pale blue in color.
2. Combine 17.53mM sodium hypophosphite and 0.1% PVP solutions in reaction vessel and add the correct glycol solution to fill the total reaction volume accounting for the copper solution to be added via the syringe pump.
3. Heat open vessel using a mineral oil bath to a reaction temperature of 140 °C. Both bath liquid and reaction vessels should be stirred while heating, using stir bars.
4. Once the reaction vessel has reached 140°C, 20mM Cu solution is added using a syringe pump. The rate used for the 15mL reaction volume in a scintillation vial was 2.5mL/hr.

Note that the concentration of the copper solution is an approximation, because the solution easily crystalizes and filtering was done to ensure that only solution was transferred in the syringe pump.

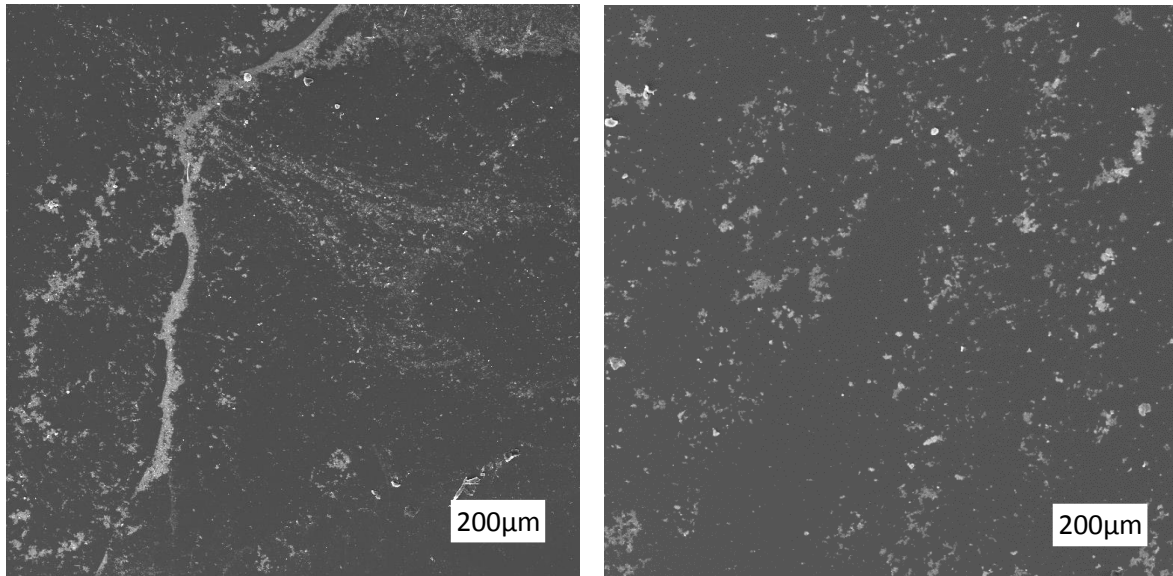
5. After the copper solution has been added. The vessel is allowed to react at 140 °C for 1 hour. As the reactants begin to form particles, aliquots of supernatant can be removed to study particle size and morphology at different stages of the reaction process. During the reaction the solution turns from clear to pale blue to dark brown/black in color as the particles form in solution.
6. Once the solution has reacted for an hour it is removed from heat, capped, and allowed to cool to room temperature. After the solution has cooled, particles are centrifuged and washed with distilled water to remove the glycol.
7. This procedure produces copper particles that are mainly mono-dispersed with a few small aggregates. The particles synthesized in an ethylene glycol have a size of about. The particles synthesized in diethylene glycol have a size of about.

Characterization:

Size characterization was done using the Zeta Sizer. Optical microscopy was used to confirm presence of particles on sample substrates, then Scanning Electron Microscopy and Energy Dispersive Electron Spectroscopy were used to classify them further.

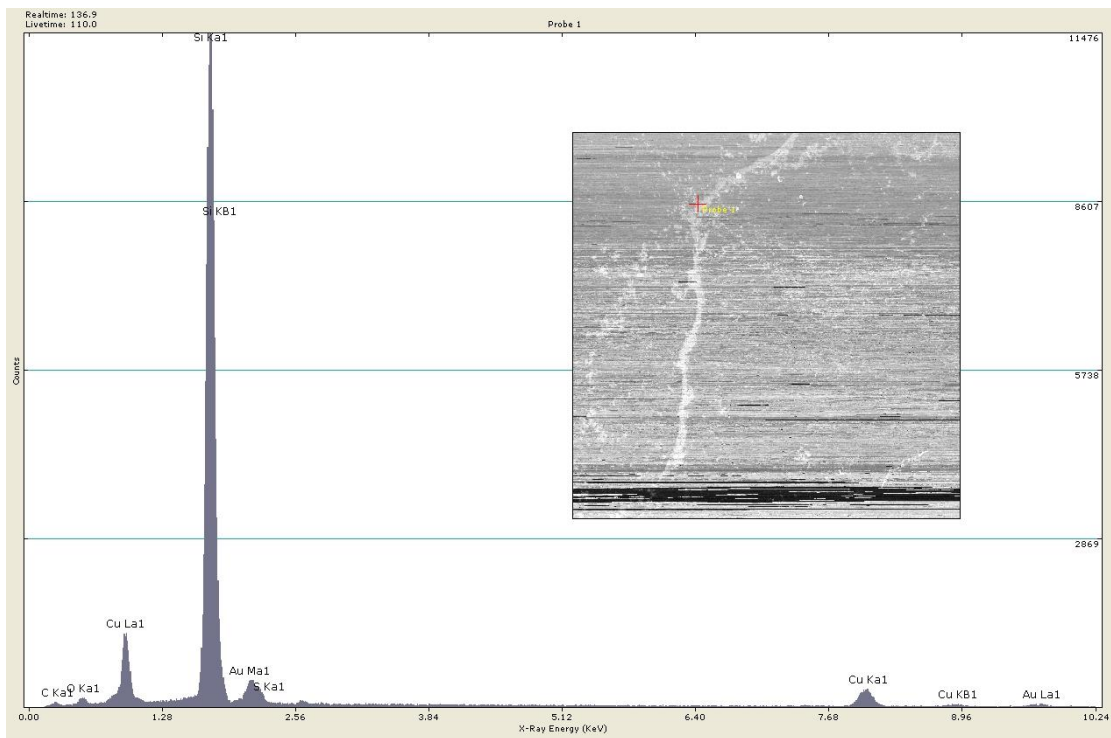


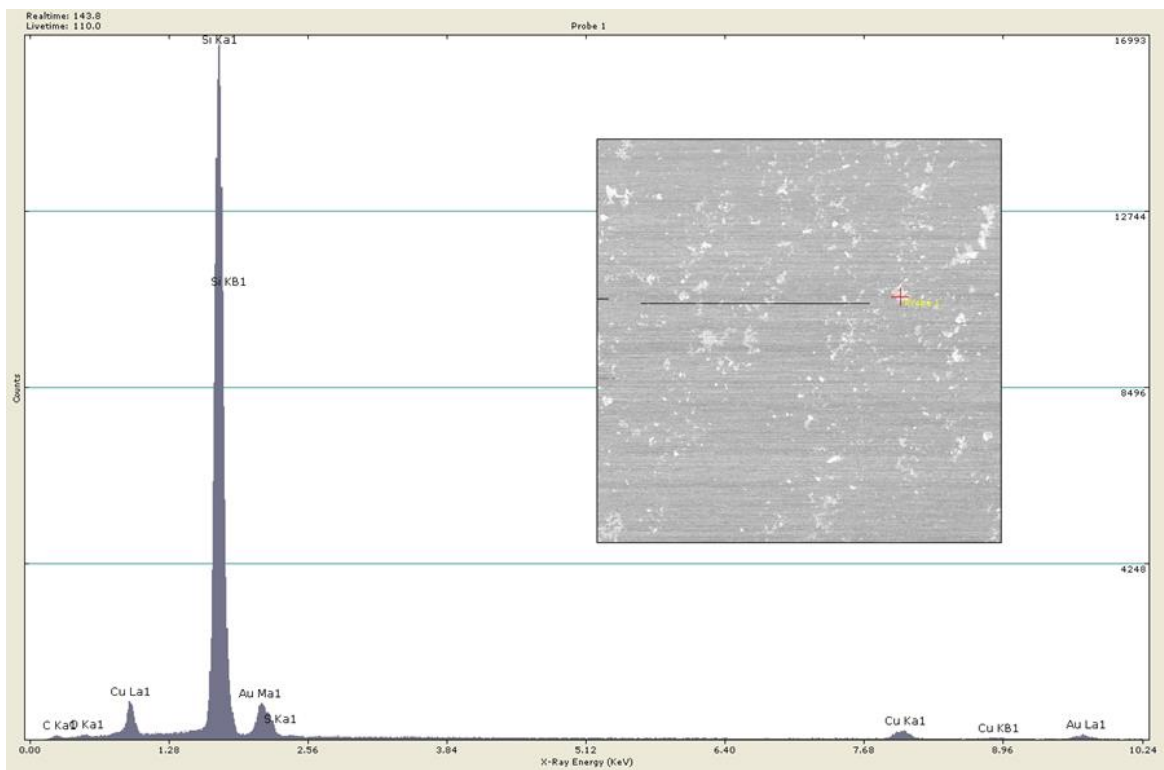
Above are the plots of the zeta sizer data for the ethylene glycol and diethylene glycol syntheses. Average particle size for the ethylene glycol final solution was 283.9 nm, while it was 2578 nm for the diethylene glycol solution.



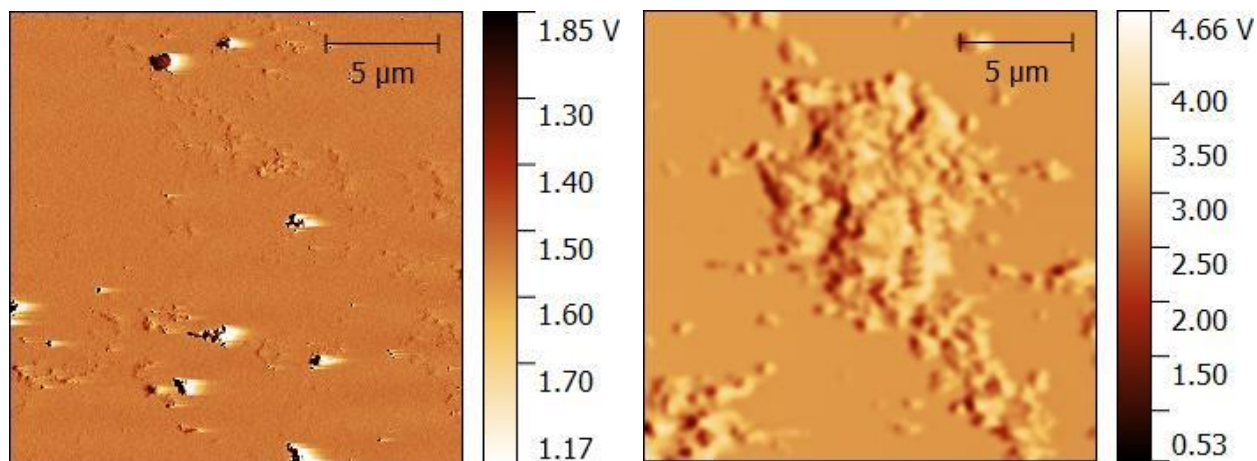
Above are SEM images of the copper nanoparticles, with the diethylene glycol synthesis on the left and ethylene glycol on the right. In both you can clearly see the different aggregates of particles as well as individual particles.

Below are EDS probe spectrums of the two different samples. In both the two characteristic copper peaks identify the particles selected as copper nanoparticles. We see gold, because the particles were sputter coated with gold and silicon because the samples have been mounted on a silicon wafer. The first figure is the diethylene glycol synthesis followed by the ethylene glycol synthesis.





AFM work was also done on the particle samples. Below are AFM scans in probe mode of the diethylene glycol synthesis (left) and in amplitude mode of the ethylene glycol synthesis (right).



References:

1. Khanna, P. A.; Gaikwad, S.; Adhyapak, P. V.; Singh, N.; Marimuhu, R. Synthesis and characterization of copper nanoparticles *Materials Letters* **2007**, *61*, 4711-4714.
2. Park, B. K.; Jeong, S.; Kim, D.; Moon, J.; Lim, S.; Kim, J. S. Synthesis and size control of monodisperse copper nanoparticles by polyol method *Journal of Colloid and Interface Science*. *2007*, *311*, 417-424.

Hydroxyapatite Nanocrystal Synthesis

Introduction

Hydroxyapatite is the primary mineral component in bones and as such has recently been garnering a lot of attention. It is currently being researched for a wide variety of applications ranging from use as either the primary component or coating in prosthetics, as thin film adhesives that will not interfere with imaging techniques, to even uses in drug delivery or as a possible cure for cancer. The goal of this research is to determine the feasibility of the synthesis of Hydroxyapatite nanoparticles and to lay the ground work for future research on this topic. To determine the viability of this synthesis process, multiple articles were consulted before selecting one method to adapt for our facilities here at Stout.

Safety

- Do all work in fume hood
- Wear Splash safety goggles, gloves, long pants and sleeves
- Observe standard lab safety procedure

Hazards

Orthophosphoric Acid

May be corrosive to metals

Causes severe skin burns and eye damage

Calcium Hydroxide

Causes burns

Harmful if swallowed

Materials

- Calcium Hydroxide 0.5M $Ca(OH)_2$
- Hot Plate
- Stir Bar
- Scintillation Vial
- Orthophosphoric Acid 0.3M H_3PO_4
- Beaker
- Temperature Regulator

Procedure

1. Fill beaker with water and place on hot plate to create a constant temperature bath using the temperature regulator (Temperatures between 25-85°, $T < 60^\circ C$ for Monocrystalline $T \geq 60^\circ C$ for Polycrystalline)
2. Fill the Scintillation vial with 5 ml of 0.5M $Ca(OH)_2$ ($\frac{1}{2}$ the volume of Hydroxyapatite desired)
3. Add Stir bar to Scintillation vial and place in temperature bath.
4. Inject 5 ml of 0.3M of H_3PO_4 (same volume as before) at a rate of 100ml/min or below for a reaction conversion rate of 100% (Essentially inject over a 3 second period)
5. Allow to react until the resulting aqueous suspension is a whitish and possesses a solid (Hydroxyapatite nanocrystals) content of 2.5 wt%

Calculations

Hydroxyapatite

$$.005L*(.5\text{mole}/1L)*(74.093\text{g}/1\text{mole})=0.1852325\text{g}$$

First Iteration Results

The first time this was ran it was done with 4 samples. Three of which followed the above procedure at various temperatures: ~60, ~30, ~80 °C. The 4th run was done at a near 1:100 dilution for the H₃PO₄ and ran for over a day at room temperature. This was done because the first three sample runs all yielded Hydroxyapatite that was much larger than desired. While the 4th run was significantly smaller, it still was in the order of microns as opposed to nanometers. This change in morphology was likely due to both a lower reaction temperature and lower concentration of orthophosphoric acid. Optical and SEM images in Appendix

Optical Microscopy Results

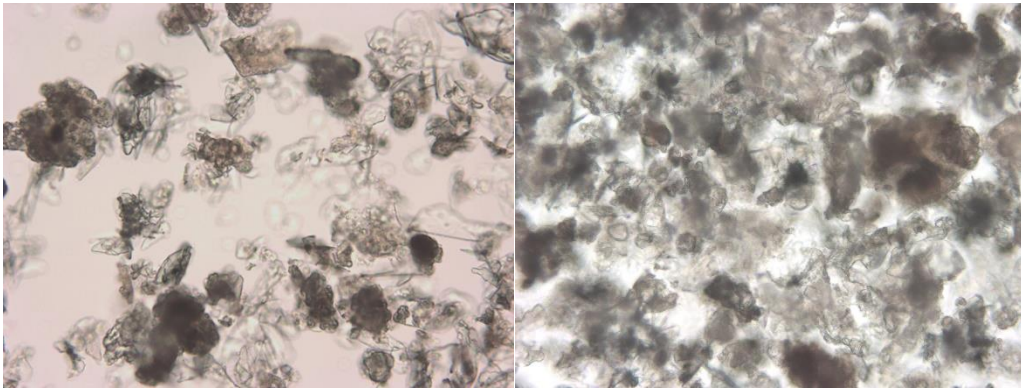


Figure 1: Sample A 20x

Figure 2: Sample B 20x

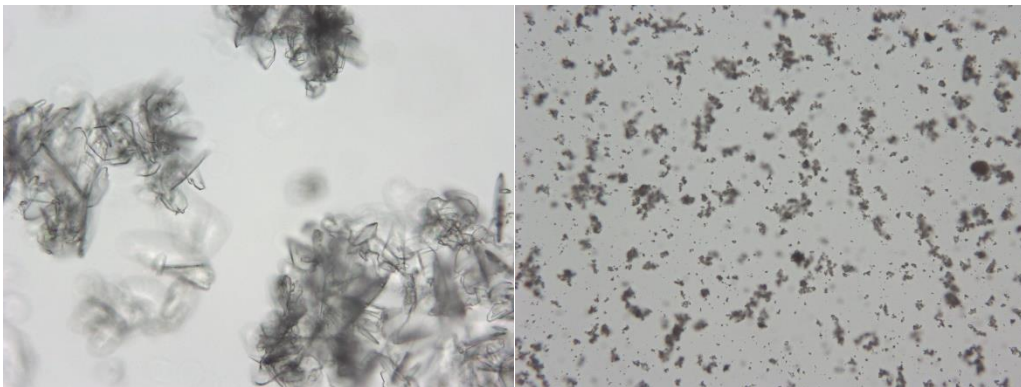


Figure 3: Sample C 20x

Figure 4: Sample D 20x

Scanning Electron Microscopy Results

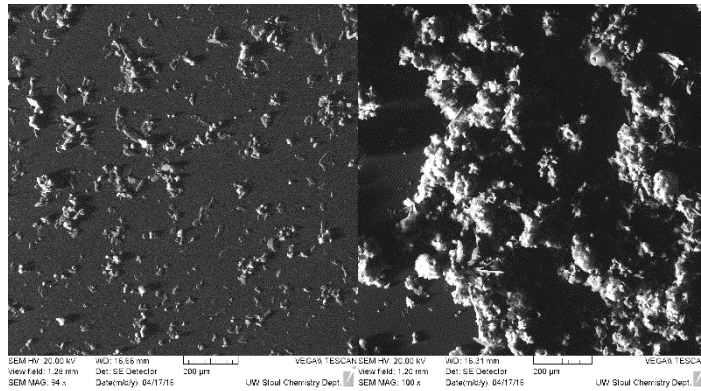


Figure 5: Sample A 100x

Figure 6: Sample B 100x

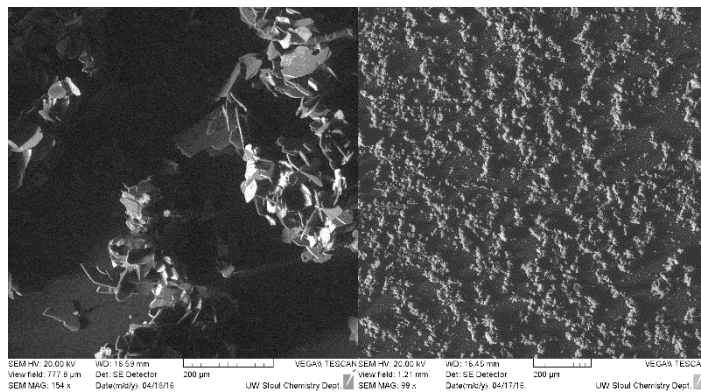


Figure 7: Sample D 100x

Figure 8: Sample C 154x

Future Direction

We believe that the major cause of our particles being much larger than those referenced in the procedure by Bouyer et al. is primarily the improper scaling of the rate of addition of the orthophosphoric acid to the solution making it too available and the reaction to happen almost instantaneously instead of evolving slowly. By properly scaling the addition rate, reacting in an ice bath as well as some fine tuning, we believe it will be possible to synthesize hydroxyapatite crystals for using in synthetic bone research here at Stout.

Reference Material

- Bouyer, E., F. Gitzhofer, and M. I. Boulos. "Morphological Study of Hydroxyapatite Nanocrystal Suspension." *Journal of Materials Science: Materials in Medicine* 11 (2000): 523-31. Web.
- Ferraz, Maria Pia, Fernando Jorge Monteiro, and Candida Maria Manuel. "Hydroxyapatite Nanoparticles: A Review of Preparation Methodologies." *Journal of Applied Biomaterials & Biomechanics (JABB)* 2 (2004): 74-80. Web.

Magnetite Nanoparticle Synthesis

Cody Lang

University of Wisconsin—Stout, Menomonie, WI 54751

Submitted 18 April, 2016

Magnetite nanoparticles around the size of 200nm and 400nm were created using both a co-precipitation method and a solvent-less thermal decomposition of ferrocene. Co-precipitation synthesis included two iterations of the exact same process to test the robustness of the process. The thermal decomposition synthesis included two reactions of different weight ratios to test how drastic of a change it would have. Every sample was sized a long period of time after they were created; showing the durability of the particles. This led to larger than anticipated sizes since magnetic nanoparticles tend to aggregate due to a strong magnetic dipole-dipole interaction. Both thermal decomposition and one co-precipitation reactions after a long time of sitting yielded nanoparticles around 200nm in size. One co-precipitation reaction, after a long period of time, yielded nanoparticles around 400nm in size. Every sample shows ferromagnetic behavior.

Introduction

Magnetite (Fe_3O_4) is a unique form of iron oxide that exhibits electric and magnetic properties that other iron oxides do not. This is due to the Fe^{2+} and the Fe^{3+} ions in each molecule. Due to these ions, electrons can easily transfer throughout the particle. Magnetite displays properties such as super paramagnetism at certain sizes. Initially the Fe^{2+} and the Fe^{3+} ion spins are oriented oppositely, canceling out their magnetic fields. When in the presence of an external magnetic field, the spins all line up, creating a new magnetic field. Due to this property and its low toxicity, magnetite nanocubes are used in magnetic biomedicine; specifically magnetic resonance imaging (MRI). The specific characteristics of magnetite depends on the exact shape and size of the particles. Other uses for magnetite nanoparticles include information storage media, heavy metal ion removal, electromagnetic wave absorption, ferrofluids, and biocatalysts.

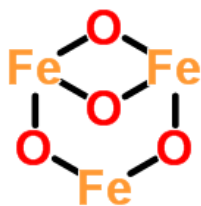


Fig 1. Iron (II, III) oxide also known as magnetite.

Experimental Method

Co-precipitation Synthesis

The suggested amounts in the original document were decreased to 10% of what was used so that smaller reactions were taking place. .28g of $\text{FeSO}_4 \cdot 7\text{H}_2\text{O}$ and .40g of $\text{Fe}_2(\text{SO}_4)_3$ were dissolved in 10mL of DI water for 5 minutes in a 50mL beaker using a magnetic stir bar. 0.08g of sodium dodecyl sulfate (SDS) was added to the solution while stirring. Then the pH of the solution was adjusted to 12 by adding solid NaOH. The approximate amount for this reaction was around 0.4g of NaOH. After the pH was adjusted to 12, the solution was left to stir for 20 minutes. The original procedure calls for a lamp (wavelength 400-750nm) to be placed within 10cm of the beaker for 0-60minutes. This was not done for the first synthesis. The black precipitate that formed was then immediately washed alternately with DI water and ethanol several times until the pH was returned to neutral. The black precipitate were dried at room temperature (fig 3a).



Fig 2. Co-precipitation reaction set up.

The second synthesis via co-precipitation was done in the exact same way except after the 12 pH solution was stirred for 20 minutes it was allowed to sit unstirred for 30 minutes in ambient light before being washed with DI water and ethanol (fig 3b). The resulting powder was left to sit for a long period of time before sizing.

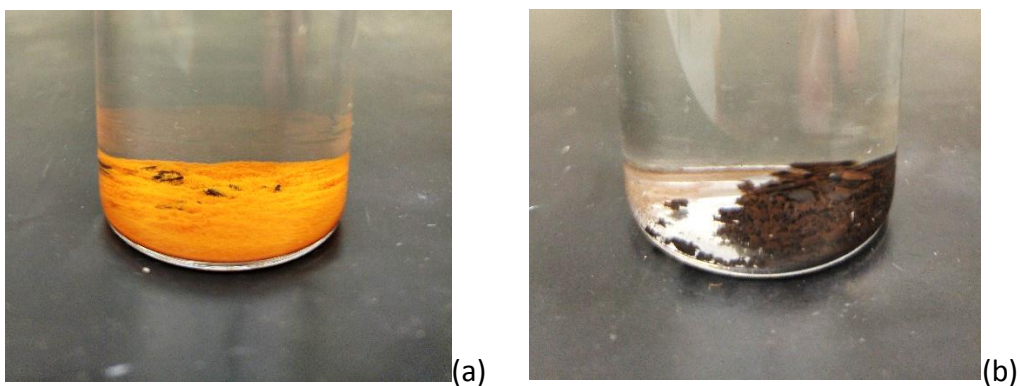


Fig 3. The precipitate that was formed during the co-precipitation synthesis. (a) First synthesis.
(b) Second synthesis.

Solvent-less Thermal Decomposition Synthesis

Ferrocene (>98%, ACROS ORGANICS) and polyvinylpyrrolidone (PVP k90, M_w 360,000) were grinded together at a 1:1 weight ratio of ferrocene to PVP, totaling 300mg. The solid mixture was then placed in an empty and cleaned stainless steel threaded CO₂ cartridge (fig 4). This was done because a 1mL stainless steel sealed cell was not available. The cell was sealed shut with Teflon tape to ensure an air tight seal. The steel cell with the solid mixture was then placed in a 350°C preheated furnace to anneal for 2 hours. The cell was then removed and allowed to cool to room temperature. The resulting black powder was then washed with ethanol extensively via centrifugation (fig 5a). The final solution was also left for a long period of time before characterization.



Fig 4. Threaded CO₂ cell used for the thermal decomposition of ferrocene

The final synthesis was also done via solvent-less thermal decomposition of ferrocene. This synthesis was completed exactly the same to the first thermal decomposition synthesis except the weight ratio of ferrocene to PVP was 1:2 instead of 1:1 (fig 5b).

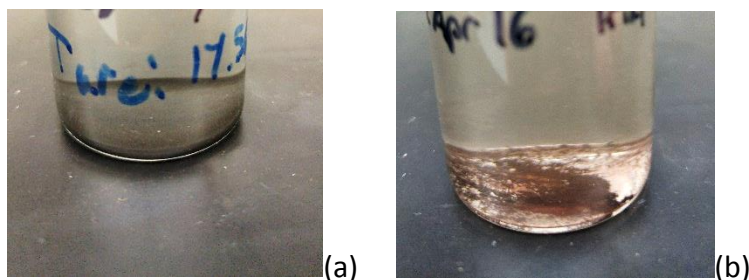


Fig 5. Powder collected from thermal decomposition reactions in ethanol. (a) 1:1 weight ratio.
(b) 1:2 weight ratio.

Sizing

All the resulting precipitates and powders were sized using a zeta sizer. A zeta sizer measures particle size by Brownian motion, which is the random movement of particles in a liquid due to bumping into surrounding particles. Smaller particles will move faster in a liquid than a larger particle will. The instrument will take two “images” of the solution at different time frames. By measuring how much a particle has moved, the size of the particle can be calculated. This is a simple explanation of the process.

Each synthesis was sized using this method. The first co-precipitation reaction (fig 4) and both thermal decomposition reactions (fig 6 and fig 7) yielded particles just under the 200nm range. The second co-precipitation (fig 5) reaction yielded particles around 400nm. As to why this is, it is still unclear. It could be due to the solution being left in ambient light for 30 minutes before washing or to the degree of washing.

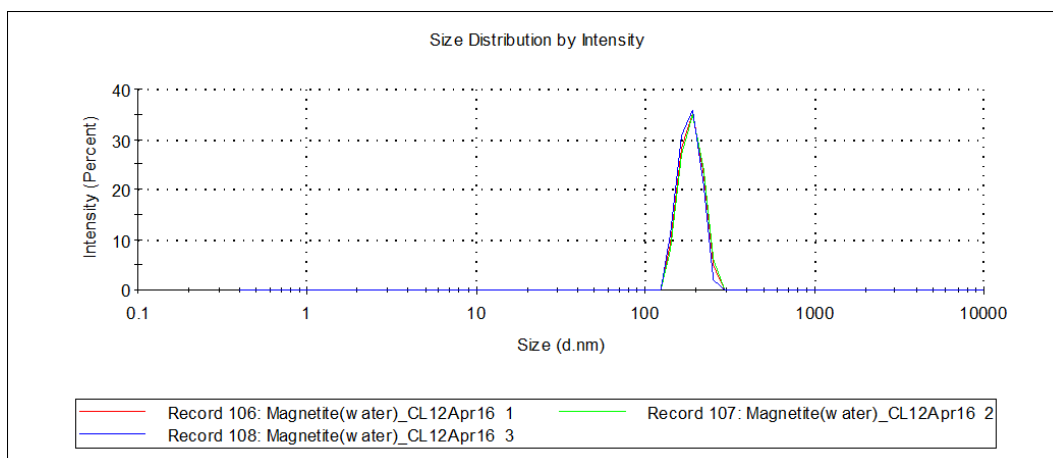


Fig 4. Zeta sizing data for first co-precipitation synthesis.

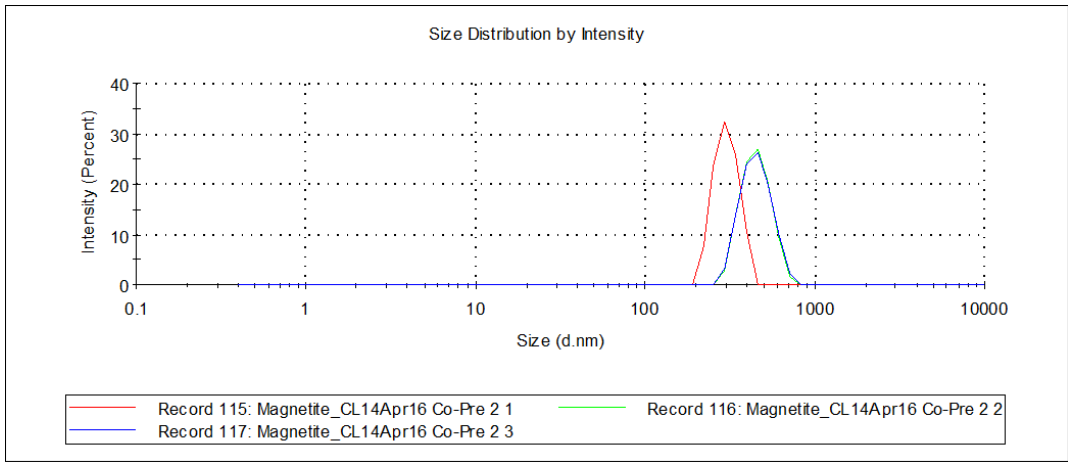


Fig 5. Zeta sizing results for second co-precipitation synthesis.

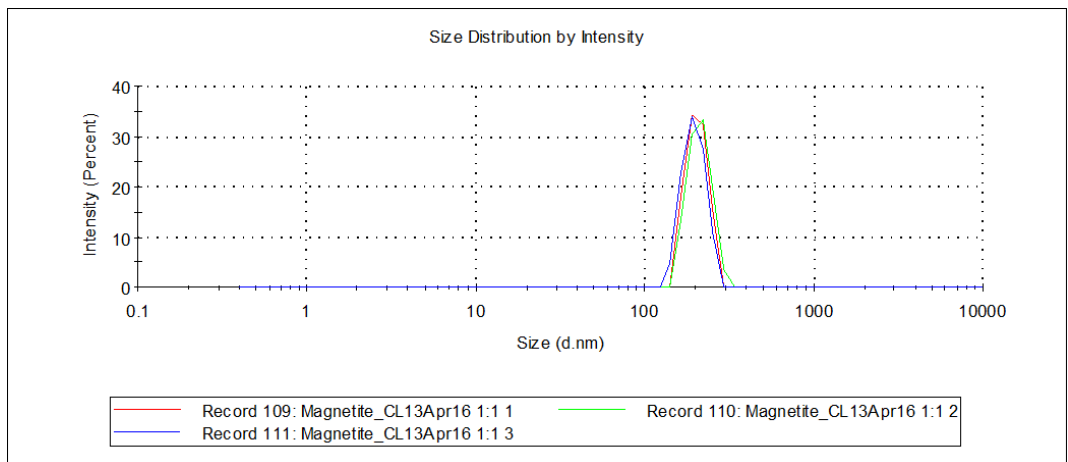


Fig 6. Zeta sizing results for first thermal decomposition synthesis. Ferrocene to PVP weight ratio 1:1.

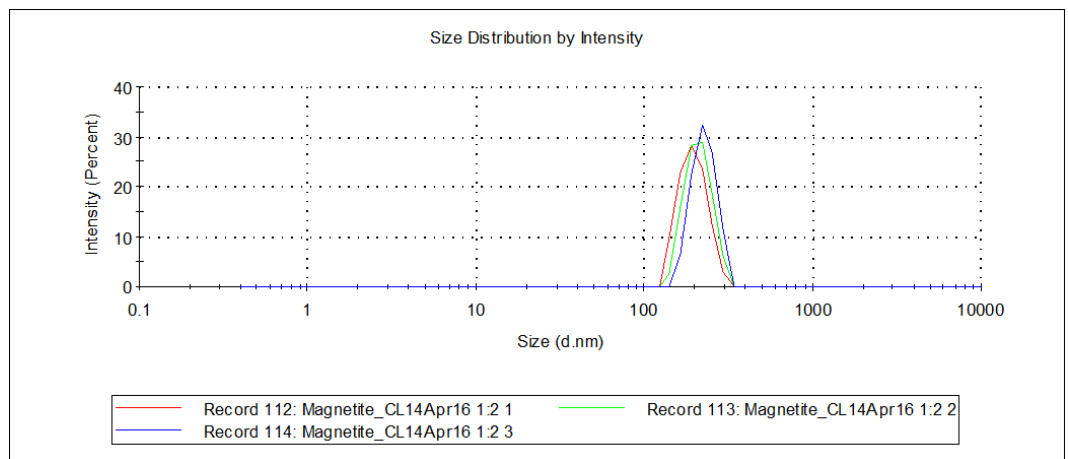


Fig 7. Zeta sizing results for first thermal decomposition synthesis. Ferrocene to PVP weight ratio 1:2.

SEM and EDX Results

SEM images and EDX characterization was attempted to be completed but some files were not saved correctly. This will be a report on what was saved and exported correctly. Samples were coated in a thin layer of gold before entering SEM. Visibly it can be seen that the first co-precipitation synthesis may not have been washed as thoroughly as the second co-precipitation synthesis. This led to it being extremely difficult to find magnetite particles by themselves in the solution under an SEM. One image was obtained and EDX spectroscopy was used at various points to determine the composition of the precipitates from the first co-precipitation reaction (figs 8a-8d).

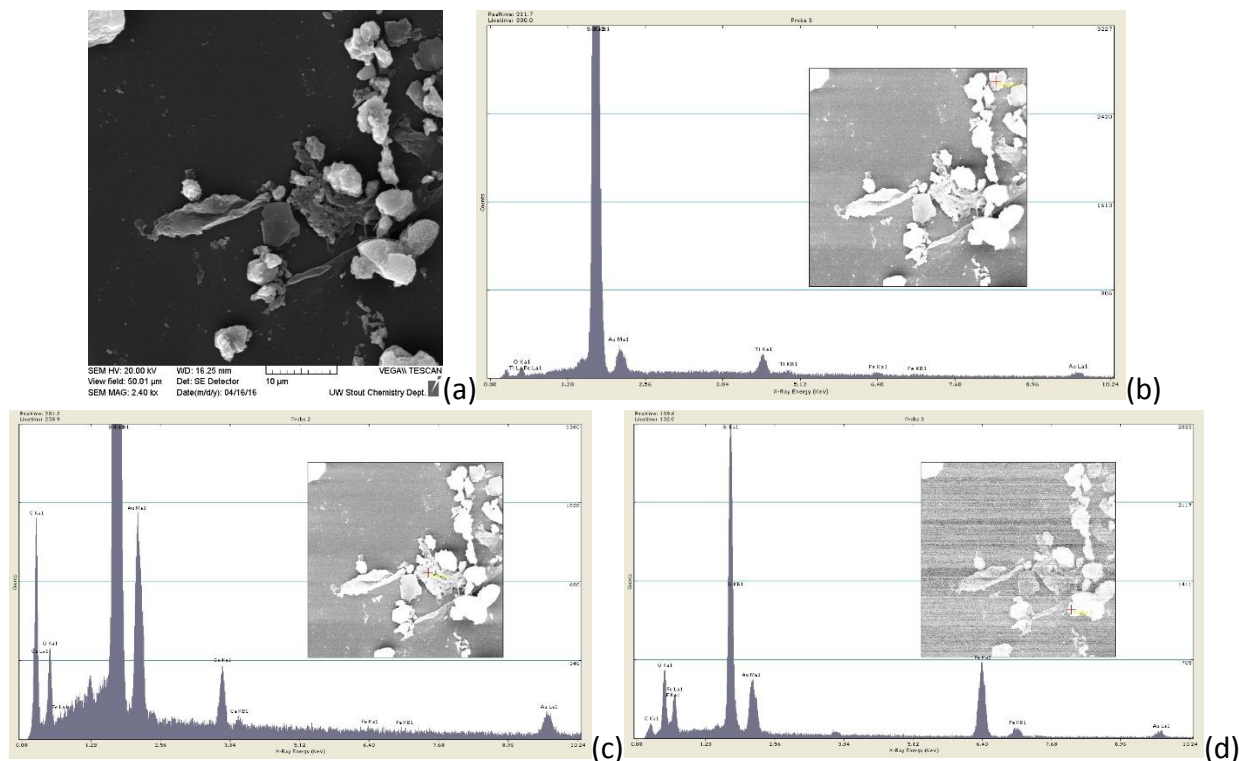


Fig 8a. SEM image of precipitates from first co-precipitation reaction. (a) and (b) EDX results not showing a whole lot of iron in the some of the sample suggesting the solution has a lot of extra stuff in it. (d) Showing that there is iron in the solution that was created.

The second iteration of the co-precipitation synthesis was washed more thoroughly than the first. This resulted in much more magnetite being present in the sample. A large area of 50μm was used for the EDX imaging with multiple probe locations. Exact morphology of individual particles was proven to be more difficult than expected with the equipment at hand. Fig 9a shows the larger area from which the EDX probes (figs 9c-9f) were taken. It can be seen that there is much more magnetite in the first co-precipitation sample. Another interesting thing to note is the large difference in the amount of oxygen to the amount of iron. Magnetite is Fe_3O_4 which has a composition ratio of 3:4 for iron to oxygen. The EDX probe results show that there is a lot more iron in the samples than oxygen. The reason for this is unknown.

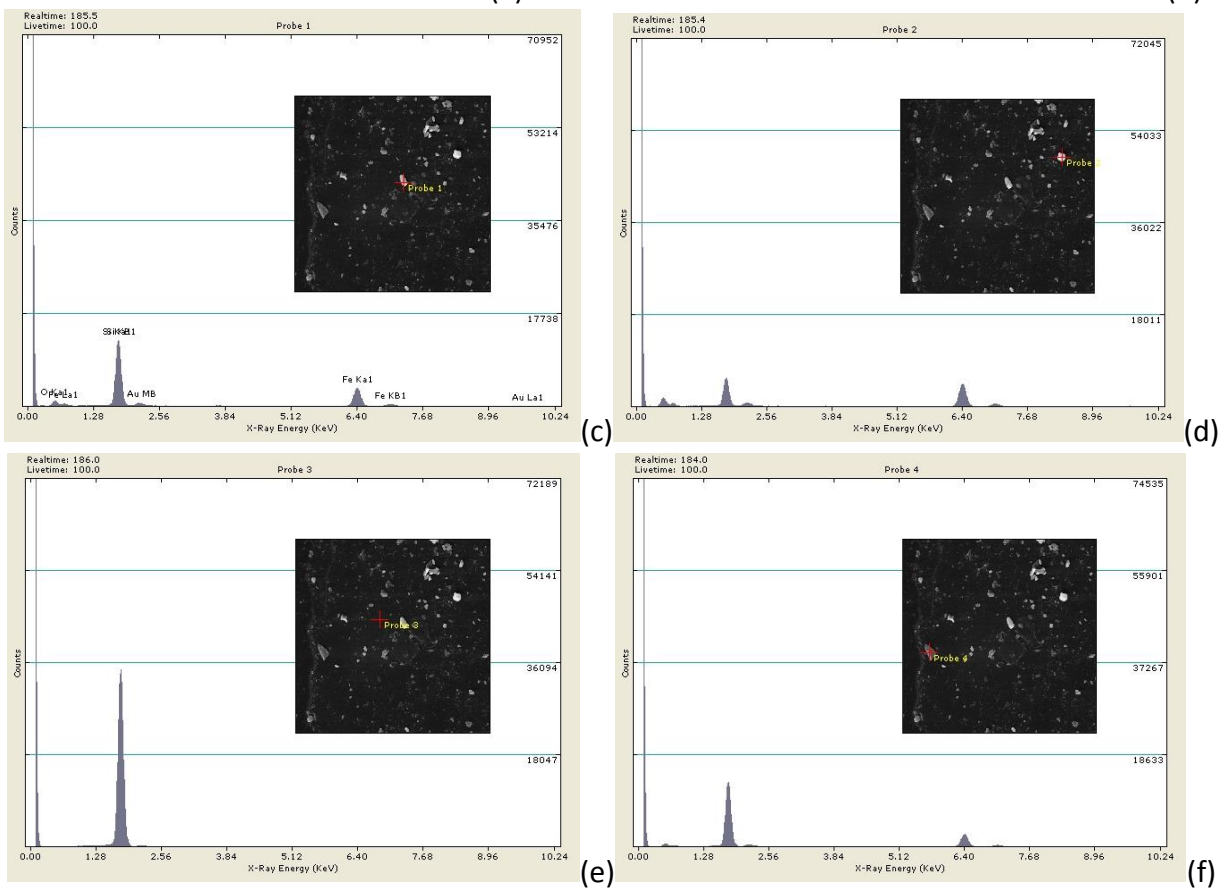
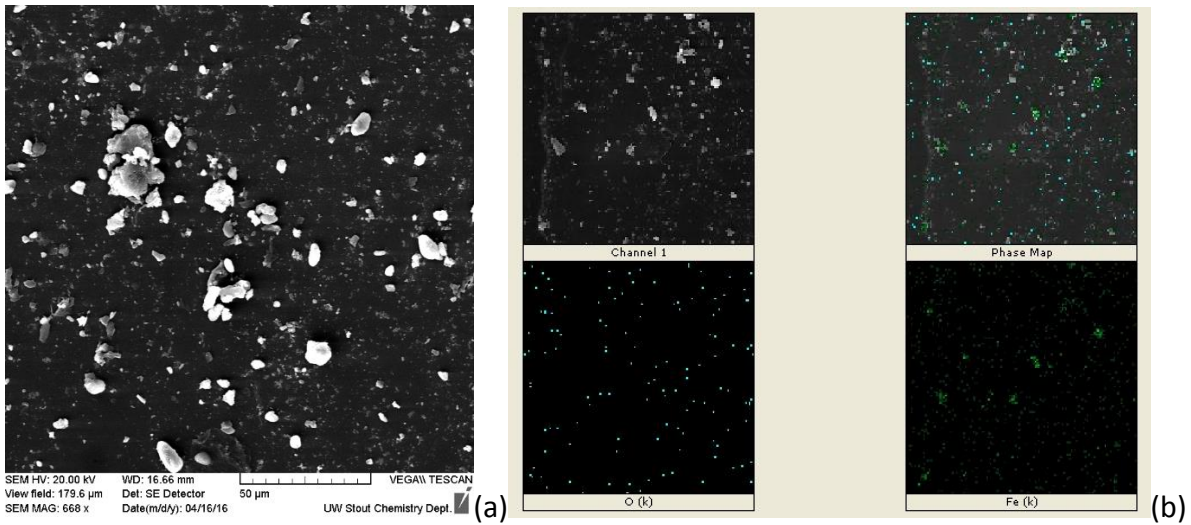


Fig 9a. Field of view in which EDX probes were taken. (b) EDX X-ray map showing the location of some of the oxygen and iron in the sample. (c)-(f) Probes results in different locations showing the iron and oxygen in the sample.

SEM images of the particles from the first thermal decomposition synthesis show a large number of smaller sized particles dispersed across the surface of the substrate. There are not as many large aggregates on the surface. Unfortunately, the probe data was saved incorrectly so it cannot be displayed. The SEM images show many small particles that could not be view clearly with the SEM on hand. Some of the larger particles, about 500nm in size, almost seem to have a cubic shape to them; this could not be verified at the time.

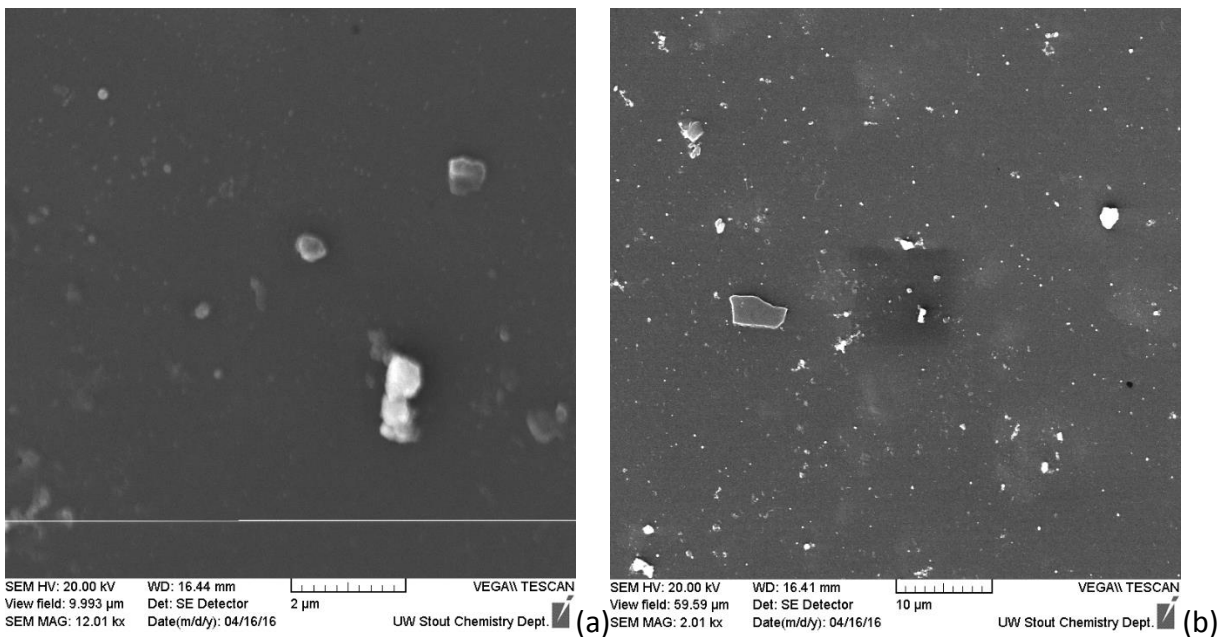


Fig 10a. A 10µm view of some magnetite nanoparticles. (b) A zoomed out view of the fig 10a.

A similar thing happened with the EDX probe data for the second thermal decomposition synthesis. It was saved but not exported so it could not be included in this report. The particles seemed to have aggregated in this sample; making individual shapes hard to make out. Although smaller clumps in the larger clumps look to be about the size that the zeta sizer reported, about 200nm (fig 11).

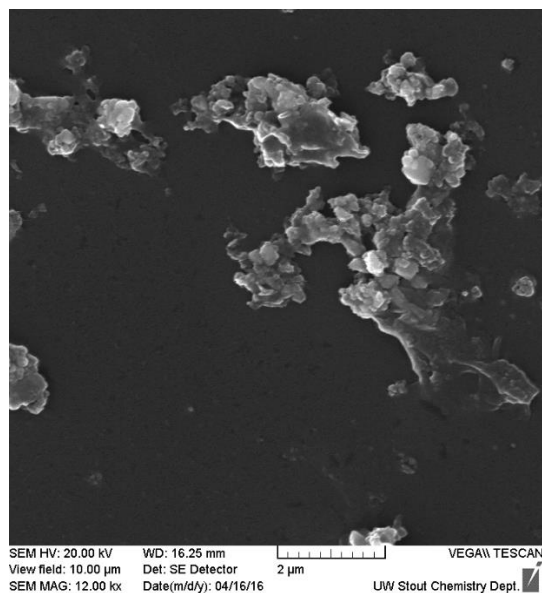


Fig 11. A 10 μ m view of a cluster of magnetite nanoparticles trapped in a PVP matrix.

Results and Conclusions

The goal of this project was to pick a nanoparticle and follow a procedure to create said particle. Magnetite nanocubes were the selected particle for this project. Two iterations of two different synthesizes were attempted and the conclusion is that nanoparticles can be very difficult to create. They are also not the most stable things. As noted above, magnetite tend to aggregate easily making disperse particles difficult. Magnetite, particles were created by they ended up be many times larger than expected. Also, due to equipment limitations, clear images of the exact morphology could not be gathered.

References

- Amara, D., & Margel, S. (2011). Solventless thermal decomposition of ferrocene as a new approach for the synthesis of porous superparamagnetic and ferromagnetic composite microspheres of narrow size distribution. *Journal of Materials Chemistry*, 21(39), 15764-15772.
- Shen, L., Qiao, Y., Guo, Y., Meng, S., Yang, G., Wu, M., & Zhao, J. (2014). Facile co-precipitation synthesis of shape-controlled magnetite nanoparticles. *Ceramics International*, 40(1), 1519-1524.
- Gao, G., Liu, X., Shi, R., Zhou, K., Shi, Y., Ma, R., ... & Qiu, G. (2010). Shape-controlled synthesis and magnetic properties of monodisperse Fe₃O₄ nanocubes. *Crystal Growth & Design*, 10(7), 2888-2894.



Aaron Forde
Stamp of Approval

Simple Sol-Gel Titanium Dioxide Nanoparticle Synthesis

Introduction:

Nanostructured Titanium Dioxide (TiO_2) is a material that has been attracting a lot of attention due to the unique properties that it exhibits. In particular, nanostructured TiO_2 powders have useful optical, dielectric, and catalytic properties which make it a prominent material in industry.

TiO_2 nanoparticles will be synthesized using a sol-gel method where a titanium precursor (titanium isopropoxide) undergoes hydrolysis to form a titanium hydroxide. The titanium hydroxide then condenses to form a hydrated TiO_2 and H_2O . The resultant hydrated TiO_2 suspension is then peptized, where the solution is heated to 70 (or 80) degrees Celsius for 18 to 20 hours.

The synthesis will be conducted in scintillation veils, with a total solution volume of 10 mL. This process can be easily scaled up, if desired.

Chemicals for Synthesis:

Titanium Precursor:

- Titanium Isopropoxide
 - Titanium Isopropoxide is sensitive to moisture in the air (it will undergo hydrolysis with the vapor in the air), so before storing primary and secondary containers it is **highly recommended to gas purge the containers** by blowing inert gas (Argon, Helium, ect) into the head of the container to remove air from the primary and secondary containers. Otherwise you end up wasting precursor.

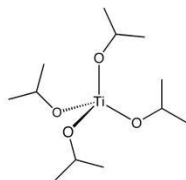
Peptization Electrolyte:

- Isopropanol

Solvent:

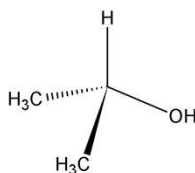
- Deionized Water

Titanium Isopropoxide



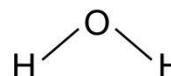
By Smokefoot - Own work, Public Domain,
<https://commons.wikimedia.org/w/index.php?curid=3037723>

Isopropanol



<https://commons.wikimedia.org/wiki/File:Isopropanol.PNG>

Water



https://commons.wikimedia.org/wiki/File:3AH2O_-_2d.svg
By Crazytony (Own work) [Public domain]
via Wikimedia Commons

Equipment:

Glasswear:

- 50mL Beaker
- 3 Scintillation Vials ----->
 - 1 of the vials is to do the reaction in
 - 2 of the vials are used as secondary containers for the precursors



Temperature Controller:

- J-KEM Scientific Model 150

Pipettors:

- 5mL Pipetter ----->
- 20-200 Microliter Pipetter----->



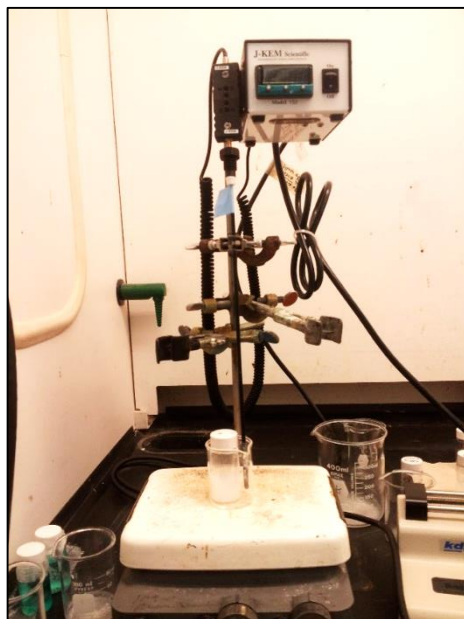
Miscellaneous:

- Hot Plate
- Stir Bar
- Eppendorf microtube ----->
- Ethylene Glycol



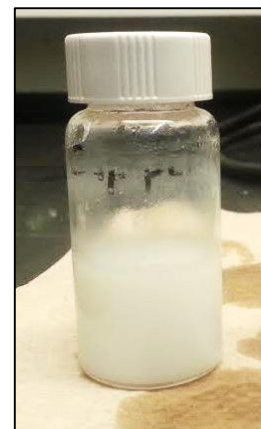
Equipment Setup:

- Follow the instruction manual with the J-KEM temperature controller to set it up.
- Put the scintillation vial that the synthesis will be conducted in into the 50ml beaker and place on the hot plate. Place the stir bar into the 50ml beaker as well. Position the scintillation vial so that it sits atop of the stir bar.
- Now pour ethylene glycol into the 50ml beaker to fill it approximately half way.
- Position the temperature probe into the beaker. The tip of the probe should be submerged so that it is about an inch from the bottom of the 50ml beaker.
- Turn on the J-KEM temperature controller and put the set-point to 60 degrees Celsius.



Process:

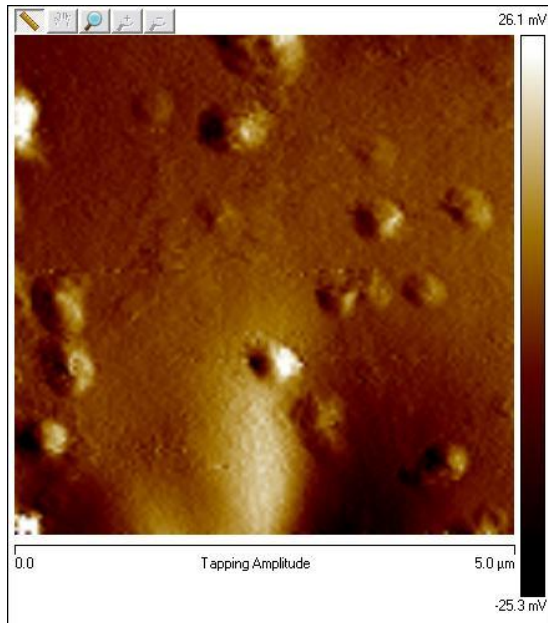
- Prepare **9.26 mL of deionized H₂O** of desired pH in a scintillation vial
- Place the scintillation vial of deionized water on a temperature controlled heating element with magnetic stirring capability.
- Heat the deionized water to 60 degrees Celsius.
- Mix together **0.17 mL of Titanium Isopropoxide** and the **0.15 mL of Isopropanol** in a 1mL Eppendorf microtube. Use the 20-200uL pipettors to take these volumes of solution out of the secondary containers.
- Transfer the mixture prepared in step 4 to a pipetter will allow it to be added dropwise to the 9.26 mL of H₂O.
- Start to add the solution from step 5 dropwise to the heated water, while stirring the water vigorously.
- You should now have a turbid (cloudy) solution.
- Let the peptization process react for 18 to 20 hours.



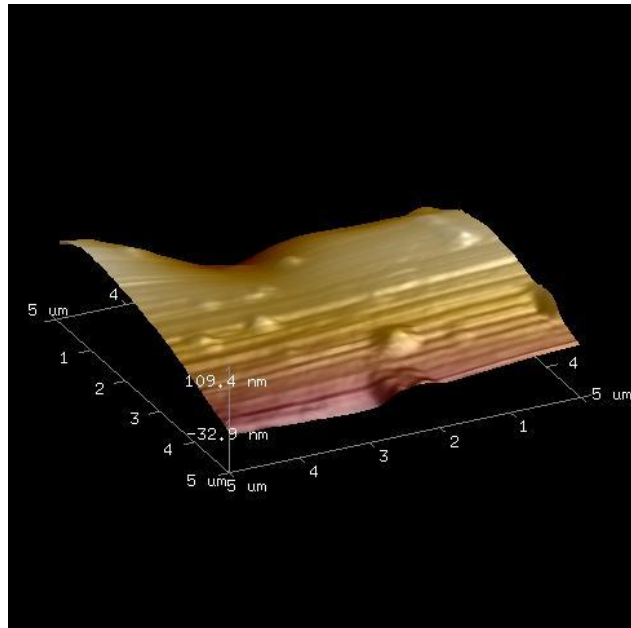
Size Analysis Results:

With this synthesis procedure you will get Titanium Dioxide nanoparticles with an average size of approximately 300 nanometers.

On an AFM you should expect the singlet (non-aggregated) nanoparticles to look similar to the images below:

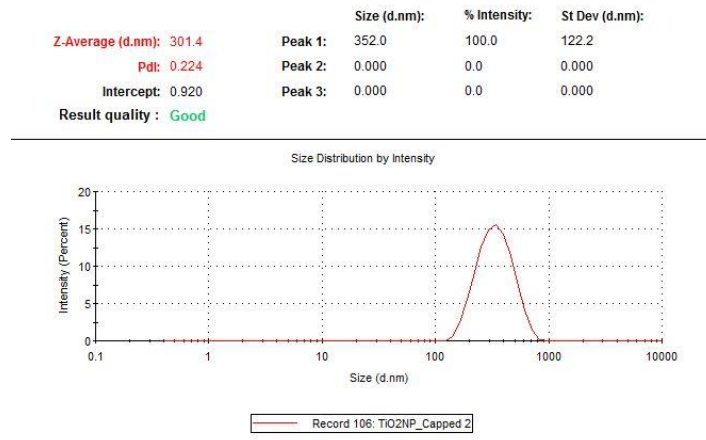


Amplitude Tapping image from the Innova AFM



3-D representation of the Amplitude Tapping image

Using the Zetasizer to characterize the particle sizes you should expect to data that looks similar to the image below:



If there is a tiny peak around the 1000nm size range that just indicates that there is a small degree of aggregation occurring between the nanoparticles.

Calculations:

The starting volumes are based on the original paper that the synthesis is based off of.

Moles of H₂O:

$$250 \text{ mL} * [1 \text{ g/mL}] = 250 \text{ g}$$

$$250 \text{ g} * [1 \text{ mol}/18 \text{ g}] = 13.89 \text{ mols H}_2\text{O}$$

Moles of Titanium Isopropoxide:

$$5 \text{ mL} * [0.937 \text{ g/mL}] = 4.685 \text{ g}$$

$$4.685 \text{ g} * [1 \text{ mol}/284.22 \text{ g}] = .016 \text{ mols}$$

Moles of Isopropanol:

$$15 \text{ mL} * [0.786 \text{ g/mL}] = 11.79 \text{ g}$$

$$11.79 \text{ g} * [1 \text{ mol}/60.1 \text{ g}] = .20 \text{ mols}$$



Aaron Forde
Stamp of Approval

Catalyzed Sol-Gel Titanium Dioxide Nanoparticle Synthesis

Introduction

This synthesis is similar to the “Simple Sol-Gel Titanium Dioxide Nanoparticle Synthesis” in that it uses the same chemical reaction that leads to titanium dioxide nanoparticles. In the case of the “Simple Sol-Gel” method the chemical reaction happens in such a large volume that the kinetics are slow so it requires an increase in temperature to drive the peptization process. In the synthesis that will be conducted here the opposite occurs. The kinetics of the nanoparticle formation happen so quickly that the synthesis can be conducted at room temperature.

The total reaction volume will be 2.87 mL and will be carried out in a scintillation vile. Two separate solutions containing the precursor and the hydrolysis agent will be added dropwise to the scintillation vile to produce the nanoparticles. Due to physical constraints, a high degree of control over the drop rate could not be achieved so the nanoparticle size distributions varied from each experiment (anywhere from 250nm to 450nm for average sizes). By following the academic paper that this synthesis is based off of a higher degree of control can be had over the nanoparticle size distribution.

Materials

Titanium Precursor:

- **Titanium Isopropoxide**
 - Titanium Isopropoxide is sensitive to moisture in the air (it will undergo hydrolysis with the vapor in the air), so before storing primary and secondary containers it is **highly recommended to gas purge the containers** by blowing inert gas (Argon, Helium, ect) into the head of the container to remove air from the primary and secondary containers. Otherwise you end up wasting precursor.

Peptization Electrolyte:

- **Isopropanol**

Solvent:

- **Deionized Water**

Hydrolysis Catalyst:

- **1M Hydrochloric Acid**

Equipment:

Glasswear:

- 3 Scintillation Vials ----->
 - 1 of the vials is to do the reaction in
 - 2 of the vials are used as secondary containers for the precursors



Pipettors:----->

- 5mL Pipetter
- 20-200 Microliter Pipetter



Miscellaneous:

- Stir Bar
- Magnetic Stirrer
- Eppendorf microtube ----->
- Disposable plastic pipets



Equipment Setup

- Place a scintillation vial on top of a magnetic stir plate
- Place an appropriately sized stir bar into the scintillation vial



Process:

- Prepare two Eppendorf microtubes to mix two separate solutions together. One microtube will be a mixture of the Titanium Isopropoxide precursor and Isopropanol. The other microtube will be a mixture of Isopropanol, Deionized water, and Hydrochloric Acid.
- Mix together into one of the microtubes (in this order):
 - 1.283 mL Isopropanol
 - 0.103 mL Deionized Water
 - 0.039 mL Hydrochloric Acid (1 M)
- In the other microtube mix together (in this order):
 - 1mL Isopropanol
 - 0.435mL Titanium Isopropoxide
- Place a scintillation vile with a magnetic stir bar in it on top of a magnetic stir plate. Turn on the magnetic stir plate so that the magnetic stir bar is rotating at a fast rate (turn the dial to approximately the 7 or 8 setting)
- Pull each of the prepared solutions into two separate disposable plastic pipettes.
- Drip each of these solutions into the scintillation vile at a slow and constant rate until each of the pipets are empty.
- Let the solutions mix for 5 minutes.
- Turn off the magnetic stir plate. Now you should have a gel like substance similar to the samples shown below.



This is what the final product should look like. It is a white, gel substance.

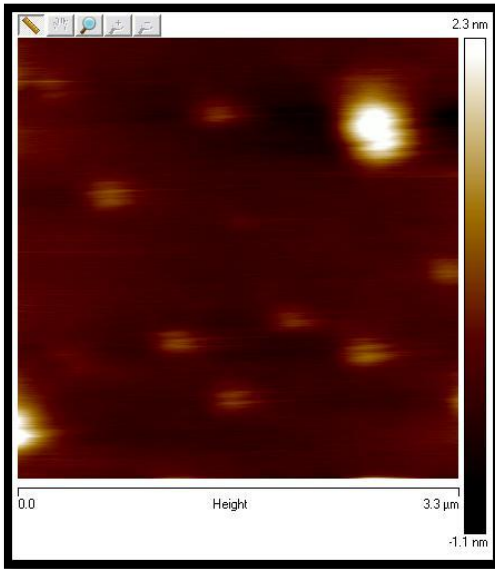


This is an illustration on how the two separate solutions were added drip-wise to the scintillation vile.

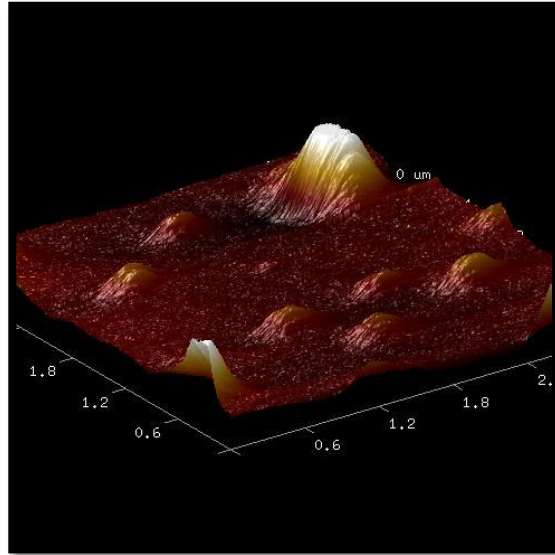
Size Analysis Results:

There is a degree in variability in the size of the nanoparticles produced using this method. In general though, the majority of the nanoparticles should have an average size on the range of 250nm to 450 nm.

On an AFM you should expect the singlet (non-aggregated) nanoparticles to look similar to the small peaks below (scan range is 3.3um x 3.3um):

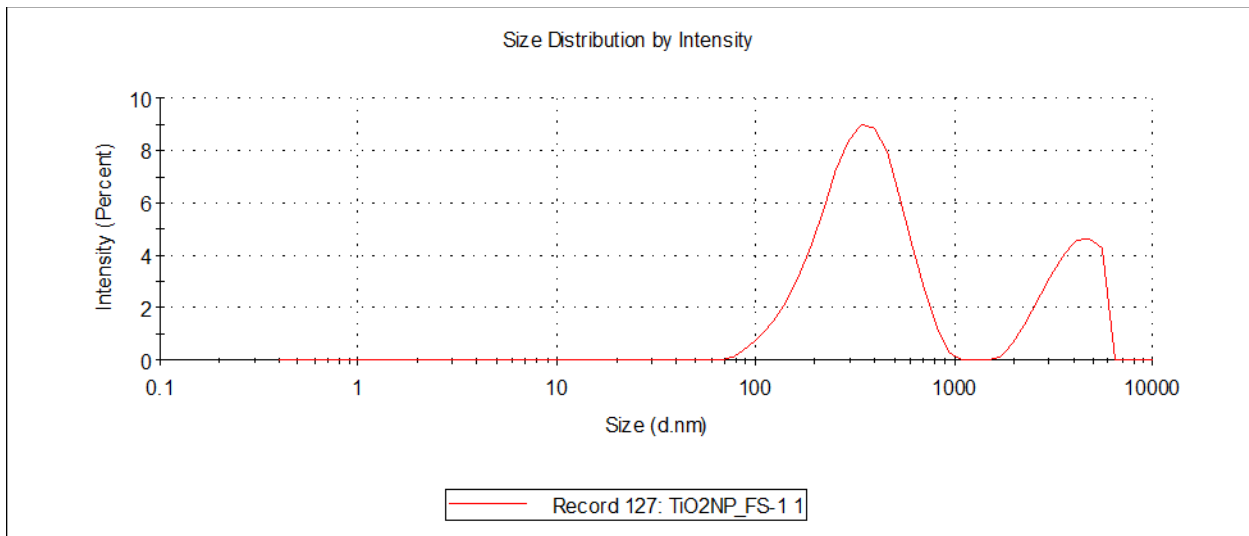


Topography image of the nanoparticles on the Innova AFM



3-D representation of the Topology

Using the Zetasizer to characterize the particle sizes you should expect to data that looks similar to the image below:



The first peak happens at 361nm and the second peak occurs at 3970nm. By using centrifugation it would be possible to filter out the larger nanoparticles to leave only the smaller distribution.

Calculations:

The volume calculations are based off the stoichiometry of the chemical reaction. For maximum yield, the molar ratio of water to titanium isopropoxide should be 4 to 1. And for the catalyst the molar ratio of hydrochloric acid to titanium isopropoxide should be 0.5 to 1.

To determine the amount of titanium isopropoxide needed for a given amount of isopropanol to get a 1 M solution of titanium isopropoxide is shown below:

$$[(x \text{ mL}) * (0.937 \text{ g/mL}) * (1 \text{ mol} / 284.22 \text{ g})] / [10^{-3} (x \text{ mL} + 1\text{mL})] = 1\text{M}$$

Where 'x' represents the unknown amount of titanium isopropoxide volume and **1mL** is the given amount of isopropanol. Solving this equation results in **0.435mL** of titanium isopropoxide needed with 1mL of Isopropoxide to get a 1 M solution of titanium isopropoxide.

Now that the total volume of the solution is known (1mL + 0.435mL = 1.435mL) the amount of deionized water, hydrochloric acid, and isopropanol needed for the second solution can be determined.

Since the molar concentration of the titanium Isopropoxide solution is 1 the calculations for the volumes of deionized water and hydrochloric acid are pretty straight forward:

Deionized Water:

$$[\text{H}_2\text{O}] = 4 = (x \text{ mol}) / (10^{-3}(1.435\text{mL}))$$

$$5.742 * 10^{-3} \text{ mol} * (18 \text{ g/mol}) * (1\text{mL/g}) = \mathbf{0.103 \text{ mL H}_2\text{O}}$$

Hydrochloric Acid:

$$[\text{HCl}] = 0.5 = (x \text{ mol}) / (10^{-3}(1.435\text{mL}))$$

$$0.718 * 10^{-3} \text{ mol} * (36.46 \text{ g/mol}) * (1.49 \text{ mL/g}) = \mathbf{0.39 \text{ mL HCl}}$$

Isopropanol:

$$(\text{total volume}) - (\text{water volume}) - (\text{HCl volume}) = (\text{isopropanol volume})$$

$$1.435 \text{ mL} - 0.103 \text{ mL} - .039 \text{ mL} = \mathbf{1.293 \text{ mL Isopropanol}}$$

To vary the total volume of the reaction, you could go through the same calculations as above by replacing the known volume of isopropanol, so you can row reduce the matrix below, where you only have to input the desired total volume:

$$\begin{bmatrix} 0.002296 & -0.0010000 \\ 1.00000 & 1.00000 \end{bmatrix} = \begin{bmatrix} 0 \\ V \end{bmatrix}$$

Where V is the desired reaction volume. The solution for the top row will be the amount of titanium Isopropoxide needed in mL and the solution to the bottom row will be the amount of isopropanol in mL. Once the titanium Isopropoxide volume is know you can find the amount of water, hydrochloric acid, and isopropanol needed by using calculations above.

Tungsten Oxide Nanoparticle Synthesis

Introduction

Tungsten and tungsten oxide have both found a number of uses in applications. Because of its low reactivity and high melting point, it is often used in alloys and other equipment used in harsh environments. Tungsten oxide retains much of that ability, but has also been used in electrochromic devices, as superconductor gas sensors, and photocatalysis. This procedure will provide a simple synthesis method for producing different morphologies of nano-tungsten oxide.

Materials

- Tungsten Hexachloride (WCl_6)
- Ethanol (99%)
- Water
- Glass capillary tubes, Teflon lined acid digestion bombs, or some other type of envelope
- Micropipette
- Electric Oven

Hazard Warnings

- Use gloves, lab coat, and goggles when handling WCl_6 . If using larger quantities, wear a face mask.
- Ethanol is highly flammable and this procedure requires use of flames and high temperature ovens.
- Sharp glass from breaking capillary tubes.

Procedure

For the stock solution the literature calls for 8.1 g of WCl_6 to be dissolved into 200 mL of ethanol. This can be scaled down as low as desired and for this synthesis, 0.290 g were used with 7.25 mL instead. Solvothermal reaction mixtures were created by taking 0.3625 mL of the stock solution and adding 2.175 mL of either ethanol or water or a mixture of the two ($[\text{WCl}_6]=0.014\text{ M}$). If capillary tubes are being used, they should be scored and sealed at one end before adding liquid to them. A micropipette should be used to measure out and add liquid into the tubes. They should also be plunged before sealing off the other end. A torch with a blue flame and a “cone” in the center should be used to melt the glass for sealing, holding the end of the tube next to, but not in the cone. A Bunsen burner should be used to anneal the finished end using a large yellow/orange flame. If the majority of the solution was ethanol, be very careful not to evaporate it during this process. Liquid nitrogen was used to cool the solution before sealing off the tube. The tubes were then wrapped in aluminum foil to contain any bursting and put in an electric oven at 200° C for between 14 and 15 hours, although the literature only calls for 10 hours. The liquid evaporated in this synthesis likely due to a small hole in the tube. Particles were still present however and can be retrieved through sonication. The particles can be suspended in either ethanol or water and should be centrifuged and worked-up several times before characterization.

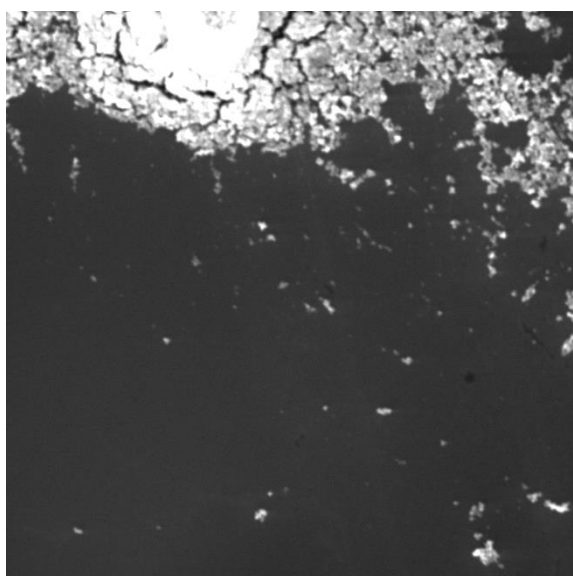


Figure 10: Torch used for sealing tubes.



Figure 9: Capillary tubes before liquid.

Results

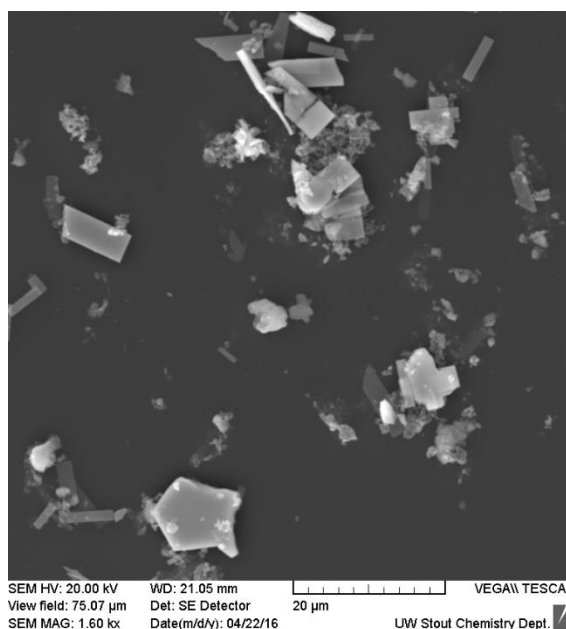


SEM HV: 20.00 kV WD: 9.250 mm VEGA\\ TESCAN
View field: 59.86 μm Det: SE Detector 10 μm
SEM MAG: 2.00 kx Date(m/d/y): 04/12/16 UW Stout Chemistry Dept.

Figure 12: Scanning Electron Microscopy of ethanol based particles.

distribution and were mostly agglomerated. The particles had to be scraped off the tube as several larger flakes. Another interesting thing to note is that the starting solution of WCl_6 and ethanol started out yellow, but over time changed to a green and finally a blue color. The reason for this change in color is mostly unknown since chemically, the solution is not changing in any way while this happens.

Particles were around a 400 nm size range with a large distribution. For the ethanol reaction mixture, nanowires or nanorods were the morphology for the literature, however spherical particles were created using this more crude and unorthodox method. For the water reaction mixture, square nanosheets were the morphology from the literature. However, a variety of different plate shapes were created. They had a large size



SEM HV: 20.00 kV WD: 21.05 mm VEGA\\ TESCAN
View field: 75.07 μm Det: SE Detector 20 μm
SEM MAG: 1.60 kx Date(m/d/y): 04/22/16 UW Stout Chemistry Dept.

Figure 11: SEM of water based particles.

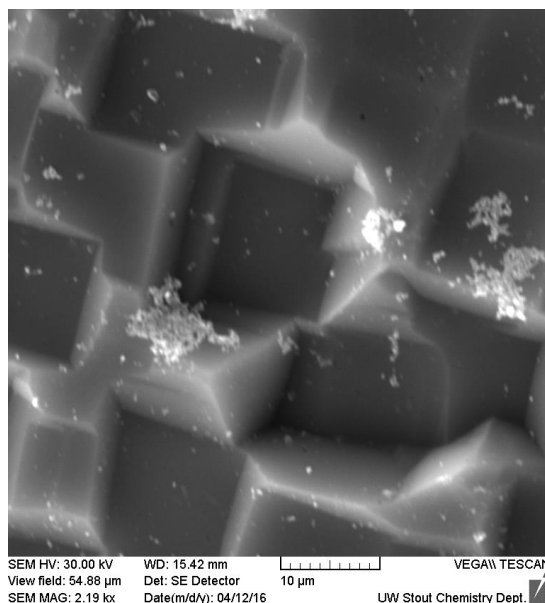
Discussion

This procedure has proved to be a viable option for synthesizing WO₃ nanoparticles. With improved technique it could be possible to make more uniform morphology of the particles as well as a more narrow distribution. It may even be possible to create the nanowire morphology instead of particles. Another path to take would be to use a mixture of water and ethanol when adding to the starting solution for reactions. This may improve morphology or give different morphologies. The simplicity allows for much more experimentation with different techniques.

References

Choi, H.G., Jung, Y.H., and Kim, D.K. (2005) Solvothermal Synthesis of Tungsten Oxide Nanorod/Nanowire/Nanosheet. *J. Am. Ceram. Soc.*, 88 [6] 1684-1686.

Zinc Oxide Nanoparticle Synthesis



I. Introduction

Zinc oxide is a semiconducting material that, in large amounts, has a white appearance. Larger samples can be grinded down to small, nearly transparent particles. These small particles also have optical properties that allow for the reflection of short wavelengths (Red – UV portion of spectrum). Due to these properties, zinc oxide is widely used in sunblock. The following procedure for synthesizing spherical particles with an average diameter of one micron ($1\ \mu\text{m}$) is based off U.S. patent 6,710,091.

II. Procedure

Materials:

Zinc Acetate Dihydrate

Potassium Hydroxide (Pellets)

Methanol

Equipment:

100 mL Volumetric flasks

100 mL plastic storage container

Stir bar

Balance

Pipettes

Addition funnel

Temperature Probe and control box

Condenser

Hotplate/Stir plate/Heating mantel

25 mL Scintillation vial

Safety:

Wear safety goggles when handling solutions and handle reaction in fume hood

Methanol – highly flammable, keep open flames away

Potassium hydroxide – corrosive, causes severe burns, harmful if inhaled, fatal if swallowed

Dispose of zinc acetate as HNOC

Stock solutions:

Dissolve 0.2143 g zinc acetate dihydrate into 100 mL methanol (0.01 M). Store in volumetric flask.

Dissolve 23.79 g potassium hydroxide pellets into 100 mL methanol (fully saturated) and keep at room temperature. Store in plastic container.

Reactor setup:

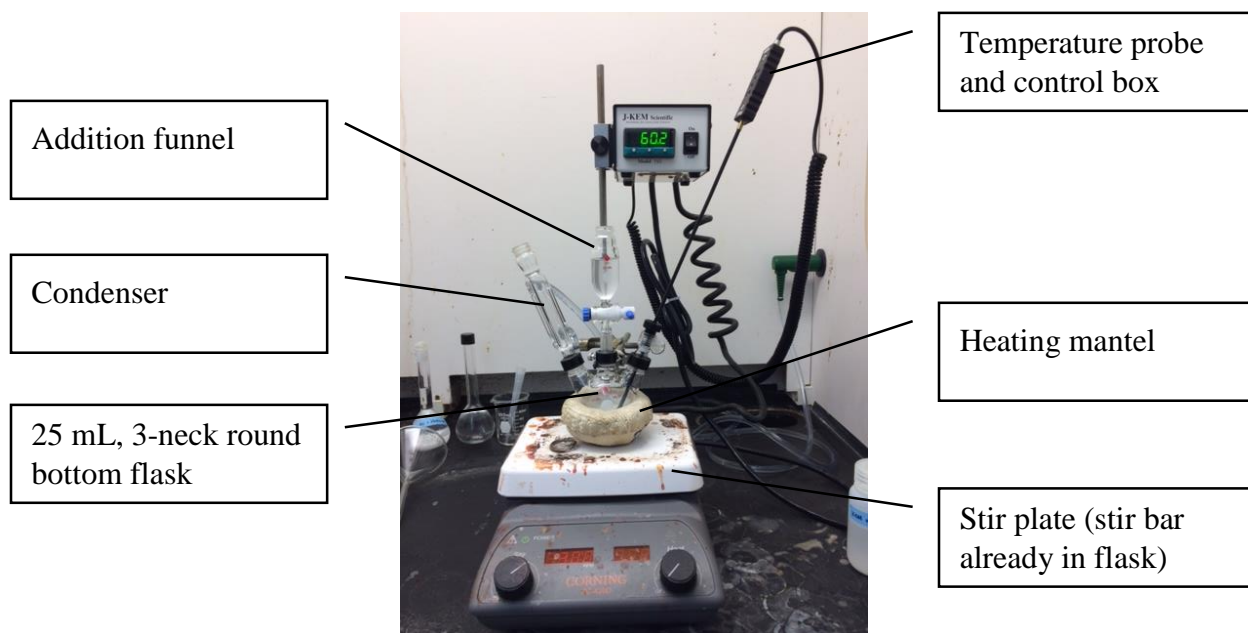


Fig 1) Labeled image of reactor setup

A condenser, addition funnel and temperature probe are sealed to a 25 mL round bottom, three necked flask (with stir bar already inside) using Teflon tape

The flask is placed on top of a heating mantle, which is then placed on a stir plate.

A ring stand and clamps may be used to hold the reactor in an upright position

Precipitation reaction:

7.0 mL of 0.01 M zinc acetate solution added to flask to charge the reactor

The solution is heated to 60 degrees C while stirred with stir rod (330 RPM)

12 mL of saturated potassium hydroxide solution is added dropwise to the heated zinc acetate solution (1.7:1) and stirred for 1.5 hours

After 1.5 hours, the reactor is removed from the heat and the mixture is poured into a centrifuge tube

Allow to cool and for particles to settle

Wash by centrifugation (see bullet points below)

- Pipette used to remove most of the supernatant.
- Rinsed with ethanol and then centrifuged 3x @ 3000 RPM for 5 min, rinsing with ethanol and vortexing between each cycle
- After final wash, the particles are re-dispersed in water

Transferred into 25 mL scintillation vial for storage until further analysis is done.

III. Analysis

Energy Dispersive X-Ray Spectroscopy (EDX):

Note: No sputter coating was done for any SEM or EDX images

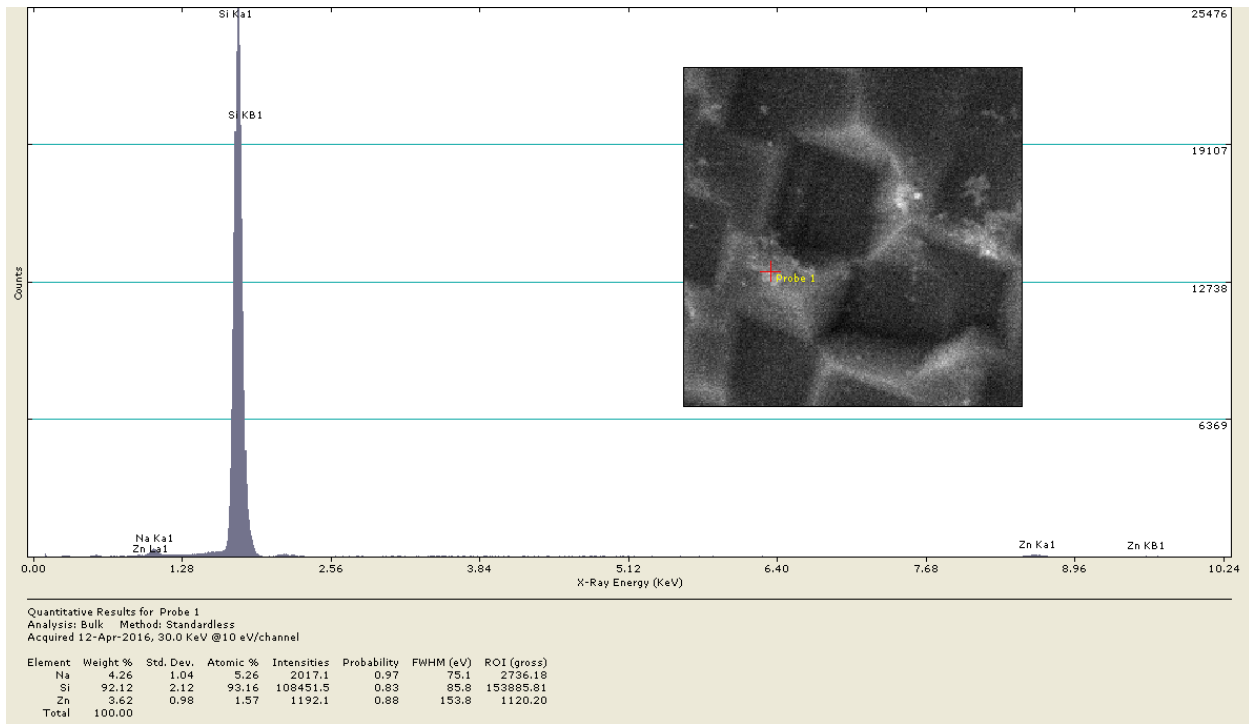
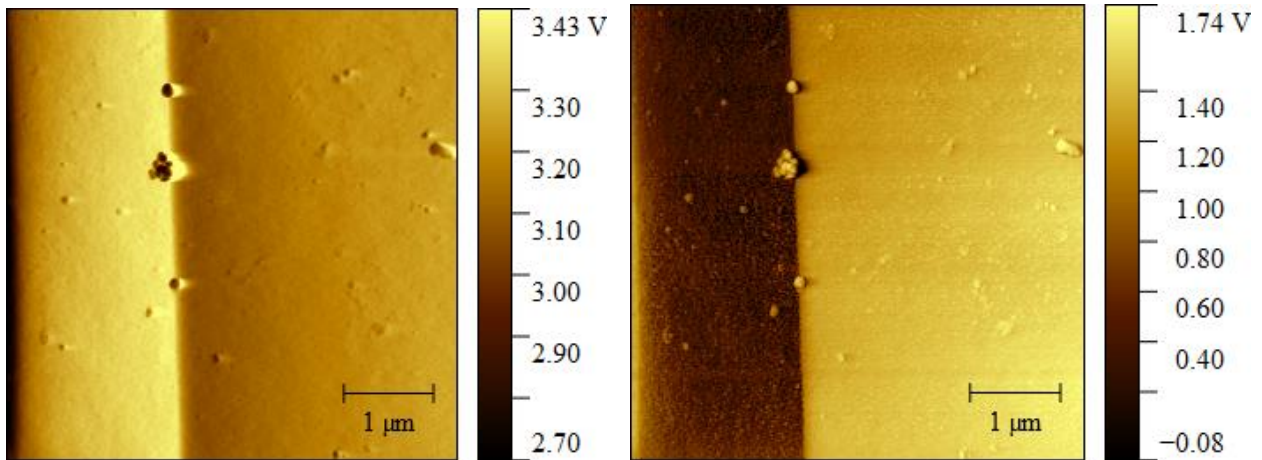


Fig 2) EDX point probe results. Despite the overwhelming strong signal from the silicon of the sample substrate, Zn is clearly present (seen by the two small peaks located at Zn x-ray energy values). Sodium is a common contaminant, explaining why that element is detected in this sample

Atomic Force Microscopy (AFM):



Tapping mode - Amplitude

Tapping Mode - Forward Phase

Scanning Electron Microscopy (SEM):

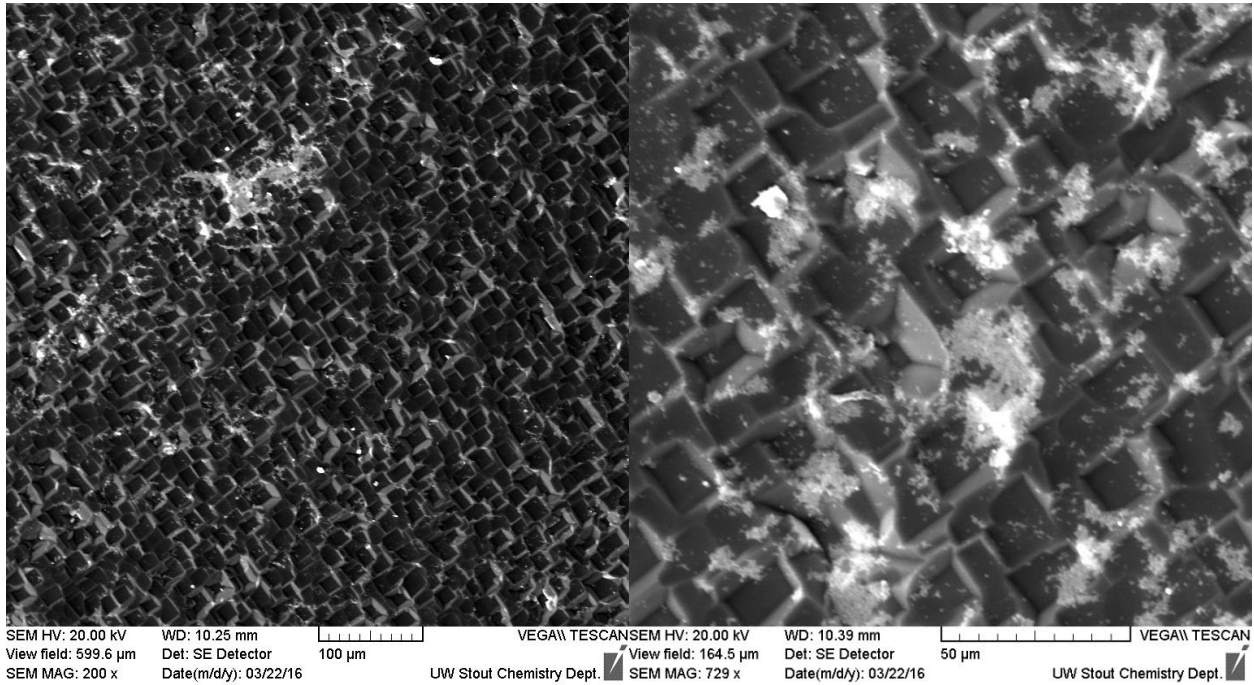


Fig 3) SEM images of ZnO particles deposited on back side of silicon wafer. Magnifications are 200x (left) and 730x (right).

Zetasizer:

Particles were sonicated using a probe sonication (runs 3/4) and bath sonication (runs 1/2).

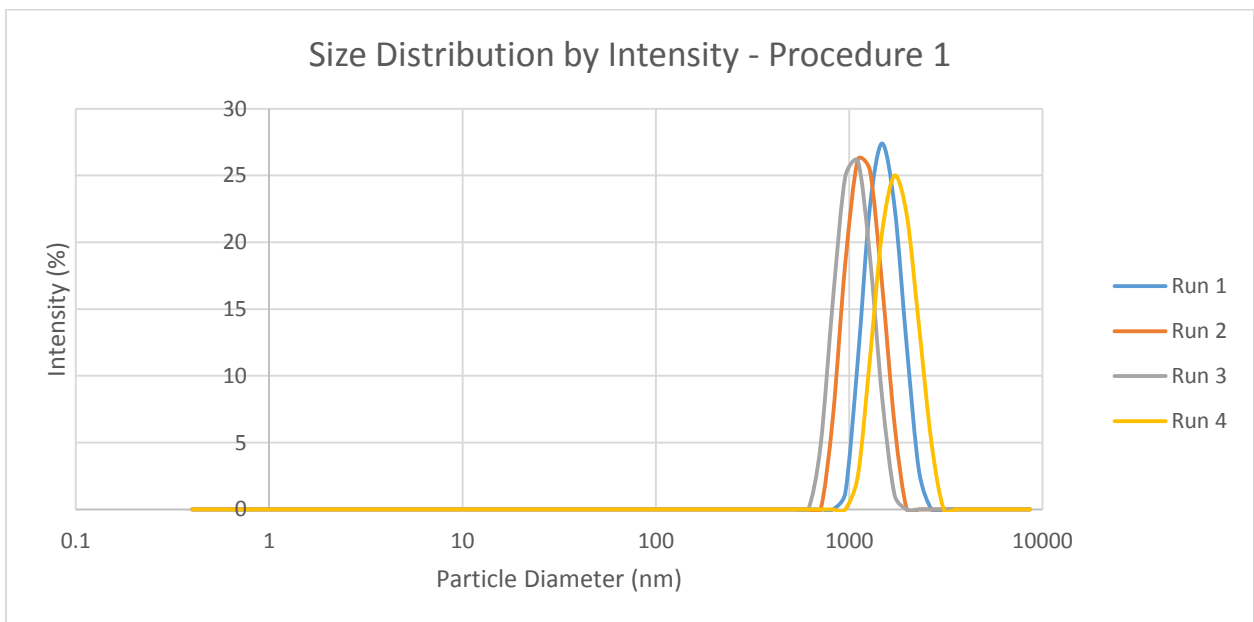


Fig 4) Unimodal curve with normal distribution. Peak diameters at 1480 (run 1), 1110 (run 2), 1110 (run 3) and 1720 (run 4).

Trial 2: Same procedure with 0.10 M KOH solution

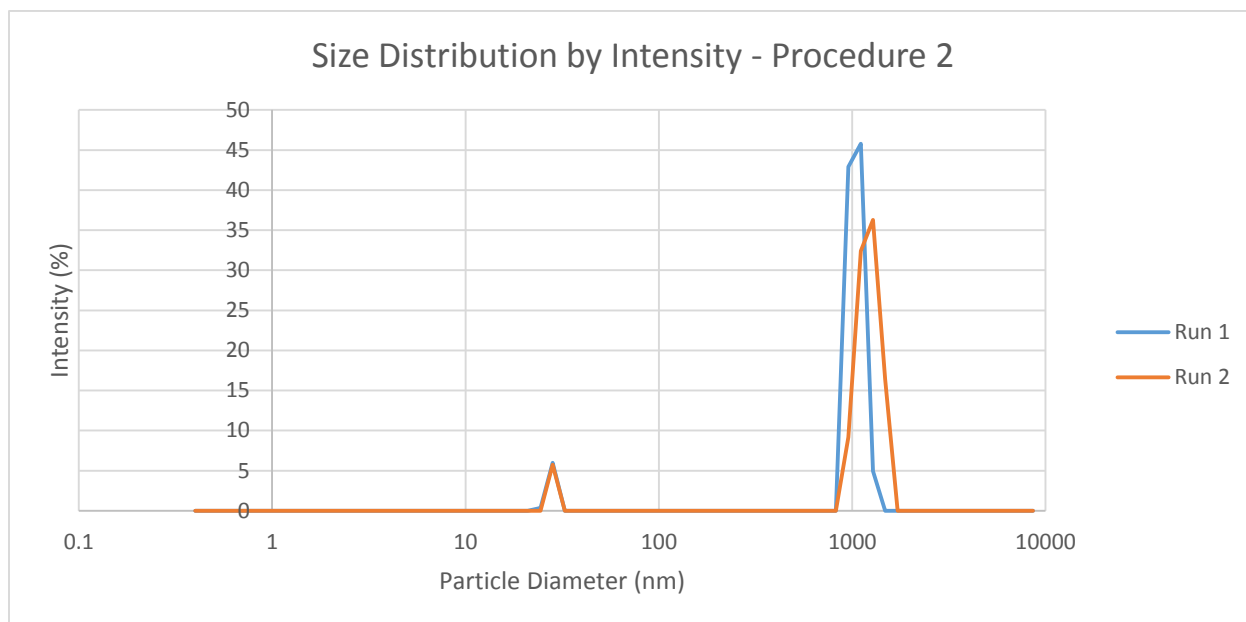


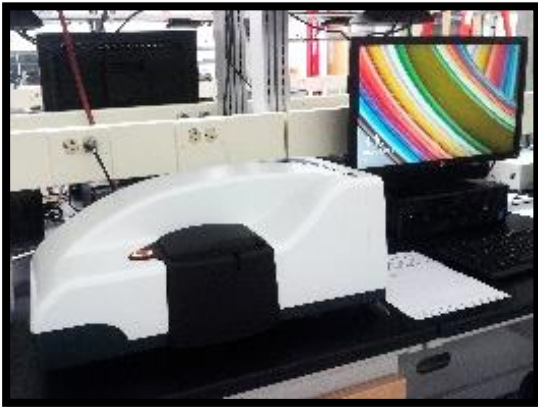
Fig 5) Bimodal curve with peaks at 24.4 and 1110 for run 1 and at 28.2 and 1280 for run 2.

References:

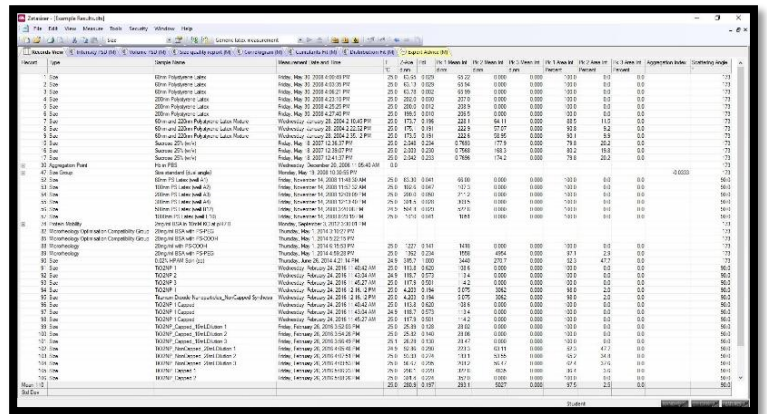
Womelsdorf, H.; Hoheisel, W.; Passing, G. Nanoparticulate Redispersible Zinc Oxide Gels. U.S. Patent 6,710,091, Mar. 23, 2004.

Zetasizer: Nanoparticle Sizing Instructions

Zetasizer Workstation



Zetasizer Software Menu



Sample Preparation:

- Make a dilute suspension by using a pipette to drop a small amount of the bulk suspension into a small beaker of water. The resultant suspension should be slightly cloudy/turbid, but light should still be able to pass through.

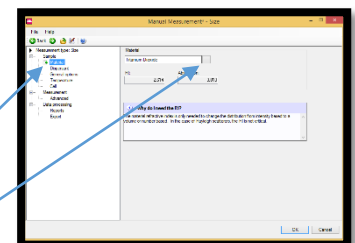
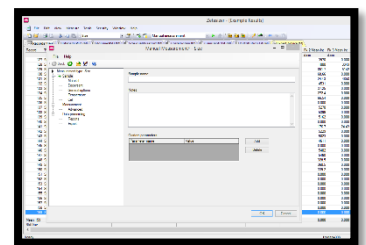
Inserting Cuvette Into Cell Area

- Fill a disposable cuvette with approximately 1 mL of the diluted suspension.
- Open the cell area lid by pushing the circular grey button adjacent to cell area.
- Place the disposable cuvette into the cuvette holder in the cell area. You should feel some resistance from the metal track ball in the cell area, but push the cuvette down until it is securely placed in the cuvette holder.
- Close the cell area lid.

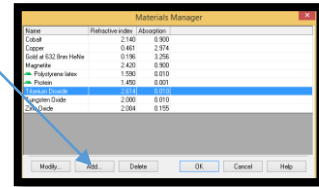


Running Size Measurements

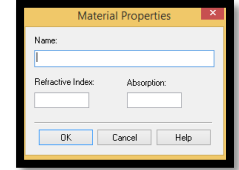
- Log into the HP computer by using your Stout email address and password
- Open the “Zetasizer Software” located on the desktop
- Click the **Measure** tab in the tool bar and select **Manual**
- Enter the identification of your sample into the **Sample Name** prompt and enter any additional information into the **Notes** prompt.
- On the left hand side of the window, select the **Material** setting. This refers to the material type of nanoparticle that is in the suspension. Click on the [...] icon next to the **Material** name prompt. The **Materials Manager** window will open and have a list of materials to select from.



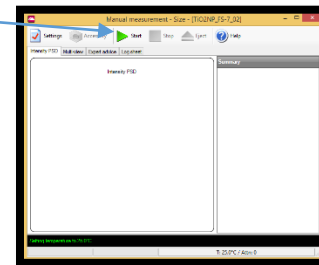
- If your material is not located on the list click on the **Add** button. The **Materials Properties** window will open. You will need to input the name, refractive index, and absorption of the material.



- Refractive Index: Find a reputable source on the internet to obtain the refractive index value.
- Absorption: If your suspensions has a milky white color, put in a value of 0,1. If your suspension has a blue or black color, put in a value of 0.9. For any other color, put in a value between 0.3-0.7



- Now select the **Dispersant** setting, which is located below the **Material** setting on the left hand side of the **Manual Measurement** window.
 - Select the dispersant medium (solvent) by clicking on the [...] icon.
- Once you have selected the **Material** type and the **Dispersant** medium, you can click **OK** at the bottom of the **Manual Measurement** window.
- A new window will appear. Click the **Start** icon which is located on the top of the window next to the green arrow icon.
 - The Zetasizer will now start taking DLS measurements of the sample. The test will take approximately 5 minutes to complete.
- To transfer a graph or chart from the Zetasizer software highlight the sample that you want the graph from in the “Records View” tab, then click on the “Intensity” tab on the top of the page, select the “Edit” header on the toolbar on the top of the page, and select “Copy Size Graph” or “Copy Size Values”, depending if you want the graph or the data.



Resources:

- For an in-depth overview on how the Zetasizer collects sizing data, how to interpret the data, and the limitations of the Zetasizer, go to the link below:
<https://www.youtube.com/watch?v=h6PYSpsDU-Q>

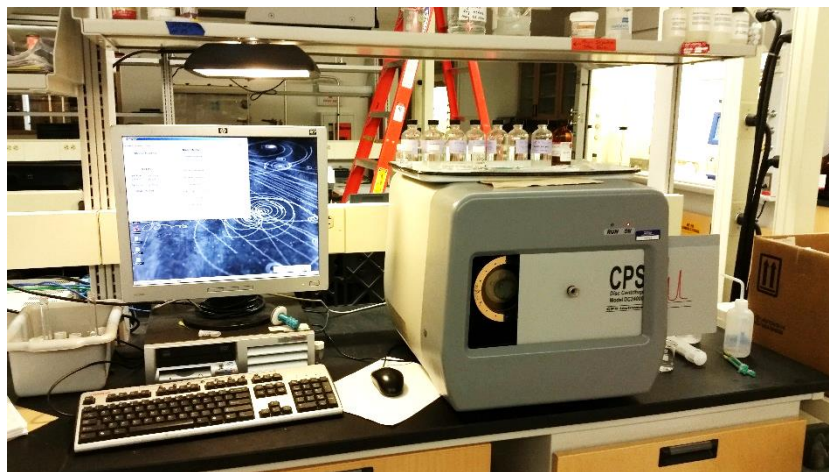
Disc Centrifuge Operation Guide

Building the Gradient

1. Turn on Disc Centrifuge and start up the program on the computer
2. Select or make a procedure for the particles you wish to size (see manual for instructions)
3. Seal disc and close the door
4. Begin the procedure by pressing run
5. Once the disc is spinning at full speed continue with building the gradient by injecting the following in order:
 - a. 2.3 ml 8% sugar solution
 - b. Repeat for each of the following concentrations 7%, 6%, 5%, 4%, 3%, 2%, 1%
 - c. 1ml dodecane

Running Your Sample

1. Following the prompts on the screen
 - a. Inject 0.1 ml of calibration standard
 - b. Inject 0.1 ml of sample
2. You may run multiple samples during one procedure
3. When finished click terminate



Shutting Down the Instrument and Clean up

1. Once the disc has stopped spinning, remove the sugar solution using the large syringe
(Remove first syringe full of solution before removing the ring plug so it doesn't spill everywhere)
2. Rinse the disc with isopropanol, wiping with paper towel as necessary
3. Close out of the Disc Centrifuge program
4. Switch off the Disc Centrifuge

Sample Preparation for Microscopy Work

Sample Prep:

1. Prepare a substrate for use, choosing either a glass or a silicon wafer.
 - a. To cut a substrate properly, use a draw out a grid of appropriate size and practice cutting glass slides into pieces using a diamond pencil.
 - b. Once you feel comfortable, use the pencil on your actual substrate of choice.
 - c. Next, wash the substrate to clean the surface. An alcohol like ethanol often works well.
2. Suspend particles in a solution if they are not already. Then, dilute the solution so that the appearance of the final solution is slightly cloudy.
3. Attach the substrate(s) to an SEM stub, or to a sample puck for an AFM using carbon black tape.
4. Add solution to an attached substrate dropwise. Allow the substrate to air dry entirely, or wait for a few minutes for the particles to settle and then wick away the extra liquid with a Kim wipe.
5. Now your sample is ready to image.

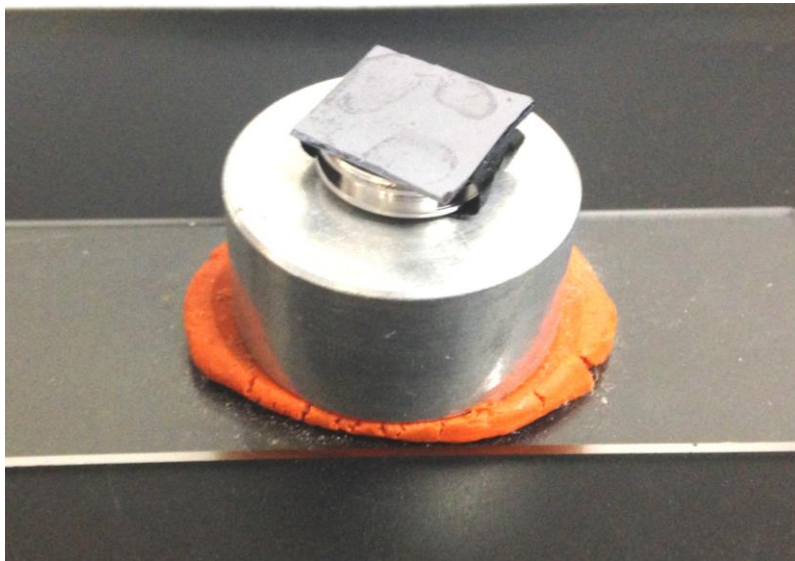


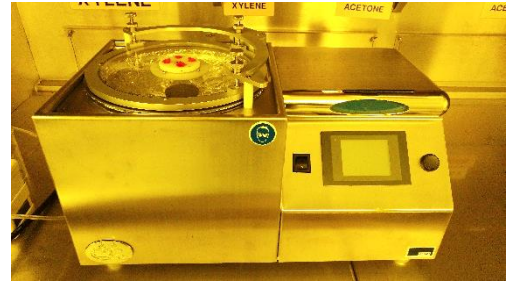
Figure:

Shown above is an SEM stub mounted into a stub holder with an attached substrate. The sample has dried down on the surface in three distinct regions.

Spin Coater

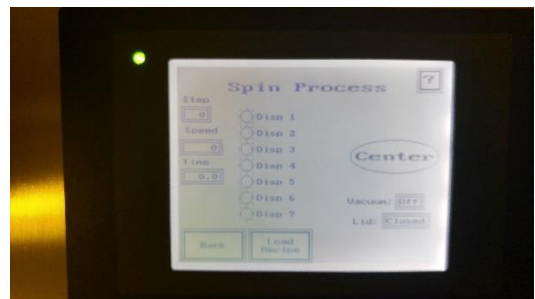
Powering on System and Setting up Spin Coater

- Turn on Spin Coater via large switch on the front.
- Select edit process (use the stylus if you'd like).
- Change the onscreen settings for speed, accel, and time. The spin coater is set up to run multiple steps during a process. You will need steps for accelerating, maintaining constant speed, and decelerating, each being a different step.
 - Speed: the top speed, highest revolutions per second, the sample will spin during this step
 - Accel: how fast the spin coater will ramp up or down to the speed.
 - Time: how long the spin coater will stay on this particular step.
- Select save and name it something memorable.
- Go back to the main menu.



Operating the Spin Coater

- Select run process.
- Press load and find your program.
- Open the lid and place substrate on the stage.
 - Place as close to the center as possible. This is to reduce excess vibrations during high speeds.
- Close lid.
- Select center. Spin coater will spin slowly at first, this is to help the user find the center. Feel free to open the lid and move the substrate closer to the exact center. After you close the lid, the centering process will resume and continue spinning. Leave the lid closed when finished and the spin coater will stop on its own.
- After the substrate is centered, place your solution in the middle of the substrate as necessary via the holes in the lid, and select spin.
- After process is complete, open lid, and remove your sample.



Turning off the Spin Coater

- Flip the switch on the front into the off position.

Gold Sputter Coater Operation Guide



Gold Coating a Sample

1. Turn on power switch for vacuum (device with 2 hoses attached and behind the sputter coating machines) and make sure the gray valve handle is pointed towards the gold sputter coater (left)
2. Turn on the argon gas using the knob on top of the tank - **Do not touch knobs near pressure dials, they are already set to the correct pressure**
3. Lift lid of gold sputter coating chamber and remove the glass cylinder for easy sample loading
4. Make sure all samples are securely loaded onto center platform and are flat (use SEM stubs for loading samples)
5. Replace cylinder and close lid
6. Turn on the sputter coater using the power switch on the front of the machine
7. Make sure a vacuum seal is made between the lid and the glass cylinder
8. Make sure timer is set to 30 seconds
9. Select AUTO (manual only needs to be used to calibrate once in a while)
 - a. Press cycle - argon gas will slowly be let into the chamber and the machine will automatically readjust to achieve about 40 mA on the front dial. Once the dial reads about 40 mA, the timer will begin to count down and you will see a purple glow (the purple glow is the gold plasma) - wait until the timer has finished before next steps
10. Turn off the power to the sputter coater - the vacuum will turn off and the lid will be able to be lifted off after about 10 seconds - **Do not force lid off. Wait until vacuum seal is completely broken**
11. Remove samples

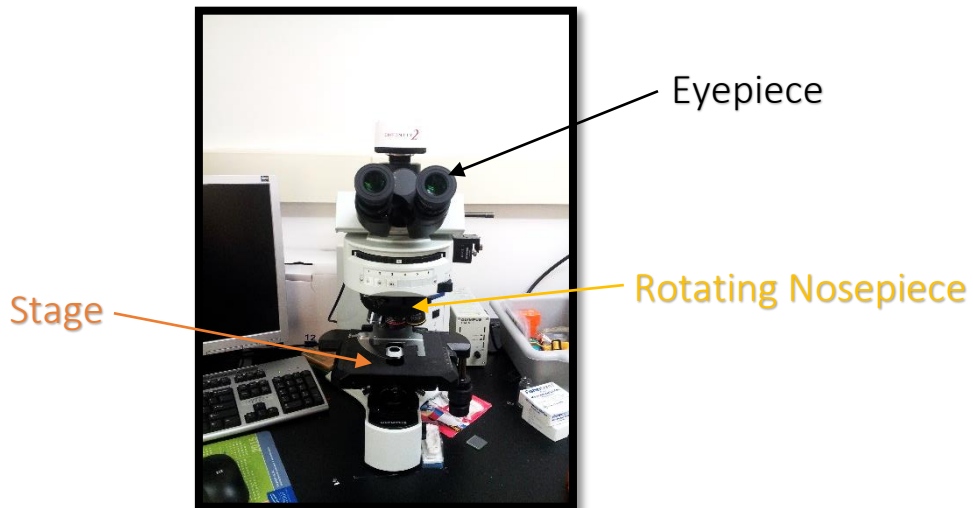
Carbon Sputter Coater Operation Guide



Carbon Coating a Sample

1. Turn on power switch for vacuum (device with 2 hoses attached and behind the sputter coating machines) and make sure the gray valve handle is pointed towards the carbon coater (right)
2. Lift lid of carbon coater and remove the glass cylinder for easy sample loading
3. Make sure all samples are securely loaded onto center platform and are flat (use SEM stubs for loading samples)
4. Check that there is a correctly shaped carbon rod installed in the inside of the lid - if the rod is misshapen or broken, the carbon coater will not work efficiently
 - a. If a new carbon rod needs to be installed, contact someone in the chemistry department to replace it or prepare a new one using the tools in the drawer below the carbon coater.
5. Turn on the carbon coater using the power switch on the front of the machine **and then turn on the power switch on the gold sputter coater** - Once the gold sputter coater machine is turned on, the vacuum pump will automatically pump down the carbon coater chamber
6. Wait for the dialog box on the front of the carbon coater to stop flashing and display a number - this number is the timer (which should be 6 seconds)
7. Make sure the switch near the bottom front panel is on auto
8. Press start and wait for sample to be coated - **Do not look at the carbon rod while coating is occurring without tinted goggles or a welding mask as it gets very bright**
9. Turn off the power on the gold sputter coater to turn off the vacuum and then turn off the carbon coater and argon gas tank
10. Remove samples - take care not to touch the carbon rod as it will be hot for a while

Optical Microscope: Operation Procedure



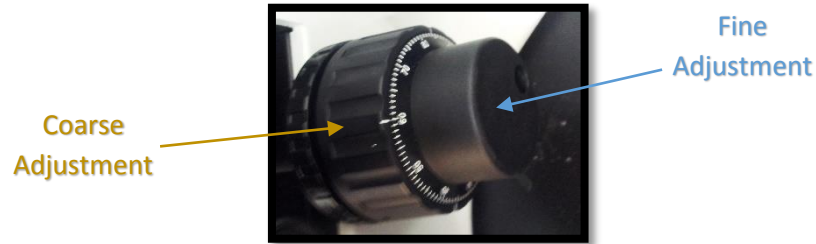
Powering on System and Setting up Microscope

- Take blue “LEEDS” cover off of the microscope. **BE CAREFUL TO NOT PULL THE EYEPIECES OUT WHEN PULLING THE COVER OFF.**
 - Check to make sure that the revolving nosepieces has the **5X OBJECTIVE LENS** in position and that that the stage is sufficiently lowered to ensure your sample will not hit the magnification lens. If not, rotate the **REVOLVING NOSEPIECE** to the **5X OBJECTIVE LENS** position and/or lower the stage by rotating the coarse adjustment knob counterclockwise.
- Turn on the surge protector, which is located to the right of the microscope, running along the wall.
- Turn on the **OLYMPUS TH4-100** box by flipping the switch to the upward position. The dial to the right of the switch provides illumination
- To place your mounted sample on the stage manually push the curved metal lever to the left, slide the glass slide up against the stage clip and release the metal lever arm so that it pushes against the corner of the glass slide.
- At this point when you look into the microscope lens it should still be dark. To illuminate the sample, turn the black dial on the **OLYMPUS TH4-100** light source clockwise until the sample becomes visible through the microscope lens.



Operating the Microscope

- Focus the sample with the **5x OBJECTIVE LENS** magnification lens by using the coarse adjust knob that is located on the lower right side of the microscope. Rotating the knob clockwise raises the stage and rotating the knob counter clockwise lowers the stage.
- Once the sample is in focus you can view the sample at higher magnifications by rotating the **REVOLVING NOSEPIECE** clockwise to switch to higher powered objective lenses.
 - When switching to higher magnifications make sure to not use the **coarse adjustments** to focus the sample, but to use the **fine adjustment** knob. Using the coarse adjust has the potential to crash the sample into the lens.



- To view different sections of your sample use the stage adjustment dials located on the right hand side of the microscope. The top dial moves the stage forward and backward while the bottom dial moves the stage right and left.



Shutting Down The System

- Lower the stage to its lowest level using the **coarse adjustment** and rotating the dial counter clockwise.
- Remove the sample from the stage.
- Rotate the **REVOLVING NOSE PIECE** so that the **5X OBJECTIVE LENS** is in position.
- Rotate the dial on the **OLYMPUS TH4-100** light source fully counter-clockwise to turn the illumination off. Then turn the **OLYMPUS TH4-100** off by pushing the switch downward.
- Turn off the surge protector that runs along the wall.
- Carefully put the blue "LEEDS" cover back over the microscope.

Scanning Electron Microscope (SEM)



1. Turn on the air and nitrogen tanks in the back of the room. Only turn the top valves on and leave the rest of the knobs alone.
2. Start up the program and log in as a student. Simply press enter without entering a password.
3. Near the bottom of the screen will be buttons that say "VENT" and "PUMP". Click on the button that says "VENT" to vent the chamber. The bars will turn green when the process is complete and you will be able to pull open the chamber door.
4. Place your sample into one of the available holes. The outer ones are usually the best. Use the screwdriver to tighten the stud into place.
5. Close the chamber without pinching the wire and click the "PUMP" button. Wait for the bars to turn green.

6. Click the button that says "HV" to turn on the high voltage electron beam. More details for actual operation of the SEM can be found in the manual on the table.
7. Use the X and Y dials to center the sample so that you can see it on the screen. Click the "AUTO" button and let the microscope make adjustments. The picture should be clearer now.
8. You can now use the functions of the microscope like magnification and working distance by simply clicking on the words and using the scrolling ball to zoom in or zoom out. Not all the functions use the ball, like scan speed and gain/black. Refer to the manual for more information on the other functions.
9. Collecting an image can be done by clicking on the symbol with an arrow pointing down over a floppy disk. Once the image is collected you will be required to name the file and save it to a folder.
10. Once you are done using the SEM, zoom the magnification out and if you adjusted the Z axis dial, raise it back up. In the binder, fill out a log entry detailing the date, column pressure, filament hours, and everything else it asks for. Turn off the high voltage by clicking HV again and then vent the chamber.
11. Open the chamber and remove your sample. Again be sure not to pinch the wire when you close it.
12. Pump the chamber once more before closing the program and turning off the gas that you turned on at the beginning.

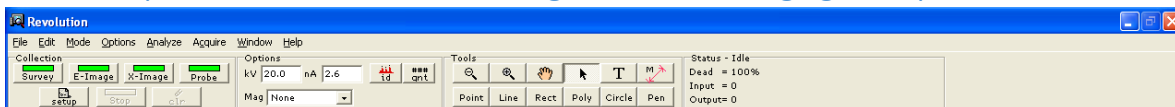
Energy-Dispersive X-ray (EDX) Spectroscopy

Equipment Check

- **Check to see if there is enough liquid nitrogen in the tank before use. The machine will need to cool for 24 hours before use if the tank is too low.**
- To do this take off the lid on top of the tank. Take the meter stick and place it in the tank with the beginning of the centimeter side down.
- Remove stick after a few seconds and proceed to wave around in the air for a few seconds.
- Check the frost level on the stick.
 - 0cm—5cm: add more liquid nitrogen. **Do not use EDX if no liquid nitrogen is present.** Wait 24 hours after addition.
 - 5cm—20cm: add more liquid nitrogen up to 22cm.
 - 20cm—24cm: ideal range. No need to add any more.
- Place top back on the tank.
- Be sure the nitrogen gas tank on the wall is not empty and open.

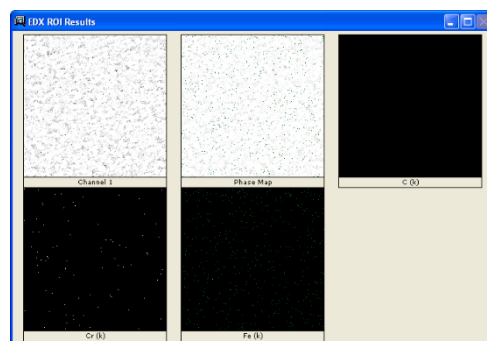


Follow SEM operation instructions for turning on SEM and imaging a sample.

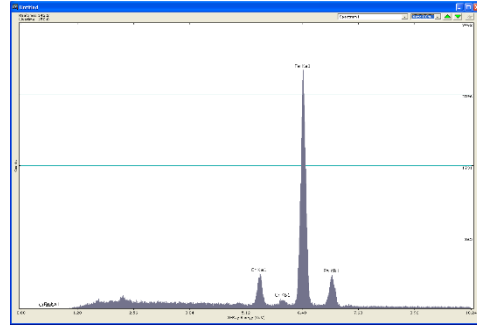


Software Use

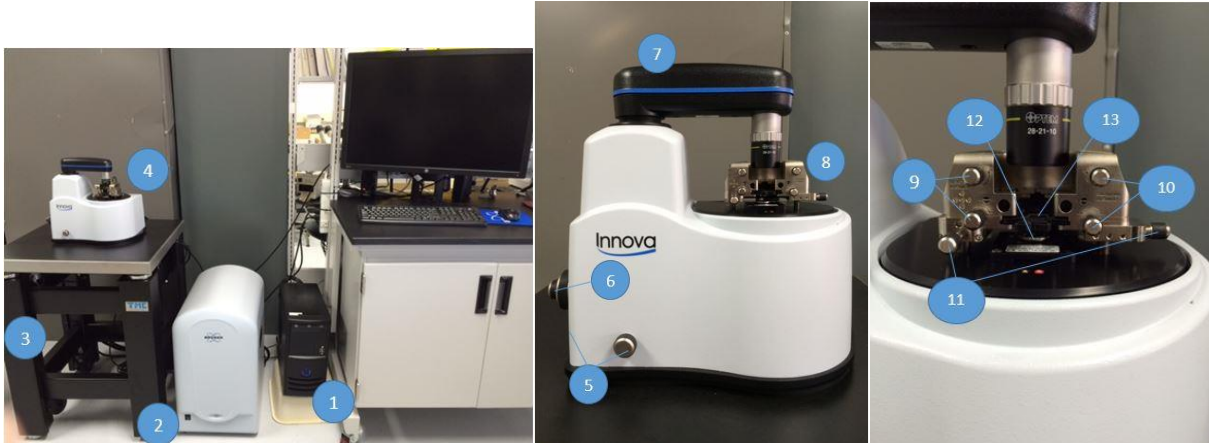
- Launch New Revolution Software
- Press OK on popup window
- In the toolbar under **Mode**, be sure **Universal** setting is selected.
- Select **Setup** in the collection section of the toolbar
- In popup window, under the probe tab, in the EDX Acquisition box, choose number of presets (300 is a good number for first quick looks), type box says LiveTime, Channels and Display should read 1024, LLD (channels) should display 10. Everything else should be fine for most uses.
- Close Universal Preferences setup window
- **Survey**: This will show you what the EDX can “see”. It should be similar to what the SEM is showing.
- **E-Image**: Shows a digital image of the sample.
 - Right click where you would like to probe and select queue EDX probe.
- **X-Image**: Shows places in the sample where certain elements are measured.



- To change which elements are shown, right click the screen, select ROI Processing and select elements in pop up window.
- **Probe:** Collects x-rays from the survey area.
 - To change which elements to look for right click the plot, select edit elements, click on desired elements. Green=yes, red=no, yellow-auto. Select OK when finished.
 - In the toolbar, in the Options box, select the **qnt** to see info about your sample, select **id** to identify the peaks present.
 - When probe is complete, save your work via the file menu.
- **Stop:** Stops whatever scan you are currently doing.
- Close Program when complete.



Innova AFM



1. Main computer
2. Bruker AFM computer
3. Air table – Do not place objects on this
4. Atomic Force Microscope (AFM)
5. Moves microscope left/right, back/forth (knob on left not pictured)
6. Adjusts focal pt. of microscope (coarse adjust = large knob, fine adjust = small knob)
7. Swinging microscope head
8. AFM head
9. Moves the detector left/right, back/forth
10. Moves the laser left/right, back/forth
11. Moves the entire AFM head left/right, back/forth
12. Magnetic sample stage
13. Cantilever/AFM tip

How to power up:

Order of powering up: Power up main computer (1) → Open Nanodrive program (icon on desktop) → Switch on Bruker AFM computer (2)

Experiment set up:

Check the "use previous experiment" box and press "load experiment". Once it has loaded, the navigator box should appear.

Select a sample. If preparing a new sample, there are magnetic discs and carbon tape in the desk drawer. Look at the AFM tip (13) to make sure it will clear the height of your sample. If it is too low, use the gears icon near the top of the screen (in Nanodrive program), and use the "up" arrow to move the tip up.

Swing the microscope head (7) out of the way. Lift the AFM head (8) gently, being careful not to drop or touch components underneath. Place the sample on the magnetic stage (12). Replace the AFM head, making sure that it is aligned with the notches and swing the microscope head back over the AFM.

Locate the icon bar near the top of the screen (icon of microscope, gears, etc). For the following steps, move from the leftmost icon towards the right to set up the instrument.

1. Check that the small bar below the microscope icon is green. If it is red, check that all cords are plugged in, turn off the instrument (2), close the program, wait 10 seconds, and then reopen.
2. Next you align the laser.
 - a. Make sure the cantilever tip is visible in the navigation window. If it is not, use the microscope focal adjustment knobs (6) to focus on a pt. above your sample, press the gears

- icon and use the “down” arrow to move the cantilever into focus, being careful not to crash into your sample.
- b. Move the laser using the knobs on the right side of AFM head (10). Move the laser so that it is bouncing off the tip of the cantilever. If you have difficulty getting in position, move the microscope out of the way and adjust the laser visually.
 3. Move to the next icon (square with a red circle). This will open a window with a coordinate plane and a colored circle. Use the knobs on the left side of the AFM (9) to adjust the sensor position. The goal is to get the circle on the laser alignment screen right in the middle. As you move the circle to the center, the number at the bottom of the window should increase to around 2.5 – 2.9 V and the circle should change from red to pink. If this is not happening, then the laser is not on the cantilever and needs to be adjusted (repeat step 2). Once the bright pink circle is directly in the middle and the bottom number reads 2.5 – 2.9 V, continue on to the next icon.
 4. Select the tuning fork icon. This will open another window. In this window, select auto tune (small check box). The tapping frequency should be 2.00V. Press the green play button, and you will notice a changing graph in the window. Once completed, a red triangle will appear. Exit out of the window.
 5. Approach the sample. If the tip is very far from the sample surface, press the gears icon and use the “down” arrow to approach manually. Once you are comfortably close to the surface, press the icon with a green, downward pointing arrow to auto approach and engage the surface. Once the tip is engaged, the main screen will split into 4 boxes and a scanning control box will open. At this point, you may begin scanning.

Collecting/Saving Data:

To capture your data boxes hit the data capture directory “save” button (bottom of window) → browse for a folder → select desired folder → give sample “file name prefix” (below data capture save button)

Next, select the camera icon (near top of window) **BEFORE YOU SCAN**. Not selecting this before the scan begins will result in data not being saved.

Hit the green play button to begin collecting data. Once the scan is finished, the data will be saved. Create a NEW file name prefix for the next scan and adjust variables as needed to obtain better images.

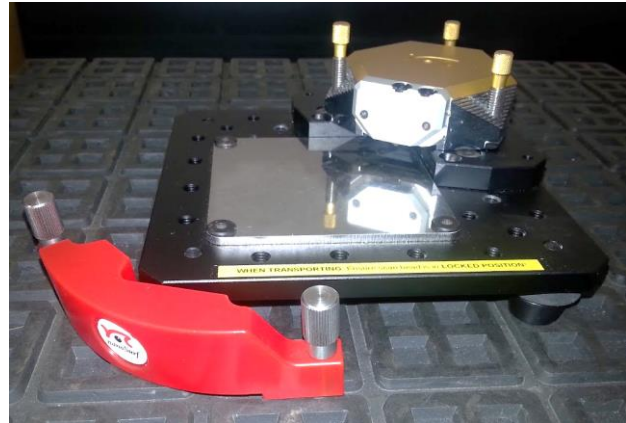
Now you have a saved image, you can use Nanoscope analysis software to get more information from your images.

If you want to move the sample or look at a new spot on your sample, make sure to **withdraw the tip first** using the icon of an upward pointing red arrow. Then use the bottom knob adjustments (11) to move the cantilever to a new location. Re-engage the surface by pressing the downward pointing green arrow icon.

Shutting down the microscope:

Withdraw the tip from the surface by pressing the red, upward pointing arrow icon. Then press the gears icon and use the “up” arrow to move the tip **FAR FAR** away from your sample. Carefully lift the AFM head and remove the sample. Exit out of the program and turn off power on the AFM Bruker box (2). **LEAVE THE MAIN COMPUTER ON** (1). Put the cover back over the instrument.

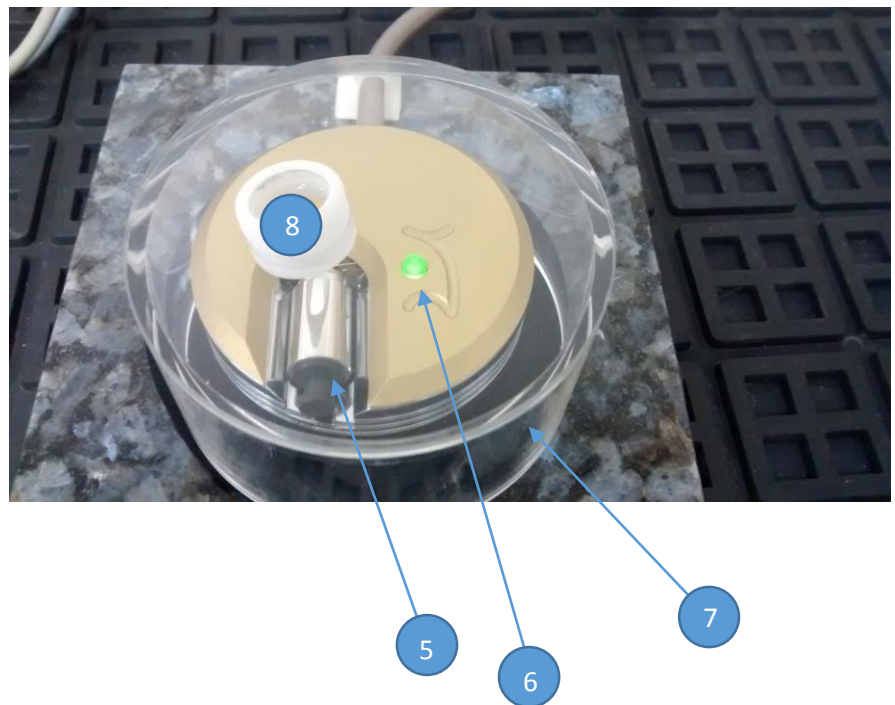
Nanosurf Atomic Force Microscope (AFM)



1. Before using the AFM, first download the free software easyscan for Nanosurf.
2. Begin by unpacking the gray boxes and the cables. Plug everything into the correct ports. There should be only one option for each port but refer to the manual for an image of the setup.
3. Next, take out the scanning head. Remove the red guard using the tool in the case and inspect the tip. If there is no tip or the tip is damaged, you may need to replace or add a tip. Refer to the manual for this operation.
4. Once the tip is ready, plug the coiled cable into the scan head and set up the scan head on a level, stable surface.
5. Use the three screws to raise, lower and level the scan head. Place your sample on the metal disk and put it under the scan head so it is below the cantilever.
6. Lower the tip down so it is as close to the sample as possible without touching the sample. **DO NOT CRASH THE TIP INTO THE SAMPLE.**

7. Next, start up the program on your computer, turn the power switch to on for the assembly, and plug the USB into your computer. It will then ask you to choose the correct COM port. Keep picking until it recognizes the AFM.
8. The computer may “lose” the AFM and so if this happens you will need to unplug the AFM and restart the program to start over.
9. Once the program recognizes the AFM you can start approaching the sample. Use the viewer on the scan head to get a better view. Use “auto approach” when there is only a small space between the tip and the sample.
10. The AFM will start scanning the surface automatically once the approach is complete. You can then change the parameters of the scan or wait for it to complete the scan.
11. You can collect data by clicking on the photo button and saving a file of the image you collected.
12. Once you are done scanning the sample, use the software to withdraw the tip and then you can manually raise the head and remove the sample.
13. Pack the parts back into the case the way they were before.

STM: Operation Procedure



1. Electronic control unit
2. Power Supply
3. Granite stand
4. Scanning Tunneling Microscope (STM)
5. Sample Holder
6. STM LED
7. Acrylic air-guard
8. Magnification window

Pt/I Tip Preparation:

- Retrieve a **Pt/In** wire and the red plastic toolbox included in the STM kit.
- Clean Pt/In wire with alcohol or other solvent, rinse with distilled water.
- Grasp wire with needle nose pliers (included in red kit), allow **1 cm** of wire to protrude from pliers.
- Use wire-cutters (included in red kit) to cut a sharp point (**$\theta < 90^\circ$**).
 - You want to pull away while cutting the wire, this will simultaneously stretch and cut the wire into a sharp point.
- After cutting, install the tip into the recessed groove and gold retaining clip -using needle-nose pliers- on the STM stage/head.

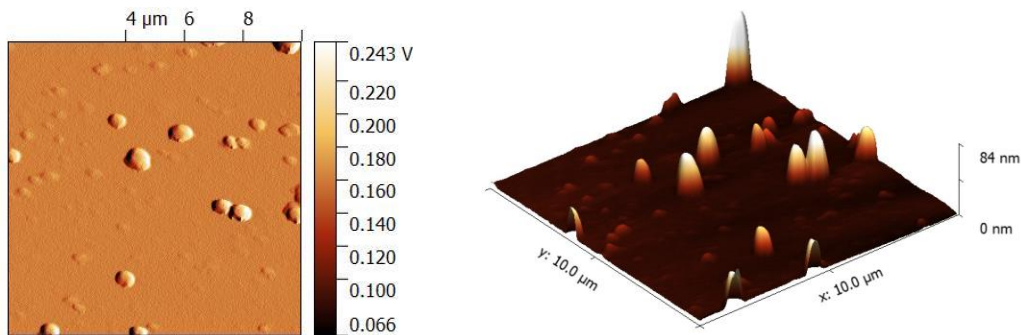
Microscope Setup

- Remove STM and accompanying electronics from plastic case. Place STM on granite tabletop; place electronic control unit and power supply **NEAR** granite table but **NOT ON IT**. Connect serial cables and power supply to appropriate electronic control unit. Turn on the power supply and verify that the STM LED is **ORANGE**.
- Connect the STM to your computer with the SERIAL to USB adapter.
 - STM must be powered on **BEFORE** it is connected to your computer.
- Place your **CONDUCTIVE** sample onto the cylindrical sample holder using conductive carbon tape and slide the sample to within 1mm of the Pt/In tip. **DO NOT CRASH THE TIP INTO THE SAMPLE**. If the sample touches the tip, cut a new tip. The LED on the STM will turn **RED** if the tip touches the sample surface.
- Cover the STM with the acrylic air-flow guard and rotate the guard until you are able to view the separation distance between the surface and the Pt/In tip (through the built-in magnification window).
- Open the *Nanosurf Easyscan STM* software and verify that the STM is connected and communicating with your computer, navigate to the **APPROACH** panel. While monitoring the tip/sample separation distance through the magnification window, use the **MANUAL** feature on the **APPROACH** panel to decrease the sample/surface separation distance until sample is barely above the surface.
- Activate the **AUTO** approach feature in the **APPROACH** panel; this will reduce the sample/tip separation distance until an appropriate tunneling current is detected between the sample surface and Pt/In tip. The STM LED should turn **GREEN**. The *Nanosurf Easyscan STM* software will begin collecting data once tunneling current is obtained.

Obtaining Quality Images

- Make sure the tip is perpendicular to the surface, by leveling both the X and Y slopes.
 - Adjust X-slope by changing its corresponding value in the X-slope input panel until it is horizontal. Adjust Y-slope by first rotating the tip 90 degrees (rotation option under [>>]) then change its corresponding value in the Y-slope input panel until it is horizontal. Rotate back to 0 degrees before scanning.
- Adjust the set-point value, as well as the proportional, integral, and differential (PID) settings. These values are sample specific so they should be adjusted each time.
- Decreasing scan rate and increasing sample rate will improve image resolution.
- After installing the Pt/In wire, if you let the STM sit for at least an hour before scanning, the tip will reach thermal equilibrium; this can minimize thermal drift artifacts.


Gwyddion SPM Analysis Software



Software Setup

- Download and install stable version of Gwyddion for respective operating system from <http://gwyddion.net/download.php>.

Image Setup

- Open scan file;
 - File > Open > [yourfile].ezd
- Show ZOutput data;
 - Info > Show Data Browser > ZOutput
- Show 3D Output data;
 - View Panel > 

Data Correction Workflow Setup




- Shift minimum to zero:
 - Data Process Panel > 
- Level data:
 - Data Process Panel > 
- Adjust Color range:
 - Tool Panel > 
- Artifact filtering;
 - Data Process > Correct Data > 2D FFT Data Filtering
 - Highlight bright features away from center (vertical bands, dots, etc...) using the FFT mask editor, toggle between *original* and *image difference* to see the results.
 - Repeat this until the image no longer improves, this is heavily trial and error.
 - Output and save image difference.

Image J

Before you start:

To download the Image J program, go to: the NIH website and select their download option that's right for you <http://rsb.info.nih.gov/ij/download.html> (with my 2014 Stout issue laptop, I selected the first windows bundle). In the folder that you download, you'll want to select the image J executor (ImageJ.exe) and say extract all. After it has finished extracting you'll select run and it will open the image J program on you laptop.

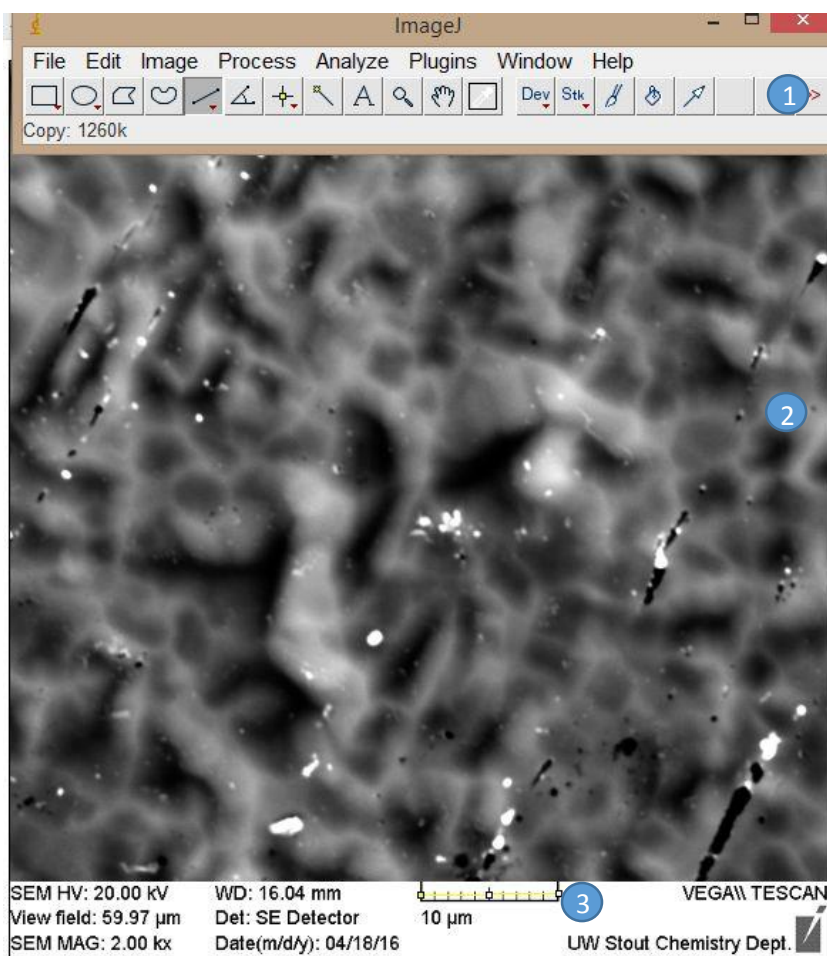


Figure:

Image J tool bar with an opened image. Displayed is the tool bar, with the various image tools shown (1), a black and white opened image (2), and the scale bar with a line drawn across it (3).

Selecting an Image:

When taking images to use in image J it is important to include a scale bar or to have an image at the same magnification with a scale bar in order to ensure proper calibration of the program to work on particle sizing. It is also helpful to have either black or white particles or an oppositely colored background to ensure proper image contrast.

Running Image J:

1. Open the image J program
2. Select File, go to open and select the name of your sample photo that you wish to analyze
3. Select the line tool, and draw a line with a known dimension onto the ruler or measuring device present in your sample image or calibration image. Next go to **Analyze**, and choose **set scale**. Enter in the know distance and choose appropriate units, mm work well. Also check the global option.
4. Now to change your image a form so it can be easily analyzed go to **Image**, select **type** and then choose **8-bit**.
5. Next go to **Edit** and choose **invert**, this works well if your background was dark and your particles were light in color on your sample image.
6. Now got to **Image**, select **adjust** and choose threshold. Set the default to black and white, with the line just short of the gray distribution. After that is set up, hit apply.
7. The following are all operations that help to remove artifacts from your sample images, you may have to try several out to get the effect you want for your end goal.
 - a. Go to **Process**, choose **binary**, and select **fill holes**
 - b. Go to **Process**, choose **noise**, and select **despeckle**
 - c. Go to **process**, choose **binary**, and select **watershed** (this separates touching particles)
8. After you are satisfied with your image, go to **Analyze** and select **set measurements**. Check the boxes for area, perimeter, bounding rectangle, ferrets diameter, and fit ellipse. Then select ok.
9. Now go to **Analyze**, and select **analyze particles**. Select an appropriate size range, and say no to pixel units by leaving the box unchecked.
10. For the final step, save your data and the altered image files for use at a later time. The particle size information can easily be uploaded into an excel document for further analysis.

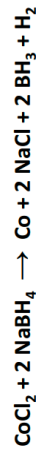
Cobalt Nanoparticles: Foam Synthesis and Characterization

Roy Lindsay, Todd Zimmerman, Matthew Ray
NANO – 230, NANO – 401

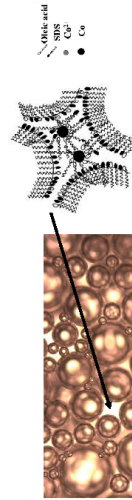
Introduction

Cobalt nanoparticles yield interesting electronic, catalytic, optical, and magnetic properties and are –subsequently– an important area of study for applications in magnetic storage, photonics, and electronics.³

While there are many techniques to produce cobalt nanoparticles such as: co-precipitation, thermal decomposition, micro-emulsion, and hydrothermal synthesis, foam synthesis remains one of the simplest techniques to date. Apart from surface passivation, the primary reaction mechanism is a redox reaction between cobalt chloride and sodium borohydride.¹



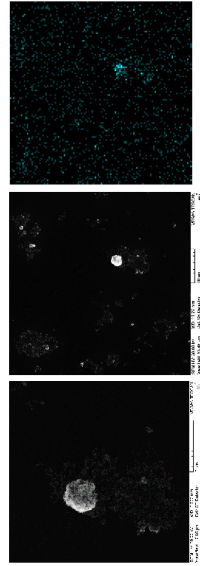
Apart from the primary redox reaction between CoCl_2 and NaBH_4 , the addition of oleic acid helps with nano-particle stabilization which affects particle size and shape. In this research project, I was specifically interested the relationship between oleic acid concentration and nanoparticle size.



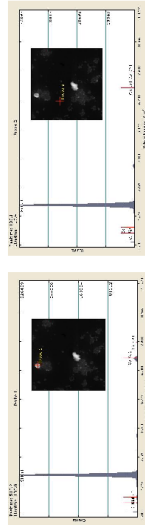
The anionic surfactant (SDS) bubbles enclose the reactants into small “micro-reactors”. Oleic acid attaches to the facets of the growing cobalt nanoparticle. As more oleic acid attaches to the nanoparticle, its growth becomes limited.

Characterization

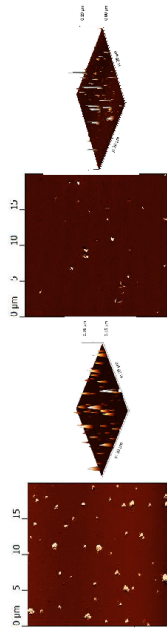
Multiple size characterization techniques were utilized including: Dynamic Light Scattering, Scanning Electron Microscopy (SEM), Atomic Force Microscopy (AFM), Electron Dispersion X-ray (EDX).



SEM scan(s) of a large 0.009M oleic capped cobalt nanoparticle aggregate. Left: 2000X magnification. Right: 6000X magnification. The right picture shows cobalt EDX element mapping, this matches the location of the cobalt aggregate.



EDX probe scans showing (left) the presence of cobalt in a nanoparticle aggregate and (right) the absence of cobalt when scanning just the underlying silicon substrate.

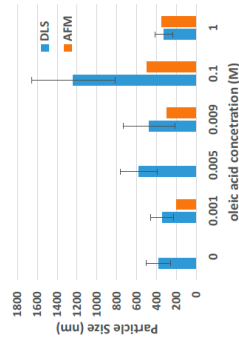


Amplitude and topographic AFM scans of (left) 100-400 nm cobalt nanoparticles capped with 0.009M oleic acid and (right) 100-300 nm cobalt nanoparticles capped with 0.001M oleic acid.

Results

Particle sizes for 0M, 0.001M, 0.005M, 0.009M, 0.1M, and 1M oleic acid capped cobalt nanoparticles were 382nm, 343nm, 579nm, 475nm, 1239nm, and 325nm respectively.

Oleic Acid (M)	DLS (nm)	AFM (nm)
0	382	124
0.001	343	114
0.005	579	187
0.009	475	263
0.1	1239	422
1	325	90



(Left) Nanoparticle size tabulation for various concentrations of oleic acid and (Right) corresponding DLS/AFM data.

Conclusion

In this experiment, cobalt nanoparticles of various sizes were synthesized using a novel foam-synthesis method. The size of the nanoparticles was measured as a function of oleic acid concentration. It was found that the particle size did not significantly change with varying oleic acid concentrations. The large standard deviations in both the 0.009M and 0.1M trials indicate more data and repeat trials are necessary to reach a confident conclusion regarding the effect oleic acid has on cobalt nanoparticle size, specifically, in a foam-style synthesis.

References

- (1) Bala, T.; Foam-Based Synthesis Of Cobalt Nanoparticles And Their Subsequent Conversion To Cocoreagshell Nanoparticles By A Simple Transmetalation Reaction. *Journal of Materials Chemistry* 2004, 14, 1057.
- (2) Brayner, Roberto, Fernand Fievet, and Thibaud Coradin. *Nanomaterials*. London: Springer, 2013. Print.

Copper Nanoparticles: Synthesis and Characterization

Ellie Raethke, Matthew Ray

Nano 401-Nanotechnology Applications

Background

Copper nanoparticles are versatile because they have good catalytic, optical, and electrical conducting properties. They are also cost effective when compared to nanoparticles made of noble metal. Their applications include use in printed circuit boards and flexible electronics. The synthesis method used for this preparation is known as a polyol method. It can create a highly controlled particles size distribution by varying temperature, injection rate of copper solution and amount of reducing agent.

Materials

- Polyvinylpyrrolidone (PVP)
- Copper (II) sulfate pentahydrate
- Reducing agent
- Sodium phosphinate monohydrate (hypophosphite)
- Ethylene glycol
- Diethylene glycol
- Mineral Oil

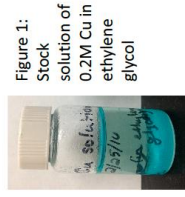


Figure 1:
Stock solution of 0.2M Cu in ethylene glycol

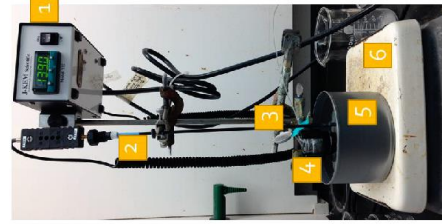


Figure 2: Reactor set-up with numbered pieces of equipment

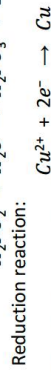
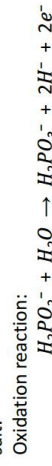
Equipment

1. Temperature Controller
2. Thermocouple and Cable
3. Ring stand and Clamps
4. Scintillation Vial
5. Mineral Oil Bath
6. Hot Plate with Stirring

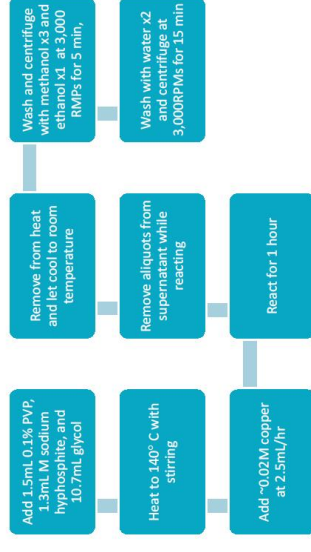
Not pictured: syringe pump, syringe, tubing and stir bars

Synthesis

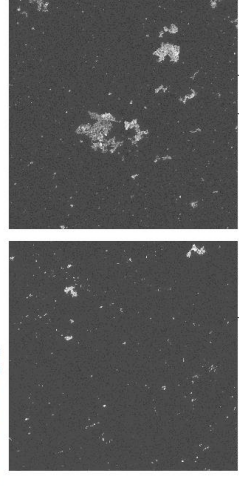
The hypophosphite acts as the reducing agent for the copper salt.



Two different syntheses were carried out, one with ethylene glycol as the solvent and the other with diethylene glycol.

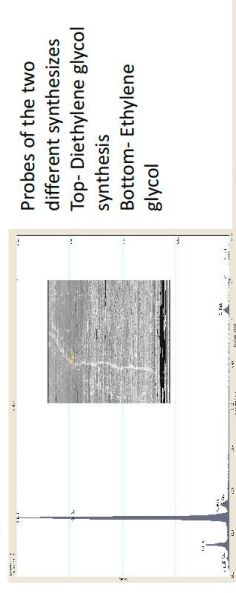


Microscopy



Secondary electron detector images of diethylene glycol (left) and ethylene glycol (right) syntheses.

Energy Dispersive X-ray:



Probes of the two different syntheses
Top- Diethylene glycol synthesis
Bottom- Ethylene glycol

Characterization

Zeta Sizer: Aliquots from both different syntheses were removed during the reaction process.

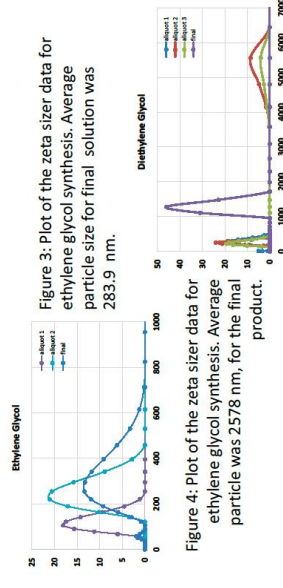


Figure 3: Plot of the zeta sizer data for ethylene glycol synthesis. Average particle size for final solution was 283.9 nm.

Figure 4: Plot of the zeta sizer data for ethylene glycol synthesis. Average particle size for final product was 2578 nm.

Conclusions

The copper particles created were on the order of hundreds of nanometers. The diethylene glycol particles had a substantial amount of aggregation, leading to overall large particle size.

References

- Park, B. K., Jeong, S., Kim, D.; Moon, J.; Lim, S.; Kim, J. S. Synthesis and size control of monodisperse copper nanoparticles by polyol method. *Journal of Colloid and Interface Science*. 2007, 311, 417-424.

Synthesis of Hydroxyapatite Nanoparticles

Thomas Palof, Matthew Ray, Todd Zimmerman
University of Wisconsin-Stout
Nano-230 and Nano- 401

Introduction

Hydroxyapatite is the primary mineral component in bones and as such has recently been garnering a lot of attention. It is currently being researched for a wide variety of applications ranging from use as either the primary component or coating in prosthetics, as thin film adhesives that will not interfere with imaging techniques, to even uses in drug delivery or as a possible cure for cancer. The goal of this research is to determine the feasibility of the synthesis of hydroxyapatite nanoparticles and to lay the ground work for future research on this topic. To determine the viability of this synthesis process, multiple articles were consulted before selecting one method to adapt for our facilities here at Stout.

Materials

- Calcium Hydroxide 0.5M $\text{Ca}(\text{OH})_2$
- Orthophosphoric Acid 0.3M H_3PO_4
- Scintillation Vial
- Hot plate
- Stir bar
- Beaker
- Temperature regulator

Procedure

- Fill beaker with water and place on hot plate to create a constant temperature bath using the temperature regulator (Sample A 50-60°C)
- Fill the Scintillation vial with 5 ml of 0.5M $\text{Ca}(\text{OH})_2$ ($\frac{1}{2}$ the volume of Hydroxyapatite desired)
- Add Stir bar to Scintillation vial and place in temperature bath.
- Inject 5 ml of 0.3M of H_3PO_4 (same volume as before) at a rate of 100ml/min or below for a reaction conversion rate of 100% (Essentially inject over a 3 second period)
- Allow to react until the resulting aqueous suspension is a whitish and possesses a solid (Hydroxyapatite nanocrystals) content of 2.5 wt%
- Run procedure for temperatures of 25-30, 70-75

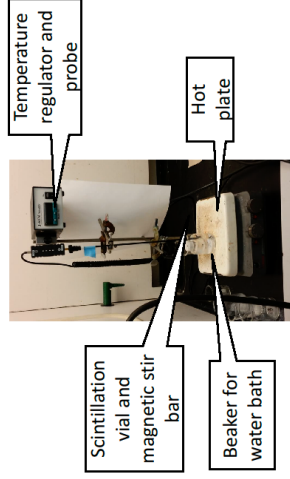


Figure 1: This is the reactor setup for this procedure

Samples

- Sample A – 50-60°C
- Sample B – 25-30°C
- Sample C – 70-75°C
- Sample D – ~25°C

(Very dilute Orthophosphoric Acid long reaction time)



Figure 2: Samples

Conclusions and Future Research:

While the hydroxyapatite particles synthesized were much larger than desired the last iteration of synthesis was on the nanoscale, with features around the 10-100 nm scale. This change in morphology was likely due to both a lower reaction temperature and lower concentration of orthophosphoric acid. We believe that the major cause of our particles being much larger than those referenced in the procedure by Bouyer et al. is primarily the improper scaling of the rate of addition of the orthophosphoric acid to the solution making it too available and the reaction to happen almost instantaneously instead of evolving slowly. With this adjustment and some fine tuning we believe it will be possible to synthesize hydroxyapatite crystals for using in synthetic bone research here at Stout.

Optical Microscopy

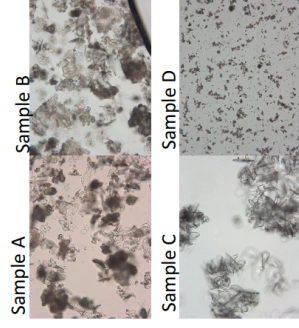


Figure 3: All images are at 20x magnification

Scanning Electron Microscopy

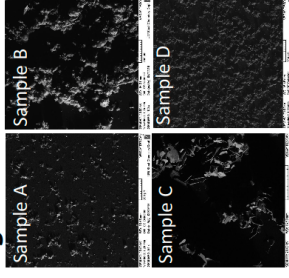


Figure 4: Samples A, B, and D are at 100x magnification, while sample C is at 154x magnification

References

- Bouyer, E., F. Gitzhofer, and M. I. Boulos. "Morphological Study of Hydroxyapatite Nanocrystal Suspension." *Journal of Materials Science: Materials in Medicine* 11 (2000): 523-31. Web.
- Ferraz, Maria Pia, Fernando Jorge Monteiro, and Candida Maria Manuel. "Hydroxyapatite Nanoparticles: A Review of Preparation Methodologies." *Journal of Applied Biomaterials & Biomechanics (JABB)* 2 (2004): 74-80. Web.

Magnetite Nanoparticle Synthesis

Cody Lang, Matthew Ray

NANO-401 Nanotechnology Applications

Introduction

Magnetite (Fe_3O_4) is a unique form of iron oxide that exhibits electric and magnetic properties that other iron oxides do not. This is due to the Fe^{2+} and the Fe^{3+} ions in each molecule. Due to these ions, electrons can easily transfer throughout the particle. Magnetite displays properties such as super paramagnetism at certain sizes. Due to this property and its low toxicity, magnetite nanocubes are used in magnetic biomedicine; specifically magnetic resonance imaging (MRI). The specific characteristics of magnetite depends on the exact shape and size of the particles. Other uses for magnetite nanoparticles include information storage media, heavy metal ion removal, electromagnetic wave absorption, ferrofluids, and biocatalysts.



Fig 1. Iron (II, III) oxide also known as magnetite.

Experimental Methods

Two different synthesis methods were used to create magnetite nanoparticles. The first of which is a co-precipitation from iron sulfates (fig 2a). The suggested amounts in the original document were decreased to 10% of what was used so that smaller reactions were taking place. .28g of $\text{FeSO}_4 \cdot 7\text{H}_2\text{O}$ and .40g of $\text{Fe}_2(\text{SO}_4)_3$ were dissolved in 10mL of DI water for 5 minutes in a 50mL beaker using a magnetic stir bar. 0.08g of sodium dodecyl sulfate (SDS) was added to the solution while stirring. Then the pH of the solution was adjusted to 12 by adding solid NaOH. The approximate amount for this reaction was around 0.4g of NaOH. After the pH was adjusted to 12, the solution was left to stir for 20 minutes. The original procedure calls for a lamp (wavelength 400-750nm) to be placed within 10cm of the beaker for 0-60 minutes. This was not done for the first synthesis. The black precipitate that formed was then immediately washed alternately with DI water and ethanol several times until the pH was returned to neutral. The black precipitate were dried at room temperature.

The second synthesis method was a solvent-less thermal decomposition of ferrocene. Ferrocene (>98% ACROS ORGANICS) and polyvinylpyrrolidone (PVP K90, M_w 360,000) were grinded together at a 1:1 weight ratio of ferrocene to PVP, totaling 300mg. The solid mixture was then placed in an empty and cleaned stainless steel threaded CO_2 cartridge (fig 2b). This was done because a 1mL stainless steel sealed cell was not available. The cell was sealed shut with Teflon tape to ensure an air tight seal. The steel cell with the solid mixture was then placed in a 350°C preheated furnace to anneal for 2 hours. The cell was then removed and allowed to cool to room temperature. The resulting black powder was then washed with ethanol extensively via centrifugation.

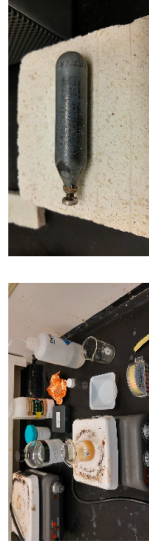


Fig 2. a) co-precipitation reaction. b) steel CO_2 cell.

Sizing

All the resulting precipitates and powders were sized using a zeta sizer. A zeta sizer measures particle size by Brownian motion, which is the random movement of particles in a liquid due to bumping into surrounding particles. Smaller particles will move faster in a liquid than a larger particle will. The instrument will take two "images" of the solution at different time frames. By measuring how much a particle has moved, the size of the particle can be calculated. This is a simple explanation of the process.

Figure 3 shows the zeta sizing results for the four synthesis reactions. Every synthesis except the 2nd co-precipitation reaction yielded particles around the size of 200nm. The 2nd co-precipitation reaction yielded particles closer to 400nm. This is due to allowing the reaction to proceed unhindered for 30 mins before washing.

Figure 4 shows SEM images of some of the nanoparticles. Figure 4a (first co-pre reaction) is interesting because it shows that the solution was not washed thoroughly enough. Figure 4b shows that magnetite likes to aggregate and form larger particles. This is confirmed in every SEM image. Figure 4c is an image of particles from the first thermal decomp synthesis. While there are still larger aggregates in the image, smaller particles can be seen

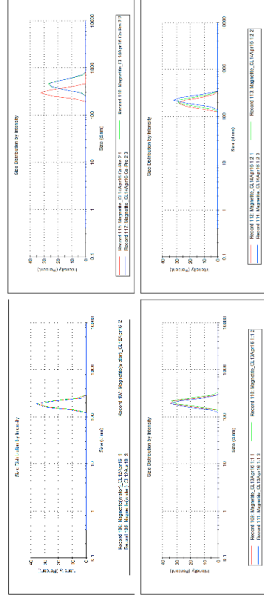


Fig 3. (top left) First co-pre synthesis. (top right) Second co-pre synthesis. (bottom left) First thermal decomp synthesis. (bottom right) Second thermal decomp synthesis.

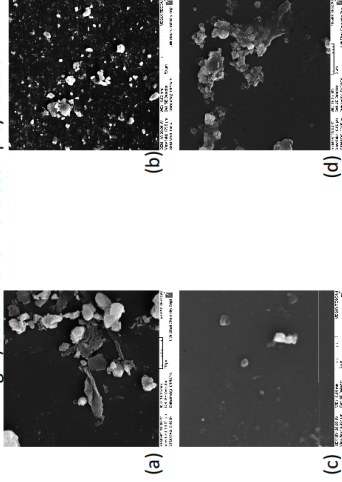


Fig 4. Showing SEM images of particles from all four syntheses. throughout the background. These are estimated to be about 50-60nm. A closer clearer image was not able to be produced. Figure 4d, the second thermal decomp, shows that due to the larger amount of PVP present, the magnetite seems to be trapped in a PVP cross linked matrix.

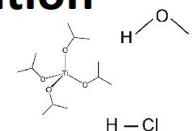
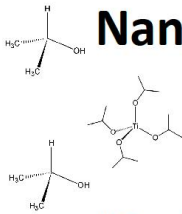
Conclusion

Magnetite was able to be synthesized, but not to the desired size or to the specific morphology wanted. Both methods are effective methods to produce magnetite nanoparticles, but need further testing to hone in on the desired outcome.

A Tale of Two Synthesis: Titanium Dioxide Nanoparticle Synthesis and Characterization

Aaron Forde, Matt Ray

Nano 401 – Nanotechnology Applications



“Simple” Sol Gel Synthesis

Background:

The sol gel method of synthesizing nanoparticles involves the hydrolysis of a metal alkoxide precursor. In this synthesis titanium Isopropoxide (TTIP) is hydrolyzed with isopropanol (IP) present as a peptization agent and heated to 60 C for 18 hours.

Method:

- 1) Prepared 9.26 mL of deionized H2O into a scintillation vile.
- 2) Heated the deionized water to 60 degrees Celsius.
- 3) Mixed together:
 - 0.17 mL of TTIP
 - 0.15 mL of IP
- 4) Added mixture to the 9.26 mL of Deionized water
- 5) Let the peptization process react for 18 to 20 hours.



Image 1: Reactor setup for “simple” synthesis.

Synthesis:

Chemical Reaction:

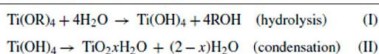


Image 2: Chemical reactions that results in TiO₂ nanoparticles.



Image 3: Final product from the “simple” sol gel synthesis.

Characterization :

Atomic Force Microscopy:

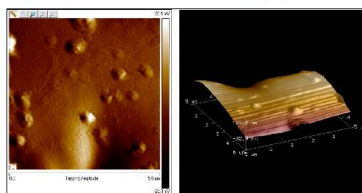


Image 4: AFM images of TiO₂ nanoparticles on a silicon substrate. The nanoparticles in this image have an average diameter of 290nm.

Dynamic Light Scattering:

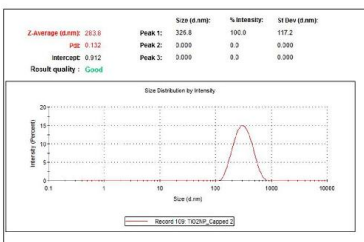


Image 5: Dynamic Light Scattering distribution of TiO₂ nanoparticles. The average size of particles in this distribution is 283.8nm. This agrees favorably with the AFM images in Image 4.

Reference: Synthesis of TiO₂ nanoparticles by hydrolysis and peptization of titanium Isopropoxide
S. Mahshida, M. Askaria, M. Sasani Ghamasrib, +

Catalyzed Sol Gel Synthesis

Background

This synthesis is almost identical to the “Simple” Sol Gel Synthesis except hydrochloric acid (HCl) is used as a catalyst for the condensation step of the chemical reaction.

Method

- 1) Mixed together the 1st solution:
 - 1.283 mL IP
 - 0.103 mL Deionized Water
 - 0.039 mL HCl (1 M)
- 2) Mixed together the 2nd solution:
 - 1.000mL IP
 - 0.435mL TTIP
- 3) Drip each of these solutions into the scintillation vile at a slow and constant rate
- 4) Let the solutions mix for 5 minutes.



Image 6: Reactor setup for “Catalyzed” synthesis.

Synthesis

Chemical Reaction

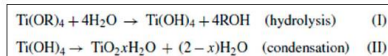


Image 7: Chemical reactions that results in TiO₂ nanoparticles. In this synthesis the HCl catalyzes reaction (2) by donating its proton to the hydroxide groups.



Image 8: Final product from “catalyzed” reaction.

Characterization

Atomic Force Microscopy:

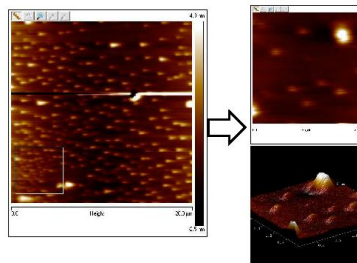


Image 9: AFM images of TiO₂ nanoparticles on a silicon substrate at a 20um x 20um scan range and 3.3um x 3.3um scan range The nanoparticles in 3umx3um image have an average diameter of 317nm.

Dynamic Light Scattering:

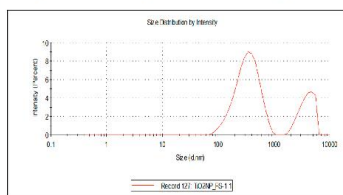


Image 10: Dynamic Light Scattering distribution of TiO₂ nanoparticles. The average size of particles in this distribution is 421nm with the first peak happening at 361nm. This agrees reasonably with the AFM images in Image 9.

Reference: Synthesis, characterization, and photocatalytic application of novel TiO₂ nanoparticles
M. Hussain, R. Ceccarelli, D.L. Marchisio, D. Fino

Tungsten Oxide Nanoparticle Synthesis

James Schroder, Matthew Ray
NANO-401 Nanotechnology Applications

Background

- Electrochromic devices
- Superconductor gas sensors
- Photocatalysis
- High melting point
- Not very reactive

Methods

A solvothermal synthesis was used to make particles of two different morphologies. The starting solution was made from tungsten hexachloride and ethanol. From there, reaction solutions were made by adding either more ethanol or water. The solutions were put in capillary tubes and sealed with a torch. They were then left in an oven for around 12 to 14 hours.



Figure 1: Capillary tubes used for reactions.



Figure 2: Starting solution changed color over a period of 48 hours.

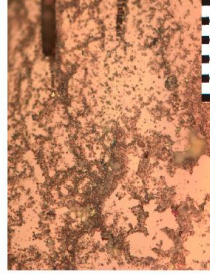
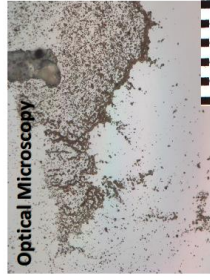


Figure 3: A) Particles made from addition of Ethanol. B) Particles made from addition of water. Scale Bars: 100 μm

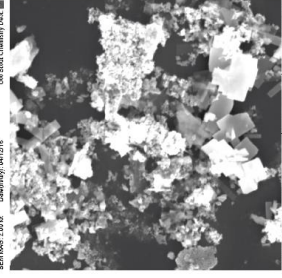
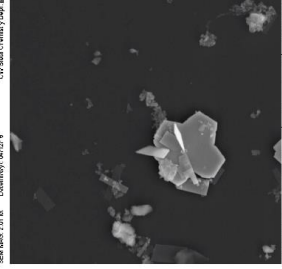
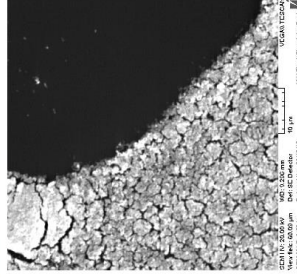
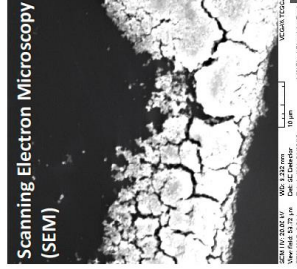


Figure 4: A and B show the particles prepared in ethanol while C and D show the particles prepared in water.

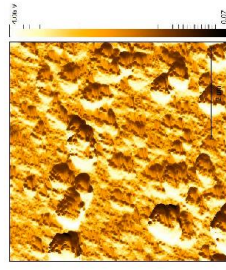
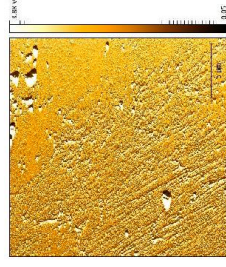
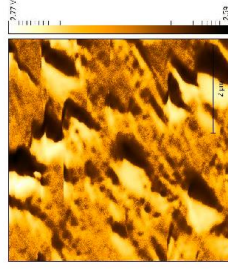
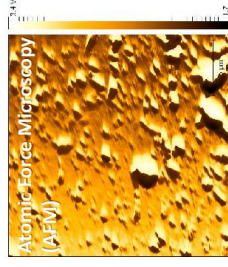


Figure 5: A and B show the ethanol particles while C and D show water particles.

Conclusions

This method is an easy and effective means of creating different morphologies of tungsten oxide nanoparticles. Given better equipment and more rigorous trials, size could become smaller and distribution could be narrower. Using capillary tubes as reaction bombs is possible but not reliable as even if a small hole remains, the liquid will vaporize and escape the tube. It may be worth continuing to find other possible morphologies by varying the proportion of added water and ethanol.

Zinc Oxide Nanoparticles: Applications, Synthesis, and Characterization

Nicole Moehring, Matthew Ray
NANO 401 – Nanotechnology Applications

Background:

Properties of Zinc Oxide:

- White appearance but almost transparent when grinded down to small particles
- Luminescent
- Semiconductor
- Piezo/pyroelectric

Applications:

- Sunblock
- Sensors
- Thin films
- Transducers
- Catalysts

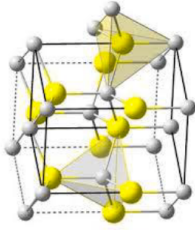


Fig 1) Wurtzite structure of Zinc Oxide, O²⁻ (yellow) and Zn²⁺ (gray)

Synthesis:

Reactor Components:

1. Temperature probe
2. Condenser
3. Addition funnel
4. Stir plate and stir bar
5. Heating mantle
6. 25 mL, 3 neck round bottom flask

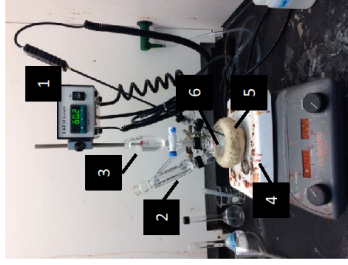


Fig 2) Labeled reactor setup used for wet synthesis of ZnO particles

Procedure:

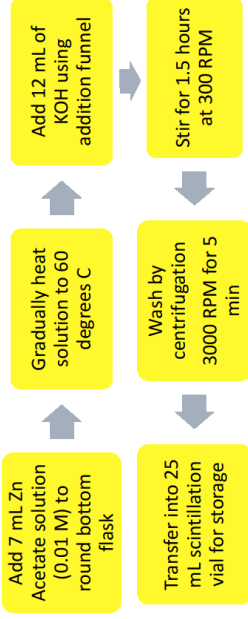


Fig 3) Flow chart describing step by step synthesis of ZnO particles. In image: (from left to right) ZnO precipitate from first procedure (using saturated KOH solution), ZnO precipitate from second procedure (using 0.1 M KOH solution), DI water.

Zetasizer:

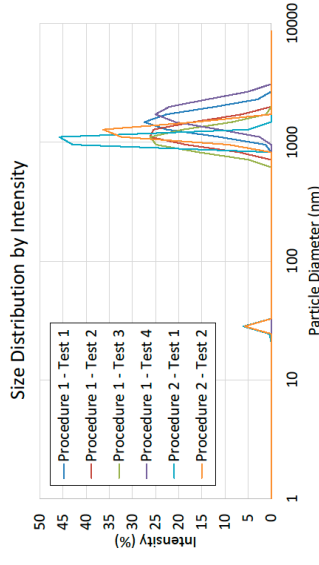


Fig 5) Procedure 1 peaks: 1480 (run 1), 1110 (run 2), 1110 (run 3) and 1720 (run 4). Procedure 2 peaks at 24.4 and 1110 (run 1) and 28.2 and 1280 (run 2).

Characterization:

Scanning Electron Microscopy (SEM):

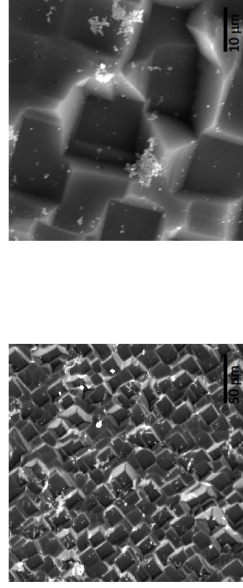
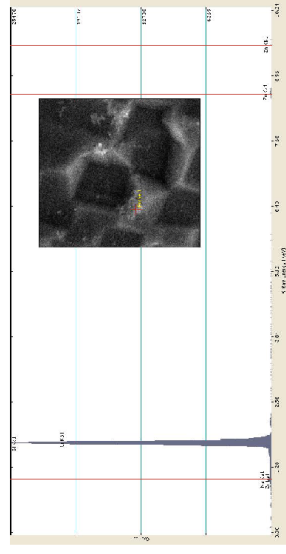


Fig 4) Left: SEM image at 500x mag. Right: SEM image at 2.2kx mag. ZnO particles seen as white specks on silicon surface

Energy Dispersive X-ray Spectroscopy (EDX):



Element	Weight %	Atomic %
Na	4.26	5.26
Si	92.12	93.16
Zn	3.62	1.57

Fig 6) Probe analysis of sample using EDX. Supports conclusion that white particles contain zinc (red lines indicate energy values for Zn).

Foam-based synthesis of cobalt nanoparticles and their subsequent conversion to Co_{core}Ag_{shell} nanoparticles by a simple transmetallation reaction

Tanushree Bala, Sujatha K. Arumugam, Renu Pasricha, B. L. V. Prasad* and Murali Sastry*

Materials Chemistry Division, National Chemical Laboratory, Pune – 411 008, INDIA.
E-mail: sastry@ems.ncl.res.in; E-mail: blyprasad@dalton.ncl.res.in

Received 19th November 2003, Accepted 21st January 2004
First published as an Advance Article on the web 18th February 2004

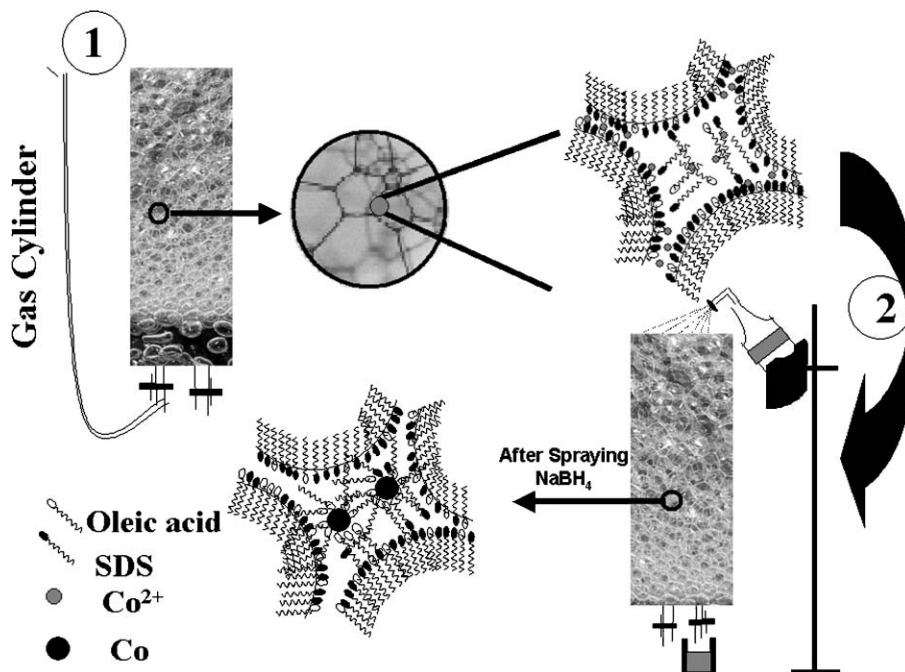
Cobalt nanoparticles have been synthesized *via* a novel, foam-based protocol. The foam is formed from an aqueous mixture of Co²⁺ ions, an anionic surfactant and oleic acid where the cobalt ions are electrostatically entrapped by the surfactant at the thin borders between the foam bubbles and their junctions. The entrapped cobalt ions may be reduced *in-situ* by a moderately strong reducing agent resulting in the formation of nanoparticles with the foam playing the role of a template. The nanoparticles are immediately capped and stabilized against oxidation by oleic acid present in the foam matrix. The oleic acid-capped Co nanoparticles can be redispersed either in an aqueous or organic medium making this procedure very attractive. The cobalt nanoparticles are readily converted to Co_{core}Ag_{shell} nanoparticles by simple addition of a silver salt to the Co nanoparticle solution, the cobalt atoms on the nanoparticle surface acting as localized reducing agents for the silver ions.

1 Introduction

Transition metal nanoparticles, especially those of Fe, Co and Ni are considered to be very important for many technological¹ and catalytic² applications. When synthesized in an aqueous medium, these nanoparticles are favored for various biological applications.³ However, one of the drawbacks of the synthesis of Fe, Co and Ni nanoparticles in an aqueous medium is that they are highly unstable and undergo oxidation necessitating their use immediately after preparation.⁴ To overcome the problem of oxidation, attempts have been made to synthesize these nanoparticles in an organic environment with suitable protective agents.⁵ In this paper we restrict our discussion to cobalt nanoparticles although the general chemistry involved in the nanoparticle synthesis of other two metals, namely Fe and Ni, is rather similar. The general synthetic procedure adopted for the synthesis of cobalt nanoparticles generally proceeds along two pathways: (i) a reverse micelle-based method, and (ii) purely organic solution-based methods. Reverse micelles are water droplets in oil stabilized by a monolayer of surfactant. Preparation of cobalt nanoparticles by this method involves multiple steps with the preparation of Co(AOT)₂ [AOT = bis(2-ethylhexyl) sulfosuccinate] being the first step.^{6a} Subsequently, micellar solutions of Co(AOT)₂ with Na(AOT) and sodium borohydride in water with Na(AOT) are mixed to carry out the reduction of Co²⁺ ions. They are then extracted under anaerobic conditions, covered with trioctylphosphine and redispersed in pyridine.^{6a} Purely organic-based methods also involve complex synthetic procedures and high temperatures where [Co₂(CO)₈] is reduced with the hot trioctylphosphane-oxide (TOPO) reagent.^{6b} The resulting Co nanoparticles are stabilized by the TOPO itself or in several cases by organic carboxylic acids like oleic acid and lauric acid, *etc.*, which are taken together with TOPO. High temperature polyol processes in which a high boiling point alcohol is used both as solvent and as reductant have also been successful in synthesizing cobalt nanoparticles.⁷ Here, the typical synthetic procedure involves the addition of 1,2-dodecanediol to hydrated cobalt

acetate in diphenyl ether, in presence of oleic acid and trioctylphosphine at 250 °C, where particle size control is achieved by changing the relative concentrations of cobalt acetate and oleic acid. The above procedures have been quite successful in obtaining good quality Co nanoparticles in organic solvents and generally result in the formation of ordered arrays of superlattices upon drying on suitable substrates.^{5–7} However, the complexity involved in the above synthetic procedures is quite evident, requiring many steps (reverse micelle method) and the use of non-regular chemicals (purely organic-based methods). It is also clear that scaling up of these synthetic procedures will be rather cumbersome. As mentioned above, for biological applications as well as scaling up purposes the synthesis of these nanoparticles in an aqueous medium is preferred. For these reasons we have been looking for alternative avenues for the synthesis of Fe, Co and Ni nanoparticles in water using simple salts routinely available in the laboratory as metal sources with an option for scaling up the yield relatively easily.

Herein we report the synthesis of cobalt nanoparticles using liquid foams as a template. Liquid foams have been restricted to the domain of physicists so far, where the majority of studies have been carried out to understand the physics of foams with respect to their formation and stability.⁸ Davey and co-workers have used foams as templates for the nucleation of calcium carbonate crystals⁹ but the possibility of carrying out chemical reactions in foams as a means of synthesis of materials with an in-built, scale-up option is still in its infancy. We have recently embarked on a program aimed at understanding the use of liquid foams in the synthesis of nanomaterials. Our strategy involves the formation of foams with aqueous solutions of metal ions and a suitable anionic or cationic surfactant (depending on the charge of the metal ion) as the first step as shown in Scheme 1. Subsequently, the desired chemical reaction such as reduction (for preparation of metal nanoparticles) or complexation (for the preparation of minerals) is carried out resulting in the formation of the required nanomaterials *within the foam*. The first studies on the formation of gold



Scheme 1 Drawing showing the different steps involved in the foam-based synthesis of stable cobalt nanoparticles. Steps 1 and 2 are described in the text in detail.

nanoparticles in foams have yielded interesting results with some indication of morphology variation in the gold nanoparticles that reflects the complex structure of the foam.¹⁰ In this paper, we extend this process for the synthesis of cobalt nanoparticles. Initial studies on the formation of Co nanoparticles by complexing Co^{2+} ions with pure sodium dodecyl sulfate (SDS) as the foaming surfactant did not yield stable nanoparticles in water. We then revised our strategy and oleic acid was taken along with SDS to form the foam. The resulting Co nanoparticles from this revised strategy were quite stable in both aqueous as well as organic media.

We have also devised a simple strategy to prepare core-shell structures of cobalt and silver, respectively. Preparation of core-shell nanomaterials assumes significance for two reasons: (i) improved stability of the nanoparticles, and (ii) flexibility in surface modification. It is recognized that it is quite easy to modify the surfaces of noble metal nanoparticles like gold and silver using simple thiol or amine chemistry.¹¹ We envisaged that if we can prepare core-shell structures of Co (core) and Ag (shell), it would not only render the cobalt nanoparticles more robust chemically but also provide us with the manipulative ability to modify the surface properties of the Co nanoparticles. To make the $\text{Co}_{\text{core}}\text{Ag}_{\text{shell}}$ nanostructures, we have employed a simple transmetallation¹² reaction wherein the cobalt atoms residing on the surface of cobalt nanoparticles were effectively used as reductants for aqueous silver ions. Thus, the use of surface cobalt atoms as a reducing agent would yield core-shell structures thereby obviating the need to employ an external reducing agent for Ag ions. The Co and $\text{Co}_{\text{core}}\text{Ag}_{\text{shell}}$ nanomaterials were characterized by transmission electron microscopy (TEM), selected area electron diffraction (SAED), Fourier Transform Infrared (FTIR) spectroscopy, UV-visible spectroscopy and powder X-ray diffraction methods. Presented below are details of the investigation.

2 Experimental details

2.1 Chemicals

Cobalt chloride hexahydrate ($\text{CoCl}_2 \cdot 6\text{H}_2\text{O}$), SDS (sodium dodecyl sulfate), silver sulfate (Ag_2SO_4), oleic acid (*cis*-9-octadecenoic acid,

$\text{C}_{17}\text{H}_{33}\text{COOH}$) and sodium borohydride (NaBH_4) were obtained from Aldrich Chemicals and used as-received.

2.2 Preparation of cobalt-silver nanocrystals in aqueous SDS/oleic acid foam

In a typical experiment, a rectangular column of 50 cm height and a square base of $10 \times 10 \text{ cm}^2$ with sintered ceramic discs embedded in it were used for generation of the foam. An aqueous mixture of 50 ml of $1 \times 10^{-3} \text{ M}$ cobalt chloride solution, 10 ml of 1×10^{-3} oleic acid in methanol and 40 ml of $1 \times 10^{-1} \text{ M}$ SDS was taken in the rectangular column and the foam built up by injecting nitrogen at a pressure of 1–5 psi through the porous ceramic disc fixed to the bottom of the foam column. Stable foams of up to 50 cm height could be routinely obtained. After carefully draining out the excess aqueous SDS/oleic acid and CoCl_2 solution in the foam, the cobalt ions in the foam were subjected to reduction by spraying sodium borohydride solution into the foam. As the cobalt ions were reduced and nanoparticle formation progressed, the foam changed to a gray color and gradually collapsed. The collapsed foam solution containing the cobalt nanoparticles was collected through an outlet provided at the bottom of the column. This solution was then subjected to centrifugation at 5000 rpm for 30 min following which the pellet and supernatant were separated. The pellet was washed several times with ethanol before further characterizations were carried out. This pellet could be easily redispersed either in water or organic solvents like toluene. In a control experiment the foam was formed without prior addition of oleic acid and the reduction carried out. Although the experiment progressed exactly the same way as in the presence of oleic acid, the final cobalt nanoparticle solution was extremely unstable and, except with TEM, no further characterization could be carried out.

For the preparation of core-shell particles, the pellet of oleic acid-stabilized Co nanoparticles (5 ml) after centrifugation was collected, washed several times with ethanol, and to this 1 ml of $5 \times 10^{-5} \text{ M}$ Ag_2SO_4 solution was added. The color of the solution immediately changed to brownish yellow indicating formation of the Ag shell.

2.3 UV-vis spectroscopic studies

The optical properties of the cobalt and $\text{Co}_{\text{core}}\text{Ag}_{\text{shell}}$ nanoparticle solutions were monitored using a Jasco UV-vis spectrophotometer (V570 UV-VIS-NIR) operated at a resolution of 2 nm.

2.4 Fourier transform infrared (FTIR) spectroscopy measurements

FTIR spectra were recorded from drop-coated films of the samples deposited on a Si (111) substrate on a Perkin Elmer, Spectrum-One Spectrometer operated in the diffuse reflectance mode at a resolution of 4 cm^{-1} . The spectrum of pure oleic acid was also recorded for comparison.

2.5 X-Ray diffraction (XRD) measurements

XRD measurements on the Co_{core} and $\text{Co}_{\text{core}}\text{Ag}_{\text{shell}}$ nanoparticles were performed by casting the respective nanoparticle solutions in the form of films on glass substrates by simple solvent evaporation. The diffraction measurements were carried out on a Philips PW 1830 instrument operating at 40 kV and a current of 30 mA with $\text{Cu K}\alpha$ radiation

2.6 Transmission electron microscopy (TEM) measurements

TEM measurements were performed on a JEOL model 1200EX instrument operated at an accelerating voltage of 120 kV. Samples for TEM studies were prepared by placing a drop of the solutions on carbon-coated copper grids. The films on the TEM grids were allowed to dry for 2 min following which the extra solution was removed using a blotting paper.

3 Results

Fig. 1A shows the TEM image of cobalt nanoparticles prepared with just SDS and cobalt ions as the foam constituents. Particles with typically tape-like morphology are observed along with a smaller percentage of spherical particles. The SAED from these particles is shown in Fig. 1B, which clearly supports the formation of crystalline cobalt nanoparticles. It is important to note here that this particular sample was imaged immediately (within minutes) after the sample preparation. The

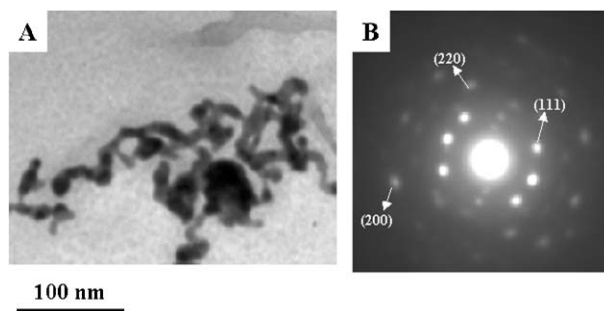


Fig. 1 (A) TEM pictures of cobalt nanoparticles. These were obtained when the foam was formed from the aqueous mixture of Co^{2+} ions and SDS. (B) Selected area electron diffraction from the same particles. The diffraction could be indexed to the fcc phase of cobalt.

cobalt nanoparticle solution prepared with only SDS as the foaming agent was generally grayish-black immediately after preparation. However, within minutes this solution was observed to turn green. Powder X-ray diffraction analysis (results not included here) of a film prepared from this green solution revealed the formation of cobalt oxide. Hence this procedure was abandoned and we have used an alternative strategy for obtaining stable cobalt nanoparticles in aqueous/organic solutions.

The TEM micrographs of the nanoparticles obtained by the alternative strategy where oleic acid was added to the surfactant/cobalt ion solution prior to the formation of foams are displayed in Fig. 2A and B. A perceptible change in the morphology and arrangement of the nanoparticles is clearly visible. This suggests an important change in the environment around the cobalt ions when the reduction is taking place inside the foam. The particles are predominantly spherical and of uniform size. Analysis of the particle size histogram obtained from measurement of the diameters of over 250 particles revealed the average size to be $11 \pm 3\text{ nm}$ (Fig. 2C). These particles are also highly crystalline as can be clearly seen from the electron diffraction which can be well indexed to fcc phase cobalt (inset Fig. 2A).^{6a} Further evidence for the existence of the fcc phase is given in the XRD pattern of solution-cast films of oleic acid-stabilized Co nanoparticles (curve 1, Fig. 2D).

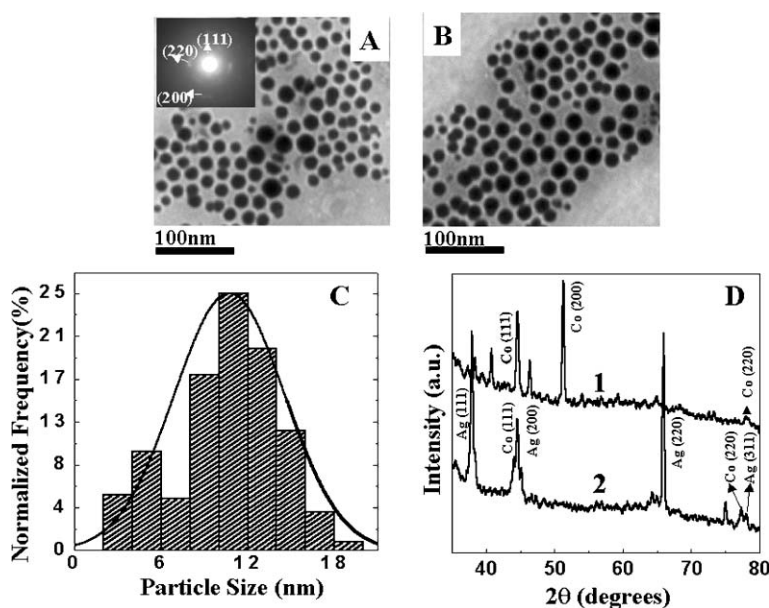


Fig. 2 (A), (B) TEM pictures, from different areas on the grid, of cobalt nanoparticles obtained when oleic acid was added to the Co^{2+} and SDS aqueous mixture prior to the formation of foam. The SAED pattern indexed to fcc cobalt is included as the inset in (A). (C) A particle size histogram of Co nanoparticles. (D) XRD patterns recorded from films of Co_{core} (curve 1) and $\text{Co}_{\text{core}}\text{Ag}_{\text{shell}}$ nanoparticles (curve 2) solution-cast onto glass substrates.

This is in agreement with earlier reports wherein it was observed that while bulk cobalt assumes an hcp phase, smaller particles, especially in the nanoscale regime, crystallize in the fcc phase.¹³ These Co nanoparticle solutions were highly stable in aqueous medium against oxidation and sedimentation and could be stored as solutions for long periods of time. An aqueous/organic dispersion of these nanoparticles could be readily obtained by separating the nanoparticles from water by centrifugation and redispersing the resulting paste-like pellet in water/organic solvents such as toluene. Efrima and co-workers obtained similar results where oleic acid-capped silver nanoparticles were found to be dispersible in both aqueous as well as organic media.¹⁴ Thus, this simple foam-based synthetic procedure yields stable dispersions of cobalt nanoparticles in aqueous as well as organic media.

As mentioned in the introduction, preparation of cobalt core and noble metal shell nanoparticles improves their stability as well as providing one with the additional manipulative ability associated with noble metal shells. For the preparation of $\text{Co}_{\text{core}}\text{Ag}_{\text{shell}}$ nanoparticles, we have used a simple transmetallation¹² reaction taking advantage of their respective redox potentials (*vide infra*). The striking difference in the contrast of the TEM pictures recorded from the Co nanoparticle solution after addition of silver salt (Figs. 3A–C) clearly reveals the darker Co core and lighter Ag shell. The electron diffraction from the core–shell structures (Fig. 3D) could be indexed based on the fcc structure of silver. The SAED pattern did not show any reflections that could be associated with the core cobalt nanoparticles. While this is not fully understood at this stage, a possible explanation could be that the presence of a thick Ag shell (*ca.* 5–10 nm thick) prevents efficient electron scattering from the cobalt core. Such penetration depth issues would not be important in XRD analysis of the core–shell structures. The XRD pattern recorded from a solution-cast film of the $\text{Co}_{\text{core}}\text{Ag}_{\text{shell}}$ nanoparticles is shown as curve 2 in Fig. 2D. In addition to the Co_{core} Bragg reflections, the crystalline Ag_{shell} contributes to the signal. The silver Bragg reflections could be indexed on the basis of the fcc structure as shown in the figure. The optical properties of the oleic acid-stabilized Co nanoparticle and the $\text{Co}_{\text{core}}\text{Ag}_{\text{shell}}$ solutions were probed by UV-vis spectroscopy (Fig. 4A, curves 1 and 2, respectively). Cobalt nanoparticles do not have any noticeable absorption in the UV-visible region (curve 1) and the spectrum obtained matches well with reported UV-vis spectra of cobalt nanoparticles.¹⁵ After reaction of the Co nanoparticle solution with Ag_2SO_4 , a

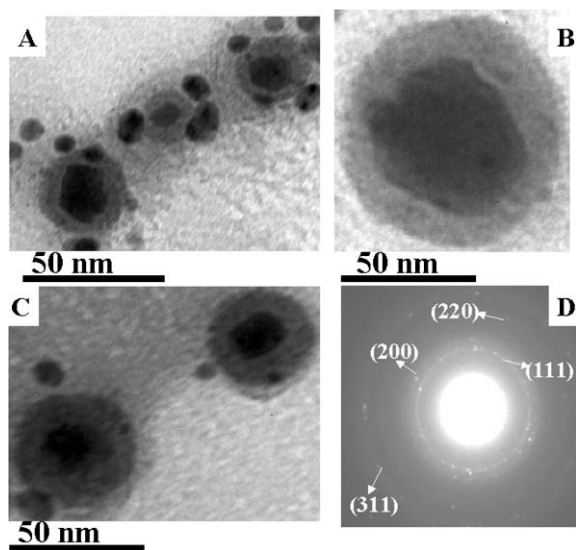


Fig. 3 (A), (B) and (C) TEM pictures of $\text{Co}_{\text{core}}\text{Ag}_{\text{shell}}$ nanoparticles from different areas of the TEM grid. (D) Selected area electron diffraction from these particles.

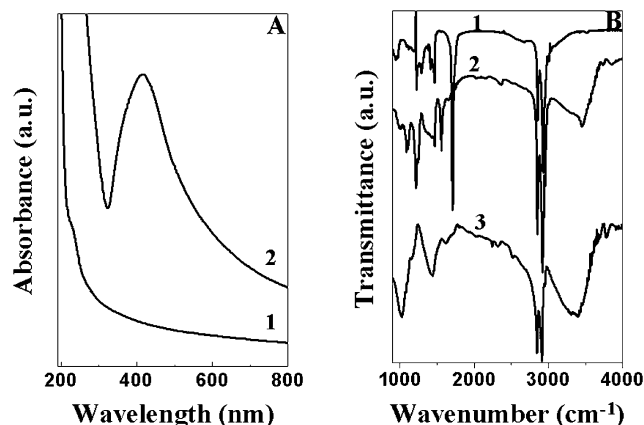


Fig. 4 (A) UV-vis spectra of the cobalt nanoparticle (curve 1) solution and that of the $\text{Co}_{\text{core}}\text{Ag}_{\text{shell}}$ nanoparticle solution (curve 2). (B) FTIR spectra of pure oleic acid (trace 1), Co nanoparticles capped with oleic acid (trace 2), and $\text{Co}_{\text{core}}\text{Ag}_{\text{shell}}$ nanoparticles capped with oleic acid (trace 3).

clear peak around 410 nm is observed and is attributed to the formation of metallic silver in the nanoscale regime. This absorption band arises due to excitation of surface plasmon vibrations in the Ag shell. The FTIR spectra obtained from pure oleic acid, Co nanoparticles covered with oleic acid and $\text{Co}_{\text{core}}\text{Ag}_{\text{shell}}$ nanoparticles are displayed in Fig. 4B (spectra 1, 2 and 3, respectively). The carboxylic acid band around 1707 cm^{-1} in pure oleic acid is shifted to 1553 cm^{-1} in the presence of Co nanoparticles and to 1611 cm^{-1} after the Ag shell is formed. These shifts clearly indicate that the chemical environment in which the carboxylic acid is present is different in each step of our synthesis: in the first step it is on the surface of the Co nanoparticles and then in the $\text{Co}_{\text{core}}\text{Ag}_{\text{shell}}$ case it is bound to the Ag surface. Although it is difficult to unequivocally ascertain the formation of core–shell structures from UV-vis and FTIR studies alone, these results in conjunction with the TEM pictures and X-ray diffraction results, and the fact that the reduction of Ag^+ ions can take place only on the surface of cobalt nanoparticles, clearly provide evidence for the formation $\text{Co}_{\text{core}}\text{Ag}_{\text{shell}}$ structures.

4 Discussion

After the excess liquid has been drained out of the foam, there are essentially two spatially distinct locations in the foam where metal nanoparticle nucleation and growth could occur. One is the extremely thin region between two air bubbles. Here, the ‘liquid lamellae’ are very similar to two Langmuir monolayers juxtaposed one on top of the other with the thickness corresponding to a few nanometers. The second location is the junction of four air bubbles (Scheme 1). This contains a slightly larger liquid pool generally of micron dimensions. In both these locations, Co^{2+} ions are expected to be present through electrostatic complexation with the anionic surfactant, SDS. The presence of two types of locations for cobalt ions may enforce a shape variation in the resulting nanoparticles. For example, the entrapment of cobalt ions in the liquid lamellae and their subsequent reduction might result in flat nanoparticles. However, we would like to caution that a number of other factors, such as preferential binding of surfactant molecules with specific crystallographic faces, *etc.*, may lead to anisotropic crystal growth. Further work is required to conclusively establish the role of spatially distinct regions in the foam in directing morphology variation and this is currently in progress. Formation of such anisotropic nanoparticles has been reported earlier where the metal ions immobilized at the air–water interface were subjected to reduction.¹⁶ On the other hand, the junction between four bubbles is

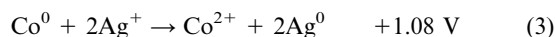
much more isotropic in extent and no such shape anisotropy would occur for cobalt nanoparticles nucleated and grown at these sites. We observe both flat particles as well as spherical particles in the case of cobalt nanoparticles obtained with just SDS present in the foam column along with cobalt ions. Similar results were also obtained for Au nanoparticles with the foam-based synthesis.¹⁰ However, the cobalt nanoparticles obtained with these experimental conditions were extremely unstable and cobalt oxide is formed within minutes, preventing us from carrying out any further analysis of this sample. This suggests that SDS is not a good capping agent for the cobalt nanoparticles and cannot protect them against oxidation.

The presence of oleic acid in the foam column changes the scenario drastically. Not only did we obtain very stable cobalt nanoparticles, the shape of the nanoparticles observed is different as well in that now more spherical particles are obtained. Both SDS and oleic acid are anionic surfactants and, hence, owing to purely entropic considerations we expect both these molecules to be present in the foam lamellae. However, it is not clear at this stage what percentage of the oleic acid molecules present in solution are transported to the surface of the bubbles. It is likely that a large fraction of oleic acid (and indeed SDS) is present in the water channels of the foam. During *in-situ* nucleation and growth of the Co nanoparticles, the stability of the Co nanoparticles formed in the foam containing oleic acid suggests that oleic acid binds more strongly to the surface of the Co nanoparticles than SDS. This may be rationalized in terms of electrostatic complexation of carboxylic acid groups in oleic acid with unreduced Co ions bound to the surface of the Co nanoparticles. This is supported by the shifts observed for the carboxylate bands in FTIR spectra from 1707 cm⁻¹ in pure oleic acid to 1553 cm⁻¹ in the presence of Co nanoparticles (Fig. 4B). This strong binding of oleic acid to the nascent Co nanoparticles could also be responsible for inhibiting anisotropic growth of the Co nanoparticles.

We have utilized the redox potentials of Ag and Co to our advantage to prepare the Co_{core}Ag_{shell} nanocomposites. From the reported redox potentials, the reduction of silver ions by cobalt metal can easily proceed and this forms the basis of core-shell structure formation in our scheme:



Therefore,



is an energetically favorable reaction. There are reports of using a similar methodology for the formation of Co-Pt core-shell structures in the literature.¹² However, those reactions are carried out at elevated temperatures and with slightly complex reaction conditions.

In conclusion, an extremely simple and hitherto unexplored foam-based synthesis of cobalt nanoparticles has been reported. The instability of cobalt nanoparticles in aqueous medium is overcome by using oleic acid as one of the constituents of the foam. The oleic acid-stabilized Co nanoparticles are extremely stable against oxidation and may be readily redispersed in both water and non-polar organic solvents such as toluene. Utilizing the redox potential matching of Co and Ag⁺ ions, Co_{core}Ag_{shell}

nanocomposites were easily synthesized by simple reaction of oleic acid-stabilized Co nanoparticles with Ag⁺ ions. This methodology is general and may be extended to the formation of other nanoparticle core-shell systems.

Acknowledgements

B. L. V. P. thanks the National Chemical Laboratory for a start-up grant. T. B. thanks the Council for Scientific and Industrial Research (CSIR), Govt. of India, for a research fellowship.

References

- D. D. Awschalom and D. P. DiVincenzo, *Phys. Today.*, 1995, **48**, 43–48; J. Shi, S. Gider, K. Babcock and D. D. Awschalom, *Science.*, 1996, **271**, 937–941; C. M. Sorensen, in *Nanoscale Materials in Chemistry*, K. J. Klabunde, ed., Wiley, New York, 2002, pp. 169–222.
- M. Moreno-Manas and R. Pleixats, *Acc. Chem. Res.*, 2003, **36**, 638–643; V. Kesavan, P. S. Sivanand, S. Chandrasekharan, Y. Kolytipin and A. Gedankan, *Angew. Chem., Int. Ed.*, 1999, **38**, 3521–3523; V. Kesavan, D. Dhar, Y. Kolytipin, N. Perkas, O. Palchik, A. Gedankan and S. Chandrasekharan, *Pure Appl. Chem.*, 2001, **73**, 85–89.
- P. Tartaj, M. del Puerto Morales, S. Veintemillas-Verdaguer, T. González-Carreño and C. J. Serna, *J. Phys. D: Appl. Phys.*, 2003, **36**, R182–R197.
- G. N. Glavee, K. J. Klabunde, C. M. Sorensen and G. C. Hadjipanayis, *Langmuir*, 1992, **8**, 771–773; G. N. Glavee, K. J. Klabunde, C. M. Sorensen and G. C. Hadjipanayis, *Inorg. Chem.*, 1993, **32**, 474–477; S. U. Son, S. I. Lee, Y. K. Chung, S. W. Kim and T. Hyeon, *Org. Lett.*, 2002, **4**, 277–279.
- For a general review of synthesis of magnetic nanoparticles, see: T. Hyeon, *Chem. Commun.*, 2003, 927–934.
- (a) C. Petit, A. Taleb and M. P. Pileni, *J. Phys. Chem. B*, 1999, **103**, 1805–1810; (b) S. Sun and C. B. Murray, *J. Appl. Phys.*, 1999, **85**, 4325–4330; (c) D. P. Dinega and M. G. Bawendi, *Angew. Chem., Int. Ed.*, 1999, **38**, 1788–1791; (d) V. F. Puentes, K. M. Krishnan and A. P. Alivisatos, *Science*, 2001, **291**, 2115–2117.
- C. B. Murray, S. Sun, W. Gaschler, H. Doyle, T. A. Betley and C. R. Kagan, *IBM J. Res. Dev.*, 2001, **45**, 47–56; C. B. Murray, S. Sun, H. Doyle and T. A. Betley, *MRS Bull.*, 2001, 985–991.
- D. Weaire and S. Hutzler, *The Physics of Foams*, Oxford University Press, Oxford, 1999; A. Bhattacharyya, F. Monroy, D. Langevin and J.-F. Argillier, *Langmuir*, 2000, **16**, 8727–8732.
- B.-D. Chen, J. J. Cilliers, R. J. Davey, J. Garside and E. T. Woodburn, *J. Am. Chem. Soc.*, 1998, **120**, 1625–1626.
- S. Mandal, S. K. Arumugam, S. D. Adyanthaya and M. Sastry, *J. Mater. Chem.*, 2004, **14**, 43–47.
- A. Kumar, S. Mandal, P. R. Selvakannan, R. Pasricha, A. B. Mandale and M. Sastry, *Langmuir*, 2003, **19**, 6277–6282; S. Mandal, P. R. Selvakannan, S. Phadtare, R. Pasricha and M. Sastry, *Proc. Indian Acad. Sci., Chem. Sci.*, 2002, **114**, 513–520; P. R. Selvakannan, S. Mandal, S. Phadtare, R. Pasricha and M. Sastry, *Langmuir*, 2003, **19**, 3545–3549; B. L. V. Prasad, S. I. Stoeva, C. M. Sorensen and K. J. Klabunde, *Chem. Mater.*, 2003, **15**, 935–942.
- J.-I. Park and J. W. Cheon, *J. Am. Chem. Soc.*, 2001, **123**, 5743–5746.
- O. Kitakami, H. Sato, Y. Shimada, F. Sato and M. Tanaka, *Phys. Rev. B*, 1997, **56**, 13 849–13 854.
- W. Wang, S. Efrima and O. Regev, *Langmuir*, 1998, **14**, 602–610.
- J. A. Creighton and D. G. Eadon, *J. Chem. Soc., Faraday Trans. 1*, 1991, **87**, 3881; B. G. Ershov, N. L. Sukhov and E. Janata, *J. Phys. Chem. B*, 2000, **104**, 6138–6142.
- A. Swami, A. Kumar, P. R. Selvakannan, S. Mandal, R. Pasricha and M. Sastry, *Chem. Mater.*, 2003, **15**, 17–19.

Synthesis and size control of monodisperse copper nanoparticles by polyol method

Bong Kyun Park^a, Sunho Jeong^a, Dongjo Kim^a, Jooho Moon^{a,*}, Soonkwon Lim^b, Jang Sub Kim^b

^a Department of Materials Science and Engineering, Yonsei University, Seoul 120-749, South Korea

^b LCD R&D Center, Samsung Electronics Co. Ltd., Gyeonggi-Do 449-711, South Korea

Received 25 November 2006; accepted 17 March 2007

Available online 24 March 2007

Abstract

We describe herein the synthesis of metallic copper nanoparticles in the presence of poly(vinylpyrrolidone), employed as a protecting agent, via a polyol method in ambient atmosphere. The obtained copper particles were confirmed by XRD to be crystalline copper with a face-centered cubic (fcc) structure. We observed monodisperse spherical copper nanoparticles with a diameter range 45 ± 8 nm. The particle size and its distribution are controlled by varying the synthesis parameters such as the reducing agent concentration, reaction temperature, and precursor injection rate. The precursor injection rate plays an important role in controlling the size of the copper nanoparticles. On the basis of XPS and HRTEM results, we demonstrate that the surface of the copper is surrounded by amorphous CuO and that poly(vinylpyrrolidone) is chemisorbed on the copper surface. © 2007 Elsevier Inc. All rights reserved.

Keywords: Cu nanoparticles; Polyol synthesis; Particle size control; Surface characterization; Conductive ink

1. Introduction

During the last two decades, a substantial body of research has been directed toward the synthesis of metal nanoparticles in efforts to explore their special properties and potential applications [1–4]. Among various metal particles, copper nanoparticles have attracted considerable attention because of their catalytic, optical, and electrical conducting properties [5–8]. Copper nanoparticles are particularly attractive for application in printed circuit boards (PCBs) and flexible electronics.

Metal nanopowders can be used as a key constituent for preparing the paste or ink from which conductive tracks are patterned by either screen printing or ink-jet printing. The melting point (T_m) of nanomaterials can be dramatically lowered by decreasing the size of the material relative to their bulk counterparts [9]. This low temperature melting ability makes metal nanopowders potentially suitable materials for use in printed electronics, since they can be annealed at lower temperatures to form conductive films of low resistance.

Currently, mainly noble metals such as gold and silver are being exploited, despite their costliness. In this regard, copper is a good alternative material as it is highly conductive and much more economical than Au and Ag. Several methods have been developed for the preparation of copper nanoparticles, including thermal reduction [5], sono-chemical reduction [5,10], metal vapor synthesis [6], chemical reduction [7], vacuum vapor deposition [8], radiation methods [11], microemulsion techniques [12–14], and laser ablation [15].

Most of the aforementioned methods utilize an oxygen-free environment to synthesize copper as it readily oxidizes in air. Lisiecki et al. [16] prepared copper nanoparticles in an aqueous solution using sodium dodecyl sulfate as capping molecules. They employed a glove box to prevent oxidation of the particles. Joshi et al. and Wu et al. independently reported the synthesis of copper nanoparticles in an aqueous system under a nitrogen atmosphere [10,17]. Unlike other techniques, in the present study, we have developed a polyol method for the preparation of highly monodisperse copper nanoparticles in air. Use of nonaqueous solvent as a reaction medium allows us to minimize the copper surface oxidation. Furthermore, poly(vinylpyrrolidone) added as a dispersing agent also effectively prevents the oxidation process. A key advantage of polyol

* Corresponding author. Fax: +82 2 365 5882.

E-mail address: jmoon@yonsei.ac.kr (J. Moon).

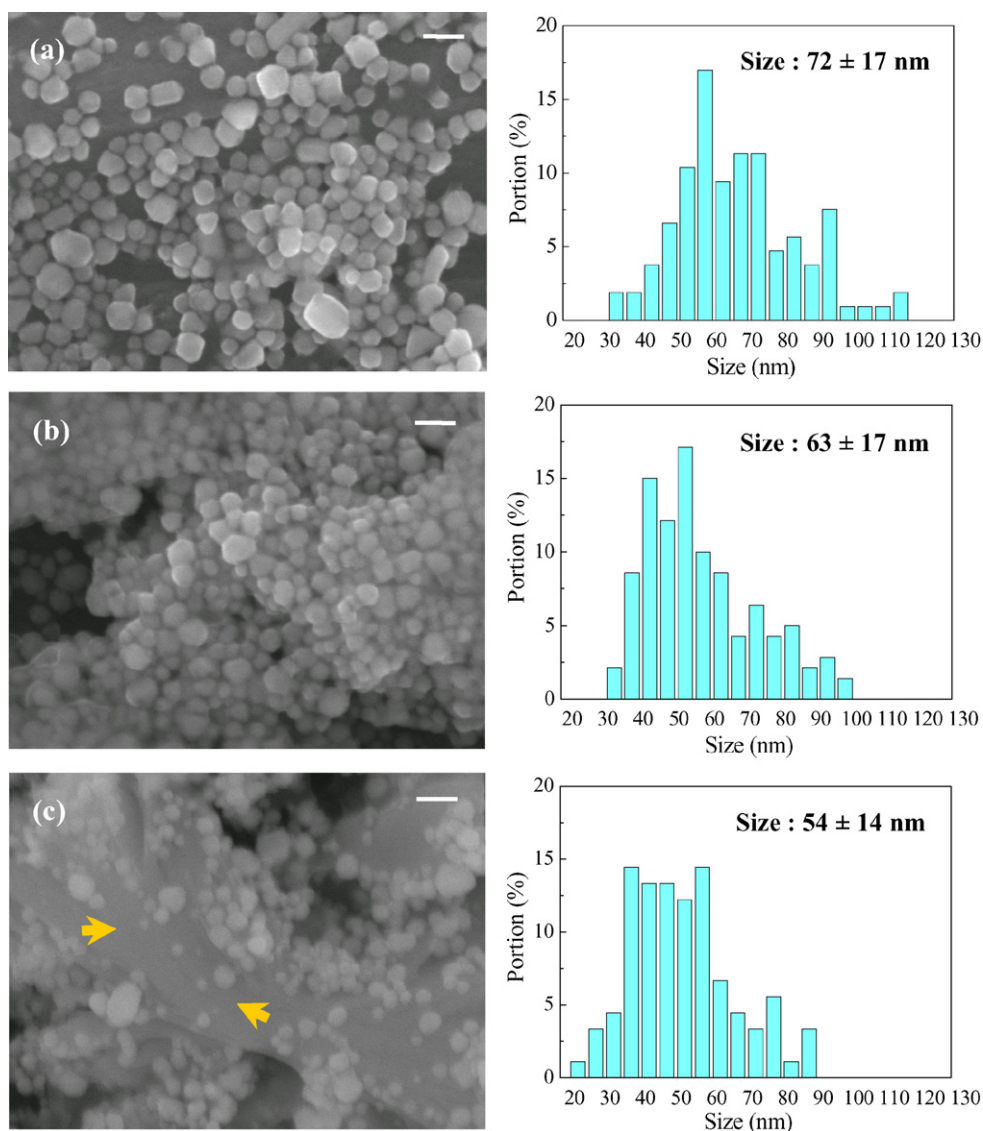


Fig. 1. SEM images and particle size distribution of synthesized copper particles as a function of the amount of reducing agent: (a) 12.75 mmol (sample #1); (b) 17.53 mmol (sample #2); and (c) 19.13 mmol (sample #3). Scale bar = 100 nm. The arrows represent an impurity phase.

process-based nanoparticle synthesis is that the reaction kinetics can be easily controlled, as demonstrated by Fievet et al. [18–21]. We have controlled the size and size distribution of the particles by varying experimental parameters such as the amount of reducing agent, reaction temperature, and precursor injection rate.

2. Experimental

2.1. Preparation of copper particles

Poly(*N*-vinylpyrrolidone) (PVP, $M_w = 40,000$, Sigma–Aldrich), acting as a capping molecule, was dissolved in diethyleneglycol (DEG, 99%, Sigma–Aldrich). Sodium phosphinate monohydrate ($\text{NaH}_2\text{·PO}_2\text{·H}_2\text{O}$, Junsei), used as a reducing agent, was added to the DEG solution and the solution was heated to reaction temperatures. The aqueous solution of copper(II) sulfate pentahydrate (98%, Sigma–Aldrich) was then injected into the hot reaction medium via a syringe pump.

The injection rate of the Cu salt solution was varied from 2 to 8 ml/min. After 1 h of reaction, the solution was cooled to room temperature and the particles were separated by centrifugation and then washed with methanol. The detailed reaction conditions employed in the particle synthesis are summarized in Table 1.

2.2. Characterization

Phase composition and crystallinity of the synthesized copper particles were investigated using an X-ray diffractometer (XRD, DMAX2500, Rigaku) employing $\text{CuK}\alpha_1$ radiation (1.51059 \AA). The morphology of the copper particles was investigated via scanning electron microscopy (SEM, JSM-6500F, JEOL) and the particle size distributions were obtained by image analysis. The surface compositions of the copper particles were investigated by X-ray photoelectron spectroscopy (XPS, ESCALAB 22i-XL, VG Scientific Instrument) and the sur-

Table 1
Synthesis conditions for the preparation of copper particles using the injection method

Sample ID	Reducing agent (mmol)	Reaction temperature (°C)	Injection rate (ml/min)	Cu salt (mmol)
#1	12.75	200	2	20
#2	17.53	200	2	20
#3	19.13	200	2	20
#4	17.53	200	8	20
#5	17.53	170	8	20
#6	17.53	140	8	20
#7	17.53	200	6	20
#8	17.53	140	2	80
#9	17.53	140	6	80
#10	17.53	140 <td 8	80	

face morphology was examined by high resolution transmission electron microscopy (HRTEM, JEM-4010, JEOL).

3. Results and discussion

3.1. Influence of reducing agent

In a typical polyol process, a polyol liquid such as diethyleneglycol acts not only as a reaction medium but also as a reducing agent. However, in the case of copper nanoparticle synthesis, the reducing ability of diethyleneglycol is insufficient to reduce the copper ions because copper is easily oxidized to either CuO or Cu₂O in air atmosphere [22]. We introduce NaH₂PO₂·H₂O as a reducing agent. NaH₂PO₂·H₂O is generally used in aqueous chemical reduction for the preparation of copper particles. It produces oxidation reaction represented by the equation



in an acidic condition, releasing electrons. The released electrons are utilized to reduce copper ions as shown in the equation



According to the equations, the rate and amount of the electrons supplied to the copper ions are determined by sodium phosphinate. In this study, we control the synthesis reaction kinetics by adjusting the amount of the reduction agent.

Fig. 1 shows SEM images of particles synthesized with varying amounts of reducing agent. At low reducing agent concentration (12.75 mmol), the reducing rate of the copper precursor is sluggish and consequently only a few nuclei are formed at the nucleation step. Precipitating copper atoms at the later period of the reaction are mostly involved in particle growth by collision with already generated nuclei rather than in the formation of new particles. This reaction mechanism leads to the formation of larger sized particles, as shown in Fig. 1a. With increasing reducing agent concentration, the enhanced reduction rate favors the generation of more nuclei, resulting in the formation of smaller copper particles (Fig. 1b). At a higher reduction rate (19.13 mmol), the number of precipitating metallic clusters steeply increases and considerably more nuclei are produced during a single event of the nucleation period. Eventually, the size of particles decreases because the amount of

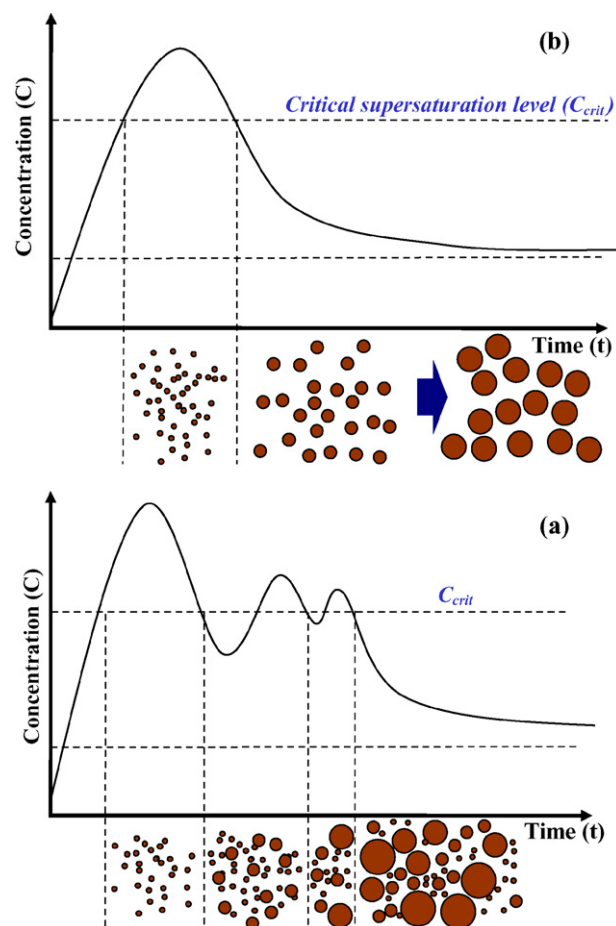


Fig. 2. Schematic illustration of nucleation and growth mechanisms based on LaMer's model: (a) mechanism for polydisperse particles and (b) mechanism for monodisperse particles.

solute available for particle growth per growing particle decreases with the increasing number of nuclei. The reaction at higher reducing agent concentration also leads to the formation of an unidentified impurity phase, as shown in Fig. 1c. In a polyol process, the dissolved metal ions are not directly reduced into a neutral metal species, but transformed into an intermediate solid phase comprised of hydroxyethyleneglycolate or corresponding alkoxide radicals prior to nucleation step. Then, the re-dissolved metal ion from the intermediate solid phase is consumed in nucleation and growth processes [23,24]. In this regard, it is considered that the intermediate solid phase itself is reduced in the presence of extremely high reducing agent, forming unidentified impurity phase.

The particle characteristics of the synthesized copper are determined by the nucleation and growth mechanisms. When the reduction rate of copper ions exceeds the consumption rate of copper clusters by particle growth, the concentration of reduced copper atoms (C) likely remains over a critical supersaturation level (C_{crit}) for longer time or fluctuates around C_{crit} . This allows an extended nucleation period or multiple nucleation events and, in turn, the growing period of each nucleus will differ (Fig. 2a). Therefore, the final particles exhibit broader size compared to that of particles grown at the same rate after a single nucleation event (Fig. 2b).

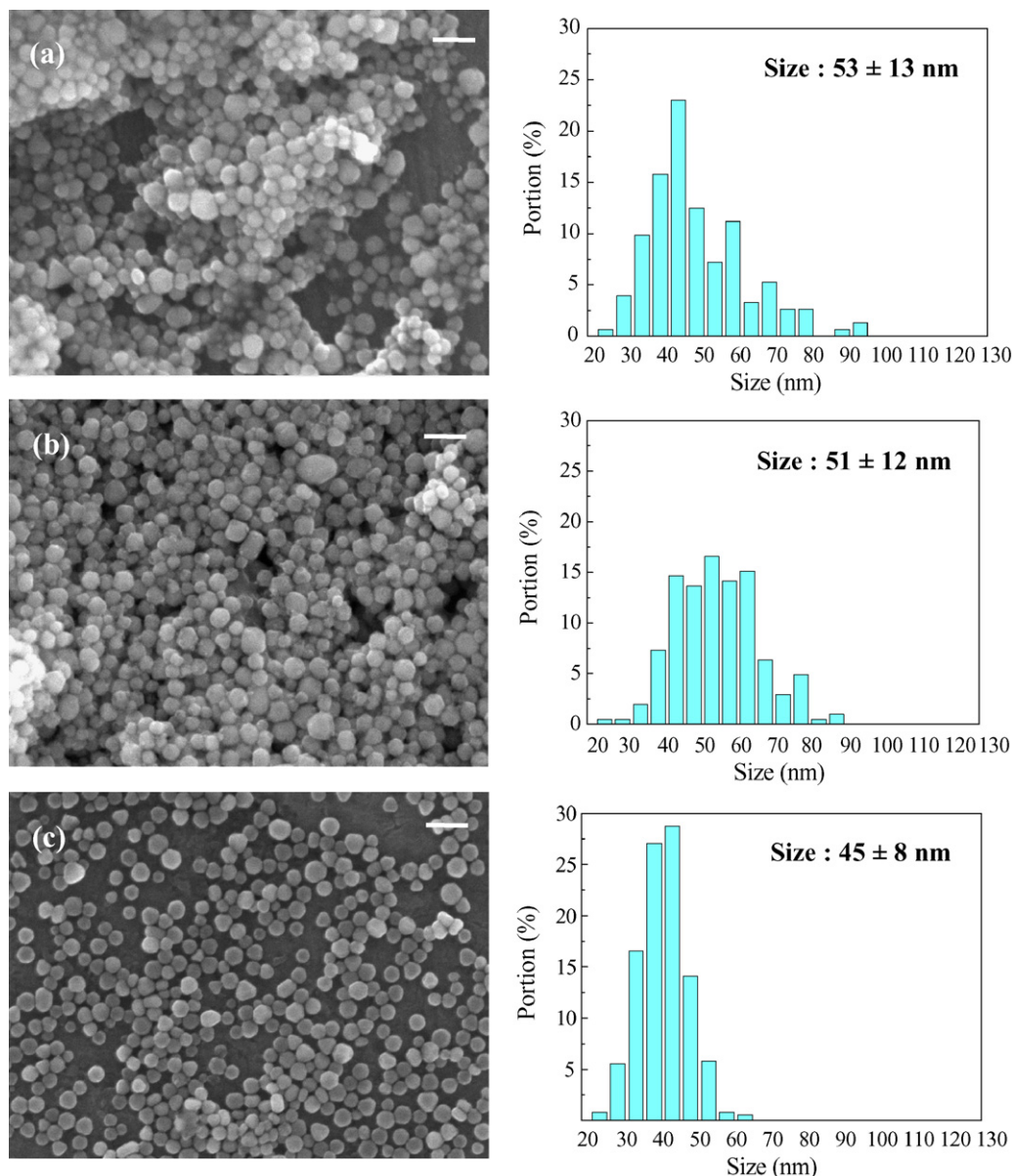


Fig. 3. SEM images and particle size distribution of synthesized copper particles as a function of the reaction temperature: (a) 200 °C (sample #4); (b) 170 °C (sample #5); and (c) 140 °C (sample #6). Scale bar = 100 nm.

3.2. Influence of reacting temperature

Fig. 3 shows SEM images of copper particles synthesized at different temperatures. With decreasing reaction temperature, the size of the resulting particles becomes smaller and the size distribution is also narrowed. At 200 °C, the obtained particle size was 53 ± 13 nm (Fig. 3a), whereas that at the synthesis temperature of 140 °C was 45 ± 8 nm (Fig. 3c). When copper salt solution is injected into a reaction medium maintained at 200 °C, the color of the medium in the vicinity where the precursor solution is added changes from light yellow to dark red. This indicates that copper particles are rapidly generated when the precursor solution is injected. A high reducing rate at the temperature of 200 °C allows instantaneous multiple nucleations to occur when the precursor solution is added dropwise. The resulting particles at this condition exhibit a rel-

atively broad size distribution due to uneven particle growth and coagulation of the primary particles.

In contrast to the reaction at 170 and 200 °C, the color of the reaction medium changes to light blue rather than dark red when the precursor solution is injected at 140 °C. The aqueous solution of copper ions has a blue color. This indicates that there is no immediate reduction of copper ions upon addition to the reaction medium. After approximately 10 s, the solution suddenly turns dark red, indicating nucleation. If the number of nuclei is large enough to lower the concentration of copper atoms below the critical supersaturation level, no further nucleation occurs and the nucleated particles continue to grow. Coagulation of the primary particles would be unlikely because the thermal energy is not sufficient for vigorous particle movement. Under these nucleation and growth conditions, as depicted in Fig. 2b, the resulting particles are relatively monodisperse. At

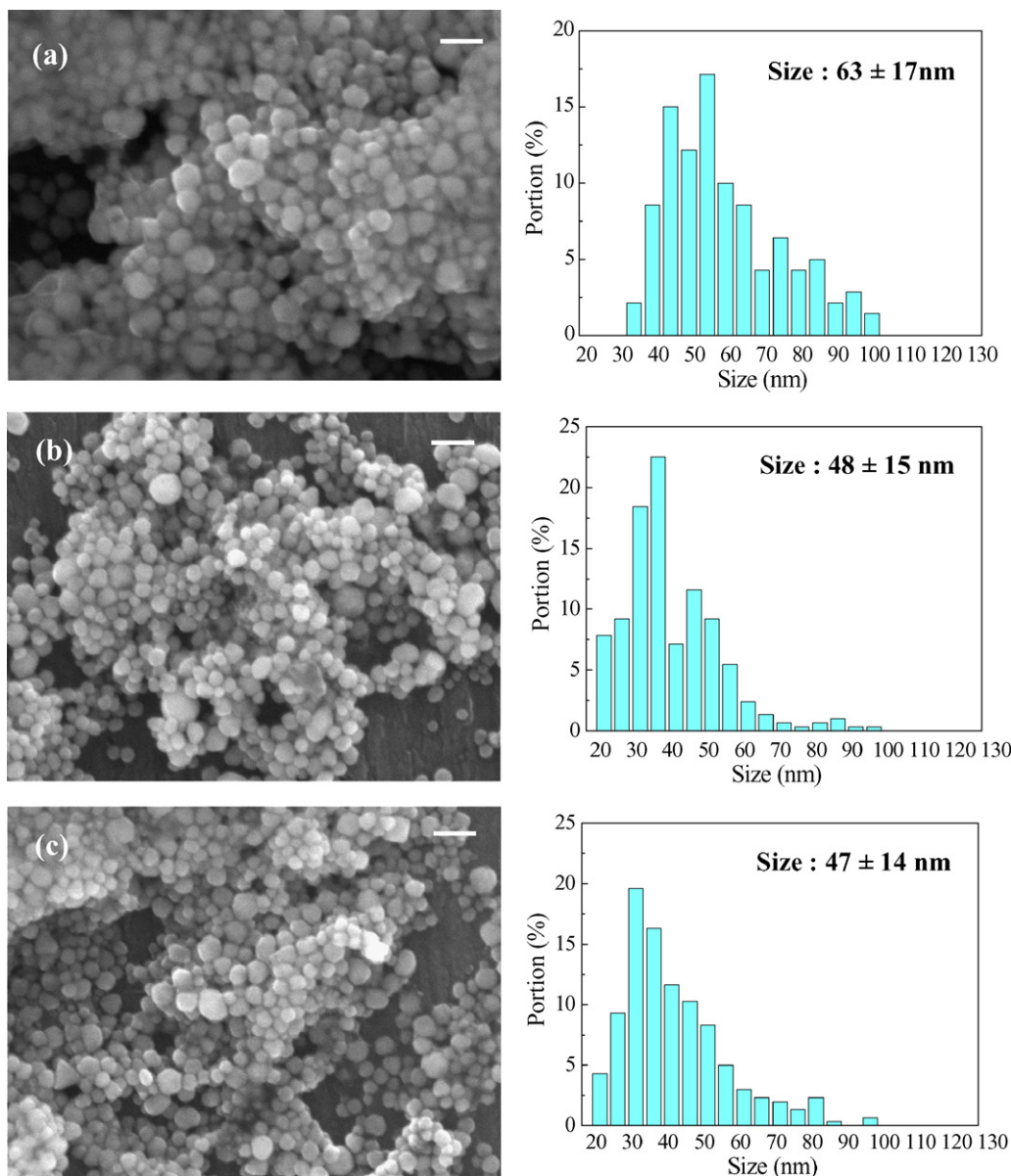


Fig. 4. SEM images and particle size distribution of copper particles synthesized at 200 °C as a function of the precursor injection rate: (a) 2 ml/min (sample #2); (b) 6 ml/min (sample #7); and (c) 8 ml/min (sample #4). Scale bar = 100 nm.

temperature lower than 140 °C, however, the reaction medium remains light blue in color, implying that the copper ions do not undergo reduction to copper atoms.

3.3. Influence of injection rate

We also controlled the injection rate of the copper salt precursor to the PVP dissolved polyol medium. Fig. 4 shows SEM images of particles with synthesized different precursor injection rates at 200 °C. The particles become smaller and narrower as the injection rate is increased. At an injection rate of 2 ml/min, the obtained particle size was 63 ± 17 nm (Fig. 4a), whereas that at 8 ml/min was 47 ± 14 nm (Fig. 4c). The injection rate determines the amount of copper ions per unit time to be reduced. When the reduction rate is high enough to reduce copper ions as soon as they are supplied, the precursor

injection rate will be equal to the production rate of copper atoms. The concentration of copper atoms slowly reaches C_{crit} at slow injection of the precursor. The nucleation rate is sluggish and the number of nuclei is small. Therefore, the resulting particles are large and broad. In contrast, fast injection of the precursor results in a steep increase in the concentration of copper atoms, permitting a short burst of nucleation and generating many nuclei. This leads to smaller particles with better monodispersity.

The influence of the precursor injection rate varies depending upon the reaction temperature. Fig. 5 shows SEM images of particles synthesized with different precursor injection rates at 140 °C. Contrary to the previous results, the particles tend to become larger and broader as the injection rate is increased. At 2 ml/min, the obtained particle size was 60 ± 10 nm (Fig. 5a) whereas that at 8 ml/min was 68 ± 20 nm (Fig. 5c). If the reac-

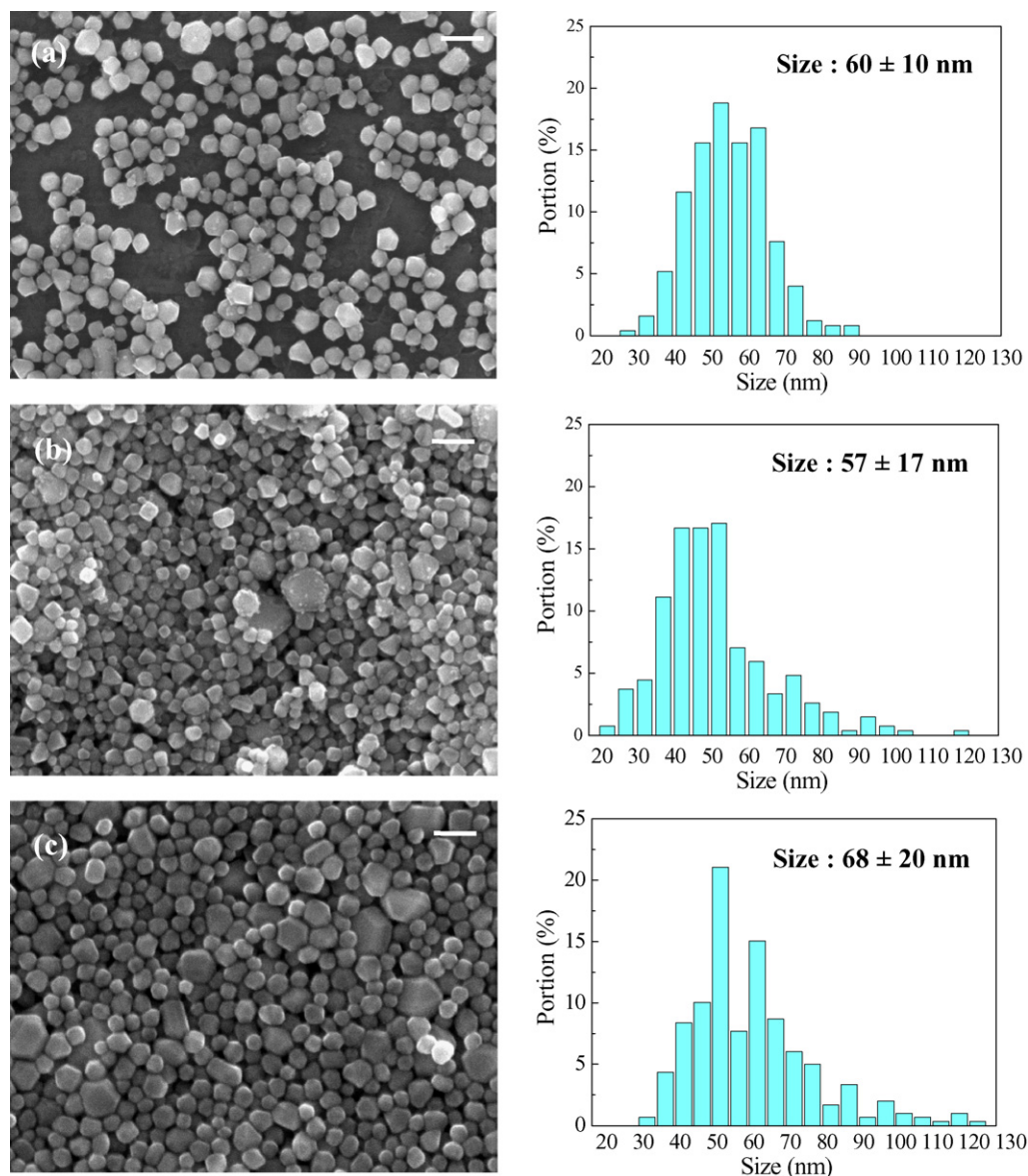


Fig. 5. SEM images and particle size distribution of copper particles synthesized at 140 °C as a function of the precursor injection rate: (a) 2 ml/min (sample #8); (b) 6 ml/min (sample #9); and (c) 8 ml/min (sample #10). Scale bar = 100 nm.

tion rate is too fast at lower temperature, the generation rate of copper atoms exceeds the rate of consumption of copper atoms by particle growth and multiple nucleations may occur, resulting in polydisperse particles.

3.4. Characteristics of copper particles

In addition to particle size and distribution, particle characteristics were also investigated. Monodisperse Cu particles (sample #6) were used for the phase and surface composition analyses. The particles synthesized in ambient atmosphere were determined to be phase-pure Cu without any impurity phase such as CuO, Cu₂O, or Cu(OH)₂. X-ray diffraction patterns correspond to crystalline copper characteristic peaks with a face-centered-cubic (fcc) crystal structure as shown in Fig. 6. The same X-ray diffraction peaks were observed for the sample stored for 30 days in ambient condition.

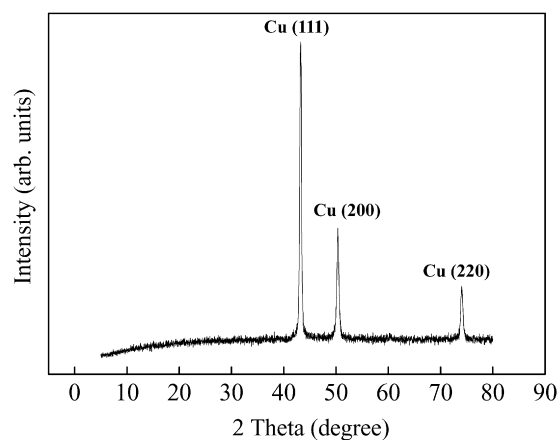


Fig. 6. X-ray diffraction pattern of copper particles synthesized at 140 °C with an injection rate of 8 ml/min (sample #6).

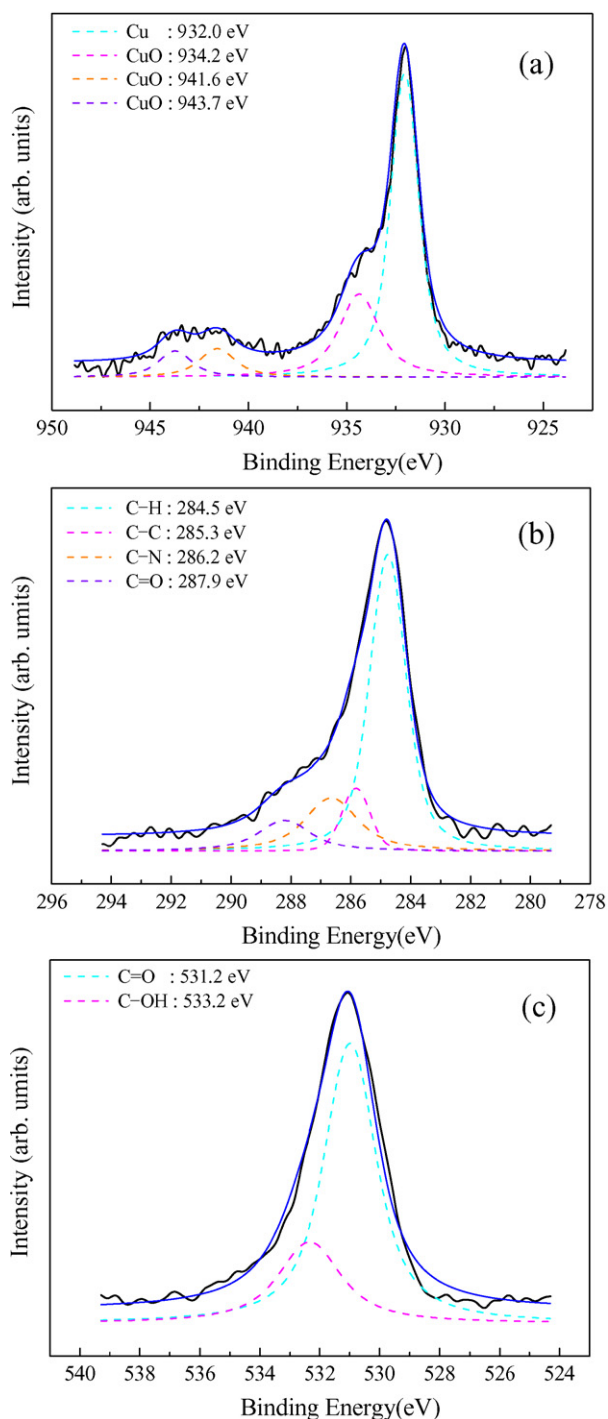


Fig. 7. X-ray photoelectron spectra of Cu nanoparticles: the peaks from (a) Cu $2p_{3/2}$, (b) C 1s, and (c) O 1s.

Surfaces of copper particles are analyzed by X-ray photoelectron spectroscopy (XPS) as shown in Fig. 7. We identified a copper peak at 932.0 eV together with weak CuO peaks at 934.2 eV, as shown in Fig. 7a [23]. The existence of PVP is also confirmed by XPS spectra of C 1s. The C 1s spectrum is composed of four peaks and the binding energies of these peaks are 284.5 eV (C–H bonding), 285.3 eV (C–C bonding), 286.2 eV (C–N bonding), and 287.9 eV (C=O bonding). These binding energies can be attributed to four types of carbon atoms in PVP.

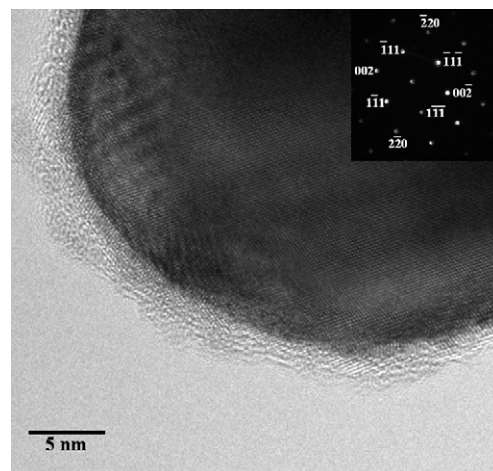


Fig. 8. HRTEM image of the synthesized Cu nanoparticles. The inset is the selected area diffraction pattern.

The O 1s peak composed of two peaks, one placed at 531.2 eV (C=O bonding) and the other placed at 533.2 eV (C–OH bonding). The O 1s peak from the carboxyl (C=O) oxygen atom at 531.2 eV shifts to higher binding energy relative to pure PVP, indicating that the PVP is strongly chemisorbed to the surface of copper particles [24]. This interaction is achieved by coordination bond between Cu ions and PVP molecules, and Cu ions are surrounded by PVP molecules prior to nucleation step [25–27]. Thus, the chemically adsorbed PVP molecules can prevent the copper particles from oxidation during the nucleation and growth processes. However, incomplete prevention from the oxidation takes place. The oxidation has two main origins. The Cu nanoparticles were synthesized from water containing polyol medium in ambient condition. Some oxygen dissolved in the reaction medium results in partial oxidation at the surface of the Cu nanoparticles. Some oxidation may also occur when the samples for analysis are prepared in air.

Fig. 8 shows an HRTEM image of the synthesized Cu particles. Most of the particles are single crystals, but some contain a twin boundary. The surface of the particle is surrounded by an amorphous layer with a thickness of ~ 1.5 nm. All the selected area diffraction patterns correspond to face-centered-cubic structured Cu, showing no crystalline CuO. Based on the XPS and HRTEM results, it appears that the surface amorphous layer consists of chemisorbed PVP and amorphous CuO.

4. Conclusions

We have synthesized copper nanoparticles in ambient atmosphere by a polyol method. The obtained copper particles were confirmed to be phase-pure crystalline copper with face-centered cubic (fcc) structure on the basis of XRD analyses. Detailed surface analyses by XPS and HRTEM revealed that the synthesized particles consist of single crystal Cu surrounded by amorphous CuO and chemisorbed PVP with a thickness of ~ 1.5 nm. We have adjusted the synthesis parameters to control the size and size distribution of the particles. Particle size decreases with increasing reducing agent concentration. The Cu precursor injection rate plays an important role in controlling

the particle size, whereas reaction temperature determines the particle size distribution. We obtained relatively monodisperse copper nanoparticles with a size range of 45 ± 8 nm at optimum conditions.

Acknowledgments

This work was supported by the Korea Science and Engineering Foundation (KOSEF) through the National Research Lab. Program funded by the Ministry of Science and Technology (No. M10500000011).

References

- [1] G.G. Ferrier, A.R. Berzins, N.M. Davey, *Platinum Metals Rev.* 29 (1985) 175.
- [2] J.H. Fendler, *Chem. Rev.* 87 (1987) 877.
- [3] N. Toshima, T. Yonezawa, *New J. Chem.* 22 (1998) 1179.
- [4] M. Brust, C.J. Kiely, *Colloids Surf. A* 202 (2002) 175.
- [5] N.A. Dhas, C.P. Raj, A. Gedanken, *Chem. Mater.* 10 (1998) 1446.
- [6] G. Vitulli, M. Bernini, S. Bertozzi, E. Pitzalis, P. Salvadori, S. Coluccia, G. Martra, *Chem. Mater.* 14 (2002) 1183.
- [7] H.H. Huang, F.Q. Yan, Y.M. Kek, C.H. Chew, G.Q. Xu, W. Ji, P.S. Oh, S.H. Tang, *Langmuir* 13 (1997) 172.
- [8] Z. Liu, Y. Bando, *Adv. Mater.* 15 (2003) 303.
- [9] D. Kim, S. Jeong, J. Moon, *Nanotechnology* 17 (2006) 4019.
- [10] R.V. Kumar, Y. Mastai, Y. Diamant, A. Gedanken, *J. Mater. Chem.* 11 (2001) 1209.
- [11] I.G. Casella, T.R.I. Cataldi, A. Guerrieri, E. Desimoni, *Anal. Chim. Acta* 335 (1996) 217.
- [12] I. Lisiecki, M.P. Pileni, *J. Am. Chem. Soc.* 115 (1993) 3887.
- [13] M.P. Pileni, B.W. Ninham, T. Gulik-Krzywicki, J. Tanori, I. Lisiecki, A. Filankembo, *Adv. Mater.* 11 (1999) 1358.
- [14] L. Qi, J. Ma, J. Shen, *J. Colloid Interface Sci.* 186 (1997) 498.
- [15] M.S. Yeh, Y.S. Yang, Y.P. Lee, H.F. Lee, Y.H. Yeh, C.S. Yeh, *J. Phys. Chem. B* 103 (1999) 6851.
- [16] I. Lisiecki, F. Billoudet, M.P. Pileni, *J. Phys. Chem.* 100 (1996) 4160.
- [17] S. Wu, D. Chen, *J. Colloid Interface Sci.* 273 (2004) 165.
- [18] G. Viau, F. Fievet-Vincent, F. Fievet, *Solid State Ionics* 84 (1996) 259.
- [19] P.Y. Silvert, K. Tekaiia-Elhsissen, *Solid State Ionics* 82 (1995) 53.
- [20] F. Fitvet, J.P. Lagier, B. Blin, B. Beaudoin, M. Figlarz, *Solid State Ionics* 32–33 (1989) 198.
- [21] F. Fievet, F. Fievet-Vincent, J.P. Lagier, B. Dumont, M. Figlarz, *J. Mater. Chem.* 3 (1993) 627.
- [22] R.A. Swalin, *Thermodynamics of Solid*, second ed., Wiley, New York, 1972, p. 114.
- [23] M. Yin, C.K. Wu, K. Lou, C. Burda, J.T. Koberstein, Y. Zhu, S. O'Brien, *J. Am. Chem. Soc.* 127 (2005) 9506.
- [24] P. Jiang, S.Y. Li, S.S. Xie, Y. Gao, L. Song, *Chem. Eur. J.* 10 (2004) 4817.
- [25] Y. Gao, P. Jiang, D.F. Liu, H.J. Yuan, X.Q. Yan, Z.P. Zhou, J.X. Wang, L. Song, L.F. Liu, J.M. Zhang, D.Y. Shen, *J. Phys. Chem. B* 108 (2004) 12877.
- [26] B. Yin, H. Ma, S. Wang, S. Chen, *J. Phys. Chem. B* 107 (2003) 8898.
- [27] I. Washio, Y. Xiong, Y. Yin, Y. Xia, *Adv. Mater.* 18 (2006) 1745.

Morphological study of hydroxyapatite nanocrystal suspension

E. BOUYER*, F. GITZHOFER, M. I. BOULOS

Plasma Technology Research Center (CRTP), Department of Chemical Engineering, Applied Science Faculty, Université de Sherbrooke, Sherbrooke, (Québec) Canada, J1K 2R1
E-mail: etienne.bouyer@dlr.de

Nanometer size hydroxyapatite (HA) crystals are prepared by a wet chemical precipitation method at different synthesis temperatures and with various reactant addition rates. The resulting aqueous suspensions are studied in terms of morphology (transmission electron microscope, specific surface area), phase (X-ray diffraction, electron diffraction and infrared spectroscopy) and rheological properties. This work shows that shape, size and specific surface area of the HA nanoparticles are very sensitive to the reaction temperature and also to the reactant addition rate. The measured pH at the end of synthesis, which is strongly linked with the reactant addition rate, is a key parameter which can be used to determine the purity of the synthesized HA nanocrystal and also for the stabilization (dispersion) of the suspension. HA nanoparticles synthesized at low temperature ($T < 60^\circ\text{C}$) are monocrystalline. A transition temperature ($T = 60^\circ\text{C}$) can be defined as a limit for the synthesis of monocrystalline HA nanocrystals, above this critical temperature nanocrystals become polycrystalline. HA monocrystals adopt a needle shape and are oriented following the c -axis of the hexagonal HA structure. The as-synthesized suspension is then concentrated and the effect of a dispersing agent addition, which is needed to get a high solid/liquid ratio coupled with good flowability of the suspension, is also shown, because this suspension is used in the suspension plasma spraying process.

© 2000 Kluwer Academic Publishers

1. Introduction

Hydroxyapatite (HA) is a well known bioceramic dedicated for biomedical applications. HA is currently used for various biomedical applications, such as a bone substitute [1]. HA, which is chemically similar to human hard tissue inorganic matter, can bond to bone without bone resorption when used as a coating on titanium implants [2]. The present study was undertaken to explore the synthesis of a suspension containing HA nanocrystals. A lot of contributions can be found in this field especially concerning the study of the temperature synthesis effect on the resulting nanocrystal morphology [3–5]. This suspension can be used either as a raw material for deposition processing such as sol gel deposition [6] or suspension plasma spraying [7], or for powder processing by atomization or spray drying.

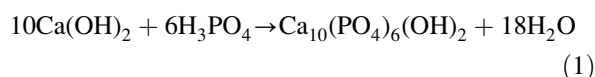
For these kinds of application, HA suspension physico-chemical characteristics are very important because the final material quality (composition, purity, flowability) will be strongly dependent on those characteristics. Obviously, HA is used as a raw material for different shaping processes. One of the key parameters is to control the composition of HA in order to prepare pure HA suspensions. The suspension

synthesized is an aqueous colloidal suspension also called sol or gel or physical gel [8, 9].

The objective of this work is to study the effect of different synthesis parameters (reaction temperature, reactant addition rate) on the morphology, phase and rheological properties of the colloidal HA suspension.

2. Materials and methods

HA suspension was prepared by a wet chemical reaction of precipitation following the reaction of Tagai and Aoki [10]:



The pH was monitored during the precipitation reaction. The acid is added to calcium hydroxide solution at different speeds. The reactant concentrations are 0.5 mole/l and 0.3 mole/l for the calcium hydroxide and for the orthophosphoric acid respectively. The resultant concentration of the suspension is 0.05 mole/l of HA nanocrystals. Chemical reaction is achieved in a double-wall beaker and heated by the water circulation

*Current address: German Aerospace Center (DLR), Institute for Technical Thermodynamics, Vaihingen, Pfaffenwaldring 38–40, D-70569 Stuttgart, Germany.

from a constant temperature bath. Reaction temperature was varied between 25 to 85 °C. Reaction stirring is performed by a magnetic stirrer. The resulting aqueous suspension is whitish and possesses a solid (HA nanocrystals) content of 2.5 wt %. In order to be used for the suspension plasma spraying process [7], the suspension has to undergo centrifugation and an evaporation process for the elimination of the water leading to a maximum weight ratio solid/liquid to about 40%. In the same way, the suspension viscosity has to be adjusted to a maximum of 10 Pa.s to allow good atomization of the suspension. The first step of the aging process is the natural settling which permits a solid/liquid ratio of 5 wt %. The further centrifugation step allows a value of more than 12 wt % for the same ratio. The final step is to remove water by heating the suspension (under stirring) at a temperature around 80 °C, then the solid/liquid ratio can reach more than 35 wt %.

The flowability of the suspension is optimized with the help of a deflocculant (dispersing agent) which improves the dispersion of the solid particles contained in the suspension by a modification of their surface charge. The dispersing agent employed (Darvan 7, R.T. Vanderbilt Company Inc., Norwalk, CT, USA) is based on sodium polymetacrylate (MW = 16 000) in aqueous solution. Darvan 7 can be used for biomedical applications, because it meets the FDA recommendations in terms of biocompatibility.

The morphology study performed on the HA nanocrystals was done on a transmission electron microscope (TEM, JEOL 100S) apparatus, the specific surface area was measured following the Brunauer-Emmett-Teller (BET) method (Micromeritics Flowsorb II 2300). Concerning the phase study the characterization was performed with both X-ray diffraction (XRD, Rigaku D/max), also with electronic diffraction (Philips EM 300G), and with the help of Fourier Transform infra-red spectrometry FTIR (Nicolet 5-DX). The viscosity was measured with a BOHLIN Visco 88 BV viscometer.

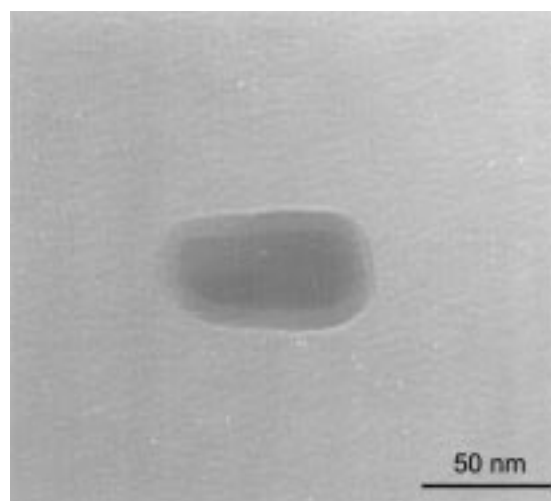
3. Results and discussion

3.1. Morphological study

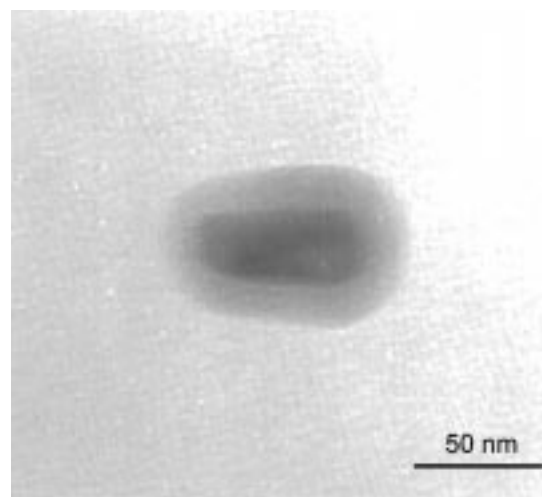
Particles used for the morphological investigations are directly sampled from the as-synthesized HA suspension. After dilution in ethanol, a small amount (< 1 vol %) of Darvan 7 is added to the suspension avoiding nanoparticle agglomeration.

HA nanocrystal observation with TEM shows a morphological evolution as a function of the electronic beam exposition time, energy and intensity [11]. The periphery of the particles becomes amorphous and this peripheral layer grows with the exposition time under electronic beam, Fig. 1 (a,b). HA is a very sensitive material susceptible to degrade under electronic beam. To overcome this problem the TEM investigations of HA were performed on TEM apparatus with a cryogenic stage for the sample holder.

The temperature synthesis effect on the nanoparticle shape shows that at low synthesis temperature the crystals carry a needle-shape, Fig. 2 (a). Increasing the



(a)



(b)

Figure 1 TEM pictures of the as-synthesized HA nanocrystals effect of electronic beam (without cryogenic stage), (a) $t = 0$; (b) $t = 3$ min.

reaction temperature changes the crystal from as-needle shape to a more regular shape close to circular, Fig. 2 (b). A shape factor can be defined by the ratio length/width of the HA nanocrystals:

$$F_s = \frac{L}{l} \quad (2)$$

where F_s , shape factor; L , particle length [m]; l , particle width [m]. The shape factor, F_s , of the HA nanocrystals decreases with an increase of the synthesis temperature. Fig. 3 shows the evolution of F_s versus the synthesis temperature.

After heating at high temperature $T = 850$ °C, 4 h, and then at $T = 1250$ °C, 4 h, the particle shape is shown in Fig. 4 (a, b) with a more regular shape in comparison with Fig. 3. Once can notice on Fig. 4a for the sample heated at 850 °C two kinds of particles:

- as-needle shaped particles such as synthesized at low temperature ($F_s = 5$)
- more homogeneous shaped particles with higher thickness ($F_s = 1.25$)

Particles of the second category are dense and result from sintering of the nanocrystals synthesized at low temperature.

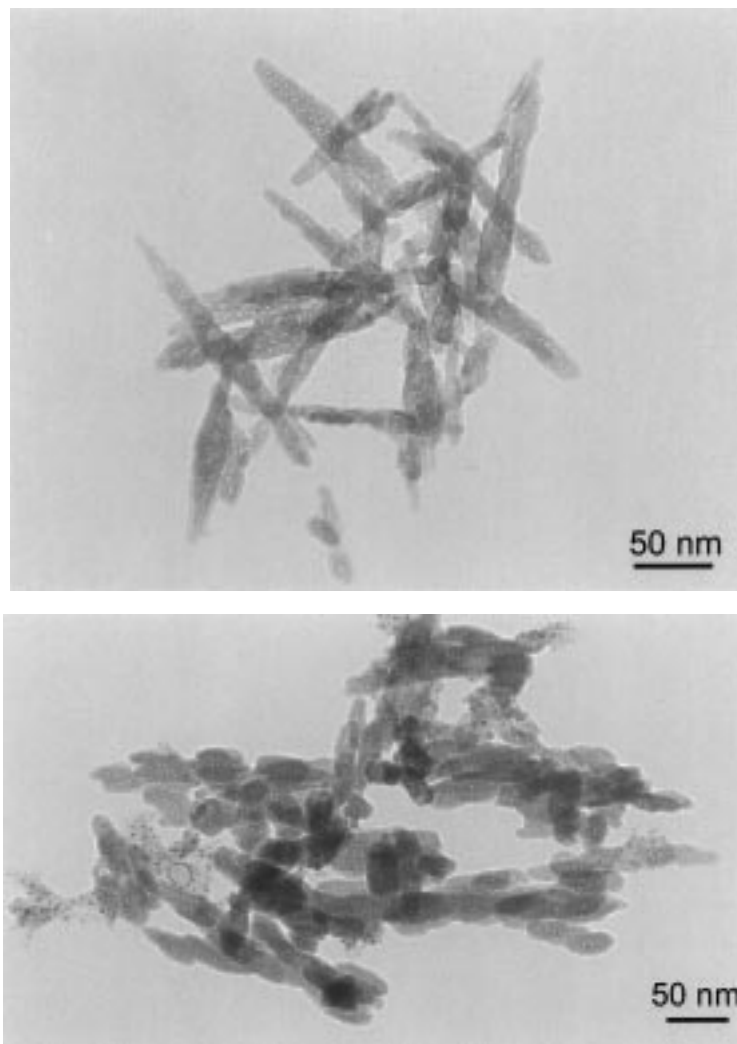


Figure 2 TEM pictures of the as-synthesized HA nanocrystals at different synthesis temperatures, (a) $T = 35\text{ }^{\circ}\text{C}$; (b) $T = 85\text{ }^{\circ}\text{C}$.

After heat treatment at $1250\text{ }^{\circ}\text{C}$ all the particles become thicker with a shape factor close to 1, this is due to the sintering of all the particles.

Fig. 5 shows the evolution of the specific surface area (SSA) measured using the BET method, SSA decreases as synthesis temperature increases. The reaction tem-

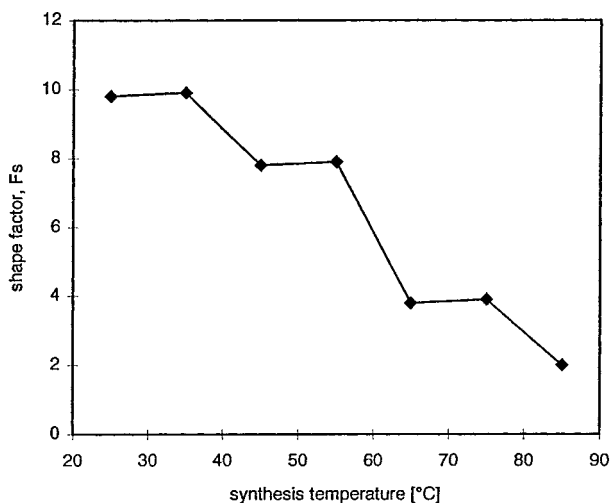


Figure 3 Evolution of the shape factor of the HA particles versus reaction temperature.

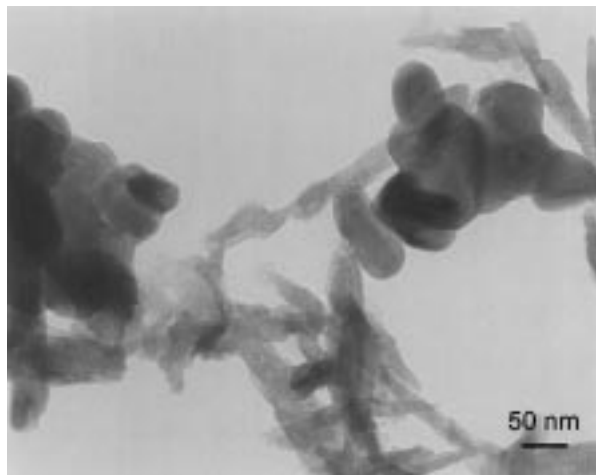
perature and the reactant addition rate seem to give opposite effects on the HA particle SSA, increasing the reaction temperature leads to SSA decrease while increasing the acid addition rate increases the SSA.

X-ray diffraction peak broadening can measure the crystallite size in a direction perpendicular to the crystallographic plane. The crystallite size $t_{(hkl)}$ perpendicular to a crystallographic family plane (hkl) can be evaluated measuring the full width at half peak maximum (FWHM) according to equation (3) expressed by the Scherrer formula [12]:

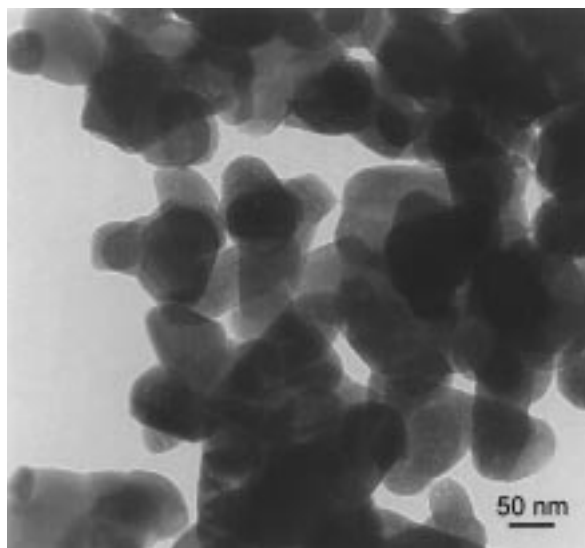
$$t_{(hkl)} = \frac{0.9\lambda}{\cos \vartheta_{(hkl)} \sqrt{\text{FWHM}^2 - \text{FWHM}_0^2}} \quad (3)$$

where $t_{(hkl)}$ crystallite size [nm]; λ , wavelength of the monochromatic X-ray beam, [nm] ($\lambda_{\text{K}\alpha\text{Cu}} = 0, 15418\text{ nm}$); FWHM full width at half maximum for the peak sample under consideration, [rad]; FWHM_0 full width at half maximum for the peak standard under consideration, [rad]; $\vartheta_{(hkl)}$, exact diffraction and satisfying the Bragg's law for the (hkl) Miller's plane [$^{\circ}$].

The peak corresponding to the (002) Miller's plane family (at $2\theta = 25.9^{\circ}$) is sharper than the other peaks. This shows a trend for the crystal growth following the c-axis of the HA structure as already mentioned in [13].



(a)



(b)

Figure 4 TEM pictures of the HA particles after heat treatment at, (a) $T = 850\text{ }^{\circ}\text{C}$, 4h (air); (b) $T = 1250\text{ }^{\circ}\text{C}$, 4h (air).

Transmission electronic diffraction provides information at a one particle scale. The main axis of the HA particle with the needle shape corresponds to the c-axis of the HA structure. This is true for nanocrystals synthesized at low temperature ($t < 45\text{ }^{\circ}\text{C}$), (Fig. 6a). Moreover the crystal looks like a monocrystal. At higher synthesis temperature, nanocrystals seem to lose the tendency to grow as a monocrystal following the c-axis of the apatitic structure, (Fig. 6b).

Fig. 7 shows the evolution of the crystallite size parallel with the c-axis of the HA structure. The size reaches a maximum value which corresponds to a temperature around $60\text{ }^{\circ}\text{C}$. This phenomenon can be explained by two temperature dependent effects which are concurrent. First of all, a temperature rise increases HA crystallinity which is thermally activated. Secondly, the temperature increase limits the tendency to the monocrystalline HA nanocrystals growth following the HA c-axis, because from this critical temperature, particles become more regular and circular. Above this temperature, the tendency to grow stops. This explains

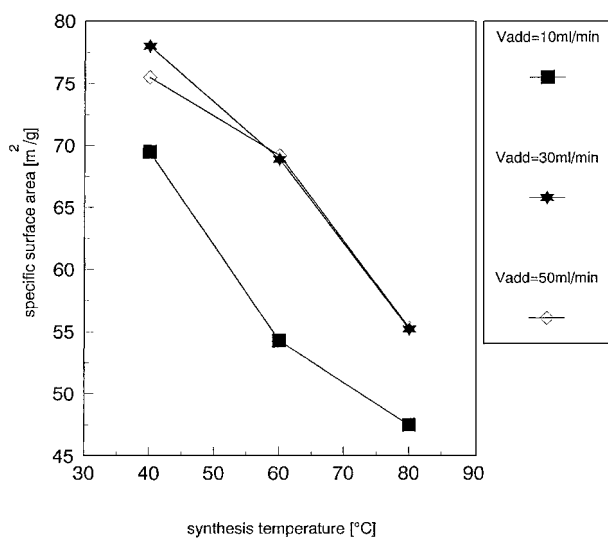
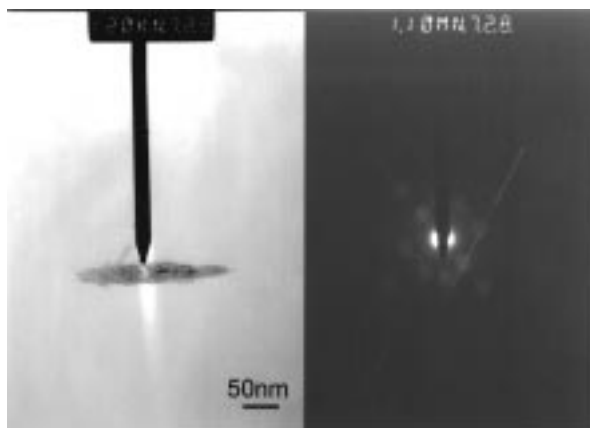


Figure 5 Specific surface area (SSA) of the as-synthesized HA nanoparticles versus reaction temperature.

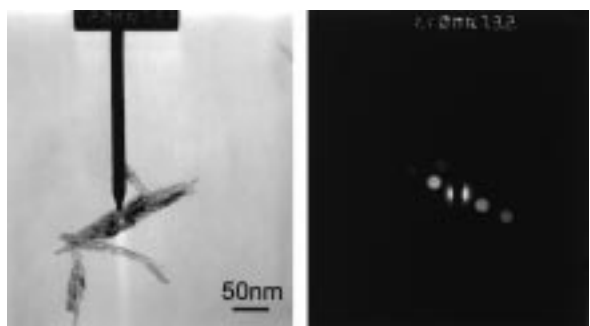
the maximum size for the HA crystallites at this temperature.

In Fig. 8, $60\text{ }^{\circ}\text{C}$ seems to be a critical temperature for the specific surface area, because at this temperature one can observe a brutal diminution of the SSA. This critical temperature can be interpreted as the limit because the speed of germination becomes higher than the speed of nucleation. In other words, above $60\text{ }^{\circ}\text{C}$ the speed of germ creation becomes higher than their speed of growth.

The HA synthesis with quasi-instantaneous acid addition ($V_{add} = 2400\text{ ml/min}$) in the basic solution



(a)



(b)

Figure 6 Electron diffraction of the as-synthesized HA particles, (a) $T = 25\text{ }^{\circ}\text{C}$; (b) $T = 75\text{ }^{\circ}\text{C}$.

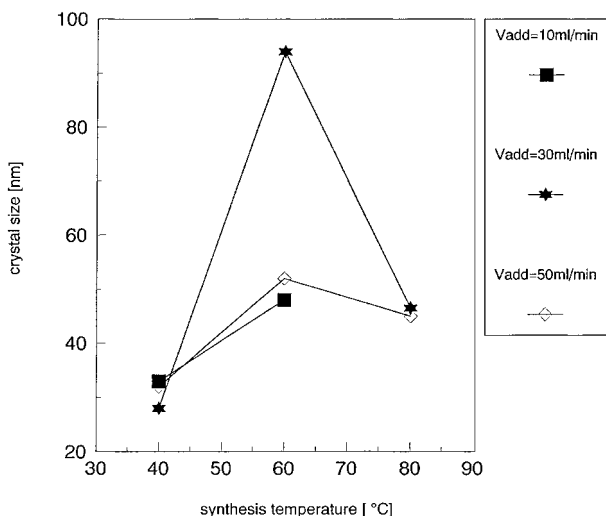


Figure 7 Crystal size following the *c*-axis of the HA nanoparticles versus the synthesis temperature.

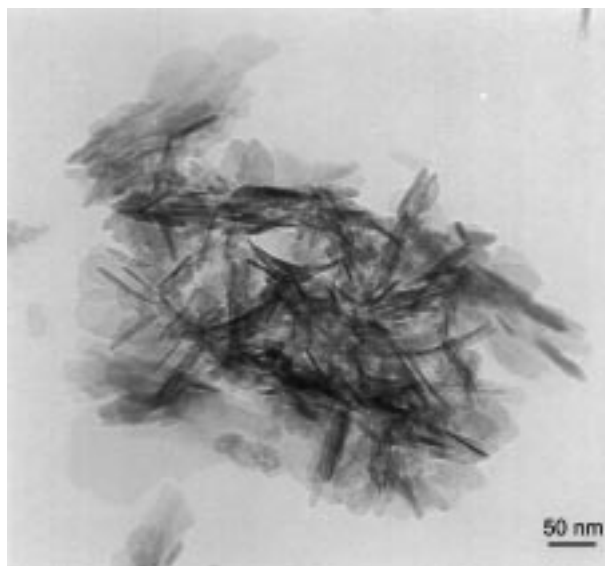


Figure 9 TEM picture of the HA nanoparticles synthesized at high acid addition rate ($V_{add} = 2400$ ml/min).

leads to a specific morphology. Indeed, particles have an elongated shape with a very small diameter, Fig. 9. The fibrous shape gives a high shape factor ($F_s > 20$). The specific surface area reaches values higher than $90 \text{ m}^2/\text{g}$.

3.2. Phase composition

Phases in the precipitate are determined by X-ray diffraction (XRD). For this investigation, the water is first removed by heating at 120°C , for 6 h. The resulting cake is crushed in a mortar. One of the problems of HA material synthesized at low temperature is the residual $\text{Ca}(\text{OH})_2$ phase, because the more intense peak of this phase is superposed with the peak of the HA structure. Indeed, the maximum intensity peak of the calcium hydroxide which corresponds to its (101) Miller's plane is situated at 34° in 2θ scale (JCPDS#4-0733). This peak is superposed with the 25% intensity peak of HA which corresponds to the (202) Miller's plane, namely the peak situated at 34.1° in 2θ scale (JCPDS#9-432). To

distinguish those phases, the sample should be submitted to a thermal heat treatment ($T = 600^\circ\text{C}$) which leads to the decomposition (dehydroxylation) of the calcium hydroxide to form lime with water release following the reaction:



Lime has its 100% intensity peak, which corresponds to the (200) Miller's plane, at 37.4° in 2θ scale (JCPDS#37-1497). This peak is well isolated in this angular domain. As shown in Fig. 10(a), peaks are relatively broad, proving the poor crystallinity of the as-synthesized HA powder. In order to check the presence of calcium hydroxide in the synthesized HA, the powder is submitted to a calcination treatment at 600°C and then to a sintering step at $T = 1250^\circ\text{C}$ for 5 h in air. On the XRD pattern shown in Fig. 10(b) there is no parasite peak situated at 39° in 2θ scale and corresponding to the lime phase. The synthesized phase corresponds to pure HA. XRD indicates that the synthesis reaction is completed,

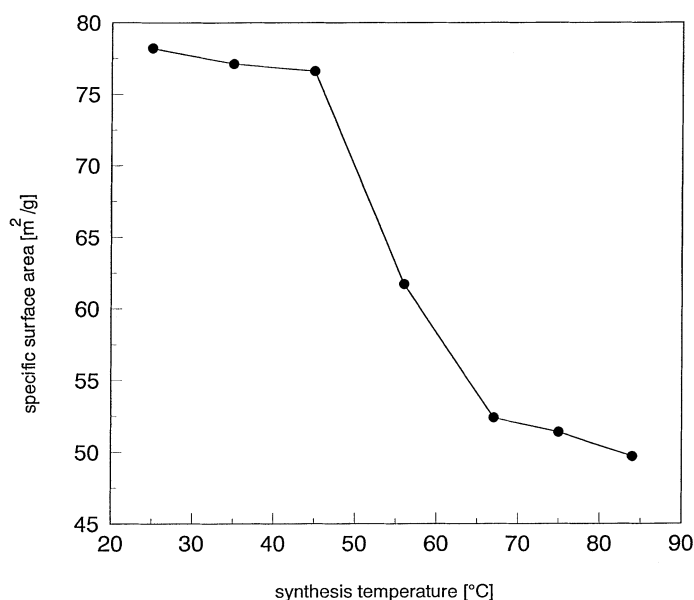


Figure 8 Specific surface area of the HA nanoparticles versus synthesis temperature.

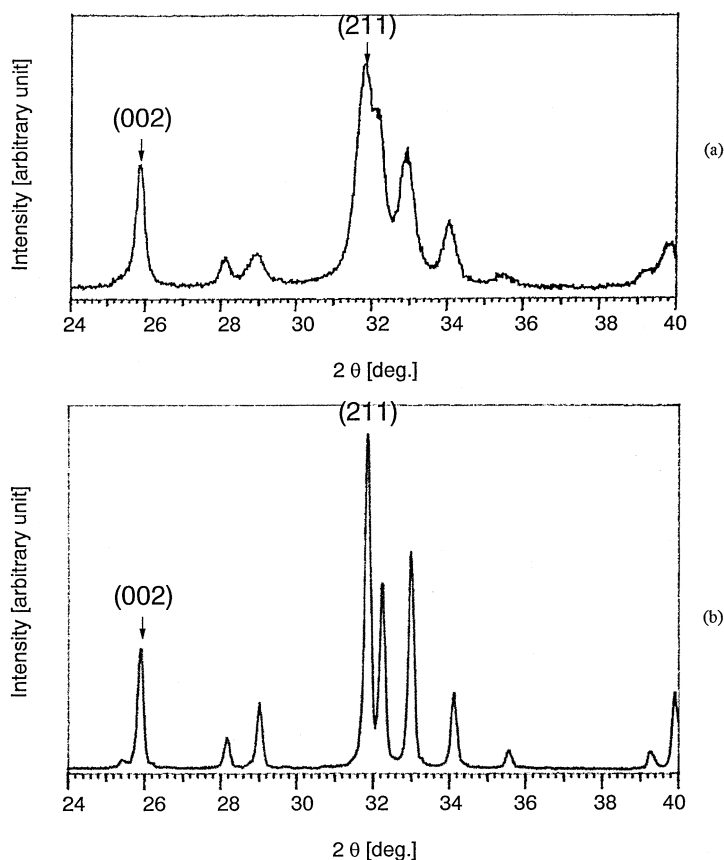


Figure 10 XRD spectra of HA nanoparticles synthesized at 45 °C and (a) heated at 120 °C; (b) heated at 120 °C calcined at 1250 °C, 5 h with air.

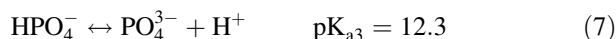
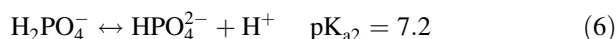
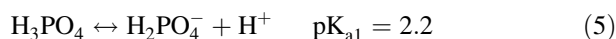
because there is no trace of residual reactant on the XRD spectra which indicates that reaction conversion is close to 100%. When the addition rate of the phosphoric acid is very high ($V_{\text{add}} = 2400 \text{ ml/min}$), the synthesis reaction conversion decreases and there is some Ca(OH)_2 appearing in the product. When the acid addition rate is below 100 ml/min, the conversion rate of the reaction is 100%.

Infra-red spectrometry gives information concerning the molecular groups included in the unit cell of the HA structure. Fig. 11(a) shows the IR spectrum of the as-synthesized HA powders after heating at 120 °C. It indicates the presence of the OH^- groups at 3571 cm^{-1} and the triplet ($564, 574$ and 603 cm^{-1}) characteristic of PO_4^{3-} groups. The large peak at 3550 cm^{-1} is assigned to the crystallization water, i.e. water molecules trapped in the apatite unit cell [14]. Generally, stoichiometric HA cannot contain water molecules in its unit cell while non-stoichiometric can contain some water molecules [15].

One can notice that synthesized HA is not carbonated (no peak relative to CO_3^{2-} group), then during the synthesis there is no substitution of phosphate group by carbonate group.

The broadening of the infra-red spectrum peaks gives an indication on the crystallization state of the HA material [16]. Nevertheless, there are no direct and quantitative relationships between peak broadening and crystallite size contrary to XRD with the Scherrer formula. The observation of the infra-red spectrum of HA synthesized at $T = 45 \text{ °C}$ shows broad peaks, this is confirmed with the peak convolution of the phosphate triple peaks. On the contrary, the synthesized HA powder heated at 1250 °C has sharper infra-red peaks than the as-

synthesized powder, Fig. 11(b). As already shown in section 3.1, the morphology of the HA particles strongly depends on the addition rate of reactant during the reaction synthesis and there is also a strong influence for the composition. A higher addition rate of acid systematically results in an increase of the Ca(OH)_2 content (which is not desired). This can be explained in terms of pH of the reaction media. When the acid is introduced at a very high addition rate, the pH of the reaction media decreases drastically ($\text{pH} < 7$). Orthophosphoric acid is a weak triacid, the acidity potentials are as follows:



If $\text{pH} > \text{pK}_a$ then the dissociation of H_3PO_4 will occur according to the Le Chatelier principle. In the other case the recombination will occur. Therefore when the acid is introduced in the reaction media at a high addition rate ($V_{\text{add}} = 2400 \text{ ml/min}$) the pH decreases leading to an incomplete dissociation of orthophosphoric acid. In the absence of PO_4^{3-} , the formation of the HA structure is compromised. This explains the presence of residual or unreacted calcium hydroxide which will further transform in lime during heat treatment. In this condition the synthesized HA can contain a fraction of dihydrogenophosphate (H_2PO_4^-) or hydrogenophosphate ions (HPO_4^{2-}) substituted for phosphate ions (PO_4^{3-}) which can explain the residual Ca(OH)_2 . Even if those hydrogenophosphated phases are quite difficult to detect by XRD, their presence induces small distortions

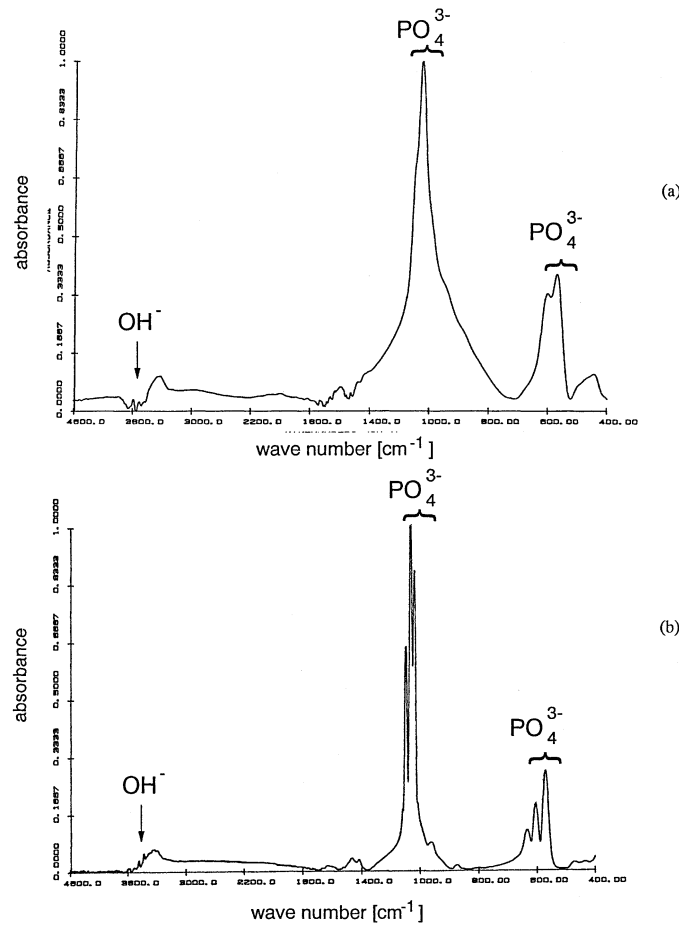


Figure 11 FTIR spectra of HA nanoparticles synthesized at 45 °C and (a) heated at 120 °C; (b) heated at 120 °C+ calcined at 1250 °C, 5 h with air.

in the unit cell. Those phases can be written in the following way: $\text{Ca}_{10-x}(\text{HPO}_4)_x(\text{PO}_4)_{6-x}(\text{OH})_{2-x}$ with $0 < x < 2$.

3.3. Rheological study

The requested property for HA suspension is good flowability, namely a low viscosity allowing the suspension to be pumped by a peristaltic pump.

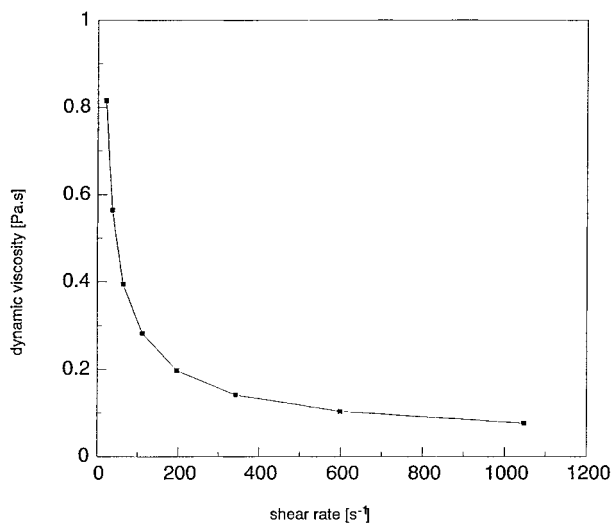


Figure 12 Viscosity of the HA suspension (40 wt % solid HA) versus shear rate (10 ml deflocculant/100 g HA).

Synthesized HA behaves as a non-Newtonian fluid, more precisely as a thixotropic fluid, Fig. 12. Elongated particles have a tendency at rest to interlace opposing any movement. Movement has to be initiated by a yield stress in order to break some link and orient the crystal. Viscosity of a thixotropic fluid decreases when shear increases. Viscosity of the as-synthesized HA suspension reach 5210 Pa with a shear rate of 1000 s^{-1} . This value is too high to permit the feeding via a peristaltic pump. To improve the flowability of the HA suspension, addition of a dispersing agent is necessary for the dispersion of HA particles in the liquid phase (water). Stability of HA depends on the zeta potential (ζ) defined by the Smoluchowski equation [17]:

$$\zeta = \frac{f_H m_e}{\epsilon} \quad (8)$$

where ζ , zeta potential [V]; f_H , constant of Henry; m_e , electrophoretic mobility [m/s]; μ , viscosity [kg/m.s]; ϵ , permittivity [F/m].

The isoelectric point (IEP) is defined as the pH value associated with a ζ potential equal to zero. For HA, IEP varies between 4 and 6. For a suspension which has its pH value in this range, the stability will be poor (flocculation). In order to maintain a stable suspension, this involves a pH out of the IEP range, higher than 6 or lower than 4. For chemical stability reasons, the range of stability is chosen at higher pH values than IEP. For a moderate addition rate of acid ($V_{\text{add}} < 100 \text{ ml/min}$) the pH at the end of the reaction is around 10. When the

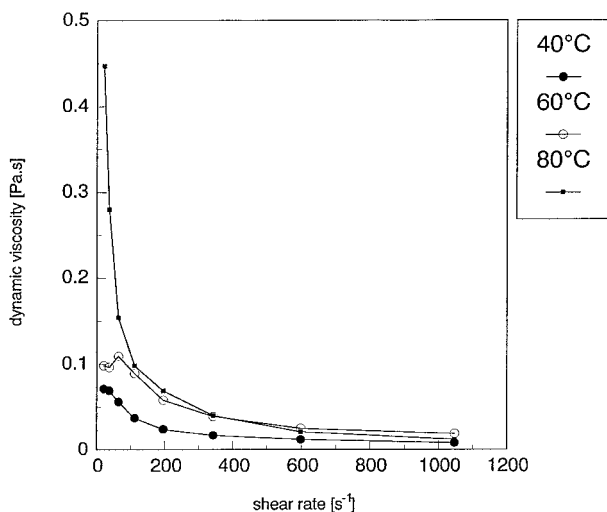


Figure 13 Viscosity of the HA suspension for different reaction temperatures (12 wt % solid HA).

addition rate of acid reaches higher values, the pH goes down close to the IEP. The natural settle time of the suspension also depends on the acid addition rate. For a high acid addition rate, the settle time is less than 5 min. Conversely, with a moderate acid addition rate, the settle time varies between 0.5 and 2 h.

The quantity of dispersing agent for the suspension suitable for atomization is 10 ml of Darvan per 100 g HA. Even with the addition of Darvan 7 the rheological behavior of the suspension is still thixotropic. Fig. 12 displays the viscosity versus the shear rate of the HA suspension suitable for atomization. The viscosity of the suspension synthesized at different temperatures is shown in Fig. 13. Viscosity seems to increase with the synthesis temperature, but the viscosity decreases with an increase of shear rate. The tendency is a diminution of the yield value and viscosity associated with a reduction of the reaction temperature. Paradoxically, the viscosity is lower when the shape factor of the particles is higher. This can be explained by the surface charge of the particle which depends on the particle specific surface area. This surface

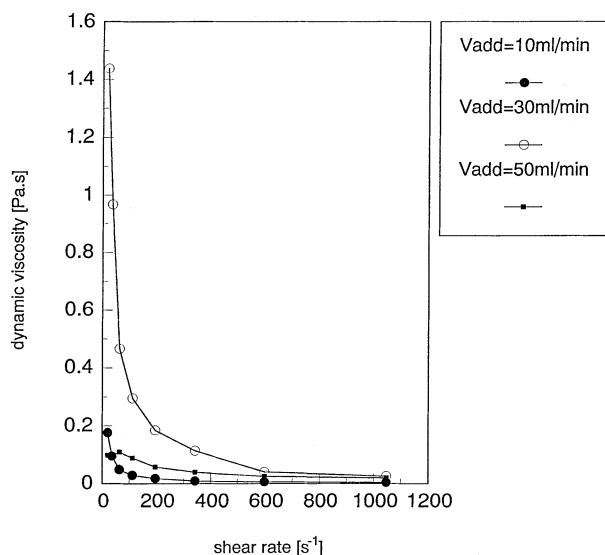


Figure 14 Viscosity of the HA suspension versus acid addition rate (12 wt % solid HA).

charge is preponderant for the stability of the suspension, therefore for good flowability and low viscosity.

In Fig. 14 the viscosity is displayed versus the shear rate for different acid addition rates. Whatever the acid addition rate, the rheological behavior is kept thixotropic. The influence of the acid addition rate is not significant. The influence of deflocculant content on suspension viscosity has been studied on suspensions with 40 wt % of HA. There is a minimum viscosity with an associated optimum deflocculant content around 10 ml/100 g HA, Fig. 15.

For the SPS application of HA suspension, which briefly allows the use of high purity suspensions or sol-gel to be atomized in a thermal plasma flame and produces either 20 μm size powder or coatings, the maximum viscosity for this process is a few Pa.s \equiv viscosity unit, above this value the suspension cannot be pumped or atomized. This is a physical limit for the use of the suspension in this process.

4. Conclusion

The chemical synthesis of HA as presented in this paper is simple to implement and the by-product (water) could be useful for the SPS process. HA synthesized particles possess a wide range of size and shape depending on the reaction temperature and also on the orthophosphoric acid addition rate. For small acid addition rates particles have an as-needle shape and for very high acid addition rates the shape factor increases until 20. The specific surface area of the as-needle shaped nanoparticles strongly varies with the reaction temperature, an increase of synthesis temperature limits the specific surface area to 55 m^2/g as well as the shape factor to two. One can define a transition temperature, around 60 $^\circ\text{C}$, which separates domains where growing and nucleation phenomena are preponderant. Quasi-instantaneous acid addition rates ($V_{\text{add}} = 2400 \text{ ml/min}$) lead to a different morphology of HA particles (fiber type) containing some residual and unreacted calcium hydroxide as observed by TEM. HA particle composition is mainly controlled by the acid addition rate which should be maintained at a low value. The pH value at the end of the reaction, which depends on the acid addition rate, is a good indicator for the calcium hydroxide residual content. The effect of deflocculant addition to the HA suspension is a 4 order magnitude reduction of viscosity, but the rheologic behavior is still thixotropic. Finally, the favorable synthesis conditions of pure and monocrystalline HA need a moderate acid addition rate coupled with a reaction temperature lower than 60 $^\circ\text{C}$, this involves a reasonably high pH at the end of the reaction ($\text{pH} > 10$). These conditions also satisfy other properties such as a good dispersion of the HA nanoparticles associated to an acceptable viscosity allowing the atomization of the HA suspension.

Acknowledgments

The authors would like to acknowledge the financial support of the Natural Sciences and Engineering Research Council of Canada (NSERC) and the Ministry of Education of the province of Quebec, Fond FCAR. The technical assistance of Mr P. Magny (Université de

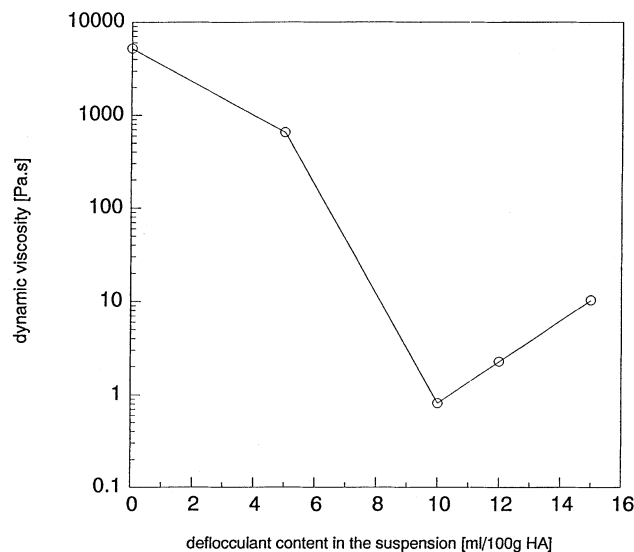


Figure 15 Viscosity of HA versus deflocculant content (40 wt% solid HA).

Sherbrooke), Dr B. Hong (CM², Ecole Polytechnique de Montréal) are gratefully acknowledged.

References

1. R. H. DOREMUS, *J. Mater. Sci.* **27** (1992) 285.
2. K. A. THOMAS, *Orthopedics* **17** (1994) 267.
3. Y. MASUDA, K. MATUBARAM and S. SAKKA, *J. Ceram. Soc. Jpn* **98** (1990) 1266.
4. C. CHAI, B. BEN-NISSAN, S. PYKE and L. EVANS, "Surface Modification Technologies VII", edited by T. S. Suddshan (Cambridge University Press, 1994) p. 509.
5. A. DEPTULA, W. LADA, T. OLCZAC, R. Z. LEGEROS and J. P. LEGEROS, in "Bioceramics" Vol. 9 (University Press, UK 1996) p. 313.
6. B. BEN-NISSAN, C. S. CHAI and K. A. GROSS, "Bioceramics" Vol. 10, edited by L. Sedel and C. Rey (Elsevier Science Ltd, UK, 1997) p. 175.
7. E. BOUYER, F. GITZHOFFER and M. I. BOULOS, *JOM* **16** (1997) 57.
8. PH. COLOMBAN, *Ceram. Int.* **15** (1989) 23.
9. C. J. BRINKER and G. W. SCHERER, "Sol-gel Science: The Physics and Chemistry of Sol-gel Processing," (Academic Press Inc., Boston, USA, 1990).
10. H. TAGAI and H. AOKI, "Preparation of synthetic hydroxyapatite and sintering of apatite ceramics: Mechanical properties of biomaterials", Chapter 39, edited by G. W. Hastings and D. F. Williams (John Wiley & Sons Ltd, 1987) p. 213.
11. J. HUAXIA and P. M. MARQUIS, *J. Mater. Sci. Lett.* **10** (1991) 132.
12. B. D. CULLITY, in "Elements of X-ray diffraction", 2nd edition (Addison-Wesley Publishing Company, Inc., Reading, MA, USA, 1978) p. 555.
13. L. YUBAO, C. P. A. T. KLEIN, J. DE WIJN, S. VAN DE MEER and K. DE GROOT, *J. Mater. Sci.: Mater. Med.* **5** (1994) 263.
14. K. C. BLAKESLEE and R. A. CONDRATE, *J. Am. Ceram. Soc.* **54** (1971) 559.
15. B. O. FOWLER, *Inorg. Chem.* **13** (1974) 194.
16. J. D. TERMINE and A. S. POSNER, *Nature* **211** (1966) 268.
17. J. S. REED, "Principles of Ceramics Processing" 2nd edition (John Wiley & Sons, Interscience, New York, USA, 1995) p. 658.

Received 21 July 1997
and accepted 8 October 1999



Facile co-precipitation synthesis of shape-controlled magnetite nanoparticles

Lazhen Shen, Yongsheng Qiao, Yong Guo*, Shuangming Meng, Guochen Yang, Meixia Wu, Jianguo Zhao

School of Chemistry and Chemical Engineering, Shanxi Datong University, Datong 037009, P R China

Received 7 May 2013; received in revised form 8 July 2013; accepted 8 July 2013

Available online 15 July 2013

Abstract

Monodispersed magnetite (Fe_3O_4) nanoparticles with high saturation magnetization, including nanospheres, nanoneedles and nanocubes, were synthesized by the co-precipitation method. The shape of magnetite nanoparticles was controlled by changing the amount of sodium dodecyl sulfate (SDS) and the particle size was adjusted by the irradiation time of visible light. The Fe_3O_4 nanospheres, nanoneedles and nanocubes were obtained with the addition of 0 g, 0.1–0.4 g and 0.5–1.0 g SDS, respectively. The particle size of nanospheres, nanoneedles and nanocubes of magnetite was ~ 15 nm, 100×12 nm² (length \times width) and ~ 50 nm under the irradiation time of 30 min. The phase structure, particle shape and size of the samples were characterized by transmission electron microscopy (TEM), X-ray diffraction (XRD) and Fourier transform infrared spectroscopy (FTIR). The as-prepared magnetite nanoparticles from TEM images exhibited a high level of crystallinity with narrow size distribution and good dispersion. The XRD results showed that all the magnetite nanoparticles were pure Fe_3O_4 phase with obvious diffraction peaks. The products exhibited the attractive magnetic properties with high saturation magnetization, which were examined by a vibrating sample magnetometer (VSM).

© 2013 Elsevier Ltd and Techna Group S.r.l. All rights reserved.

Keywords: Magnetite; Nanoparticles; Shape-controlled; Saturation magnetization; Visible light irradiation

1. Introduction

Magnetite (Fe_3O_4) exhibits the unique electric and magnetic properties based on the transfer of electrons between Fe^{2+} and Fe^{3+} in the cubic sites [1]. Due to the unique properties and advantages of magnetite, such as strong magnetism, good biocompatibility, long durability, low toxicity and low cost [2,3], it is widely used in magnetic biomedicine [4–6], heavy metal ions removal [7,8], electromagnetic wave absorption [9] and other fields [10–12]. These properties of magnetite strongly depend on their dimension, shape, saturation magnetization as well as monodispersion [13,14].

Many research groups have worked to synthesize magnetite nanospheres, nanocubes, nanoneedles and nanoporous particles by hydrothermal methods [15], co-precipitation methods [16]

solvothermal methods [17,18], sonochemical methods [13] and self-assembly methods [19]. These studies provided many useful preparation technologies for the preparation of Fe_3O_4 with different shapes. However, most of Fe_3O_4 nanoparticles obtained by the co-precipitation method are spherical shaped. For instance, the magnetite nanospheres have been synthesized using the co-precipitation method, but the hexanoic acid and loeic acid were employed as the coating agents during the initial crystallization phase of the magnetite [20]. These organic acids are expensive reagents and not environment friendly, and the products obtained have wide particle size distribution of 10–40 nm and small saturation magnetization of 58.72 emu/g. The various methods have been applied to synthesize the nanocubes, nanoplates, nanoneedles or nanorods of magnetite using a solvothermal method [17], hydrothermal method [21], and template method [22] rather than the co-precipitation method. In recent years, Gao et al. have synthesized Fe_3O_4 nanocubes using the solvothermal method at 260 °C in the presence of oleic acid and oleylmine [17].

*Corresponding author. Tel.: +86 352 609 0032.

E-mail address: ybsy_guo@163.com (Y. Guo).

A series of Fe_3O_4 morphologies (nanorods, nanocubes and nanoneedles) were synthesized via a hydrothermal process [21]. Zheng et al. have prepared different morphologies of Fe_3O_4 nanostructures, including spherical, cubic, rod-like, and dendritic nanostructure, using polyethylene glycol as a template [22].

In this study, a simple and efficient one-step co-precipitation method is reported to synthesize the shape-controlled magnetite nanoparticles using FeSO_4 and $\text{Fe}_2(\text{SO}_4)_3$ as reactants at room temperature. In order to improve the shape-dependent functional properties, such as electric property and magnetism, the relation between technological parameters and the shape of products were investigated in this paper. Different nanostructures and particle sizes of Fe_3O_4 nanospheres, nanocubes and nanoneedles were successfully synthesized by carefully controlling the amount of SDS and the time of irradiation with visible light. The crystalline structure, shape and size of the as-obtained Fe_3O_4 nanoparticles were characterized by XRD and TEM technique and the magnetic properties were investigated by VSM at room temperature. The results show that the shape-controlled Fe_3O_4 nanoparticles exhibit strong monodispersity and high saturation magnetization.

2. Experimental

2.1. Characterization

A BDX-3300 model JEOL 100CX-II transmission electron microscope (TEM) was used to carry out the TEM measurements to investigate the morphology and size of magnetite nanoparticles at an accelerating voltage of 200 kV. The obtained samples were characterized on a BDX-3300 diffractometer using $\text{CuK}\alpha$ radiation (wavelength, $\lambda = 1.5406 \text{ \AA}$) with variable slits at 45 kV/40 mA to obtain X-ray powder diffraction (XRD) patterns. The structural properties of the samples were determined by using a NEXUS 870 Fourier transform infrared spectroscopy (FTIR) from 450 cm^{-1} to 2000 cm^{-1} . The magnetic measurement of the products was carried out in a USA LDJ 9600-1 vibrating sample magnetometer (VSM). Magnetic hysteresis loops were recorded at room temperature in a field of 10,000 Oe to determine the saturation magnetization (M_s) for the samples.

2.2. Preparation of magnetite nanoparticles

In the typical synthesis, 2.8 g of $\text{FeSO}_4 \cdot 7\text{H}_2\text{O}$ and 4.0 g of $\text{Fe}_2(\text{SO}_4)_3$ were dissolved in 100 mL distilled water for 5 min using a magnetic stirrer in a 250 mL beaker. Different amounts (0–1.0 g) of sodium dodecyl sulfate (SDS) were added to this solution under stirring. The pH value of the mixture was adjusted to 12 by solid NaOH with stirring for 20 min at room temperature. The visible light was generated by a lamp. The wavelength of the visible light was about 400–750 nm. The reactor was placed at a fixed distance of 10 cm from the lamp for 0–60 min. The black precipitates were formed and then were washed several times with distilled water and ethanol in turn until the pH was neutral. Finally, the resultant black precipitates were dried in air at room temperature to obtain magnetite nanoparticles. The magnetite

nanoparticles obtained at different SDS concentrations and visible light time were nanospheres, nanocubes and nanoneedles.

3. Results and discussion

3.1. TEM results

Different shaped magnetite nanoparticles were prepared by the facile co-precipitation method in the presence of SDS. The experimentations have been performed by adjusting the amount of SDS and the irradiation time of the visible light to investigate their influence on the shape and particle size of magnetite nanoparticles. The nanospheres, nanoneedles and nanocubes of magnetite were synthesized, and the TEM images of the as-prepared Fe_3O_4 are given in Fig. 1. It could be observed that all of the three synthesized Fe_3O_4 nanoparticles displayed a relatively narrow particle size distribution, good dispersion and a perfect and uniform morphology with distinct crystalline structure. Without SDS, the prepared Fe_3O_4 nanoparticles were nanospheres with monodispersity under the visible light irradiation time of 0–60 min. The particle size of magnetite nanospheres could be controlled by increasing the visible light irradiation time. As the irradiation time of the visible light increased from 30 min to 60 min, the size of the as-prepared magnetite nanospheres increased from $\sim 15 \text{ nm}$ to $\sim 50 \text{ nm}$ as shown in Fig. 1a and b. The Fe_3O_4 nanoneedles could be produced when 0.1–0.4 g SDS was added. As seen from Fig. 1c, the monodispersible Fe_3O_4 nanoneedles were obtained by adding 0.4 g SDS under the visible light irradiation time of 30 min. Under the visible light irradiation time of 60 min, the Fe_3O_4 nanoneedles were prepared with the addition of 0.3 g SDS as shown in Fig. 1d. Furthermore, the diameter of magnetite nanoneedles increased from 100×12 to $115 \times 14 \text{ nm}$ (length \times width) with the visible light irradiation time increasing from 30 min to 60 min. With the addition of 0.5–1.0 g SDS, the shape of magnetite nanostructures changed from nanoneedles to nanocubes. As shown in Fig. 1e and f, the Fe_3O_4 nanocubes were prepared by adding 0.8 g and 1.0 g SDS, respectively. Similarly, the particle size of the as-obtained Fe_3O_4 nanocubes increased from about 50 nm to about 100 nm with the increase of the irradiation time from 30 min to 60 min. It can be inferred from Fig. 1 that the particle shape of magnetite is controlled by adjusting the SDS amount, and the particle size increases with the increase of the visible light irradiation time. In fact, the visible light irradiation will not influence the particle shape but the particle size and crystalline structure. The reason may be that the visible light irradiation is favorable to the growth of grain. Therefore, the longer the irradiation time of visible light, the larger the particle size, the better the crystallinity of Fe_3O_4 nanoparticles. The particle size is small but with poor crystalline structure without visible light irradiation.

3.2. XRD results

The phase and crystallinity of magnetite nanospheres, nanoneedles and nanocubes prepared at visible light irradiation time of 30 min were investigated using the XRD technique and the results are given in Fig. 2. The XRD patterns indicated that all of the

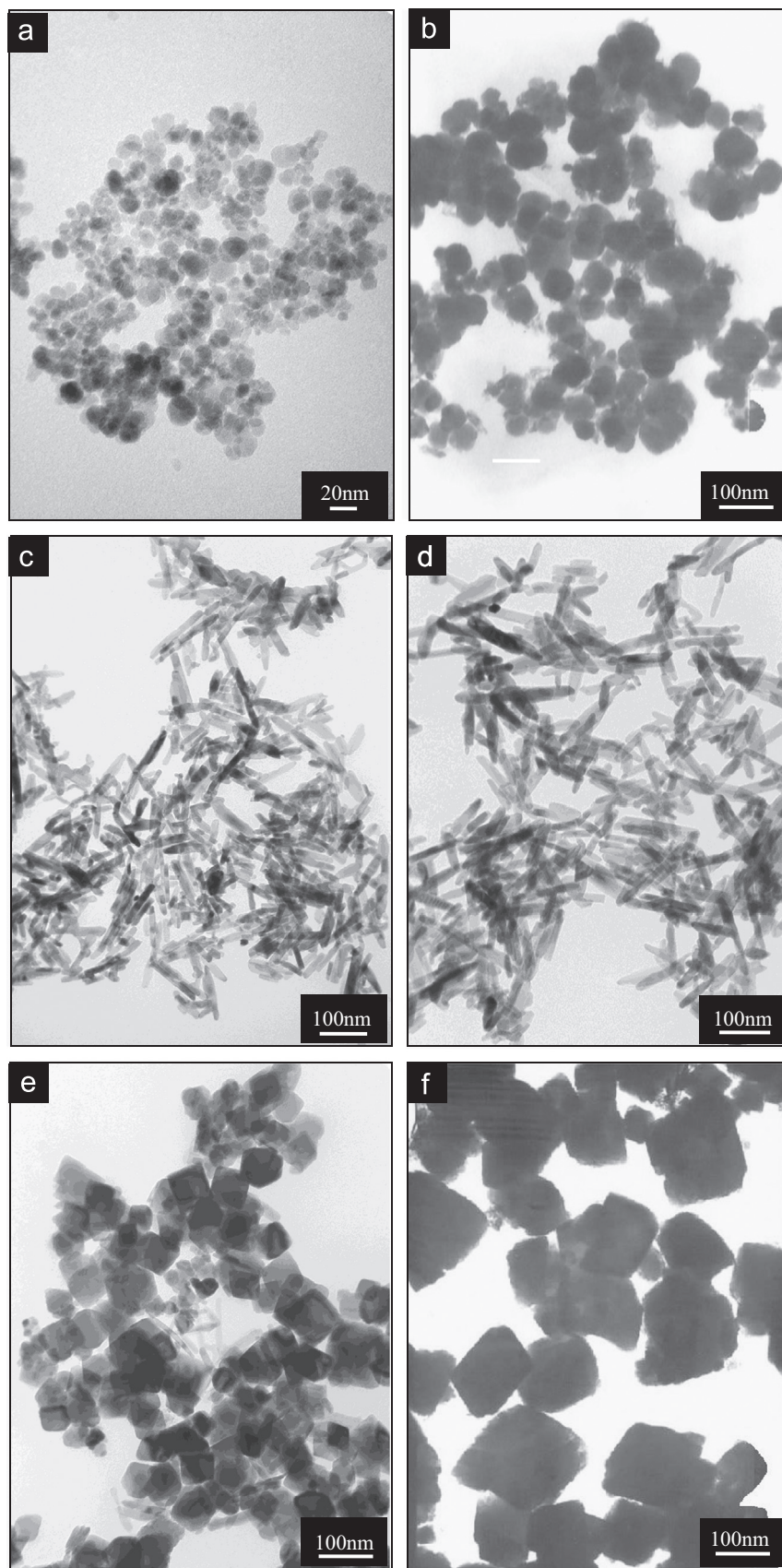


Fig. 1. TEM images of (a, b) nanospheres, (c, d) nanoneedles and (e, f) nanocubes of magnetite obtained at different irradiation times of visible light: (a, c, e) 30 min, and (b, d, f) 60 min and different SDS amounts of 0 g (a, b), 0.4 g (c), 0.3 g (d), 0.8 g (e) and 1.0 g (f).

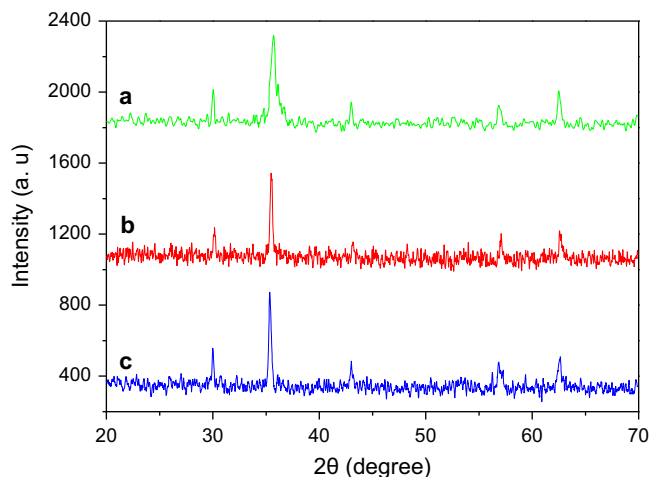


Fig. 2. XRD patterns of (a) nanospheres, (b) nanoneedles and (c) nanocubes of magnetite obtained at the visible light irradiation time of 30 min.

samples had five obvious diffraction peaks at 2θ of 30.1, 35.4, 42.9, 57.5 and 62.7, representing corresponding indices (220), (311), (400), (511) and (440) of magnetite, respectively [13,23]. The position and relative intensity of all diffraction peaks matched well with the standard of the Fe_3O_4 reflections. No other impurity phase was observed from Fig. 2a–c, indicating the as-synthesized magnetite nanospheres, nanoneedles and nanocubes were pure Fe_3O_4 nanoparticles with an inverse spinel structure. The strong and sharp peaks revealed that Fe_3O_4 particles were highly crystallized, which was consistent with the morphologies from the TEM images. The diffraction peak broadening suggested the small size of magnetite nanoparticles. The particle size of the three samples could be estimated from XRD patterns using Scherrer's equation. The calculated crystal grain size of the magnetite nanospheres, nanoneedles and nanocubes was 15.4 nm, 36.8 nm and 51.2 nm, respectively. The sizes of Fe_3O_4 nanoparticles calculated from the XRD patterns were in good agreement with the average sizes determined by TEM images (Fig. 1a, c and e). The accordant results about the size indicated the single crystalline nature of Fe_3O_4 nanoparticles.

3.3. FTIR results

To obtain additional data for characterization of nanospheres, nanoneedles and nanocubes of magnetite, the products were measured by FTIR spectra. The FTIR spectra recorded from 2000 to 500 cm^{-1} of the magnetite nanoparticles obtained at the visible light irradiation time of 30 min are shown in Fig. 3. It was reported that the characteristic absorption band of Fe–O bond of bulk Fe_3O_4 was at 570 cm^{-1} [24]. From Fig. 3, the FTIR spectrum of the magnetite nanospheres, nanoneedles and nanocubes was characterized by a strong absorption band at 606 cm^{-1} , 609 cm^{-1} and 612 cm^{-1} , respectively and no additional peaks. The reason of a small increment in wavenumber is that the surface bond force constant increases with the decrease of particle size to nanoscale dimensions. Therefore, the FTIR spectrum of the three cases exhibited a blue shift and the characteristic absorption band

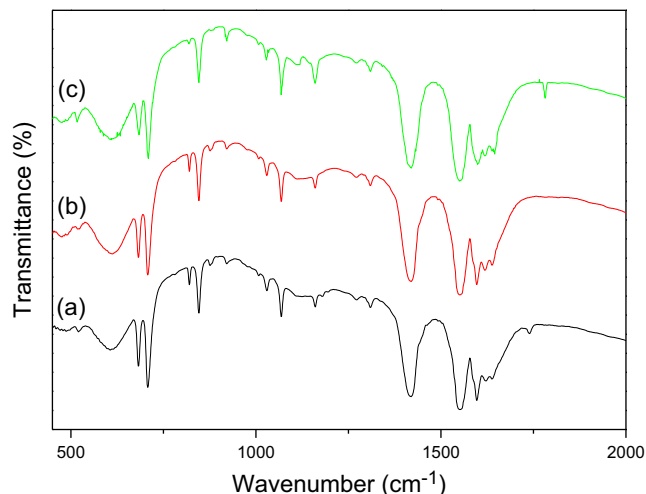


Fig. 3. FTIR spectra of (a) nanospheres, (b) nanoneedles and (c) nanocubes of magnetite obtained at the visible light irradiation time of 30 min.

of Fe–O in Fe_3O_4 had a higher wavenumber than that of bulk Fe_3O_4 [25]. These results strongly support to assignment of the contained iron oxide as Fe_3O_4 , which suggests that pure magnetite nanospheres, nanoneedles and nanocubes can be prepared at the experimental conditions of this paper.

3.4. Magnetic properties

The magnetic properties of the as-prepared magnetite nanospheres, nanoneedles and nanocubes obtained at visible light irradiation time of 60 min were measured at room temperature, and the magnetic hysteresis (M–H) loops are presented in Fig. 4a–c. From this figure, it was clear that the saturation magnetization of magnetite nanospheres, nanoneedles and nanocubes was 75.9 emu/g (Fig. 4a), 94.2 emu/g (Fig. 4b) and 108.1 emu/g (Fig. 4c). Nanoneedles magnetization is higher than nanospheres, and is close to the theoretical value of bulk Fe_3O_4 ($\sim 90\text{ emu/g}$) [26]. This result indicates the formation of the well-defined crystalline structure for the as-synthesized magnetite nanoparticles. The Fe_3O_4 nanocubes exhibit higher saturation magnetization than that of magnetite nanospheres and nanoneedles, which indicates that the magnetic properties show the shape dependence. In addition, the magnetic behavior of Fe_3O_4 nanoparticles is sensitive to the particle size [27]. It is clearly evident from the TEM images as shown in Fig. 1 that the size of magnetite nanoparticles increases from nanospheres to nanoneedles and to nanocubes. It is well-known that the decrease in particle size can lead to an increasing surface-to-volume ratio, which in turn causes more surface spin disorder, and consequently a reduction in the saturation magnetization [28,29]. The third reason for the increasing saturation magnetization in case of magnetite nanocubes may be related to the increased crystallinity as shown in TEM images of Fig. 1f, comparing with slightly low crystallinity of nanospheres and nanoneedles as in Fig. 1b and d. Therefore, the increase in the crystallites size from nanospheres to nanoneedles then to

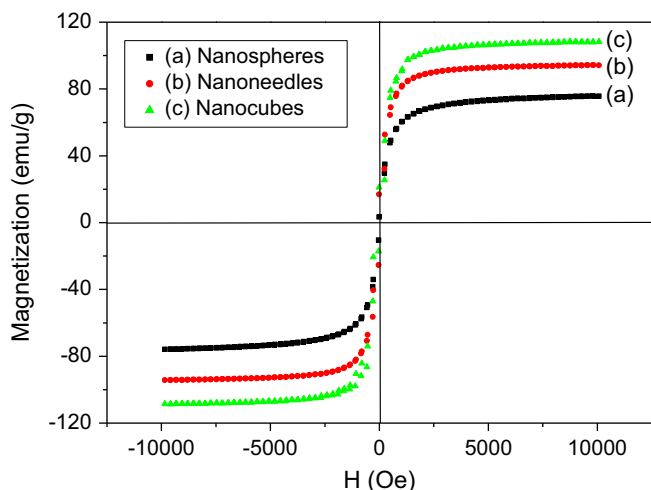


Fig. 4. Magnetic hysteresis loops of (a) nanospheres, (b) nanoneedles and (c) nanocubes of magnetite obtained at the visible light irradiation time of 60 min.

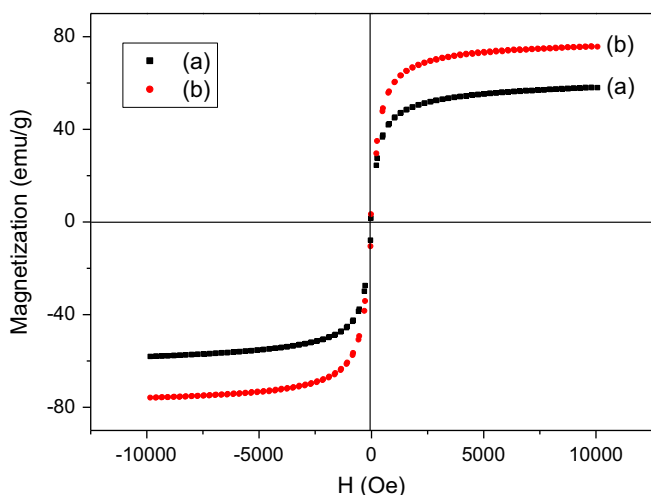


Fig. 5. Magnetic hysteresis loops of magnetite nanospheres obtained at the visible light irradiation time of (a) 30 min and (b) 60 min.

nanocubes of magnetite leads to a corresponding increase in the magnetization value.

In order to illustrate the influence of the particle size on the magnetization value, Figs. 5 and 6 show the magnetite nanospheres and nanocubes synthesized at the visible light irradiation time of 30 min and 60 min, respectively. As seen from Fig. 5, the saturation magnetization of the as-prepared magnetite nanospheres increases from 58.0 emu/g to 75.9 emu/g with the irradiation time of the visible light increased from 30 min to 60 min. The saturation magnetization of the magnetite nanocubes also exhibits an increase to 108.1 emu/g from 97.6 emu/g with the visible light irradiation time increasing from 30 min to 60 min. It was reported that the magnetic anisotropy of the nanoparticles depends on their crystallinity and thus high crystalline structure will cause an increase in the magnetic moment of the nanoparticles [30]. Therefore, the increase in the saturation magnetization may be attributed to the increase in the size and the degree of crystallinity of the magnetite nanoparticles with the irradiation time increasing.

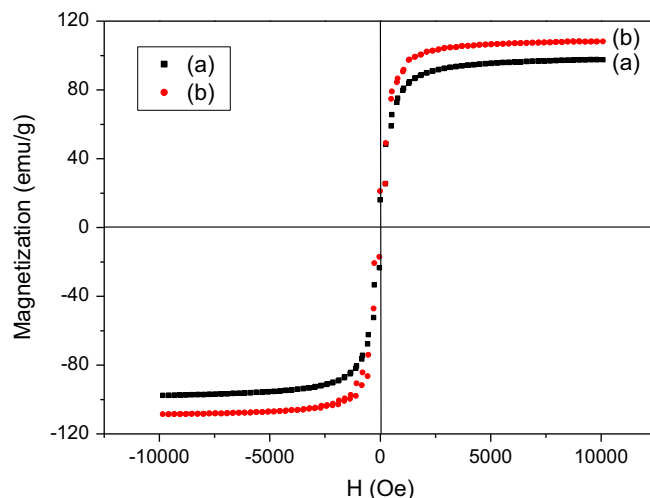


Fig. 6. Magnetic hysteresis loops of magnetite nanocubes obtained at the visible light irradiation time of (a) 30 min and (b) 60 min.

In addition, it was reported that magnetite nanoparticles smaller than approximately 20–30 nm contain a single magnetic domain with a single magnetic moment and exhibit superparamagnetism [31,32]. Therefore, the Fe_3O_4 nanospheres obtained at the visible light irradiation time of 30 min are superparamagnetic at room temperature due to the small particle size of about 15 nm, which is evident from the TEM images as shown in Fig. 1.

4. Conclusions

The shape-controlled magnetite nanoparticles have been successfully prepared via a convenient co-precipitation method. TEM showed that the morphology of magnetite nanoparticles changed from nanospheres to nanoneedles and to nanocubes by varying the amount of SDS. The obtained Fe_3O_4 nanoparticles displayed the perfect regular nanostructure with monodispersion and a narrow distribution in particle size. And the particle size of Fe_3O_4 samples increased with the increase in the visible light irradiation time. From the XRD patterns and FTIR spectra, all shapes of magnetite nanoparticles are pure Fe_3O_4 phase. The Fe_3O_4 nanoparticles exhibited the attractive magnetic properties with high saturation magnetization from the magnetic hysteresis loops. The magnetite nanospheres obtained at the visible light irradiation time of 30 min without SDS are superparamagnetic at room temperature on account of the particle size of about 15 nm, which could be a potential material for the application in biomedicine.

Acknowledgments

The authors are grateful for the supports from the Scientific and Technological Innovation Programs of Higher Education Institutions in Shanxi, China (No. 20121017), the National Natural Science Foundation of China (Nos. 21073113 and 51072105), and the Natural Science Foundation for Young Scientists of Shanxi Province, China (No. 2012021020-5).

References

- [1] B.Y. Geng, J.Z. Ma, J.H. You, Controllable synthesis of single-crystalline Fe_3O_4 polyhedra possessing the active basal facets, *Crystal Growth and Design* 8 (2008) 1443–1447.
- [2] L. Cabrera, S. Gutierrez, N. Menendez, M.P. Morales, P. Herrasti, Magnetite nanoparticles: electrochemical synthesis and characterization, *Electrochimica Acta* 53 (2008) 3436–3441.
- [3] W. Wu, Q.G. He, C.Z. Jiang, Magnetic iron oxide nanoparticles: synthesis and surface functionalization strategies, *Nanoscale Research Letters* 3 (2008) 397–415.
- [4] F.H. Chen, L.M. Zhang, Q.T. Chen, Y. Zhang, Z.J. Zhang, Synthesis of a novel magnetic drug delivery system composed of doxorubicin-conjugated Fe_3O_4 nanoparticle cores and a PEG-functionalized porous silica shell, *Chemical Communications* 46 (2010) 8633–8635.
- [5] Y. Chen, H.Y. Chen, D.P. Zeng, Y.B. Tian, F. Chen, J.W. Feng, J.L. Shi, Core/shell structured hollow mesoporous nanocapsules: a potential platform for simultaneous cell imaging and anticancer drug delivery, *ACS Nano* 4 (2010) 6001–6013.
- [6] F.Y. Cheng, C.H. Su, Y.S. Yang, C.S. Yeh, C.Y. Tsai, C.L. Wu, M. T. Wu, D.B. Shieh, Characterization of aqueous dispersions of Fe_3O_4 nanoparticles and their biomedical applications, *Biomaterials* 26 (2005) 729–738.
- [7] S.K. Giri, N.N. Das, G.C. Pradhan, Synthesis and characterization of magnetite nanoparticles using waste iron ore tailings for adsorptive removal of dyes from aqueous solution, *Colloids and Surfaces A: Physicochemical and Engineering Aspects* 389 (2011) 43–49.
- [8] H. Karami, Heavy metal removal from water by magnetite nanorods, *Chemical Engineering Journal* 219 (2013) 209–216.
- [9] J. Kong, J.R. Liu, F.L. Wang, L.Q. Luan, M. Itoh, K. Machida, Electromagnetic wave absorption properties of Fe_3O_4 cubic nanocrystallines in gigahertz range, *Applied Physics A: Materials Science and Processing* 105 (2011) 351–354.
- [10] L.Z. Shen, Y.S. Qiao, Y. Guo, J.R. Tan, Preparation of nanometer-sized black iron oxide pigment by recycling of blast furnace flue dust, *Journal of Hazardous Materials* 177 (2010) 495–500.
- [11] H.W. Wang, H.C. Liu, Y.C. Yeh, Synthesis of Fe_3O_4 nanowire arrays via precipitation in templates and microwave hydrothermal process, *International Journal of Applied Ceramic Technology* 7 (2010) E33–E38.
- [12] A.S. Teja, P.Y. Koh, Synthesis, properties and applications of magnetic iron oxide nanoparticles, *Progress in Crystal Growth and Characterization of Materials* 55 (2009) 22–45.
- [13] M. Abbas, M. Takahashi, C. Kim, Facile sonochemical synthesis of high-moment magnetite (Fe_3O_4) nanocube, *Journal of Nanoparticle Research* 15 (2013) 1354–1365.
- [14] Y. Lee, J. Lee, C. Bae, J. Park, H. Noh, J. Park, T. Hyeon, Large-scale synthesis of uniform and crystalline magnetite nanoparticles using reverse micelles as nanoreactors under reflux conditions, *Advanced Functional Materials* 15 (2005) 503–509.
- [15] T. Togashi, M. Umetsu, T. Naka, S. Ohara, Y. Hatakeyama, T. Adschiri, One-pot hydrothermal synthesis of an assembly of magnetite nanoneedles on a scaffold of cyclic-diphenylalanine nanorods, *Journal of Nanoparticle Research* 13 (2011) 3991–3999.
- [16] M.M. Rashad, H.M. El-Sayed, M. Rasly, M.I. Nasr, Induction heating studies of magnetite nanospheres synthesized at room temperature for magnetic hyperthermia, *Journal of Magnetism and Magnetic Materials* 324 (2012) 4019–4023.
- [17] G.H. Gao, X.H. Liu, R.R. Shi, K.C. Zhou, Y.G. Shi, R.Z. Ma, T.E. Takayama, G.Z. Qiu, Shape-controlled synthesis and magnetic properties of monodisperse Fe_3O_4 nanocubes, *Crystal Growth and Design* 10 (2010) 2888–2894.
- [18] G.H. Gao, R.R. Shi, W.Q. Qin, Y.G. Shi, G.F. Xu, G.Z. Qiu, X.H. Liu, Solvothermal synthesis and characterization of size-controlled monodisperse Fe_3O_4 nanoparticles, *Journal of Materials Science* 45 (2010) 3483–3489.
- [19] Y.F. Zhu, W.R. Zhao, H.R. Chen, J.L. Shi, A simple one-pot self-assembly route to nanoporous and monodispersed Fe_3O_4 particles with oriented attachment structure and magnetic property, *Journal of Physical Chemistry C* 111 (2007) 5281–5285.
- [20] K. Petcharoen, A. Sirivat, Synthesis and characterization of magnetite nanoparticles via the chemical co-precipitation method, *Materials Science and Engineering B: Advanced Functional Solid-State Materials* 177 (2012) 421–427.
- [21] X. Zhou, Y.F. Shi, L. Ren, S.X. Bao, Y. Han, S.C. Wu, H.G. Zhang, L.B. Zhong, Q.Q. Zhang, Controllable synthesis, magnetic and biocompatible properties of Fe_3O_4 and $\alpha\text{-Fe}_2\text{O}_3$ nanocrystals, *Journal of Solid State Chemistry* 196 (2012) 138–144.
- [22] Y.Y. Zheng, X.B. Wang, L. Shang, C.R. Li, C. Cui, W.J. Dong, W.H. Tang, B.Y. Chen, Fabrication of shape controlled Fe_3O_4 nanostructure, *Materials Characterization* 61 (2010) 489–492.
- [23] K. Aslam, Preparation and characterization of magnetic nanoparticles embedded in microgels, *Materials Letters* 62 (2008) 898–902.
- [24] R.M. Cornell, U. Schwertmann, *The Iron Oxides*, second ed., Wiley-VCH Verlag GmbH & Co., KGaA, Weinheim, 2003.
- [25] M. Ma, Y. Zhang, W. Yu, H.Y. Shen, H.Q. Zhang, N. Gu, Preparation and characterization of magnetite nanoparticles coated by amino silane, *Colloids and Surfaces A: Physicochemical and Engineering Aspects* 212 (2003) 219–226.
- [26] D.E. Zhang, X.J. Zhang, X.M. Ni, J.M. Song, H.G. Zheng, Fabrication and characterization of Fe_3O_4 octahedrons via an EDTA-assisted route, *Crystal Growth and Design* 7 (2007) 2117–2119.
- [27] K.Y. Yoon, C. Kotsmar, D.R. Ingram, C. Huh, S.L. Bryant, T.E. Milner, K.P. Johnston, Stabilization of superparamagnetic iron oxide nanoclusters in concentrated brine with cross-linked polymer shells, *Langmuir* 27 (2011) 10962–10969.
- [28] M. Rajendran, R.C. Pullar, A.K. Bhattacharya, D. Das, S.N. Chintalapudi, C.K. Majumdar, Magnetic properties of nanocrystalline CoFe_2O_4 powders prepared at room temperature: variation with crystalline size, *Journal of Magnetism and Magnetic Materials* 232 (2001) 71–83.
- [29] S. Roy, I. Dubenko, D.D. Edorth, N. Ali, Size induced variations in structural and magnetic properties of double exchange $\text{La}_{0.8}\text{Sr}_{0.2}\text{MnO}_{3-\delta}$ nano-ferromagnet, *Journal of Applied Physics* 96 (2004) 1202–1208.
- [30] R.P. Patil, P.P. Hankare, K.M. Garadkar, R. Sasikala, Effect of sintering temperature on structural, magnetic properties of lithium chromium ferrite, *Journal of Alloys and Compounds* 523 (2012) 66–71.
- [31] S.R. Dave, X. Gao, Monodisperse magnetic nanoparticles for biodetection, imaging, and drug delivery: a versatile and evolving technology, *Wiley Interdisciplinary Reviews: Nanomedicine and Nanobiotechnology* 1 (2009) 583–609.
- [32] J.Y. Jing, Y. Zhang, J.Y. Liang, Q.B. Zhang, E. Bryant, C. Avendano, V.L. Colvin, Y.D. Wang, W.Y. Li, W.W. Yu, One-step reverse precipitation synthesis of water-dispersible superparamagnetic magnetite nanoparticles, *Journal of Nanoparticle Research* 14 (2012) 827–834.

Solventless thermal decomposition of ferrocene as a new approach for one-step synthesis of magnetite nanocubes and nanospheres

Daniel Amara, Judith Grinblat and Shlomo Margel*

Received 13th August 2011, Accepted 31st October 2011

DOI: 10.1039/c1jm13942h

Magnetite (Fe_3O_4) nanocubes and nanospheres were synthesized by solventless thermal decomposition of various mixtures of ferrocene and polyvinylpyrrolidone (PVP). Magnetite nanocubes were prepared by grinding and mixing solid mixtures of ferrocene and PVP. The mixtures were then annealed at 350 °C for 2 h in a sealed cell. The nanocubes' size was controlled by adjusting the [ferrocene]/[PVP] weight ratio. Increasing the annealing time to 4 h when the [ferrocene]/[PVP] weight ratio was 1 : 5 led to the formation of magnetite nanospheres. The formed nanocubes/spheres exhibit ferromagnetic behavior at room temperature. The magnetite nanocubes/spheres were formed by a CVD reaction through which the ferrocene molecules, which are in the gas phase at the reaction conditions, decomposed to magnetite nanocubes/spheres dispersed in the solid PVP matrix. The described method offers a new simple, single-step process for the preparation of magnetite nanocubes/spheres. This approach will be extended in future work for one-step synthesis of other metal oxide nanocubes/spheres, *e.g.*, ZnO, Bi_2O_3 , *etc.*

Introduction

Magnetic nanoparticles have been intensively studied in recent years due to their unique chemical and physical properties, which differ significantly from those of the bulk materials. This led to a broad range of applications such as hyperthermia,^{1,2} information storage media,^{3,4} magnetic resonance imaging (MRI),⁵ biomedical applications,⁶ and catalysis.⁷ The shape, size and size distribution of the magnetic materials are the key factors that determine their chemical and physical properties. Thus, the development of size- and shape-controlled magnetic materials became very important for end use. Iron and its oxides are the most useful among the ferromagnetic and the ferrimagnetic elements; Fe has the highest magnetic moment at room temperature, and a Curie temperature that is sufficiently high for the vast majority of practical applications. In addition, iron is a widespread element, and therefore significantly cheaper than other ferromagnetic elements such as nickel and cobalt.⁸ Iron oxides such as magnetite (Fe_3O_4) and maghemite ($\gamma\text{-Fe}_2\text{O}_3$) are considered as being biocompatible and non-toxic, and therefore possess a broad range of potential biomedical applications.^{9–11} Magnetic nanoparticles tend to aggregate due to a strong magnetic dipole–dipole and van der Waals attraction. Thus, the main challenge in the synthesis process is to overcome these aggregation phenomena. This is usually done by coating the nanoparticle's surface with the desired functional polymers or

surfactants. The surfactant also plays a role in the nucleation process and in limiting particle growth. The functional groups belonging to the organic coating also allow the binding of biological molecules, such as proteins, oligonucleotides, *etc.*, to the particle's surface for biomedical applications.¹² Iron and iron-oxide nanoparticles are typically prepared by the decomposition of soluble iron precursors in solutions containing an appropriate stabilizer. The decomposition of the iron precursors is accomplished by means of processes such as sonochemistry,^{7,13,14} thermal decomposition,¹⁵ electrochemical¹⁶ and laser decomposition.¹⁷ Among the iron precursors, iron carbonyl compounds are the most useful ones, since they can easily decompose and release CO molecules, which can easily be removed from the reaction mixture. Recently, we published a novel method for the preparation of superparamagnetic and ferromagnetic iron oxide and Fe nanoparticles by the thermal decomposition of triiron dodecacarbonyl in diethylene glycol diethyl ether with oleic acid as a stabilizer.^{18,19} Han *et al.* recently published a novel method to synthesize highly magnetized iron nanoparticles by a solventless thermal decomposition method of iron oleate at 400 °C.²⁰ The formed iron oxide nanoparticles were then solventless reduced into $\alpha\text{-Fe}$ nanoparticles by hydrogen in the presence of sodium chloride as a separating medium. Ferrocene, $\text{Fe}(\text{C}_5\text{H}_5)_2$, is an organometallic sandwich compound consisting of two cyclopentadienyl rings bound to opposite sides of an iron atom. It is an air-stable orange solid that readily sublimates.²¹ Recently, we published a novel method for the synthesis of porous superparamagnetic and ferromagnetic iron oxide composite nano/microspheres of narrow size distribution, by solventless thermal decomposition of ferrocene.²² The nano/microparticles were prepared by entrapping *via* vacuum separating media and then

Institute of Nanotechnology & Advanced Materials, Department of Chemistry, Bar-Ilan University, 52900 Ramat Gan, Israel. E-mail: shlomo.margel@mail.biu.ac.il; amara.daniel@gmail.com; Fax: +972-3-7384053; Tel: +972-3-5318994

ferrocene within porous poly(divinyl benzene) microspheres, followed by thermal decomposition of the entrapped ferrocene and then removing the separating media. The present manuscript describes a novel simple one-step method to prepare magnetite nanocubes and nanospheres. This was accomplished by solventless thermal decomposition under different conditions of ferrocene in the presence of PVP. Characterization of the formed nanocubes/spheres was accomplished by routine methods such as TEM, elemental analysis, XRD, SQUID, TGA, and DSC.

Experimental section

Materials

Ferrocene (>98%), polyvinylpyrrolidone (PVP, M_w 360 000) and ethanol (HPLC) were purchased from Aldrich (Israel) and were used without further purification.

Synthesis of magnetic nanocubes and nanospheres

Fe_3O_4 nanocubes were formed by grinding mixtures of ferrocene and PVP of various weight ratios (1 : 1, 1 : 2 and 1 : 5). 300 mg of the solid mixtures were then introduced into a 1 ml stainless steel sealed cell. The solid mixtures were then introduced into a tube furnace preheated to 350 °C for 2 h in ambient atmosphere. The sealed cell was then cooled to room temperature and the resulting black powder was collected. The obtained magnetite nanocubes were then washed from excess reagents by extensive centrifugation cycles with ethanol. Fe_3O_4 nanospheres were obtained by a similar solventless process by increasing the annealing time to 4 h at a [PVP]/[ferrocene] weight ratio of 5 : 1.

Characterization of the magnetic nanocubes and nanospheres

Transmission Electron Microscope (TEM) images were obtained by employing a 200 kV JEOL-2100 device. The average size and size distribution of the magnetite nanocubes and nanospheres of the electronic images were determined by measuring the diagonal length or diameter, respectively, of more than 100 cubes per spheres with Image Analysis software, ANALYSIS Auto (Soft Imaging System GmbH, Germany). C, H and O analysis of the various nanocubes/spheres was performed using an elemental analysis instrument, model FlashEA1112 Instruments, Thermoquast. Powder X-ray diffraction (XRD) patterns were recorded using an X-ray diffractometer (model D8 Advance, Bruker AXS) with Cu $K\alpha$ radiation. Isothermal magnetization measurements at room temperature were performed in a commercial (Quantum Design) super-conducting quantum interference device (SQUID) magnetometer. Mössbauer studies were performed using a conventional constant acceleration drive and a 50 mCi ^{57}Co :Rh source. The velocity calibration was performed using a room temperature α -Fe absorber, and the isomer shift (I.S.) values are relative to that of iron. The observed spectra were least-square fitted by theoretical spectra, assuming a distribution of hyperfine interaction parameters, corresponding to non-equivalent iron locations differing in local environment. Fourier transform infrared (FTIR) analysis was performed with a Bruker FT-IR Spectrometer model ALPHA-P. The analysis was performed with 13 mm KBr pellets that contained 2 mg of the detected material and 198 mg of KBr. The thermal behavior

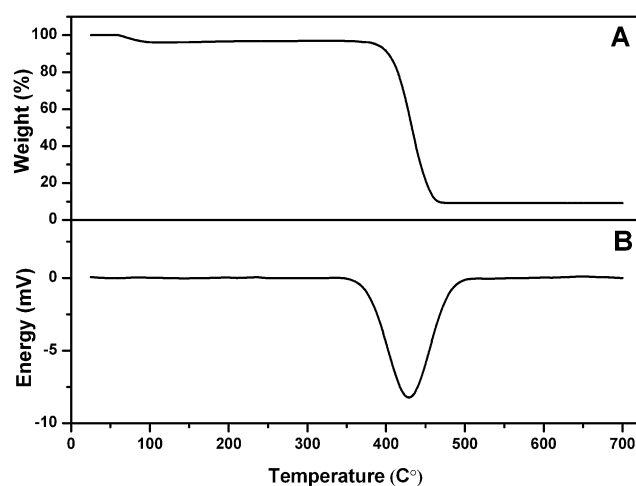


Fig. 1 TGA (A) and DSC (B) thermograms of the PVP.

of the PVP was measured by Thermo Gravimetric Analysis (TGA) and Differential Scanning Calorimetry (DSC), STAR-1 System, Mettler Toledo. The thermal analysis was performed under ambient atmosphere at a heating rate of 5 °C min⁻¹.

Results and discussion

Magnetic nanocubes/spheres were formed by solventless thermal decomposition of ferrocene at 350 °C within a sealed cell in the presence of PVP. The PVP was used as a separating medium and stabilizer of the formed iron-oxide nanocubes/spheres. Fig. 1A and B show the thermal behaviour of the PVP. The TGA curve (A) exhibits a steep slope between 400 and 450 °C, indicating a 91% weight loss due to PVP decomposition, leaving residual

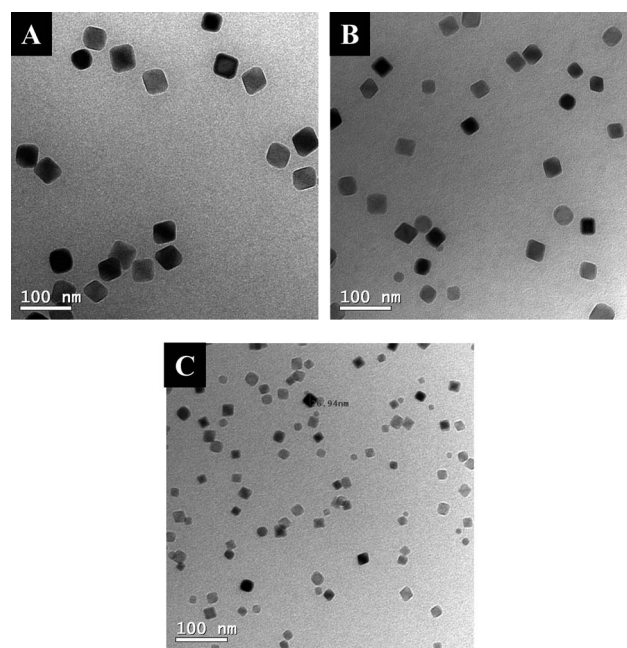


Fig. 2 TEM micrographs of the iron oxide nanocubes obtained by thermal decomposition at 350 °C for 2 h of solid mixtures of ferrocene and PVP of weight ratios of 1 : 1 (A), 1 : 2 (B) and 1 : 5 (C).

Table 1 Elemental analysis, size and size distribution of the nanocubes/spheres obtained by annealing different ratios of ferrocene and PVP mixtures for different time periods^a

[Ferrocene]/ [PVP] (w/w)	Annealing time (h)	Size (nm)	Mass%					[Fe ₃ O ₄]/ [Fe ₃ O ₄ + PVP]
			C	O	N	Fe		
1 : 1	2	49 ± 4.0	31.1	21.6	6.5	37	51	
1 : 2	2	41 ± 5.2	46.5	18.4	8.9	20.3	28	
1 : 5	2	29 ± 3.4	54.2	17.4	10.6	11.5	—	
1 : 5	4	32 ± 5.4	57	16.1	11	8.8	12.1	

^a The magnetite nanocubes/spheres were prepared according to the Experimental part. The size of the nanocubes and the nanospheres relates to the diagonal length of the cubes and the diameter of the spheres, respectively. The Fe amount was calculated by reducing the sum of the other elements from 100.

carbon. This observation is in good agreement with the DSC curve (B) that exhibits an endothermic peak around 430 °C, related to the decomposition of the polymer. TGA isothermal measurements at 350 °C for 2 h at ambient atmosphere also did not exhibit any significant weight loss of the PVP. These thermogravimetric studies demonstrate the durability of the PVP at the annealing temperature of 350 °C at which the ferrocene decomposed to give magnetic iron oxide nanocubes/spheres. TEM images of nanocubes obtained by thermal decomposition at 350 °C for 2 h of solid mixtures of ferrocene and PVP of weight ratios of 1 : 1, 1 : 2 and 1 : 5 are presented in Fig. 2A–C, respectively. The images demonstrate the cubic morphology of the obtained nano-iron oxides. Moreover, the images clearly

demonstrate that the size of the nanocubes depends directly on the [ferrocene]/[PVP] weight ratio. The nanocubes' size, as measured by the diagonal length of the cubes, decreased from 49 ± 4 to 41 ± 5.2 and 29 ± 3.4 nm as the [ferrocene]/[PVP] weight ratio decreased from 1 : 1 to 1 : 2 and 1 : 5, respectively (see Table 1 and Fig. 3). It should be noted that the ferrocene has a boiling point of 249 °C and the various nanocubes were formed at 350 °C. Thus, the decomposition of the ferrocene was accomplished in the gas phase, resulting in the formation of the nanocubes in the PVP domain that is stable at this temperature, as confirmed by thermogravimetric measurements (Fig. 1). This process is actually a chemical vapor deposition (CVD) reaction in which the ferrocene is the volatile precursor and the PVP is the solid substrate. Moreover, the TEM images clearly demonstrate individual nanocubes for the various samples. This may suggest that the solid PVP matrix is used in this process as a separating medium during the decomposition of the ferrocene to form the iron oxide nanocubes. It is remarkable that the decomposition temperature of ferrocene is above 450 °C, and annealing the ferrocene at 350 °C for 2 h in a sealed cell in the absence of PVP did not lead to the decomposition of the organometallic compounds. However, the thermal decomposition of ferrocene in the presence of PVP leads to its decomposition to iron-oxide nanocubes/spheres. This may imply that the PVP catalyzes the thermal decomposition of the ferrocene. Fig. 4A and B show by low and high magnification TEM pictures the perfect spherical shape of the nanospheres of 32 ± 5.4 nm obtained by annealing the solid mixture of ferrocene and PVP of a 1 : 5 weight ratio for 4 h. On the other hand, to our surprise, annealing of the other solid mixtures of the ferrocene and PVP of 1 : 1 and 1 : 2 weight

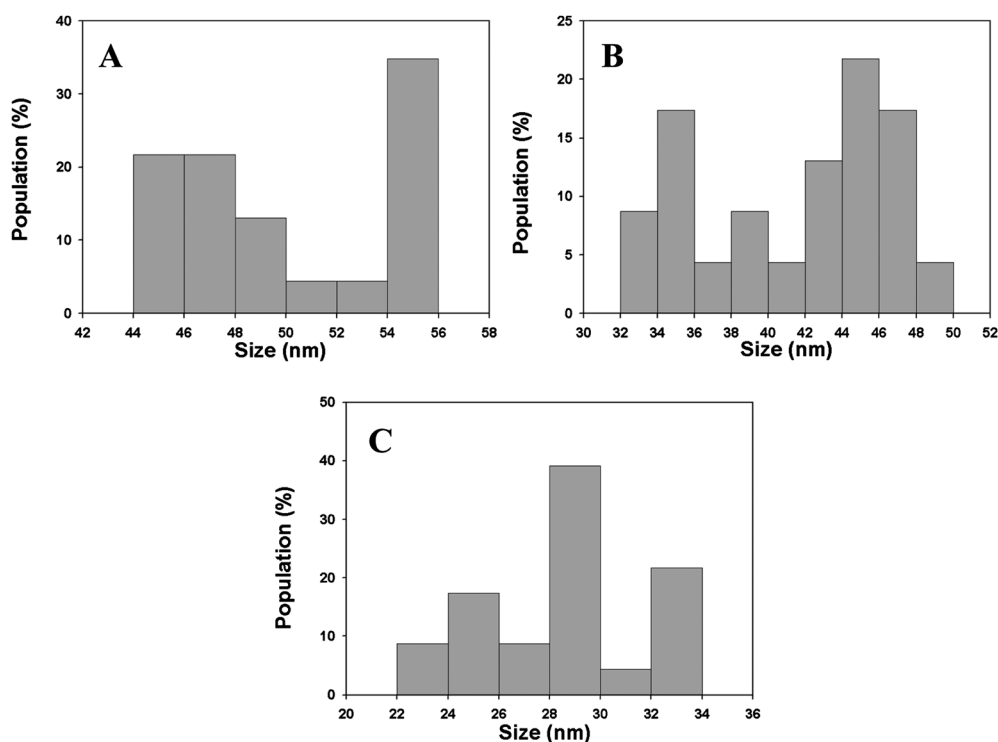


Fig. 3 Size distribution of the nanocubes obtained by thermal decomposition at 350 °C for 2 h of solid mixtures of ferrocene and PVP of weight ratios of 1 : 1 (A), 1 : 2 (B) and 1 : 5 (C).

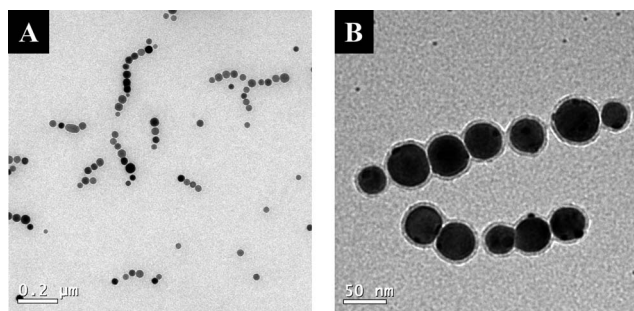


Fig. 4 Low (A) and high (B) magnification TEM micrographs of the iron oxide nanospheres obtained by thermal decomposition at 350 °C for 4 h of a solid mixture of ferrocene and PVP of a weight ratio of 1 : 5.

ratios for 4 h did not alter their cubic shape to spheres. Fig. 4B demonstrates a core–shell architecture of the iron oxide spherical particles. The core is composed of the iron-oxide phase, while the shell is composed of the PVP. Fig. 5A–D illustrate the XRD patterns of the iron nanocubes/spheres obtained by thermal decomposition at 350 °C for 2 or 4 h of solid mixtures of ferrocene and PVP of weight ratios of 1 : 1 (A), 1 : 2 (B) and 1 : 5 (C and D). The nanocubes (A, B, and C) were formed by the thermal decomposition of the ferrocene for 2 h, and for 4 h for the nanospheres (D). Fig. 5 A, B and D demonstrate well the crystallized iron-oxide phases of the nanocubes/spheres. On the other hand, Fig. 5C demonstrates an iron-oxide phase which is not well crystallized. In addition, this pattern demonstrates the presence of a small impurity fraction of FeO. All the XRD patterns can be attributed either to magnetite (Fe_3O_4) or to maghemite ($\gamma\text{-Fe}_2\text{O}_3$), because of the similarity in their XRD patterns. Thus, Mössbauer spectroscopy (MS) at RT was employed and showed that this fraction was indeed composed of the Fe_3O_4 phase, as described below. Thus, all the XRD patterns were indexed as magnetite. Table 1 demonstrates the mass% of C, H, O, N and Fe, as well as the size and size distribution of the

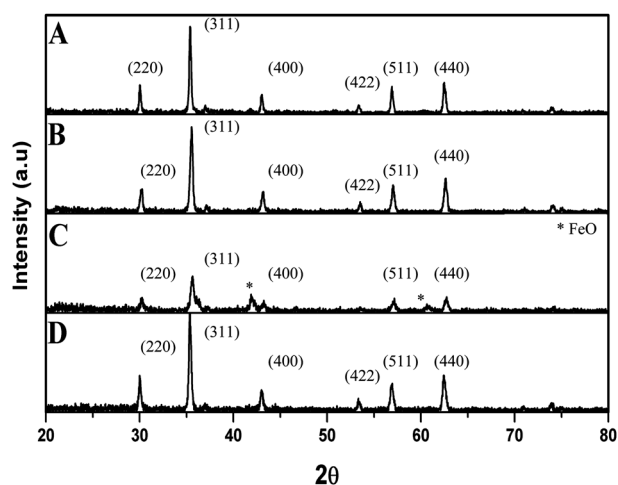


Fig. 5 XRD patterns of the magnetite nanocubes/spheres obtained by thermal decomposition at 350 °C for 2 or 4 h of solid mixtures of ferrocene and PVP of weight ratios of 1 : 1 (A), 1 : 2 (B) and 1 : 5 (C and D). The nanocubes (A, B and C) were formed by thermal decomposition of the ferrocene for 2 h, and the nanospheres (D) for 4 h, according to the Experimental part.

different nanocubes/spheres. A simple calculation indicates that the weight ratio of $[\text{Fe}]/[\text{O}]$ in magnetite is 2.62/1. Thus, the % magnetite content of the nanocubes obtained by the thermal decomposition at 350 °C for 2 h of solid mixtures of ferrocene and PVP of weight ratios of 1 : 1 and 1 : 2 and of the nanospheres obtained by thermal decomposition at 350 °C for 4 h of a solid mixture of ferrocene and PVP of a weight ratio of 1 : 5 are 51, 28 and 12.1%, respectively. Table 1 also exhibits that the $[\text{C}] : [\text{H}] : [\text{N}] : [\text{O}]$ (oxygen belonging to the PVP only) weight ratios of these nanocubes/spheres are 8.2 : 1.0 : 1.7 : 2.0, 7.9 : 1.0 : 1.5 : 1.8 and 8.0 : 1.0 : 1.5 : 1.8, respectively. These ratios are almost the same as those calculated for pure PVP ($\text{C}_6\text{H}_9\text{NO}$). The % magnetite content of the nanocubes obtained by the thermal decomposition for 2 h of solid mixtures of ferrocene and PVP of a weight ratio of 1 : 5 cannot be calculated due to the presence of small FeO phase impurity as shown previously by the XRD measurements. It should be noted that the mixtures obtained after decomposition of the various ferrocene/PVP mixtures, before ethanol washing, did not indicate the presence of ferrocene traces, as verified by FTIR spectra (by the absence of the ferrocene peaks for example at 3922, 2253, 1776 cm^{-1} , etc.). The yield of the ferrocene decomposition to iron oxide was almost 100% whereas excess PVP was removed by ethanol washing. Thus, the $[\text{PVP}] : [\text{Fe}]$ weight ratios are lower than their original ratios in the reagents as shown in Table 1. Fig. 6A–D exhibit the RT MS spectra of the nanocubes/spheres obtained by thermal decomposition at 350 °C for 2 and 4 h of solid mixtures of ferrocene and PVP of weight ratios of 1 : 1, 1 : 2, and 1 : 5, and for the nanospheres obtained by thermal decomposition at 350 °C for 4 h of a solid mixture of ferrocene and PVP of a weight ratio of 1 : 5, respectively. All the samples exhibit two magnetic sextets with I.S. = 0.29 and 0.69 mm s^{-1} and $H_{\text{eff}} = 490 \pm 5$ and 460 ± 5 kOe, respectively, which are related to the two crystallographic sites of magnetite. However, the particles obtained by thermal decomposition at 350 °C for 2 h of ferrocene and PVP with a weight ratio of 1 : 5 for 2 h contain 31% of small particles above the blocking temperature. The effect of the PVP concentration and reaction time on the particles size can be explained as follows: previous studies have demonstrated by FT-IR spectrometry that PVP molecules may coordinate with metal ions to form a stable metal–PVP complex.^{23,24} The PVP used in this study probably influences the nucleation, growth and aggregation of the obtained magnetite crystallites, by forming iron–PVP complex molecules. This complex formation may explain the effect of PVP concentration on the size and morphology of the formed magnetite nanocubes/spheres. The generation of this complex inevitably increases the time for iron atoms to reach supersaturation and to their final size. This means that the growth rate of the magnetite crystallites will decrease as their faces adsorbed PVP molecules, because the crystal growth rate is generally lowered with adsorbed polymer.²⁵ Moreover, the number of ‘free sites’ on the PVP surface that can serve as binding sites to form the iron–PVP complex increases with increasing the PVP concentration, thereby resulting in nanocubes/spheres of decreasing size. The PVP concentration and the annealing time are also probably the key factors in explaining the shape alteration of the magnetite crystallites, by effecting crystal growth in different directions. It is known that the crystal growth rate generally decreases with the adsorbed polymer, and crystallite morphology can be altered by the presence of polymer specifically

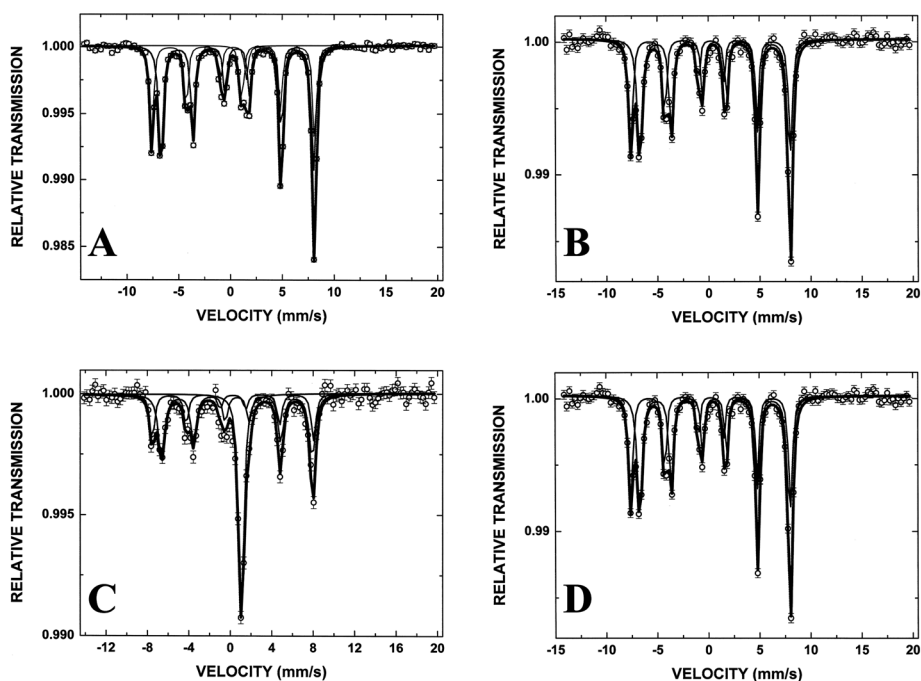


Fig. 6 Mössbauer spectra at room temperature of the magnetite nanocubes/spheres obtained by thermal decomposition at 350 °C for 2 or 4 h of solid mixtures of ferrocene and PVP of weight ratios of 1 : 1 (A), 1 : 2 (B) and 1 : 5 (C and D). The nanocubes (A, B and C) were formed by thermal decomposition of the ferrocene for 2 h and 4 h for the nanospheres (D), according to the Experimental part.

interacting with the crystal faces.²⁶ Magnetite was formed as cubes when the growth in some direction was restricted by the adsorbed PVP molecules, while one direction was free to allow growth. This led to the formation of nanocubes. In contrast, magnetite nanospheres were formed when the annealing time increased, allowing the growth of the crystallites in different directions. Previous studies reported that a shift of carbonyl band was observed in the IR spectra of PVP in the presence of various metal ions. According to these previous studies this band shift is due to the interaction between the carbonyl oxygen of PVP and the metal ions.^{27–29} Indeed, a pure PVP spectrum demonstrates a C=O band at 1650 cm^{-1} (Fig. 7A) while the various nanocubes/spheres demonstrated this carbonyl peak at 1644 cm^{-1} , a shift of 6 cm^{-1} (Fig. 7B). Please note that Fig. 7B illustrates the carbonyl PVP peak of the magnetite nanocubes obtained by thermal decomposition at

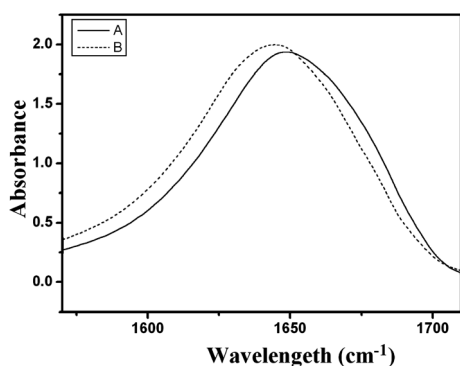


Fig. 7 FT-IR spectra of the carbonyl peaks of pure PVP(A) and of the magnetite nanocubes obtained by thermal decomposition at 350 °C for 2 h of a solid mixture of ferrocene and PVP of a weight ratio of 1 : 5.

350 °C for 2 h of a solid mixture of ferrocene and PVP of a weight ratio of 1 : 5. However, the same carbonyl peak was also observed for the other nanocubes/spheres.

The carbonyl peak shift in the nanocube/sphere samples probably implies the formation of the Fe-PVP complex which directly relates to the previously suggested mechanism. Fig. 8 represents the isothermal field dependent on or independent of the magnetization measured at 300 K. The hysteresis loops for the magnetite nanocubes/spheres are presented in curves A–D.

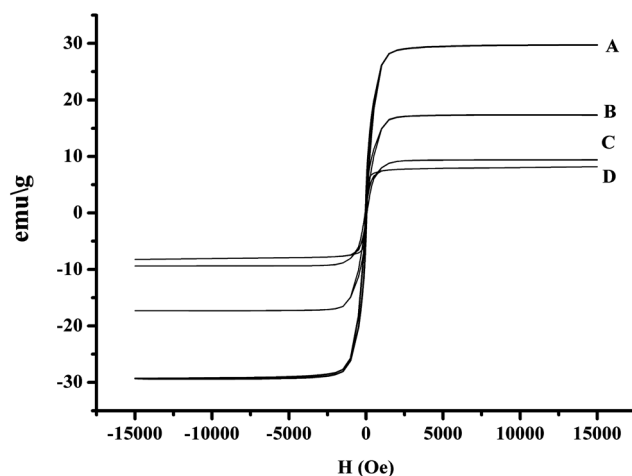


Fig. 8 Magnetization (M) vs. magnetic field (H) at 300 K of the magnetite nanocubes/spheres obtained by thermal decomposition at 350 °C for 2 or 4 h of solid mixtures of ferrocene and PVP of weight ratios of 1 : 1 (A), 1 : 2 (B) and 1 : 5 (C and D). The nanocubes (A, B and C) were formed by thermal decomposition of the ferrocene for 2 h, and 4 h for the nanospheres (D), according to the Experimental part.

Table 2 Magnetic properties of the nanocubes/spheres obtained by annealing different ratios of ferrocene and PVP mixtures for different time periods^a

[Ferrocene]/ [PVP] (w/w)	Annealing time (h)	M_s (emu g ⁻¹)	Coercivity (Oe)
1 : 1	2	29.7	50
1 : 2	2	17.3	40
1 : 5	2	9.4	36
1 : 5	4	8.2	15

^a The magnetite nanocubes/spheres were prepared according to the Experimental part. The size of the nanocubes and the nanospheres relates to the diagonal length of the cubes and the diameter of the spheres, respectively.

The magnetic saturation moments (M_s), as well as the coercive fields of these particles, are shown in Fig. 8 and summarized in Table 2. The M_s values obtained at 300 K are 29.7, 17.3 and 9.4 emu g⁻¹, for the magnetite nanocubes obtained by the thermal decomposition of mixtures of ferrocene and PVP of 1 : 1, 1 : 2 and 1 : 5 weight ratios, respectively, and 8.2 emu g⁻¹ for the magnetite nanospheres. By subtracting the PVP content, the calculated M_s values in terms of emu per g of Fe₃O₄ are 58.2 and 61.7 for the nanocubes obtained by the thermal decomposition of mixtures of ferrocene and PVP of 1 : 1 and 1 : 2, respectively, and 67.8 for the nanospheres (the value for the nanocubes obtained by the thermal decomposition for 2 h of a solid mixture of ferrocene and PVP of a weight ratio of 1 : 5 cannot be calculated due to the presence of FeO impurity). It should be noted that the M_s bulk value of magnetite is 92 emu g⁻¹.³⁰ The relatively lower M_s values of the magnetic nanocubes/spheres compared to the bulk values arise from the non-magnetic PVP content, which leads to the decrease in the magnetization per weight. Another explanation for the relatively low magnetization values is the surface effect that can occur in the case of magnetic core and non-magnetic shell structures. This effect leads to the reduction in the magnetic moment by a different mechanism, *e.g.*, the existence of a magnetically dead layer on the cubes/spheres' surface, the existence of canted spins, or the existence of a spin glass-like behavior of the surface spins.³¹ The merging temperature of the two ZFC/FC branches is defined as the blocking temperature (T_b) of superparamagnetic particles. Fig. 9 shows the FC and ZFC curves of the nanocubes obtained by thermal decomposition at 350 °C for 2 h of a solid mixture of ferrocene and PVP of a weight ratio of 1 : 5. The two curves tend to merge around 210 K (which is taken as T_b), but no complete overlap is observed up to 300 K, indicating the existence of both superparamagnetic and ferromagnetic phases in this material. This observation is in a good agreement with the Mössbauer studies.

The structure of the obtained nanocubes/spheres was also investigated in HRTEM mode using either the conventional selected area electron diffraction (SAED) and nano-beam (NBD) diffraction technique or Fourier Transform Analysis (FFT) of high resolution images, depending on the size and the orientation of the materials. The two possible oxides maghemite (γ -Fe₂O₃) and magnetite (Fe₃O₄) are structurally similar; hence they cannot be distinguished according to their electron diffraction patterns. All our electron diffraction patterns could be indexed in terms of the FCC structure of both maghemite and magnetite, $a = 8.34 \text{ \AA}$

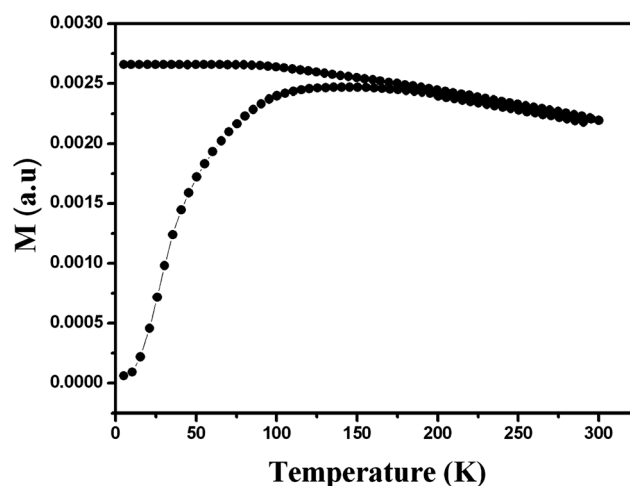


Fig. 9 Zero field cooled (ZFC) and field (FC) cooled temperature dependent magnetization of the nanocubes obtained by thermal decomposition at 350 °C for 2 h of solid mixtures of ferrocene and PVP of a weight ratio of 1 : 5.

and $a = 8.39 \text{ \AA}$ (PDF#000391346 and PDF#010890950), respectively. The Mössbauer spectra results provided the supporting evidence that the resulting compounds are indeed magnetite. Fig. 10A is a high resolution electron micrograph (HRTEM) of a typical single crystalline nanocube obtained by thermal decomposition of a 1 : 1 weight ratio of a ferrocene and PVP mixture. This figure displays lattice-fringe contrast of the d_{022} family of planes (0.3 nm). The nanocube was identified and characterized using the SAED pattern shown in Fig. 10B. This electron diffraction pattern was taken from an area of 300 nm comprising several nanocubes and it shows a typical ring diffraction pattern as expected from polycrystalline materials. The marked reflections correspond to the interplanar spacings, d_{220} , d_{311} and d_{400} in the FCC structure of magnetite Fe₃O₄ $a = 8.39 \text{ \AA}$ and the pattern was indexed as magnetite. Fig. 10C and E are the HRTEM micrographs of individual Fe₃O₄ nanocubes obtained by thermal decomposition of 1 : 2 and 1 : 5 weight ratios of ferrocene and PVP mixtures for 2 h, respectively. Both nanocubes display well resolved lattice-fringe contrast as displayed in the respective figures (Fig. 10C and D) and their identification was based on the analysis of these high resolution images. The inset on the top right in Fig. 10C is the computed Fourier transform of the portion of the image outlined by the white square which, like a diffraction pattern, was indexed on the basis of the unit cell of magnetite. Marked are the d_{022} and d_{113} family of planes. The inset on the bottom right represents the filtered and magnified portion of the image outlined by the square. The distances measured between lattice fringes were 0.3 nm (d_{022}) and 0.25 nm (d_{113}) of the cubic FCC structure of Fe₃O₄ ($a = 8.35 \text{ \AA}$). Fig. 10E shows the lattice fringe d_{113} (0.25 nm) plane of the nanocubes obtained by 1 : 5 weight ratios of ferrocene and PVP for 2 h. Fig. 10D and F are the NBD patterns taken from the nanocubes obtained by thermal decomposition of 1 : 2 and 1 : 5 weight ratios of ferrocene and PVP for 2 h, respectively. All NBD patterns were taken from a nano-area of 4–7 nm of the nanocubes. The NBD pattern (10D) shows sets of reflections for d_{022} planes and $\langle d_{113} \rangle$ family of planes and the

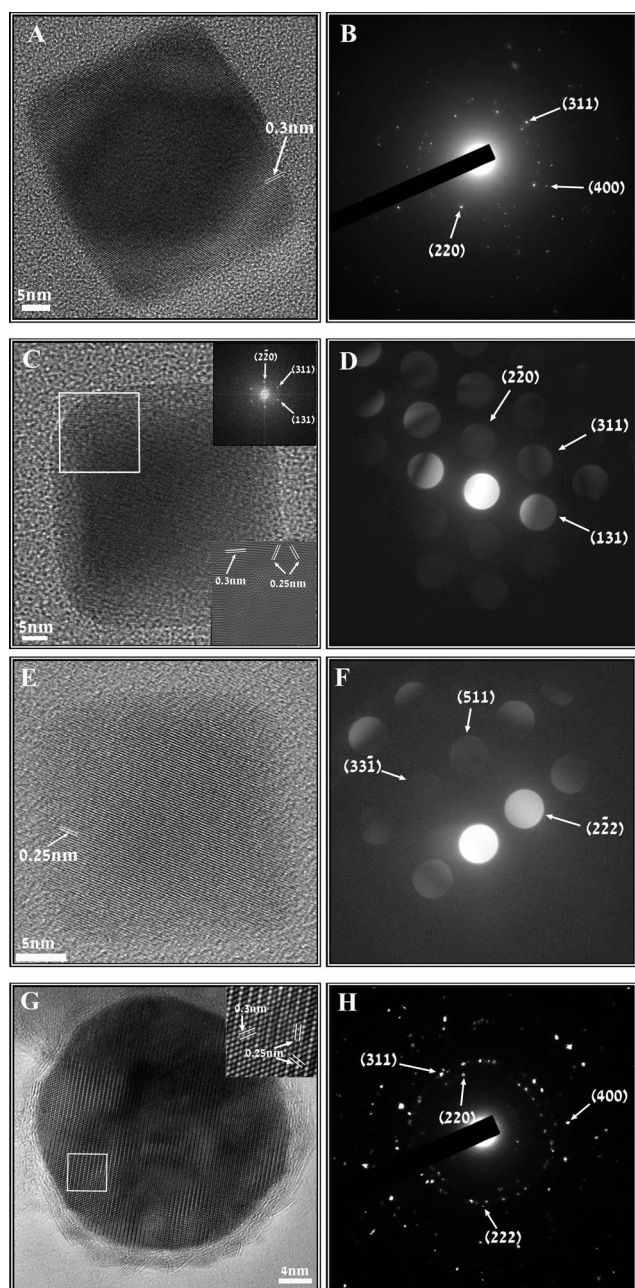


Fig. 10 High resolution electron micrograph of typical magnetite nanocubes/spheres obtained by thermal decomposition at 350 °C for 2 or 4 h of solid mixtures of ferrocene and PVP of weight ratios of 1 : 1 (A), 1 : 2 (C) and 1 : 5 (E and G) and the corresponding ED pattern (B, D, F and H, respectively). The nanocubes (A–F) were formed by thermal decomposition of ferrocene for 2 h, and 4 h for nanospheres (G and H), according to the Experimental part. The inset marked by the white square (C and G) is the magnified image and Fourier transform taken from the area (C).

NBD pattern (10F) shows sets of reflections for d_{222} , d_{133} and d_{115} planes. These patterns were also indexed according to the FCC cubic structure of Fe_3O_4 . Fig. 10G is the HRTEM micrograph of a crystalline Fe_3O_4 nanosphere coated with a thin amorphous layer of PVP. The inset represents the magnified portion of the image outlined by the white square. The distances measured between lattice fringes were 0.24 nm and 0.25 nm matching the

interplanar spacings for d_{222} and d_{113} family of planes, respectively. Fig. 10H is the SAED pattern taken from several nanospheres showing reflections that correspond to the interplanar spacing, d_{220} , d_{311} , d_{222} and d_{400} , and was indexed on the basis of the FCC structure of magnetite. Utilization of these advanced nano-techniques, together with the Mössbauer spectra results, provided unambiguous evidence that the resulting compounds are the FCC structure magnetite with unit cell parameter $a = 8.39 \text{ \AA}$.

Summary and conclusions

This manuscript describes a novel, simple process for the preparation of monodisperse magnetite nanocubes and nanospheres, by a single-step solventless thermal decomposition of ferrocene in the presence of PVP. This work demonstrates that the shape and size of the formed magnetite can be controlled by adjusting the [PVP]/[ferrocene] weight ratio and the ferrocene decomposition reaction time period. This manuscript presents preliminary studies. Further extension of this work is ongoing in our laboratory, in order to better understand the reason for obtaining cubes and the change to a spherical shape. We also plan on extending this work for the one-step synthesis of other metal oxide nanocubes/spheres, e.g., ZnO , Bi_2O_3 , etc.

Acknowledgements

This study was partially supported by a Minerva Grant (Microscale & Nanoscale Particles). Thanks to Prof. Israel Felner from The Racah Institute of Physics, Hebrew University, Jerusalem, Israel, for his help in the Mössbauer spectroscopy measurements.

References

- 1 R. Hergt, R. Hiergeist, I. Hilger, W. A. Kaiser, Y. Lapatnikov, S. Margel and U. Richter, *J. Magn. Magn. Mater.*, 2004, **270**, 345–357.
- 2 J. P. Fortin, C. Wilhelm, J. Servais, C. Menager, J. C. Bacri and F. Gazeau, *J. Am. Chem. Soc.*, 2007, **129**, 2628–2635.
- 3 S. Sun, C. B. Murray, D. Weller, L. Folks and A. Moser, *Science*, 2000, **287**, 1989–1992.
- 4 S. Sun and H. Zeng, *J. Am. Chem. Soc.*, 2002, **124**, 8204–8205.
- 5 M. C. Bautista, O. Bomati-Miguel, X. Zhao, M. P. Morales, T. Gonzalez-Carreno, R. P. Alejo, J. Ruiz-Cabello and S. Veintemillas-Verdaguer, *Nanotechnology*, 2004, **15**, 154–159.
- 6 E. Carpenter, *J. Magn. Magn. Mater.*, 2001, **225**, 17–20.
- 7 S. Suslick, T. Hyeon and M. Fang, *Chem. Mater.*, 1996, **8**, 2172–2179.
- 8 L. H. Dale, *Small*, 2005, **1**, 482–501.
- 9 A. Z. Wang, V. Bagalkot, C. Vasiliou, F. Gu, F. Alexis, L. Zhang, M. Shaikh, K. Yuet, M. Cima, R. Langer, P. W. Kantoff, N. H. Bander, S. Jon and O. C. Farokhzad, *ChemMedChem*, 2008, **3**, 1311–1315.
- 10 C. Stefaniu, M. Chanana, D. Wang, D. V. Novikov, G. Brezesinski and H. Möhwald, *ChemPhysChem*, 2010, **11**, 3585–3588.
- 11 M. Furlan, J. Kluge, M. Mazzotti and M. Lattuada, *J. Supercrit. Fluids*, 2010, **54**, 348–356.
- 12 M. V. Yigit, D. Mazumdar and Y. Lu, *Bioconjugate Chem.*, 2008, **19**, 412–417.
- 13 K. V. Shafi, A. Ulman, X. Yan, N. L. Yang, C. Estournes, H. White and M. Rafailovich, *Langmuir*, 2001, **17**, 5093–5097.
- 14 S. Wizen, S. Margel and A. Gedanken, *Polym. Int.*, 2000, **49**, 445–448.
- 15 J. Lai, K. V. Shafi, A. Ulman, K. Loos, Y. Lee, T. Vogt, W. L. Lee and N. P. Ong, *J. Phys. Chem. B*, 2005, **109**, 15–18.
- 16 D. E. Weisshaar and T. Kuwana, *J. Electroanal. Chem.*, 1984, **163**, 395–399.

- 17 E. Ye, B. Liu and W. Y. Fan, *Chem. Mater.*, 2007, **19**, 3845–3849.
- 18 D. Amara, I. Felner, I. Nowik and S. Margel, *Colloids Surf., A*, 2009, **339**, 106–110.
- 19 W. Yu, J. C. Falkner, C. T. Yavuz and V. L. Colvin, *Chem. Commun.*, 2004, 2306–2307.
- 20 Y. C. Han, H. G. Cha, C. W. Kim, Y. H. Kim and Y. S. Kang, *J. Phys. Chem. C*, 2007, **111**, 6275–6280.
- 21 A. Federman Neto, A. C. Pelegrino and V. A. Darin, Ferrocene: 50 years of transition metal organometallic chemistry—from organic and inorganic to supramolecular chemistry, *ChemInform*, 2004, **35**, DOI: 10.1002/chin.200443242.
- 22 D. Amara and S. J. Margel, *J. Mater. Chem.*, 2011, **21**, 15764–15772.
- 23 Z. T. Zhang, B. Zhao and L. M. Hu, *J. Solid State Chem.*, 1996, **121**, 105–110.
- 24 B. L. Rivas, E. D. Pereira and I. M. Villoslada, *Prog. Polym. Sci.*, 2003, **28**, 173–208.
- 25 P. J. Van der Put, in *The Inorganic Chemistry of Materials: How to Make Things Out of Elements*, Plenum, New York, 1998, p. 278.
- 26 Y. G. Sun and Y. N. Xia, *Science*, 2002, **298**, 2176–2179.
- 27 J. L. Wuepper and A. L. Popov, *J. Am. Chem. Soc.*, 1969, **91**, 4352–4356.
- 28 N. H. Agnew, *J. Polym. Sci., Polym. Chem. Ed.*, 1976, **14**, 2819–2830.
- 29 B. P. Grady, E. M. O'connell, C. Z. Yang and S. L. Cooper, *J. Polym. Sci., Part B: Polym. Phys.*, 1994, **32**, 2357–2366.
- 30 B. D. Cullity, *Introduction to Magnetic Materials*, Addison-Wesley Pub. Co, Reading, Mass, 1972, p. 200.
- 31 R. H. Kodama, *J. Magn. Magn. Mater.*, 1999, **200**, 359–372.



Synthesis, characterization, and photocatalytic application of novel TiO₂ nanoparticles

M. Hussain, R. Ceccarelli, D.L. Marchisio, D. Fino, N. Russo*, F. Geobaldo

Department of Materials Science and Chemical Engineering, Politecnico di Torino, Corso Duca degli Abruzzi 24, 10129 Torino, Italy

ARTICLE INFO

Article history:

Received 17 July 2009

Received in revised form 15 October 2009

Accepted 16 October 2009

Keywords:

TiO₂
Nanoparticles
Sol-gel
Ethylene
Oxidation
Photocatalysis

ABSTRACT

Novel TiO₂ nanoparticles (TNP) having a high specific surface area were successfully synthesized in a vortex reactor by sol-gel process with optimized operating parameters. These 10–20 nm TNP were characterized and compared with TiO₂ synthesized by solution combustion (TSC) method and commercially available TiO₂ (degussa P25 and anatase by Aldrich). Characterization was performed by X-ray diffraction spectroscopy (XRD), specific surface area analysis, energy dispersive X-ray spectroscopy (EDX), scanning electron microscopy (SEM), diffuse reflectance ultraviolet–visible spectroscopy (DR/UV–vis), and Fourier transformed-infrared spectroscopy (FT-IR). TNP showed comparatively smaller size with little porosity between them, good crystalline anatase with small rutile phase, higher BET surface area, confined band gap energy, and higher OH groups. Photocatalytic oxidation of ethylene (a naturally occurring gas produced by plant tissues, engine exhausts, and plant and fungi metabolism) has been investigated at ambient temperature in an ad hoc designed pyrex glass photocatalytic reactor, by using these TNP and compared with TSC, and commercial TiO₂. Higher photocatalytic conversion of ethylene was observed for TNP compared to TSC and commercial TiO₂. Mixed phase of TN with high surface area might induce the adsorption of ethylene pollutant and water with generation of OH groups (oxidizing agent) on the surface of TNP leading to higher photocatalytic activity.

© 2009 Elsevier B.V. All rights reserved.

1. Introduction

The first discovery of the photochemical hydrolysis of water by Fujishima and Honda [1] has opened the field of diverse applications of titania in areas such as photovoltaics [2], self-cleaning coatings [3], photocatalysis [4], and electrochromic display devices [5]. Photocatalysts are solids that can promote reactions in the presence of light without being consumed [6].

TiO₂ is an ideal photocatalyst in several ways. It is relatively cheap, highly stable from a chemical viewpoint, and easily available. Moreover, its photogenerated holes are highly oxidizing, and the photogenerated electrons are reducing enough to produce superoxide from dioxygen. It promotes ambient temperature oxidation of the major classes of indoor air pollutants, and does not need any chemical additives [7–9]. Air pollution is considered worldwide a serious problem. Volatile organic compounds (VOCs) the main part of the air pollution are from the indoor as well as external sources. Conventionally, VOC pollutants are removed by air purifiers that employ filters to remove particulate matters or use sorption materials (e.g. granular activated carbon) to adsorb the pollutants. These techniques only transfer the contaminants to

another phase rather than eliminating them. Hence, additional disposal or handling steps are needed. Photocatalytic oxidation (PCO) of VOCs is a promising alternative technology for air purification. It has been demonstrated that organics can be oxidized to carbon dioxide, water and simple mineral acids at low temperature on TiO₂ catalysts in the presence of UV or near-UV illumination [10–19].

Most of the studies have shown that the photocatalytic activity of titanium dioxide is greatly influenced by the crystalline form, although controversial results are reported in the literature. For example, some authors state that anatase works better than rutile [17,20], others found the best photocatalytic activity for rutile [21–23], and some others detected synergistic effects in the photocatalytic activity for anatase–rutile mixed phases [24–26]. Besides, recently it was demonstrated that photoactivity in organics degradation depends on the phase composition and on the oxidizing agent [27]. Moreover the ability of titanium dioxide particles to degrade organic compounds depends also on the size of the particles, since small particles offer larger specific surface areas [28].

Many processes can be employed for the production of titanium dioxide particles, such as flame aerosol synthesis [29], hydrothermal synthesis [30], and sol-gel synthesis [31]. Flame aerosol synthesis presents the main advantage of being easily scalable to the industrial level, but shows all the disadvantages of high temperature synthesis. Hydrothermal synthesis is instead particularly interesting for it directly produces a crystalline powder, without the

* Corresponding author. Tel.: +39 011 0904710; fax: +39 011 5644699.
E-mail address: nunzio.russo@polito.it (N. Russo).

need of a final calcination step, which is necessary in the sol–gel process. However, the lack of knowledge of the chemical equilibria of the species in solution and of the kinetics of nucleation and growth of the different phases makes it difficult to control the overall process. Therefore, the sol–gel process is at the moment the most common and promising one at a lab scale. Although the sol–gel process has been known almost for a century and some of the most important aspects have been cleared, there exists room for improvement for individuating synthesis conditions that result in a powder with improved properties, when compared with the commercial products available at the moment. Furthermore, up-scaling the process from the laboratory to the industrial scale is still a complex problem of difficult solution. Mixing plays indeed a big role but its effects are usually underestimated, as proven by the qualitative statements (e.g. add drop wise or mix vigorously) generally used to define ideal mixing conditions.

In our previous studies of synthesis of TiO₂ nanoparticles [32,33], we have investigated quantitatively the effect of mixing and other operating parameters. This synthesis study was done on small scale, where the reported results clearly show that mixing plays a key role. The use of adaptable mixing devices, such as the one described, allows tuning the mixing rate in order to obtain the desired particle size and morphology.

In the present work, we particularly focused on the synthesis of novel TiO₂ nanoparticles (TNP) on large scale by controlling the optimized operating conditions and using a special passive mixer, i.e. a vortex reactor (VR). We made an attempt to get TNP with high surface area and mixed crystalline phase with more anatase and small amounts rutile. Because of the mentioned synergistic effect, the mixed phases are expected to be more attractive for gas-phase photocatalytic application of VOC in the presence of oxygen [24]. Ethylene was chosen as a probe reactant for the application of TNP. It is generated by engines; biomass fermentators; pyrolysis of hydrocarbons; fruit ripening; and plants biosynthesis. Besides, it is also the parent compound of more widespread class of VOCs of environmental concern (e.g. trichloroethylene and tetrachloroethylene). Some researchers [10–13] have already focused on the ethylene degradation by catalysts at relatively higher temperature than the ambient temperature. However, in this study we have focused on the use of the synthesized TNP photocatalyst for ethylene degradation at ambient temperature. A new fabricated photocatalytic reaction system with pyrex glass reactor is used. Comparison was accomplished with TiO₂ synthesized by solution combustion method (TSC) or commercial TiO₂. Characterization was performed by X-ray diffraction spectroscopy (XRD), Brunauer–Emmet–Teller (BET) analysis, energy dispersive X-ray spectroscopy (EDX), field emission scanning electron microscopy (FE-SEM), diffuse reflectance ultraviolet–visible spectroscopy (DR/UV–vis), and Fourier transformed-infrared spectroscopy (FT-IR).

2. Experimental

2.1. Synthesis of TiO₂

TNP were synthesized on large scale (2 L gel) by controlling the optimized operating parameters using the VR shown in Fig. 1, and by adopting the small scale (200 mL gel) synthesis procedure [32,33]. Titanium tetra-isopropoxide (TTIP: Sigma–Aldrich) was used as a precursor in this work, because of its very rapid hydrolysis kinetics. Two solutions of TTIP in isopropyl alcohol and of water (Milli-Q) in isopropyl alcohol were prepared separately under nitrogen flux to control the alkoxide reactivity with humidity. Hydrochloric acid (HCl: Sigma–Aldrich) was added to the second solution as a hydrolysis catalyst and deagglomeration agent. TTIP/isopropanol concentration was taken equal to 1 M to

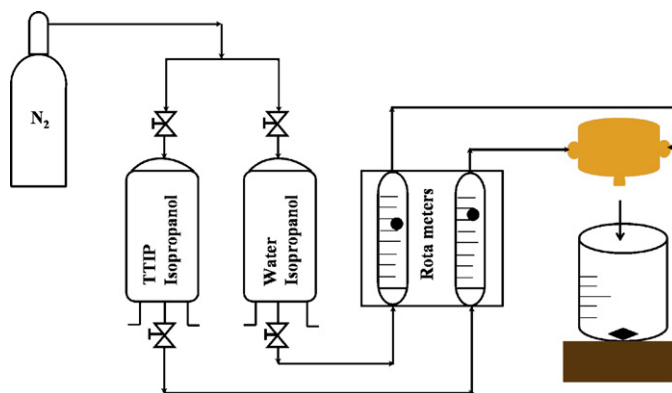
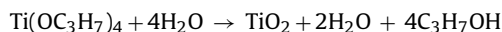


Fig. 1. TNP (sol–gel method) synthesis set-up.

get the maximum TiO₂ (1 M), whereas the water and hydrochloric acid concentrations were chosen in order to result in a water to precursor ratio, $W = [\text{H}_2\text{O}]/[\text{TTIP}]$, equal to four, and acid to precursor ratio, $H = [\text{H}^+]/[\text{TTIP}]$, equal to 0.5. The two solutions of TTIP and water in isopropyl alcohol were stored in two identical vessels, then pressurized at 2 bars with analytical grade nitrogen, and eventually fed and mixed in the VR. The inlet flow rates were kept equal to 100 mL/min by using two rotameters. This inlet flow rate guarantees very fast mixing, thus inducing the formation of very fine particle. Equal volumes of reactant solutions (i.e. 1 L) were mixed at equal flow rates at 28 °C and then for both configurations the solutions exiting the VR were collected in a beaker thermostated at 28 °C and gently stirred. The TTIP conversion into TiO₂ through hydrolysis and condensation can be summarized into the following global chemical reaction:



As it is well known that a very fast chemical reaction characterized by an equilibrium completely shifted toward the products, as TiO₂ is a thermodynamically very stable substance, thus resulting in almost 100% yield.

The reaction product (i.e. gel) was then dried in three different ways; dried by rotavapor, directly in oven, and in oven after filtration. The resulting dried powders were eventually calcined at 400 °C for 3 h.

TSC was synthesized by following the procedure reported in [34] but with modified precursors and ratios. Particularly TTIP was used as precursor, glycine/urea as fuel, under stoichiometric as well as non-stoichiometric ratios, and 400/500 °C as combustion temperature. After combustion reaction, the samples were followed for calcinations at 400 °C for 3 h. Different commercial TiO₂ were purchased from Sigma–Aldrich and Aerosil to make comparison.

2.2. Characterization

In order to determine the different polymorphs, XRD patterns were recorded on a X'Pert Phillips diffractometer using Cu K α radiation, in the following conditions: range = (10–90°) 2 θ ; step size 2 θ = 0.02°. The BET surface area measurement and pore size analysis were carried out on powders previously outgassed at 150 °C, by N₂ sorption at 77 K on a Quantachrome Autosorb 1C instrument. FE-SEM pictures were collected on a high-resolution FE-SEM instrument (LEO 1525) equipped with a Gemini field emission column to see the particle morphology; with the same instrument, elemental composition was checked by EDX analysis.

Information about the nature of OH groups was obtained with a FT-IR spectroscopy. Powders were pressed into thin, self-supporting wafers. Spectra were collected, at a resolution of 2 cm⁻¹

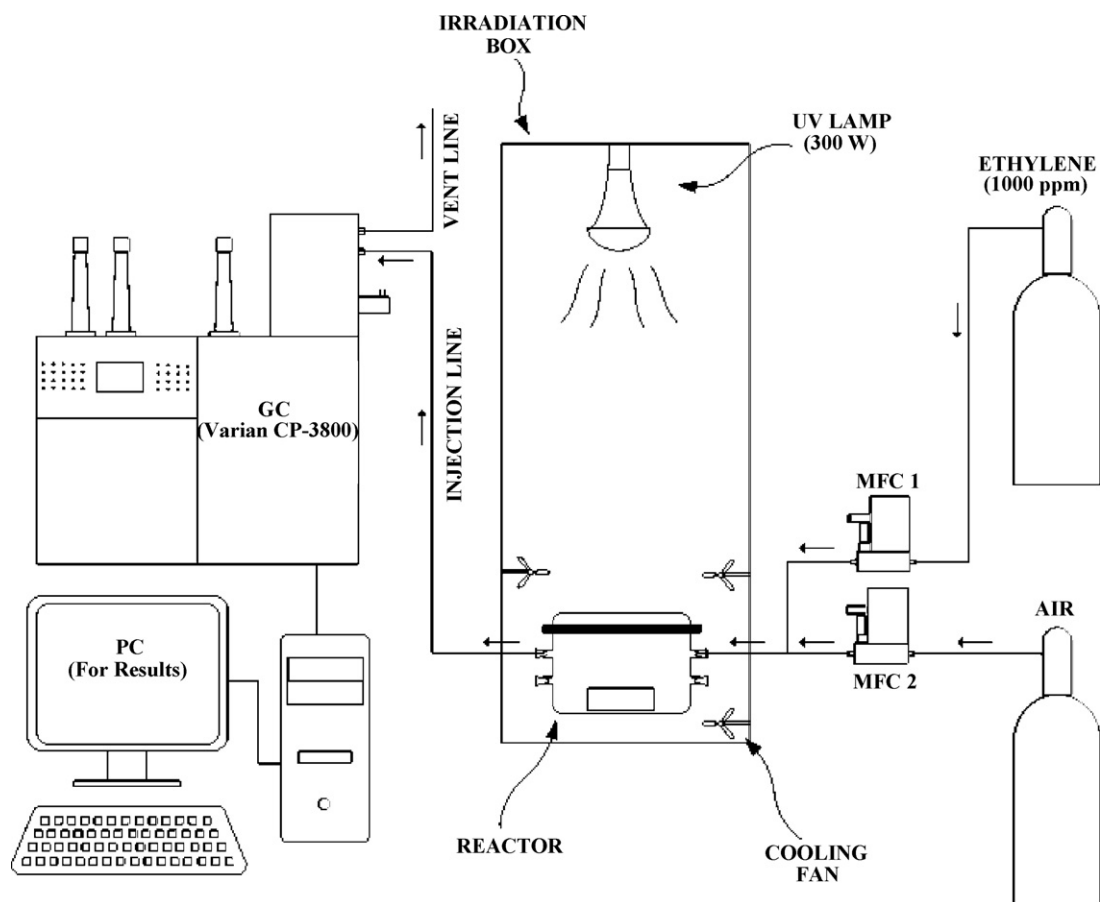


Fig. 2. Photocatalysis reaction experimental setup.

on a Perkin Elmer FT-IR spectrophotometer equipped with a MCT detector.

DR/UV–vis was done by a UV–vis double beam spectrophotometer Varian Cary 500, equipped with an integrating sphere. For background subtraction, the reference was Spectralon® and spectra were collected in 200–600 nm regions with a resolution of 2 nm. The measuring set-up permits the analysis of diffuse radiation, excluded the specular one.

2.3. Ethylene photocatalytic reaction

All tests of ethylene photocatalytic degradation were performed in a pyrex glass reactor with total volume of 2000 cm³. A schematic of the experimental setup is depicted in Fig. 2, that includes the pyrex glass reactor (transparent to UV light), connectors, mass flow controllers (MFC, Bronkhorst high tech), UV lamp (Osram ultra vitalux, 300 W), gas cylinders (1000 ppm ethylene, air), and gas chromatograph (Varian CP-3800) equipped with capillary column (CP7381, fused silica) and flame ionization detector (FID) with a patented ceramic flame tip for ultimate peak shape and sensitivity, used for the product gas analysis.

1 g calcined TiO₂ sample was dispersed inside the pyrex glass reactor. 100 ppm ethylene was continuously flushed in the reactor with the help of MFC at constant flow rate of 50 mL/min. After achieving equilibrium in the peak intensity, UV light was turned on, reaction products were analyzed by GC, and ethylene conversion was calculated.

We repeated our experiments and the results were reproducible. Therefore, we safely state that the errors are quite limited and can be neglected.

3. Results and discussion

3.1. Characterization and comparison of TiO₂ samples

TNP were dried in three different commercial process leading easy ways to find the optimized one. After drying and before calcination the powder is mainly amorphous and no distinct peak is found, as shown in Fig. 3(a). However, after calcination at 400 °C for 3 h the main crystalline form was anatase (denoted as “A”) and minor part in rutile (denoted as “R”) (Fig. 3(a)). The optimal drying condition was found by drying in rotavapor, resulting in an anatase to rutile ratio of 80:20. Details and comparison with the other drying conditions are reported in Table 1. For most photocatalytic reaction systems, it is generally accepted that anatase demonstrates a higher activity than rutile and this enhancement in photoactivity has been ascribed to the Fermi level

Table 1
BET surface area and crystalline phases of different TiO₂.

Sample	S _{BET} (m ² /g)	Anatase:rutile (%)
TNP (rotavapor dried and calcined)	151	80:20
TNP (filtered, dried and calcined)	130	71:29
TNP (oven dried and calcined)	121	69:31
TSC (glycine, 400 °C, 1:1)	85	55:45
TSC (glycine, 500 °C, 1:1)	90	60:40
TSC (urea, 500 °C, 1:3)	108	61:39
TSC (urea, 500 °C, 1:1)	65	58:42
TiO ₂ commercial (Aldrich, technical)	15	80:20
TiO ₂ commercial (Aldrich, anatase)	10	100:0
TiO ₂ commercial (degussa P25)	53	70:30

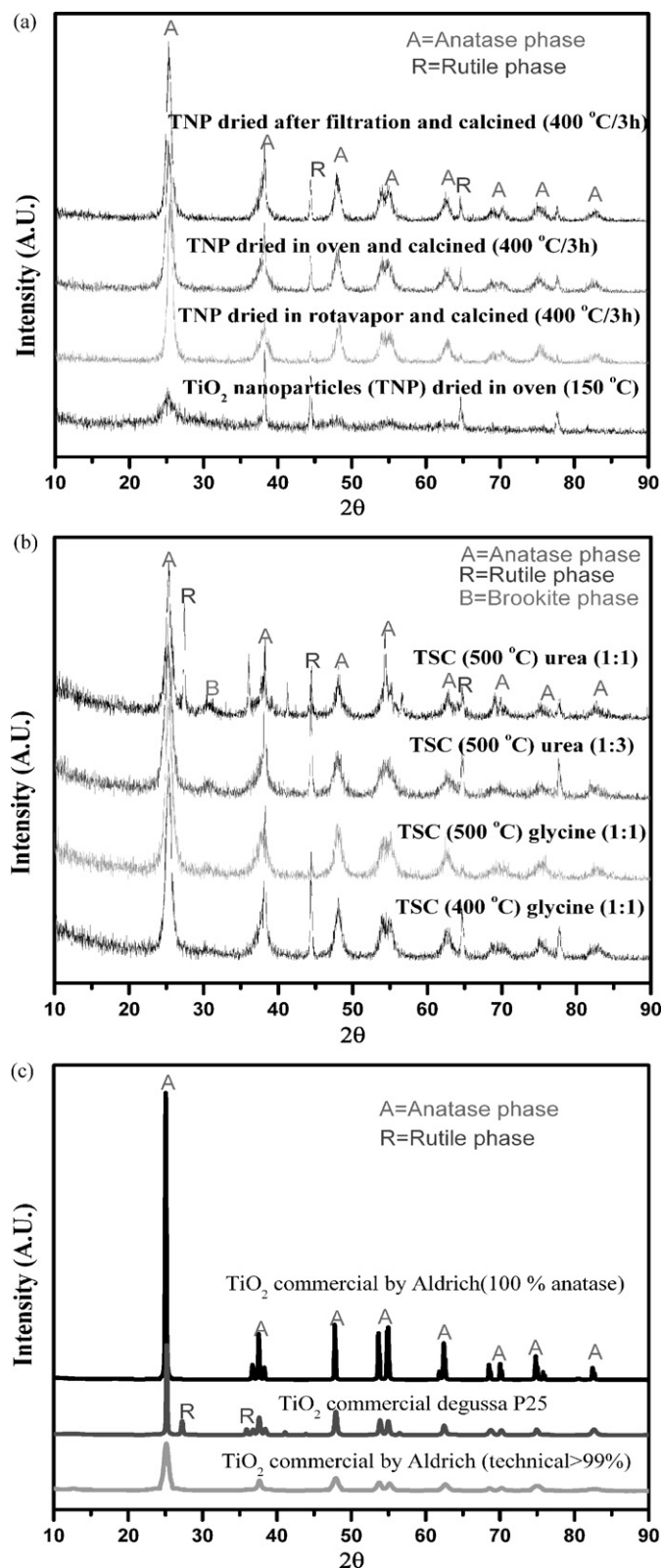


Fig. 3. XRD patterns of (a) TNP, (b) TSC, and (c) different commercial titania.

of anatase being higher than that of rutile [35]. The origin and the method of preparation affect the physico-chemical properties of the specimen. In recent years degussa P25 TiO₂ has set the standard for photoreactivity in environmental VOC applications. Degussa P25 is a non-porous 70:30% (anatase to rutile), having

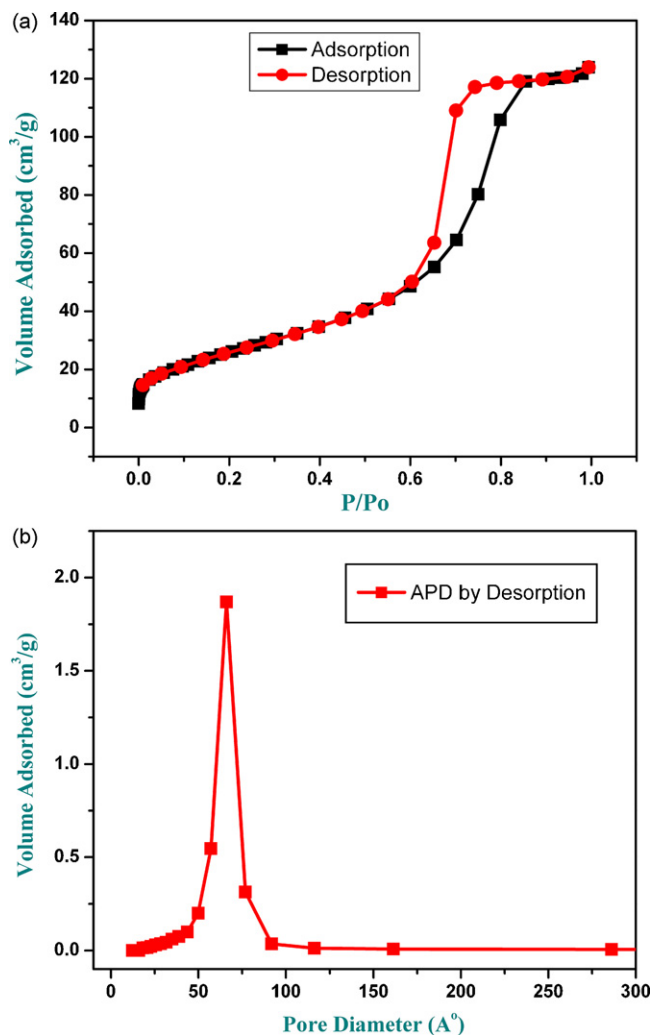


Fig. 4. TNP (rotavapor dried): (a) adsorption/desorption isotherm, (b) average pore diameter.

rutile phase but considered even more reactive than pure anatase [6].

Compared to TNP, TSC showed more rutile phase in all the cases shown in Fig. 3(b). However, TSC (glycine, 500 °C, 1:1) and TSC (urea, 500 °C, 1:3) were comparatively better in this category as shown in Table 1. Also, Fig. 3(c) represents the XRD patterns of three different commercial TiO₂ for the comparison. TiO₂ by Aldrich (anatase) showed the pure anatase phase whereas the TiO₂ by Aldrich (technical) has a mixed phase. Degussa P25 also showed mixed anatase and rutile phases.

The effect of the specific surface area of TiO₂ in photocatalysis is always important [6,16]. The primary objective was to synthesize the TNP that have the highest surface area. Table 1 shows that all the TNP samples exhibit higher specific surface area than the TSC as well as all the commercial TiO₂. TNP dried in rotavapor and calcined showed the highest surface area (i.e. 150 m²/g), in contrast to the degussa P25 (53 m²/g). It was also reported [6] and shown in Table 1 that surface area of degussa P25 is five times that of Aldrich TiO₂. Therefore comparing all, TNP showed the best available surface area. As shown in Fig. 4(a and b) by adsorption/desorption isotherm and average pore diameter (APD), TNP also have porosity with a pore volume of 0.20 cm³/g and average pore diameter of 7 nm. This porosity is considered to be the void spaces between the particles in contrast to the non-porous degussa P25. The sample with a porosity and rough surface showed a characteristics of high surface area

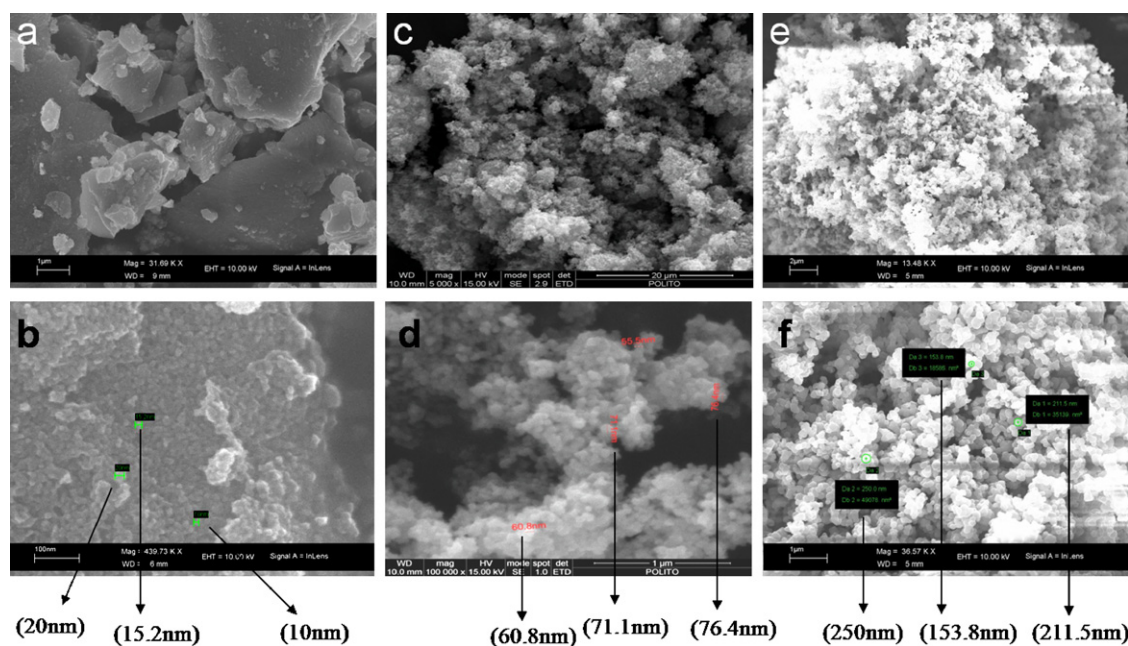


Fig. 5. SEM images of TNP (a and b), degussa P25 (c and d), and TiO_2 commercial by Aldrich (e and f) showing the morphology and particle size difference.

and high adsorptive capacity [16]. Also, the increased surface area of TiO_2 should be helpful to enhance the surface reaction of TiO_2 [36].

FE-SEM was used to analyze the particle size and shape of the calcined TNP and comparison with commercial TiO_2 . The SEM images of the calcined TNP showed fine nanoparticles of 10–20 nm range (Fig. 5a and b). Even though the sample was calcined at high temperature of 400°C for 3 h, the nanoparticles are more in the dispersed phase and very less in the aggregates. On the other hand, degussa P25 showed an aggregates of 60–70 nm nanoparticles (Fig. 5c and d) and Aldrich TiO_2 has much larger size nanoparticles in the range of 150–250 nm (Fig. 5e and f).

EDX a chemical microanalysis technique is used to characterize the elemental composition of the calcined TNP. It demonstrates that the main components are O and Ti with 67 and 32 at.%, respectively confirms the formation of TiO_2 and a small amount of Cl that is actually from HCl added during the synthesis.

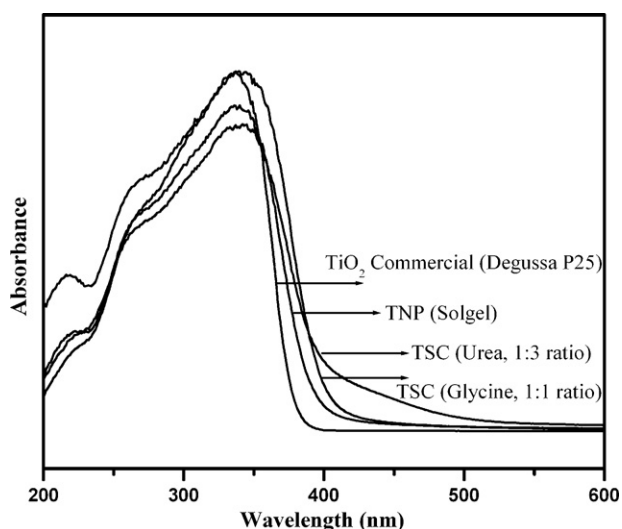


Fig. 6. DR/UV-vis spectra of different titania samples showing the difference in wavelength.

DR/UV-vis directly provides some insight into the interactions of the photocatalytic materials (e.g. TiO_2) with photon energies [9,35,37]. Fig. 6 shows the UV-vis absorption profiles of TNP and TSC calcined at $400^\circ\text{C}/3\text{h}$, and compares then with those of commercial TiO_2 . It is clear that the absorption spectrum of TNP exhibits an onset of absorption at $\lambda = 391\text{ nm}$ compared to TSC which shows at $\lambda = 402, 413\text{ nm}$, whereas degussa P25 represents at $\lambda = 380\text{ nm}$ as shown in Fig. 6 and Table 2. The band gap energy of the titania samples was calculated by using this UV-vis DRS spectra with the equation, $E(\text{eV}) = hc/\lambda = 1239.95/\lambda$ [37], where E is the band gap energy (eV), h is Planck's constant, c is the velocity of light (m/s) and λ is the wavelength in nm. Table 2 shows the calculated band gap energies and the comparison. The average literature values for the absorption and corresponding band gap energies for bulk anatase TiO_2 is $\lambda_{\text{on}} 385\text{ nm}$ and $E = 3.2\text{ eV}$ [38]. It has also been reported that the increased band gap energy could be attributed to the effect of quantum size [37].

The FT-IR spectra of TNP and TSC calcined at $400^\circ\text{C}/3\text{h}$, and degussa P25 is shown in Fig. 7. It is believed that the broad peak at 3400 and the peak at 1650 cm^{-1} correspond to the surface water and hydroxyl groups [39]. Obviously, the calcined TNP has more surface water and hydroxyl groups than the calcined TSC as well as the degussa P25. This can be attributed to the larger surface area of the calcined TNP (Table 1). TNP of large surface area might offer more active sites to adsorb water and generate hydroxyl groups.

3.2. Ethylene photocatalysis

PCO of ethylene over TNP was performed at ambient temperature (Fig. 2) and compared with different TSC and commercial TiO_2

Table 2
Comparison of band gap energies of different TiO_2 .

Sample name	Absorption edge wave length, λ (nm)	Band gap energy, E (eV)
TNP (sol-gel)	391	3.17
TSC (glycine)	402	3.08
TSC (urea)	413	3.00
TiO_2 commercial (degussa P25)	380	3.26

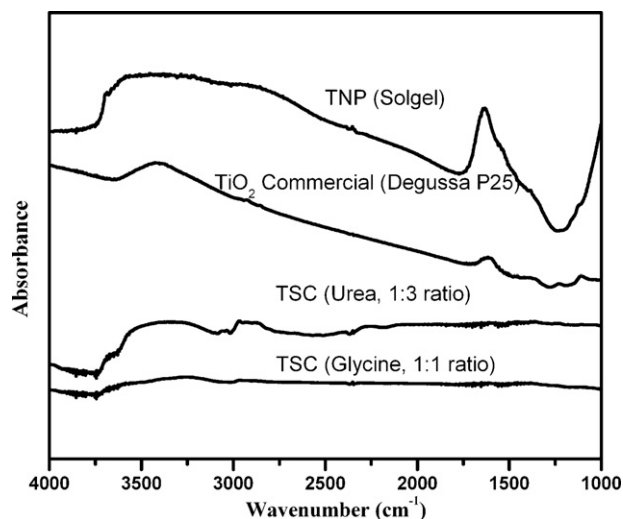


Fig. 7. FT-IR spectra of different titania samples showing the difference in OH groups.

photocatalysts. The important feature of this reaction is the use of air instead of conventional oxygen. In this situation, the required oxygen for the photocatalytic reaction is obtained from the air, leading towards the commercialization step. Fig. 8 shows the percentage conversion of ethylene as a function of time. TNP showed significantly higher conversion than all other samples. Degussa P25 showed comparable results. Even 100% anatase commercial TiO_2 showed very low conversion in this reaction. As it is clear, TSC synthesized with different ways using urea and glycine were also not suitable for this application. TNP was stable active until 6 h of reaction time in contrast to the degussa P25, which starts deactivation at this time. This deactivation of degussa P25 is due to its inferior properties. Moreover, TNP showed higher activity and good stability because of several superior properties which are being discussed in the following paragraphs.

The first superior characteristic of TNP in ethylene photodegradation is that it has main anatase with small rutile phase (Table 1). The photocatalyst derives its activity from the fact that when photons of a certain wavelength hit upon a surface, electrons are

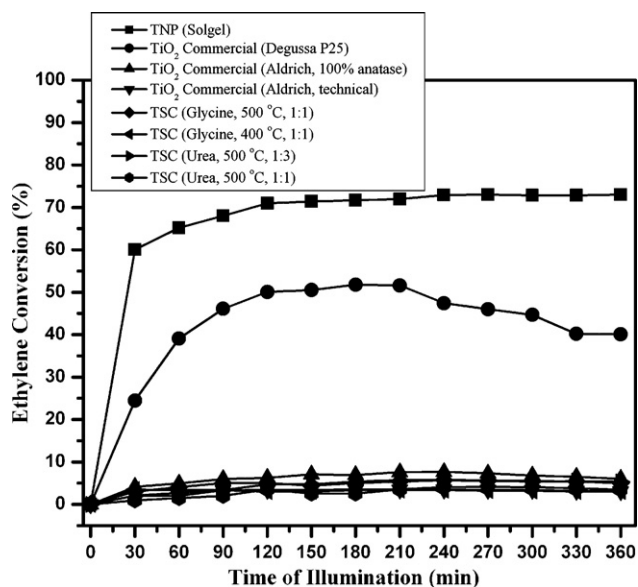


Fig. 8. Ethylene photodegradation over different titania photocatalysts with time of illumination.

promoted from the valence band and transferred to the conduction band [6]. This leaves positive holes in the valence band, which react with the hydroxylated surface to produce OH^{\bullet} radicals which are the most active oxidizing agents. In the absence of suitable electron and hole scavengers, the stored energy is dissipated within a few nanoseconds by recombination. If a suitable scavenger or a surface defect state is available to trap the electron or hole, their recombination is prevented and subsequent redox reaction may occur. In TNP, similar to degussa P25, the conduction band electron of the anatase part jumps to the less positive rutile part, reducing the rate of recombination of electrons and positive holes in the anatase part.

A second favorable feature of TNP in this application is the small size in combination with little porosity (Fig. 5) accompanied by large surface area (Table 1). It is reported that the photochemical characteristics of ultra small particles (i.e. Q-sized particles) has many advantages over comparatively macroparticles such as degussa P25 [40]. These small particles exhibit characteristics between molecular and bulk semiconductor. The high surface area-to-volume ratios lead to improved effectiveness for surface-limited reactions. Porosity between the TNP also make it superior to degussa P25 in ethylene photodegradation. The substances which are readily adsorbed are degraded at faster rate, indicating that the reaction is a surface phenomena [6]. The adsorption of ethylene which is competitive to OH groups on TNP surface might be increased due to this porosity, which causes the higher conversion after reaction.

The third attractive point of TNP is the numerous OH groups on the surface (Fig. 7). It is also noted that the type and amount of surface OH groups and or physisorbed H_2O plays a significant role in the photocatalytic reactions through the formation of OH radicals. The holes can react with water to produce the highly reactive hydroxyl radicals (OH^{\bullet}). These holes and the hydroxyl radicals are very powerful oxidants, which oxidize the organic materials [41]. The large surface area of the TNP was one of the most important factors in achieving a high efficiency through higher OH groups adsorbed on the surface of TNP in the PCO of the ethylene.

Another factor which is dominant in TNP (mostly anatase) is its higher bandgap energy (Fig. 6, Table 2) close to degussa P25. It also shows higher band gap energy than TSC due to more anatase phase. Moreover, when the crystallite dimension of a semiconductor particle falls below a critical radius of approximately 10 nm, the charge carriers appear to behave quantum mechanically [36]. As a result of this confinement, the band gap between the valence and conduction bands is enlarged as the particle size of the TiO_2 decreases. Thus, the oxidation potential of the photon generated holes (h^+) and the reducing potential of the electrons (e^-) could increase with increasing bandgap.

4. Conclusions

In this work, novel TNP was successfully synthesized on large scale by sol-gel method using VR with optimized operating parameters and conditions. Characterization comparison was done with the synthesized TSC and commercially purchased TiO_2 using different analysis techniques in detail. TNP showed many superior characteristics to other samples such as: main anatase with small rutile phase, small nanoparticles with little porosity accompanied by a large surface area, high band gap energy, and numerous OH groups.

Photocatalytic application of TNP was tested in the newly fabricated reaction system for the photocatalytic degradation of ethylene and compared with different TSC and commercial TiO_2 in activity. TNP revealed higher photocatalytic conversion of ethylene even than degussa P25, which is the best commercial TiO_2 . The enhancement in activity is believed to be due to the all combined

superior features of TNP, mentioned above. The obtained results in this study are very encouraging, showing further way for optimizations and promising applications especially in the photocatalysis of VOCs and many more.

Acknowledgements

This work is supported by Fondazione Cassa di Risparmio di Cuneo. M. Hussain is also thankful to Regione Piemonte and Politecnico di Torino, Italy for the post-doctoral fellowship grant. Prof. Guido Saracco is highly acknowledged for the review of the manuscript.

References

- [1] A. Fujishima, K. Honda, Electrochemical photolysis of water at a semiconductor electrode, *Nature* 238 (1972) 37–38.
- [2] B. O'Regan, M. Gratzel, A low-cost, high-efficiency solar cell based on dye-sensitized colloidal TiO₂ films, *Nature* 353 (1991) 737–740.
- [3] R. Blossey, Self-cleaning surfaces-virtual realities, *Nat. Mater.* 2 (2003) 301–306.
- [4] M. Yamagishi, S. Kuriki, P.K. Song, Thin film TiO₂ photocatalyst deposited by reactive magnetron sputtering, *Thin Solid Films* 442 (2003) 227–231.
- [5] U. Bach, D. Corr, D. Lupo, F. Pichot, M. Ryan, Nanomaterials-based electrochromics for paper-quality displays, *Adv. Mater.* 14 (2002) 845–848.
- [6] D.S. Bhatkhande, V.G. Pangarkar, A.A.C.M. Beenackers, Photocatalytic degradation for environmental applications—a review, *J. Chem. Technol. Biotechnol.* 77 (2001) 102–116.
- [7] A. Fujishima, T.N. Rao, D.A. Tryk, Titanium dioxide photocatalysis, *J. Photochem. Photobiol. C: Photochem. Rev.* 1 (2000) 1–21.
- [8] A. Fujishima, X. Zhang, Titanium dioxide photocatalysis: present situation and future approaches, *C. R. Chimie* 9 (2006) 750–760.
- [9] D.B. Hamal, K.J. Klabunde, Synthesis, characterization, and visible light activity of new nanoparticle photocatalysts based on silver, carbon, and sulfur-doped TiO₂, *J. Colloids Interf. Sci.* 311 (2007) 514–522.
- [10] X. Fu, L.A. Clark, W.A. Zeltner, M.A. Anderson, Effects of reaction temperature and water vapor content on the heterogeneous photocatalytic oxidation of ethylene, *J. Photochem. Photobiol. A: Chem.* 97 (1996) 181–186.
- [11] T.W. Tibbitts, K.E. Cushman, X. Fu, M.A. Anderson, R.J. Bula, Factors controlling activity of zirconia–titania for photocatalytic oxidation of ethylene, *Adv. Space Res.* 22 (1998) 1443–1451.
- [12] A. Sirisuk, C.G. Hill Jr., M.A. Anderson, Photocatalytic degradation of ethylene over thin films of titania supported on glass rings, *Catal. Today* 54 (1999) 159–164.
- [13] D.R. Park, J. Zhang, K. Ikeue, H. Yamashita, M. Anpo, Photocatalytic oxidation of ethylene to CO₂ and H₂O on ultrafine powdered TiO₂ photocatalysts in the presence of O₂ and H₂O, *J. Catal.* 185 (1999) 114–119.
- [14] S. Kumar, A.G. Fedorova, J.L. Golea, Photodegradation of ethylene using visible light responsive surfaces prepared from titania nanoparticle slurries, *Appl. Catal. B: Environ.* 57 (2005) 93–107.
- [15] A. Strini, S. Cassese, L. Schiavi, Measurement of benzene, toluene, ethylbenzene and o-xylene gas phase photodegradation by titanium dioxide dispersed in cementitious materials using a mixed flow reactor, *Appl. Catal. B: Environ.* 61 (2005) 90–97.
- [16] L. Zou, Y. Luo, M. Hooper, E. Hu, Removal of VOCs by photocatalysis process using adsorption enhanced TiO₂–SiO₂ catalyst, *Chem. Eng. Process.* 45 (2006) 959–964.
- [17] G.M. Zuo, Z.X. Cheng, H. Chen, G.W. Li, T. Miao, Study on photocatalytic degradation of several volatile organic compounds, *J. Hazard. Mater.* 128 (2006) 158–163.
- [18] D.S. Tsoukleris, T. Maggos, C. Vassilakos, P. Falaras, Photocatalytic degradation of volatile organics on TiO₂ embedded glass spherules, *Catal. Today* 129 (2007) 96–101.
- [19] M. Lamalle, H. El Ayadi, C. Gennequin, R. Cousin, S. Siffert, F. Aissi, A. Aboukais, Effect of the preparation method on Au/Ce–Ti–O catalysts activity for VOCs oxidation, *Catal. Today* 137 (2008) 367–372.
- [20] A.L. Linsebigler, G.Q. Lu, J.T. Yates, Photocatalysis on TiO₂ surfaces—principles, mechanisms, and selected results, *Chem. Rev.* 95 (1995) 735–758.
- [21] S.S. Watson, D. Beydoun, J.A. Scott, R. Amal, The effect of preparation method on the photoactivity of crystalline titanium dioxide particles, *Chem. Eng. J.* 95 (2003) 213–220.
- [22] A. Mills, N. Elliott, G. Hill, D. Fallis, J.R. Durrant, R.L. Willis, Preparation and characterization of novel thick solgel titania film photocatalyst, *Photochem. Photobiol. Sci.* 2 (2003) 591–596.
- [23] M.H. Habibi, H. Vosoghian, Photocatalytic degradation of some organic sulfides as environmental pollutants using titanium dioxide suspension, *J. Photochem. Photobiol. A* 174 (2005) 45–52.
- [24] R.R. Bacsa, J. Kiwi, Effect of rutile phase on the photocatalytic properties of nanocrystalline titania during the degradation of p-coumaric acid, *Appl. Catal. B: Environ.* 16 (1998) 19–29.
- [25] J.M. Warson, A.T. Cooper, J.R.V. Flora, Nanoglued titanium dioxide aerogels for photocatalysis, *Environ. Eng. Sci.* 22 (2005) 666–675.
- [26] M.C. Yan, F. Chen, J.L. Zhang, M. Anpo, Preparation of controllable crystalline titania and study on the photocatalytic properties, *J. Phys. Chem. B* 109 (2005) 8673–8678.
- [27] A. Testino, I.R. Bellobono, V. Buscaglia, C. Canevali, M. D'Arienzo, S. Polizzi, R. Scotti, F. Morazzoni, Optimizing the photocatalytic properties of hydrothermal TiO₂ by the control of phase composition and particle morphology. A systematic approach, *J. Am. Chem. Soc.* 129 (2007) 3564–3575.
- [28] C. Su, B.Y. Hong, C.M. Tseng, Solgel preparation and photocatalysis of titanium dioxide, *Catal. Today* 96 (2006) 119–126.
- [29] S.E. Pratsinis, Synthesis of ceramic powders, *Prog. Energy Combust. Sci.* 24 (1998) 197–219.
- [30] Y.V. Kolen'ko, V.D. Maximov, A.A. Burukhin, V.A. Muhanov, B.R. Churagulov, Synthesis of ZrO₂ and TiO₂ nanocrystalline powders by hydrothermal process, *Mater. Sci. Eng. C* 23 (2003) 1003.
- [31] X.Z. Ding, X.H. Liu, Synthesis and microstructure control of nanocrystalline anatase titania powders via solgel process, *Mater. Sci. Eng. A* 224 (1997) 210–215.
- [32] D.L. Marchisio, F. Omegna, A.A. Barresi, P. Bowen, Effect of mixing and other operating parameters in solgel processes, *Ind. Eng. Chem. Res.* 47 (2008) 7202–7210.
- [33] D.L. Marchisio, F. Omegna, A.A. Barresi, Production of TiO₂ nanoparticles with controlled characteristics by means of a vortex reactor, *Chem. Eng. J.* 146 (2009) 456–465.
- [34] G. Sivalingam, K. Nagaveni, M.S. Hegde, G. Madras, Photocatalytic degradation of various dyes by combustion synthesized nano anatase TiO₂, *Appl. Catal. B: Environ.* 45 (2003) 23–38.
- [35] K. Porkodi, S.D. Arokiamary, Synthesis and spectroscopic characterization of nanostructured anatase titania: a photocatalyst, *Mater. Charact.* 58 (2007) 495–503.
- [36] H.J. Kim, Y.G. Shul, H.S. Han, Photocatalytic properties of silica-supported TiO₂, *Top. Catal.* 35 (2005) 287–293.
- [37] P. Periyat, K.V. Baiju, P. Mukundan, P.K. Pillai, K.G.K. Warriar, High temperature stable mesoporous anatase TiO₂ photocatalyst achieved by silica addition, *Appl. Catal. A: Gen.* 349 (2008) 13–19.
- [38] K. Mogyrosi, I. Dekany, J.H. Fendler, Preparation and characterization of clay mineral intercalated titanium dioxide nanoparticles, *Langmuir* 19 (2003) 2938–2946.
- [39] G. Tian, H. Fu, L. Jing, C. Tian, Synthesis, photocatalytic activity of stable nanocrystalline TiO₂ with high crystallinity and large surface area, *J. Hazard. Mater.* 161 (2009) 1122–1130.
- [40] J. Zhao, X. Yang, Photocatalytic oxidation for indoor air purification: a literature review, *Build. Environ.* 38 (2003) 645–654.
- [41] A. Fujishima, K. Hashimoto, T. Watanabe, *TiO₂ Photocatalysis: Fundamentals and Applications*, English ed., BKC, Tokyo, 1999.

Synthesis of TiO₂ nanoparticles by hydrolysis and peptization of titanium isopropoxide solution

S. Mahshid^a, M. Askari^a, M. Sasani Ghamsari^{b,*}

^a Department of Material Science & Eng., Sharif Industrial University, 11365-9466 Tehran, Iran

^b Solid State Laser Division, Laser Research Center, North Karegar, 11365-8486 Tehran, Iran

Received 12 July 2006; received in revised form 16 December 2006; accepted 29 January 2007

Abstract

Titanium dioxide nanoparticles have been prepared by hydrolysis of titanium isopropoxide. Aqueous solution with various pH and peptizing the resultant suspension has been applied for preparation of the TiO₂ nanopowder with narrow size distribution. The influence of pH on the particle size and morphology of prepared powder has been evaluated. Synthesized powder is characterized by X-ray diffraction, scanning electron microscopy (SEM) and transmission electron microscopy (TEM). Experimental results have shown that the as-prepared powders have entirely consisted with anatase crystalline phase. Only powder acquired from an acidic solution has fine particle size with spherical morphology. The anatase to rutile transformation occurred at temperatures lower than 600 °C.

© 2007 Elsevier B.V. All rights reserved.

Keywords: Hydrolysis; Peptization; Titanium isopropoxide; Crystallinity; TiO₂

1. Introduction

One of the most important nanomaterials which have attracted a great attention due to its unique properties is titanium dioxide. Titania (TiO₂) powders possess interesting optical, dielectric, and catalytic properties, which leads to industrial applications such as pigments, fillers, catalyst supports, and photo-catalysts [1–5].

It has been demonstrated that the final properties of this material depend to size, morphology and crystalline phase of the prepared TiO₂ nanopowder. In order to prepare of TiO₂ nanostructured material with significant properties several processes have been developed over the last decade and can be classified as liquid process (sol–gel [6–9], solvothermal [10,11], hydrothermal [5,12,13]), solid state processing routes (mechanical alloying/milling [14,15], mechanochemical [16,17]), RF thermal plasma [18] and other routes such as laser ablation [19]. From the above methods, the sol–gel method is normally used for preparation nanometer TiO₂ powder. Experimental results have shown that the prepared powders by uncontrolled sol–gel method generally lack the properties of uniform size, shape, and unagglomerated state and providing the titanium oxide with

favour properties need to control process conditions. There are several parameters for controlling sol–gel process to prepare TiO₂ nanopowder with significant properties. It has been demonstrated that the precursor's concentration of titanium alkoxide greatly affects the crystallization behavior and characteristics of the final powder [20]. In addition, the size, stability, and morphology of the produced sol from alkoxides is strongly affected by the water titanium molar ratio ($r = [\text{H}_2\text{O}]/[\text{Ti}]$) [21,22]. The formation of colloidal TiO₂ at high r ratio is of great interest, because the small size of particles is formed under this condition. Also, the peptization process in which the reaction can be carried out at molecular level by heating the solution or using peptization agent has the same effect on the characteristics of the final powder which has been prepared by sol–gel method [23–25]. Finally, the pH of prepared solution has a great influence on the final size of TiO₂ nanoparticles [26,27]. Therefore, the controlled size and narrow size distribution of prepared powder can be obtained with optimization the preparation conditions. In this research work, we have tried to optimize preparation condition for providing narrow size distribution of the nanometer TiO₂ powders by controlling the pH of the solution.

2. Experimental

In this work, the precursor solution was a mixture of 5 ml titanium isopropoxide, TTIP (97%, and supplied by Aldrich Chemical) and 15 ml isopropanol

* Corresponding author.

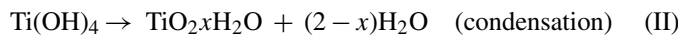
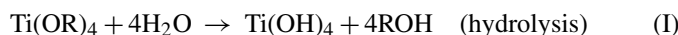
E-mail address: msghamsari@yahoo.com (M.S. Ghamsari).

(99%, supplied by Merck). A 250 ml solution of distilled water with various pH was used as the hydrolysis catalyst. The desired pH value of the solution was adjusted by adding HNO_3 or NH_4OH . The gel preparation process started when both solutions were mixed together under vigorous stirring. Hydrolysis of TTIP offered a turbid solution which heated up to 60–70 °C for almost 18–20 h (peptization). After peptization process, the volume of the solution decreases to 50 cm^3 and a suspension was produced. Depending on the preparation conditions, the resultant suspension was white-blue or opaque with high viscosity. The prepared precipitates were washed with ethanol and dried for several hours at 100 °C. After being washed with ethanol and dried at 100 °C in a vacuum system for 3 h, a yellow-white powder is obtained. Finally, the prepared powder was annealed at temperature ranging from 200 to 800 °C for 2 h.

Several techniques were employed for characterization of the powders. Powder X-ray diffraction (Philips PW 1800) was used to identify the crystal phase and to estimate the average crystallite size as well. The particle size and morphology of the powder were observed by Philips XL 30 scanning electron microscope (SEM) and Philips 200 transmission electron microscope (TEM).

3. Results and discussion

The preparation of the TiO_2 colloids in the nanometer range can be effectively conducted through the hydrolysis and condensation of titanium alkoxides in aqueous media. In the presence of water, alkoxides are hydrolyzed and subsequently polymerized to form a three-dimensional oxide network. These reactions can be schematically represented as follows:



where R is ethyl, *i*-propyl, *n*-butyl, etc. [28]. It is well known that the tetravalent cations are too much acidic so that the nucleation of stable hydroxide $\text{Ti}(\text{OH})_4$ cannot occur.

Water molecules formed according to reaction (II) always bear a positive partial charge [29]. Therefore, oxolation and olation can proceed simultaneously during nucleation and growth leading to amorphous hydrous oxide ($\text{TiO}_2 \cdot n\text{H}_2\text{O}$) where the number *n* of water molecules depends on experimental conditions. Depending on the experimental procedure, the precipitation of TiO_2 lead to rutile or anatase phases [30,31]. The formation of such structures from aqueous molecular precursors can be described as follows. When deoxolation ($\text{O}=\text{Ti}-\text{OH}_2 \rightarrow \text{HO}-\text{Ti}-\text{Ti}-\text{OH}$) dose not occur during nucleation olation lead to a linear growth along one of the two equivalent directions in the equatorial plan of $[\text{Ti}_2\text{O}_2(\text{OH})_4(\text{OH}_2)_4]^0$ dimers. Then, oxolation between the resulting $\text{TiO}(\text{OH})_2(\text{OH})_2$ linear chains after an internal proton transfer leads to corner-sharing octahedral chains (Ti_3O bridges) characteristics of the rutile structure. The formation of rutile may then be associated to the metastability of apical $\text{Ti}=\text{O}$ bonds within monomers or dimers. Now, if deoxolation occur prior to olation, condensation can proceed along apical direction leading to skewed chains typical of the anatase structure. Controlling the stage of deoxolation prior to olation can be obtained by adjusting the pH and initial water concentration. This control leads to precipitation of anatase nanopowder TiO_2 in the experimental procedure. Fig. 1 shows the XRD pattern of the prepared powder in the different pH. When the pH level of the solution is higher than 2, a white suspension of rough precipitant is formed immediately after hydrolysis reaction. Otherwise, when the pH

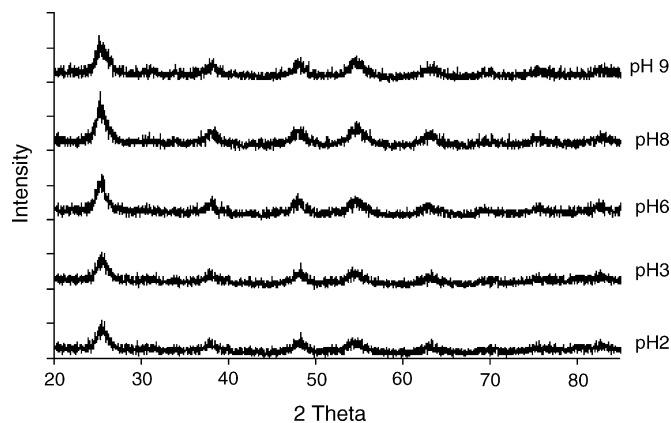


Fig. 1. XRD patterns for TiO_2 particles obtained from different pH solutions and dried at 100 °C for 3 h.

level of the solution is 2, a homogenous suspension of fine particles is formed. The crystallite size of the particles has been estimated from the Debye–Scherrer’s equation using the XRD line broadening as follows [32]:

$$B = \frac{k\lambda}{s \cos \theta} \quad (\text{I})$$

where *s* is the crystallite size, λ the wavelength of the X-ray radiation ($\text{Cu K}\alpha = 0.15406 \text{ nm}$), *k* a constant taken as 0.94, θ the diffraction angle and *B* is the line width at half maximum height. The (1 0 1) plane diffraction peak is used for anatase and (1 1 0) peak for rutile. Fig. 2 shows the crystalline size of as-prepared TiO_2 nanoparticles in the different pH. As it can be found from Fig. 2 the smallest crystallites have been obtained from the hydrolysis of TTIP in the acidic solution (pH 2) and the dried powder at 100 °C. Fig. 3, shows the XRD pattern of the prepared powder from acidic solution (pH 2) and calcined at various temperatures in atmospheric condition for 2 h. It can be found that all samples are crystalline and the dried powder at 100 °C has anatase phase. It shows that the control of deoxolation process by initial water concentration and peptization could accelerate the anatase crystallization and shift it to temperatures lower than even 100 °C. The temperature observed in our result is much lower than that achieved by others [33]. The effect of calcination temperatures on the crystalline size of TiO_2 was shown in Figs. 4 and 5. When the temperature has been

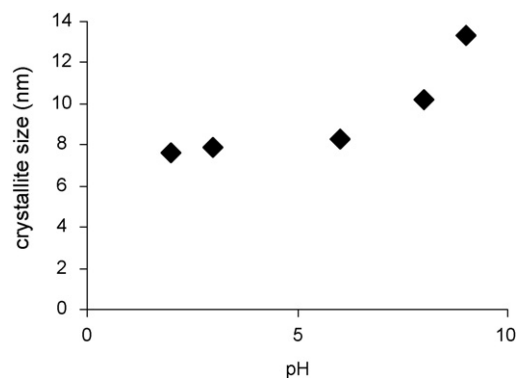


Fig. 2. Crystalline size variation of prepared powders at different pH.

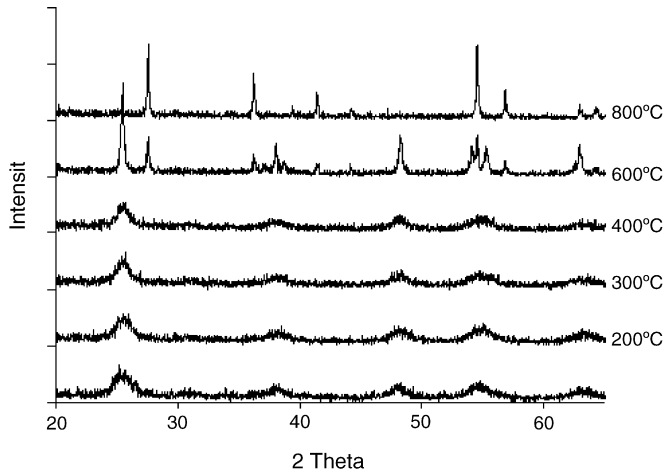


Fig. 3. XRD patterns of prepared powders at different calcination temperatures.

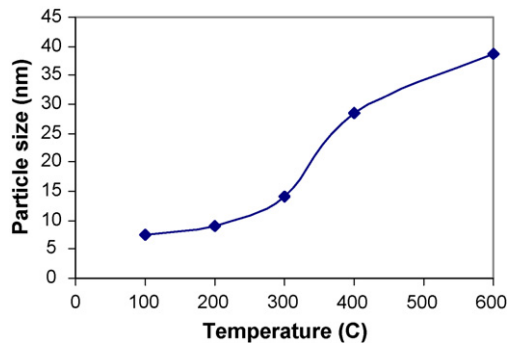


Fig. 4. Particle size variation via calcination temperatures.

raised to 200 and then 400 °C, the size of formed crystallites has increased which could be attributed to the thermally promoted crystallite growth. The size of anatase crystallites increases from 7.6 to 38.7 nm when calcination temperature has been elevated to 600 °C. At 600 °C, apart from anatase, sharp rutile peaks was also observed in the XRD result. The formed rutile showed quite different behavior having larger size than the remained anatase particles. This, in fact, reveals that nucleation and growth of rutile phase would have been initiated at temperature somewhere from 400 to 600 °C [34]. Anatase to rutile transformation temperature is shifted to the very low temperature level for nanosize crystallites because of the high surface energy of the particles.

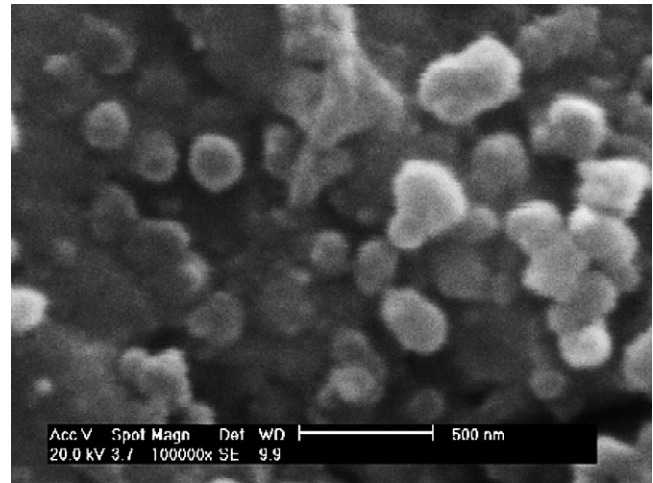


Fig. 6. SEM micrographs of powders prepared at 400 °C.

This temperature has been mostly reported from 600 to 900 °C for the initiation and finishing temperature respectively [32]. It is then possible to assume that the growth of rutile particle starts right after its nucleation. Furthermore, the rutile crystallite size is 47.5 nm at 600 °C, while it increases slightly to 53.4 nm when the temperature goes to 800 °C. At this temperature, anatase phase has been eliminated and there were only large rutile particles in the sample. Fig. 6 shows the SEM micrographs of TiO₂ particles prepared at different pH and calcined at 100 °C temperatures. As shown in Fig. 6, the as-prepared powder in acidic solution (pH 2) consist of spherical particles with poor agglomeration and aggregation takes place during the particle growth process at higher temperatures. On the other hand, the as-prepared powder in basic solution (pH 9) consists of nonspherical particles with high agglomeration.

It is observed that, in the higher calcination temperatures, the larger particle size with spherical morphology is obtained. For the sample calcined at 400 °C (Fig. 7), the particle size is almost 100 nm. Shape and morphology is clearly observed in the SEM micrographs of the samples calcined at that temperature. From the SEM photographs of samples prepared under different pH values, it has been revealed that the spherical morphology was a specification of the prepared powder under acidic solution of pH 2 and it was not seen in other samples. The TEM image and the select-area electron diffraction (SAED) pattern

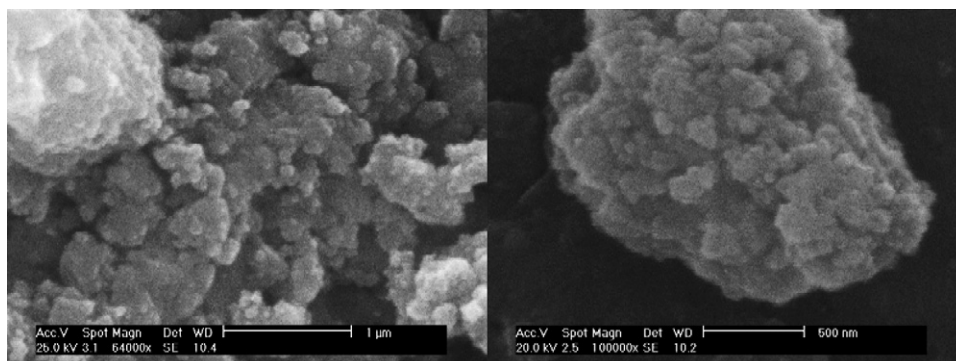


Fig. 5. SEM micrographs of dried powders at 100 °C: (a) pH 2; (b) pH 9.

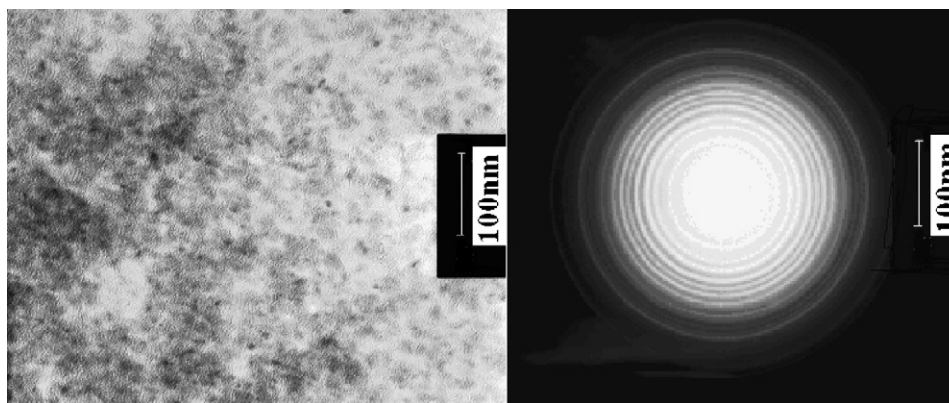


Fig. 7. (a) TEM and (b) SAED photograph of as-prepared sample dried at 100 °C for 3 h.

of the as-prepared sample are shown in Fig. 7(a and b), respectively. It is obviously shown that the as-prepared powder is completely crystalline and entirely consists of anatase phase. From the micrograph their diameter is estimated to be below 10 nm which is in good agreement with XRD results. In Fig. 7(b) the SAED pattern of as-prepared TiO₂ particles which is dried at 100 °C is shown. The first four rings are assigned to the (1 0 1), (0 0 4), (2 0 0), (0 0 5) reflections of the anatase phase. The SAED studies are in good agreement with XRD measurements.

4. Conclusion

Nanocrystalline TiO₂ powder can be prepared by the hydrolysis of titanium isopropoxide alcoholic solution and then peptization of the resultant suspension up to 60–70 °C for 18–20 h. According to the particle size obtained from Debye–Scherrer equation, the powder obtained from a solution at pH 2 consist of very fine anatase crystallites even at temperature lower than 100 °C. When the powder is treated thermally at 400 °C, the diameter of nanoparticles is approximately 28 nm and still consists of pure anatase phase. As the calcinations temperature is increased, the particle size increases. Rutile phase is formed at calcinations temperatures below 600 °C and grows slightly when heated up to 800 °C. Powder morphology in these criteria is almost spherical which is due to acidic condition that prevents agglomeration.

References

- [1] C.J. Barbe, F. Arendse, P. Comte, M. Jirousek, M. Grätzel, Nanocrystalline titanium oxide electrodes for photovoltaic applications, *J. Am. Ceram. Soc.* 80 (1997) 3157.
- [2] R. Monticone, A.V. Tufeu, E. Kanaev, C. Scolan, Sanchez, Quantum size effect in TiO₂ nanoparticles: does it exist, *Appl. Surf. Sci.* 162–163 (2000) 565–570.
- [3] S. Boujday, F. Wunsch, P. Portes, J.-F. Bocquet, C.C. Justin, Photocatalytic and electronic properties of TiO₂ powders elaborated by sol–gel route and supercritical drying, *Solar Energy Mater. Solar Cells* 83 (2004) 421–433.
- [4] O. Carp, C.L. Huisman, A. Reller, Photoinduced reactivity of titanium dioxide, *Prog. Solid State Chem.* 32 (2004) 133–177.
- [5] A.M. Ruiz, G. Sakai, A. Cornet, K. Shimano, J.R. Morante, N. Yamazoe, Microstructure control of thermally stable TiO₂ obtained by hydrothermal process for gas sensors, *Sens. Actuators B: Chem.* 103 (2004) 312–317.
- [6] T. Trung, W.-J. Cho, C.-S. Ha, Preparation of TiO₂ nanoparticles in glycerol-containing solutions, *Mater. Lett.* 57 (2003) 2746–2750.
- [7] T. Sugimoto, X. Zhou, A. Muramatsu, Synthesis of uniform anatase TiO₂ nanoparticles by gel–sol method. 1: Solution chemistry of Ti(OH)_n⁽⁴⁻ⁿ⁾⁺ complexes, *J. Colloid Interface Sci.* 252 (2002) 339–346.
- [8] T. Sugimoto, X. Zhou, A. Muramatsu, Synthesis of uniform anatase TiO₂ nanoparticles by gel–sol method. 2: Adsorption of OH⁻ ions to Ti(OH)₄ gel and TiO₂ particles, *J. Colloid Interface Sci.* 252 (2002) 347–353.
- [9] P. Arnal, R.J.P. Corriu, D. Leclercq, P.H. Mutin, A. Vioux, A solution chemistry study of nonhydrolytic sol–gel routes to titania, *Chem. Mater.* 9 (1997) 694–698.
- [10] C.-S. Kim, B.K. Moon, J.-H. Park, S.T. Chung, S.-M. Son, Synthesis of nanocrystalline TiO₂ in toluene by a solvothermal route, *J. Cryst. Growth* 254 (2003) 405–410.
- [11] C.-S. Kim, B.K. Moon, J.-H. Park, B.-C. Choi, H.-J. Seo, Solvothermal synthesis of nanocrystalline TiO₂ in toluene with surfactant, *J. Cryst. Growth* 257 (2003) 309–315.
- [12] J.-N. Nian, H. Teng, Hydrothermal synthesis of single-crystalline anatase TiO₂ nanorods with nanotubes as the precursor, *J. Phys. Chem. B* 110 (2006) 4193–4198.
- [13] Y.V. Kolen'ko, B.R. Churagulov, M. Kunst, L. Mazerolles, C. Colbeau-Justin, Photocatalytic properties of titania powders prepared by hydrothermal method, *Appl. Catal. B: Environ.* 54 (2004) 51–58.
- [14] D.H. Kim, H.S. Hong, S.J. Kim, J.S. Song, K.S. Lee, Photocatalytic behaviors and structural characterization of nanocrystalline Fe-doped TiO₂ synthesized by mechanical alloying, *J. Alloys Compd.* 375 (2004) 259–264.
- [15] P. Xiaoyan, M. Xueming, Study on the milling-induced transformation in TiO₂ powder with different grain sizes, *Mater. Lett.* 58 (2004) 513–515.
- [16] J.L. Guimaraes, M. Abbate, S.B. Betim, M.C.M. Alves, Preparation and characterization of TiO₂ and V₂O₅ nanoparticles produced by ball-milling, *J. Alloys Compd.* 352 (2003) 16–20.
- [17] M. Kamei, T. Mitsuhashi, Hydrophobic drawings on hydrophilic surfaces of single crystalline titanium dioxide: surface wettability control by mechanochemical treatment, *Surf. Sci.* 463 (2000) L609–L612.
- [18] S.-M. Oh, T. Ishigaki, Preparation of pure rutile and anatase TiO₂ nanopowders using RF thermal plasma, *Thin Solid Films* 457 (2004) 186–191.
- [19] M. Matsubara, T. Yamaki, H. Itoh, H. Abe, K. Asai, Preparation of TiO₂ nanoparticles by pulsed laser ablation: ambient pressure dependence of crystallization, *Jpn. J. Appl. Phys.* 42 (5A Pt 2) (2003) L479–L481.
- [20] B.L. Bischoff, M.A. Anderson, Peptization properties in the sol–gel preparation of porous anatase (TiO₂), *Chem. Mater.* 7 (1995) 1772–1778.
- [21] X.-Z. Ding, Z.-Z. Qi, Y.-Z. He, Effect of hydrolysis water on the preparation of nano-crystalline titania powders via a sol–gel process, *J. Mater. Sci. Lett.* 14 (1995) 21–22.
- [22] D. Vorkapic, T. Matsoukas, Effect of temperature and alcohols in the preparation of titania nanoparticles from alkoxides, *J. Am. Ceram. Soc.* 81 (1998) 2815–2820.

- [23] J.-L. Look, C.F. Zukoski, Alkoxide-derived titania particles: use of electrolytes to control size and agglomeration levels, *J. Am. Ceram. Soc.* 75 (1992) 1587–1595.
- [24] J.-L. Look, C.F. Zukoski, J.L. Look, C.F. Zukoski, Colloidal stability of titania precipitate morphology: influence of short-range repulsions, *J. Am. Ceram. Soc.* 78 (1995) 21–32.
- [25] T. Zeng, Y. Qiu, L. Chen, X. Song, Microstructure and phase evolution of TiO₂ precursors prepared by peptization-hydrolysis method using polycarboxylic acid as peptizing agent, *Mater. Chem. Phys.* 56 (1998) 163–170.
- [26] T. Sugimoto, X. Zhou, A. Muramatsu, Synthesis of uniform anatase TiO₂ nanoparticles by the gel-sol method. 3: Formation process and size control, *J. Colloidal Interface Sci.* 259 (2003) 43–52.
- [27] T. Sugimoto, X. Zhou, A. Muramatsu, Synthesis of uniform anatase TiO₂ nanoparticles by the gel-sol method. 4: Shape control, *J. Colloidal Interface Sci.* 259 (2003) 53–61.
- [28] J. Livage, M. Henry, C. Sanchez, Sol–gel chemistry of transition metal oxides, *Prog. Solid State Chem.* 18 (1988) 259–341.
- [29] C. Sanchez, J. Livage, M. Henry, F. Babonneau, Chemical modification of alkoxide precursors, *J. Non-Cryst. Solids* 100 (1988) 65–76.
- [30] Shin, H.S. Jung, K.S. Hong, J.-K. Lee, Crystallization process of TiO₂ nanoparticles in an acidic solution, *Chem. Lett.* 33 (2004) 1382–1383.
- [31] N. Phonthammachai, T. Chairassameewong, E. Gulari, A.M. Jamieson, S. Wongkasemjit, Structural and rheological aspect of mesoporous nanocrystalline TiO₂ synthesized via sol–gel process, *Microporous Mesoporous Mater.* 166 (2003) 261–271.
- [32] G. Oskam, A. Nellore, R. Lee Penn, P.C. Searson, The growth kinetics of TiO₂ nanoparticles from titanium (IV) alkoxide at high water/titanium ratio, *J. Phys. Chem. B* 107 (2003) 1734–1738.
- [33] X.Z. Ding, X.H. Liu, Grain growth enhanced by anatase to rutile transformation in gel-derived nanocrystalline titania powders, *J. Alloys Compd.* 248 (1997) 143–145.
- [34] B. Li, X. Wang, M. Yan, L. Li, Preparation and characterization of nano-TiO₂ powder, *Mater. Chem. Phys.* 78 (2002) 184–188.



Production of TiO₂ nanoparticles with controlled characteristics by means of a Vortex Reactor

Daniele L. Marchisio*, Federica Omegna, Antonello A. Barresi

Dipartimento di Scienza dei Materiali e Ingegneria Chimica, Politecnico di Torino, C.so Duca degli Abruzzi 24, 10129 Torino, Italy

ARTICLE INFO

Article history:

Received 18 March 2008

Received in revised form 13 October 2008

Accepted 17 October 2008

Keywords:

Sol–gel

Titanium dioxide

Mixing

Titanium alkoxide

Computational fluid dynamics

Vortex Reactor

Population balance modelling

ABSTRACT

In this work titanium dioxide nanoparticle formation and evolution via the sol–gel route is investigated. Alcoholic solutions of titanium tetra-isopropoxide and water are mixed in a Vortex Reactor, where the mixing time can be accurately controlled by manipulating the inlet flow rates. Particle synthesis is carried out in operating conditions ranging from poor to excellent mixing performances and the effect of mixing on the formation of titanium dioxide nanoparticles and on their evolution is investigated from the modelling and the experimental view points. Experiments are in fact interpreted by using a simple population balance model and mixing in the reactor is accurately described by a computational fluid dynamics model based on the calculation of characteristics mixing times. Results show that particle formation is strongly influenced by mixing and that particle aggregation/condensation occurs in the reaction limited regime.

© 2008 Elsevier B.V. All rights reserved.

1. Introduction

Titanium dioxide is widely used as white pigment, and its optical properties are governed by refractive index and grain size. In fact, micrometric particles are generally opaque for visible light, whereas smaller nano-sized particles are transparent to visible light but still UV blocker [1]. Another important property is related to the fact that titanium dioxide is a super-hydrophilic material, thank to the almost null contact angle with water. Therefore it can be used to develop surfaces easy to clean and when a natural source of water exists, it can be used to develop self-cleaning surfaces.

Titanium dioxide is moreover well known for its ability to generate, when exposed to light, high mobility electrons and holes, that in turn are able to promote chemical reactions, resulting in a material with unique photo-catalytic properties [2,3]. The ability of titanium dioxide to degrade several organic compounds has been widely studied and it has been shown that this material can be profitably used to treat liquid and gaseous waste streams. Kinetic studies have shown that the photo-catalytic activity of titanium dioxide is greatly influenced by the crystalline form, although controversial results are reported in the literature. For example, some authors state that anatase works better than rutile [4,5], others found the best photo-catalytic activity for rutile [6–8], and some

others detected synergistic effects in the photocatalytic activity for anatase–rutile mixed phases [9–11]. Besides, recently it was demonstrated that photo-activity in organics degradation depends on the phase composition and on the oxidizing agent; for example, when the performance of different crystalline forms is compared, it turns out that rutile shows the highest photo-catalytic activity with H₂O₂ whereas anatase with O₂ [12,13]. Naturally the ability of titanium dioxide particles to degrade organic compounds depends also on the size of the particles, since small particles offer larger surface areas [14]. For its properties titanium dioxide has been recently implemented as filler for inorganic materials (plaster, mortar, and concrete [15]) and organic polymeric materials [16,17]. Also for these applications particle size is crucial, since only by using nano-sized fillers, materials with synergic properties, rather than compromising ones, are obtained. The improved properties of nano-composites are due to the large interfacial area offered by the nano-scale filler that controls the degree of interaction between the filler and the matrix [18].

Many processes for the production of titanium dioxide particles exist, namely flame aerosol synthesis [19], hydrothermal synthesis [20–23] and sol–gel synthesis [24]. Flame aerosol synthesis presents the main advantage of being easily scalable to the industrial level, but presents all the disadvantages of high temperature syntheses. Hydrothermal synthesis is instead particularly interesting for it directly produces a crystalline powder, without the need of resorting to a final calcination step, which is instead required in the sol–gel process. However the lack of knowledge of the chemical

* Corresponding author.

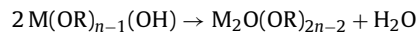
E-mail address: daniele.marchisio@polito.it (D.L. Marchisio).

equilibria of the species in solution and of the kinetics of nucleation and growth of the different phases, makes it difficult to control the overall process. The sol–gel route is at the moment the most common and promising one at the laboratory scale. It is based on the reaction between some precursor (e.g., titanium alkoxide) and water that are usually mixed as alcoholic solutions, with the addition of some catalysts to control the reaction (e.g., hydrochloric acid).

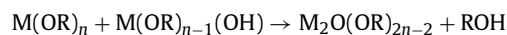
After mixing a fast hydrolysis reaction occurs:



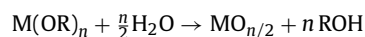
followed by de-hydration:



and de-alcoholation:



resulting in the following overall reaction [25]:



Water consumption measurements [26,27] seem to show that in the case of many titanium alkoxides, hydrolysis is generally faster than condensation, and that the first hydrolysis step corresponds to the creation of a supersaturated solution. From this supersaturated solution, after nucleation (i.e., formation of small nuclei of hydrolysed monomers) and molecular growth (addition of a single monomer to the nuclei), a colloidal suspension (i.e., sol) is generated, that subsequently, because of collisions due to Brownian motions, further condensation, and depending on the inter-particle potential, aggregates and may be transformed into a gel [28]. Although generally hydrolysis is faster than condensation their relative rates still depend on the operating parameters during particle formation, and under particular operating conditions (e.g., initial concentration of alkoxide in the alcohol solution, water to alkoxide ratio, concentration and nature of the catalyst, pH, etc.) hydrolysis and condensation can be almost simultaneous, leading immediately to the formation of a gel. Generally the formation of the gel is followed by a drying stage, that usually involves further condensation, and by a calcination step, where the amorphous material is transformed in crystalline particles. The final calcination step is crucial, because of the difficulties in controlling the crystalline form (anatase versus rutile) and in avoiding undesirable phenomena, such as grain growth with reduction of the superficial area [29].

Although the sol–gel process has been known almost for a century and some of the most important chemical aspects have been cleared, there exists room for improvement for individuating synthesis conditions that result in a powder with improved properties, when compared with commercial products available at the moment. Moreover up-scaling the process from the laboratory to the industrial scale is still a complex problem of difficult solution. The main issue stands in the fact that mixing plays a big role but its effects are usually underestimated, as proven by the qualitative statements (e.g., add dropwise or mix vigorously) with which ideal mixing conditions are usually identified. Mixing (usually turbulent) plays a very important role in the initial formation of the sol and as a consequence in the subsequent gelation process. In order to evaluate the relative importance of the different phenomena involved, it is crucial to quantify the characteristic time-scales for mixing, hydrolysis, and condensation/aggregation. Turbulent mixing occurs at several time- and length-scales; it starts on a scale of the same order of magnitude of the equipment in which the process occurs and it ends on a very small scale (Batchelor scale), that is determined by the fluid transport properties (i.e., viscosity and

diffusivity) and by turbulence intensity (i.e., turbulence dissipation rate) [30]. The characteristic mixing time is therefore given by the summation of the time required to reduce the scale of segregation from the macro-scale (macro-mixing) down to the molecular scale (micro-mixing) and can be determined by experimental techniques [31] or mathematical models based on computational fluid dynamics (CFD) [32,33]. The characteristic time for hydrolysis is usually related to the induction time, namely the time required for the formation of a visible solid phase [34] whereas the characteristic time for aggregation/condensation is evaluated based on the local particle concentration and on the aggregation kernel [35].

A number of investigations show that the ratio between these characteristic time-scales controls the final characteristics of the solid product. For example, in many particle formation processes the initial particle size is determined by the relative values of mixing and particle formation time-scales, and only if mixing is very fast ultra fine particles are formed [36–39] whereas in the case of sol–gel processes only some preliminary results were obtained [40]. Moreover, the size of the initial particles and their local concentration control the formation of the gel affecting its most important features, such as its rheological and fractal properties. The aggregation process, leading to the formation of the gel, is often studied by resorting to the Smoluchowski theory [41], by adopting population balance models (PBM) [42,43] and is driven by Brownian motions (i.e., perikinetic aggregation) [28].

The main objective of this work is to quantitatively investigate the effect of mixing on TiO₂ nanoparticles formation and evolution. To this end a specific sol–gel process is considered, based on the reaction between titanium tetra-isopropoxide and water in isopropanol. The effect of the different operating parameters on this sol–gel process was recently studied from the experimental point of view [44]. The experimental campaign was conducted by means of a statistical analysis (i.e. Design of Experiment) and results showed that the mixing rate strongly affects the final Particle Size Distribution (PSD). However, a number of issues related to the CFD simulation of mixing dynamics, the quantitative analysis of the resulting mixing time-scales, as well as the quantitative investigation of the final aggregation/condensation process were not discussed. All these aspects are instead investigated and discussed in details in this work. In fact, CFD is used here to quantify the mixing time and moreover the evolution of the formed particles is treated with a PBM in order to extract useful kinetics parameters. This investigation is carried out in a passive mixer, namely the Vortex Reactor, where simply changing the inlet flow rates of the reactant solutions the characteristic mixing time can be easily manipulated, as demonstrated in similar works [45,46]. Different titanium dioxide samples are prepared under different mixing conditions and their time evolution is tracked with time, since some of them result in stable sols, whereas some others aggregate and evolve in bigger clusters or degenerate into gels. Therefore the effect of mixing is quantified not only on the nanoparticles immediately formed after the first stages of hydrolysis and condensation, but also on the final particulate products obtained from the overall sol–gel process.

The manuscript is structured as follows: firstly the equations governing mixing dynamics and nanoparticle evolution are presented and discussed. Then the experimental set up, numerical details and operating conditions are described. Eventually the experimental and modelling results are presented and some relevant conclusions are drawn.

2. Governing equations

Turbulent mixing of two (or more) fluid streams into a chemical reactor is often described in terms of the mixture fraction ξ . This

quantity is a normalized inert scalar concentration that is assumed equal to one in one feed stream and zero in the other, and therefore represents the amount of fluid coming from one inlet with respect to the other. When the Reynolds-averaged Navier–Stokes (RANS) approach is used the problem is described in terms of Reynolds-averaged mixture fraction (ξ) whose transport equation reads as follows:

$$\frac{\partial \langle \xi \rangle}{\partial t} + \langle u_j \rangle \frac{\partial \langle \xi \rangle}{\partial x_j} - \frac{\partial}{\partial x_i} \left[(\Gamma + \Gamma_t) \frac{\partial \langle \xi \rangle}{\partial x_i} \right] = 0, \quad (1)$$

where the fluid is assumed to be incompressible (i.e., constant density flow), where Γ and Γ_t are the molecular and turbulent diffusion coefficients, respectively, and where the source term is null since the mixture fraction is a non-reacting scalar. It is important to highlight here that the solution of Eq. (1) and the knowledge of the mixture fraction values throughout the reactor is very useful, since it contains information on the mixing efficiency at the macroscopic level. Moreover, although the mixture fraction is a non-reacting scalar it is very much used also for the description of reacting systems. In fact, when the chemical reactions involved are infinitely fast, mixing is the limiting step for their completion, and therefore the mixture fraction alone suffices to completely describe the reacting systems. Moreover, when the chemical reactions are characterized by finite-rates the reacting system is still described in terms of the mixture fraction and in terms of additional reaction progress variables.

The turbulent diffusion coefficient appearing in Eq. (1) is calculated as follows:

$$\Gamma_t = \frac{C_\mu k^2}{Sc_t \varepsilon} \quad (2)$$

where $Sc_t \cong 0.7/1.0$ is the turbulent Schmidt number and C_μ is a numeric constant equal to 0.09. The turbulent kinetic energy k and the turbulent kinetic energy dissipation rate ε are usually calculated by resorting to a two-equation model (e.g., standard $k - \varepsilon$, RNG $k - \varepsilon$, realizable $k - \varepsilon$, standard and shear-stress-transport $k - \omega$) or by resorting to more sophisticated closures such as the Reynolds Stress Model (RSM) [47]. It is interesting to highlight that some of these models appear to be more indicated to the treatment of swirling flows as in the case of the Vortex Reactor. The Realizable $k - \varepsilon$ contains for example a special correction for swirling flows, and the RSM is also known to perform well for such flows. However, in order to discern among the possible modelling choices, detailed experimental data on the velocity and turbulent fields are needed.

When mixing in a chemical reactor is very efficient the mixture fraction (ξ) will assume almost everywhere in the reactor a constant value, corresponding to complete mixing conditions (i.e., $\bar{\xi}$). Based on this quantity, a large-scale variance is defined:

$$\langle \xi'^2 \rangle_L = (\langle \xi \rangle - \bar{\xi})^2, \quad (3)$$

equal to zero where mixing is complete and greater than one in regions where macro-scale gradients are still present. Although it is not directly solved, it is useful to derive the transport equation for this quantity, that reads as follows [32]:

$$\frac{\partial \langle \xi'^2 \rangle_L}{\partial t} + \langle u_j \rangle \frac{\partial \langle \xi'^2 \rangle_L}{\partial x_j} - \frac{\partial}{\partial x_i} \left[(\Gamma + \Gamma_t) \frac{\partial \langle \xi'^2 \rangle_L}{\partial x_i} \right] = -2\Gamma_t \frac{\partial \langle \xi \rangle}{\partial x_i} \frac{\partial \langle \xi \rangle}{\partial x_i}, \quad (4)$$

where as it is possible to see the large scale variance is dissipated by turbulent diffusion (negative term on the right-hand side) whereas it has no generation term, since the large-scale variance is generated by feeding the reactants in different inlets.

This large-scale variance is transported to smaller time- and length-scales thank to turbulent diffusion, and generates what is

called the small-scale variance. This quantity represents the segregation (or variance) at the molecular level and is defined as the average mixture fraction fluctuations ξ' , around the average value $\langle \xi \rangle$:

$$\langle \xi'^2 \rangle_s = \langle (\xi - \langle \xi \rangle)^2 \rangle = \frac{1}{\Delta t} \int_t^{t+\Delta t} (\xi - \langle \xi \rangle)^2 dt, \quad (5)$$

and its transport equation reads as follows [21]:

$$\begin{aligned} \frac{\partial \langle \xi'^2 \rangle_s}{\partial t} + \langle u_j \rangle \frac{\partial \langle \xi'^2 \rangle_s}{\partial x_j} - \frac{\partial}{\partial x_i} \left[(\Gamma + \Gamma_t) \frac{\partial \langle \xi'^2 \rangle_s}{\partial x_i} \right] \\ = 2\Gamma_t \frac{\partial \langle \xi \rangle}{\partial x_i} \frac{\partial \langle \xi \rangle}{\partial x_i} - 2 \frac{C_\phi \varepsilon}{2k} \langle \xi'^2 \rangle_s, \end{aligned} \quad (6)$$

where as it is possible to see the generation of small-scale variance equals the dissipation of large-scale variance; as already reported, segregation is generated originally from feeding the reactants in two separate feed streams, then is transported to smaller length-scales, and is finally dissipated at the molecular level through molecular mixing (see the last term on the right-hand side of Eq. (6)). The micro-mixing rate is usually written in terms of the integral time scale of turbulence (i.e., k/ε) and of the scalar-to-turbulence ratio C_ϕ , that is equal to two for fully turbulent flows, and can be calculated accurately by using the interpolation formula proposed by Liu and Fox [32], valid for Schmidt numbers much higher than one.

Based on these equations it is possible to calculate the overall mixing time as the summation of the time required to destroy macro-scale gradients, also known as macro-mixing time, and the time required to destroy micro-scale gradients, also known as micro-mixing time:

$$t_m = \frac{\langle \xi'^2 \rangle_L}{2\Gamma_t (\partial \langle \xi \rangle / \partial x_i) (\partial \langle \xi \rangle / \partial x_i)} + \frac{1}{C_\phi} \frac{k}{\varepsilon}, \quad (7)$$

where the first and the second term are the macro- and micro-mixing characteristic times respectively

As far as particle formation and evolution is concerned in sol–gel processes traditionally two steps are identified. In the first step particles are nucleated and grow from addition of single molecules, forming almost instantaneously a suspension of ultra-fine particles, referred to as sol. Then, depending on the operating conditions, this sol can aggregate evolving into a gel or can remain stable. The first step (i.e., particle formation) is very fast and is generally assumed to coincide with hydrolysis; during this step some water and most of the precursor are consumed. The second step is instead much slower and its rate is usually controlled by condensation. Since this second step is much slower than mixing, as shown by our previous work [35], the population balance equation can be simplified as follows:

$$\begin{aligned} \frac{\partial n(v; t)}{\partial t} = \underbrace{\frac{1}{2} \int_0^v \beta(v - \epsilon, \epsilon) n(v - \epsilon; t) n(\epsilon; t) d\epsilon}_{(1)} \\ - \underbrace{n(v; t) \int_0^\infty \beta(v, \epsilon) n(\epsilon; t) d\epsilon}_{(2)}, \end{aligned} \quad (8)$$

where $n(v; t)$ is the number density function in terms of the particle volume (or mass), identifying the number of particles having volume (or mass) in between v and $v + dv$; $\beta(v, \epsilon)$ is the volume-based aggregation kernel that describes the frequency that particles with volume v and ϵ collide to form a particle of volume $v + \epsilon$. As concerns the terms on the right-hand side of Eq. (8) they have the

following meaning. The first term (1) represents the rate of birth of particles of volume v due to aggregation of smaller particles, whereas the second term (2) is the rate of death of particles of volume v due to aggregation with other particles. The aggregation kernel, describing the frequency that particle collide and stick, is usually evaluated by combining two contributions, the first one taking into account the frequency of aggregation due to Brownian motions (i.e., diffusion limited aggregation, DLA) and the second one taking into account the frequency of aggregation due to condensation (i.e., reaction limited aggregation, RLA). Soloviev et al. [48] has shown that DLA cannot be responsible for the gelation time required in many sol–gel processes, because in this range of operating conditions it would result in very fast aggregation in comparison with what is experimentally observed. The RLA regime has therefore been suggested resulting in the following aggregation kernel:

$$\beta(v, \epsilon) = k_0 c_W^p, \quad (9)$$

where k_0 is the kinetic constant of the controlling condensation reaction, c_W is the water residual concentration after hydrolysis, and p is an exponent calculated as follows:

$$p = 2n - k + 1, \quad (10)$$

where n is the number of functional groups available for condensation (after hydrolysis), whereas k is the controlling condensation step, with $1 < k \leq n$. For example, if four functional groups are available and after hydrolysis one group has reacted, n results to be equal to three; if the condensation of the second group is the controlling one then $p = 5$ whereas if the condensation of the third group is controlling then $p = 4$, and so on.

As it is seen from Eq. (9) the aggregation kernel does not depend on particle volume and for this reason this equation can be solved analytically by using the method of moments. The final time evolution of the moment of zero order (the total particle number density, N) results in what follows:

$$N(t) = N_0 - \frac{k_0 c_W^p c_{Ti}^2}{2} t, \quad (11)$$

where $N(t)$ represents the time evolution of the total number of titanium dioxide particles of all size per unit volume, c_W is the water residual concentration after hydrolysis, N_0 is the total particle number density after hydrolysis (before condensation) and c_{Ti} is the titanium concentration in the solution. This model describes therefore particle formation as instantaneous and resulting in the formation of N_0 particles per unit volume and it predicts a linear decrease with time of the total particle number density $N(t)$ until gelation occurs; the gelling time corresponds to the time required to aggregate all the primary particles into one single particle, and therefore can be easily calculated from Eq. (11).

3. Operating conditions and numerical details

In this work titanium dioxide particle formation has been investigated from the experimental and modelling viewpoints. Titanium dioxide was synthesized by mixing a solution of micro-filtered water and reagent grade isopropanol with a solution of titanium tetra-isopropoxide (TTIP) in isopropanol. The solutions were prepared separately under nitrogen flux to control the alkoxide reactivity with humidity and moreover hydrochloric acid (HCl) was added at different initial concentrations as a hydrolysis catalyst and de-agglomeration agent. Equal volumes of reactant solutions (i.e., 100 ml) were mixed at equal flow rates at 30 °C in a VR and then for both configurations the solutions exiting the reactor were collected in a small vessel thermostated at 30 °C and gently stirred. The VR used in this work is constituted by a cylindrical chamber of 12 mm

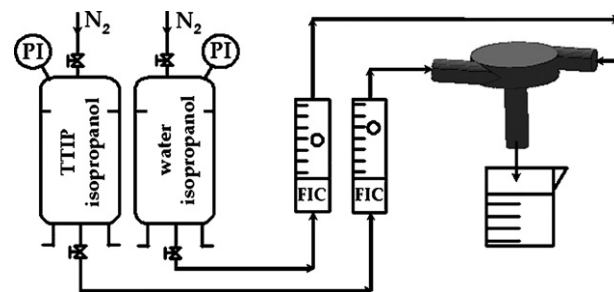


Fig. 1. Sketch of the experimental set-up.

in diameter and 3 mm in height; two reactant streams are fed tangentially at opposite sides of the reactor through two pipes of 3 mm of diameter, whereas the mixed solutions leave the reactor from the bottom through an outlet pipe of 3 mm of diameter. Because of the size of the reactor wall effects are very important, as reflected by the choice of the wall treatment in the CFD simulations.

The reactant solutions were stored in two small identical vessels, then pressurized at 3 bar with analytical grade nitrogen; the inlet flow rates were manipulated with two rotameters in the range from 10 to 400 ml/min. A sketch of the experimental apparatus is reported in Fig. 1. When the inlet flow rates of the two reactant solutions are varied from 10 to 400 ml/min, the mean residence time in the mixer approximately changes from about 5–0.05 s and the flow field is completely modified, moving from low turbulence and very poor mixing performances, to highly turbulent conditions with very rapid and efficient mixing dynamics, as it will be shown later.

The characterization of the particulate systems obtained in the different experiments is carried out assuming an instantaneous formation of solid particles and a subsequent slow aggregation/condensation process. The particle size distribution (PSD) of the sol instantaneously obtained after mixing was measured immediately by dynamic light scattering (DLS) with Malvern Nano ZS90 providing reliable information in the size range from 1 to 6000 nm; the PSD was then used to determine the mean particle size (d_{mean}) and the initial total particle number density (N_0) simply assuming that all the TTIP had reacted immediately. Then the PSD is tracked with time with regular measurements, approximately every 3 to 5 min depending on the operating conditions. The suspensions were then filtered with a micro-filtration system (Sartorius P.47, 200 ml) using a 0.1 μ m membrane, dried at 120 °C, washed with a solution of 0.02 % in weight of isopropanol and poly-acrylic-acid (PAA 2000, Aldrich) and after 15 min of ultrasonic treatment the suspension was filtered again. The ultrasonic treatment was carried out in order to break aggregates that might have been formed during filtration. The resulting powders were eventually calcined at 400 °C for 2 h. Scanning electron microscopy (SEM) and field emission scanning electron microscopy (FESEM) were carried out before and after thermal treatments.

Different experiments were carried out by varying the operating conditions during synthesis and by ranging the initial TTIP concentration in the isopropanol solution (c_{Ti}) between 0.1 and 2 mol/l, the ratio between the water and the TTIP concentrations in their initial solutions (W), also known as hydrolysis ratio, was varied between 1 and 4, whereas the ratio between the hydrochloric acid and the TTIP concentrations (H) was kept in between 0.25 and 0.5. The FR of the two solutions were kept at equal values and were varied between 10 and 400 ml/min, resulting in Reynolds numbers in the inlet jets (Re_j) ranging between 40 and 1000. Each experiment was repeated twice (and in some cases three times) to assess the syn-

Table 1
Summary of the operating conditions of experiments

c_{Ti}	W	H	FR
0.1	2	0.25	110
0.5	2	0.25	110
0.5	2	0.5	110
0.5	4	0.25	110
0.5	4	0.5	110
1	2	0.25	3
1	2	0.25	83
1	2	0.25	110
1	2	0.25	220
1	2	0.25	330
1	2	0.5	110

thesis and characterization protocol reproducibility. A summary of the different experiments performed is reported in Table 1.

Mixing in the reactor was investigated by running CFD simulations with the commercial code Fluent 6.3.26. Different computational grids were tested, and after subsequent refinements a grid-independent solution was obtained. The final grid contained about 200,000 computational cells. Simulations in turbulent conditions were run using the so-called RANS approach, by employing the realizable $k-\epsilon$ turbulence model and non-equilibrium wall functions for the near wall treatment. Other turbulence models and near wall treatments were tested, but the use of more sophisticated approaches did not affect very much the final predictions. In order to avoid the insidious effects of numerical diffusion higher order discretization schemes were employed (i.e., third order scheme). Due to the very wide range of operating conditions investigated, some of the simulations were run at very low jet Reynolds, corresponding to very low turbulence. Under these conditions the RANS approach is well known to fail in predicting accurately the velocity field in the reactor and the mixing dynamics. Moreover the lack of experimental data concerning the velocity field inside the reactor does not allow for a direct validation of CFD predictions. Therefore, although the absolute values of the mixing times extracted should be treated with great caution, this CFD analysis is still valid and very useful to estimate trends and orders of magnitude.

The flow field was first simulated assuming that the two reactant solutions (mainly constituted by isopropanol) were characterized by identical physical properties, namely a density of 0.785 kg/l and a viscosity of 2 cP. The transport equations for the mean mixture fraction (see Eq. (1)) and for the mixture fraction variance (see Eq. (6)) were instead solved by introducing them as user defined scalars. The boundary conditions were such that the mean mixture fraction was equal to one in one inlet and equal to zero in the other one, whereas the mixture fraction variance was set equal to zero in both inlets since it is not defined in pure feed streams. With the same subroutines the global mixing time was evaluated by solving Eq. (7).

4. Results and discussion

As it has been reported each experiment has been repeated twice (and in some cases three times) to verify the reproducibility of the synthesis and characterization protocol. In Fig. 2 the PSD of the three different samples prepared under the same operating conditions is reported and as it is possible to see the three curves are quite close. The overall reproducibility of the synthesis and characterization protocol resulted in standard deviation for the mean particle size of about 15 to 20%.

The effect of the initial concentration of titanium alkoxide (c_{Ti}) is reported in Fig. 3; as it is possible to see an increase in the initial alkoxide concentration results in the formation of bigger particles.

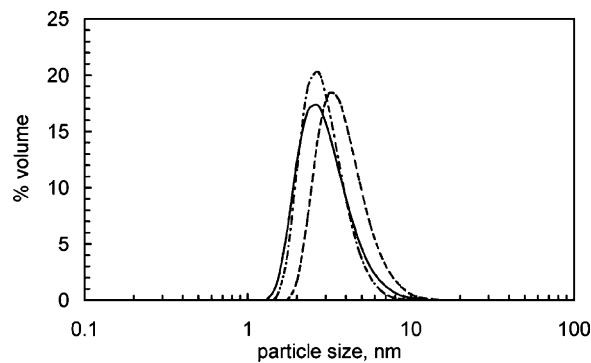


Fig. 2. Volume particle size distributions of titanium dioxide particles synthesized under the following operating conditions $c_{Ti} = 1$ mol/l, $W = 2$, $H = 0.25$, and $FR = 220$ ml/min; the three lines correspond to three different measurements carried out on three different samples prepared under the same synthesis conditions.

This is probably related to the fact that higher reactant concentrations favour, in this concentration range, the growth of particles rather than the nucleation of new ones. Also the hydrolysis ratio (W) has the same effect (result not shown here); in fact, the formed particles get bigger as the hydrolysis ratio is increased, when the other parameters are kept at their original values.

The hydrochloric acid content, quantified in this work by the H value, has little effect on the initial mean particle size. In fact, comparison of PSDs of titanium dioxide particles obtained at different H values, showed very similar results. However, a tremendous effect was detected on particle stability. In fact, as it is clear from Fig. 4

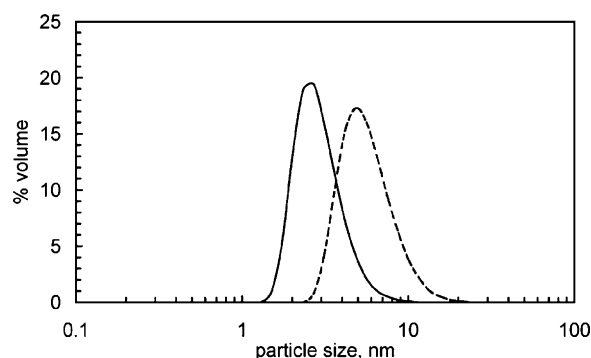


Fig. 3. Volume particle size distributions of titanium dioxide particles synthesized for $H = 0.25$, $W = 2$, $FR = 110$ ml/min and $c_{Ti} = 0.1$ mol/l (continuous line) and $c_{Ti} = 1$ mol/l (dashed line).

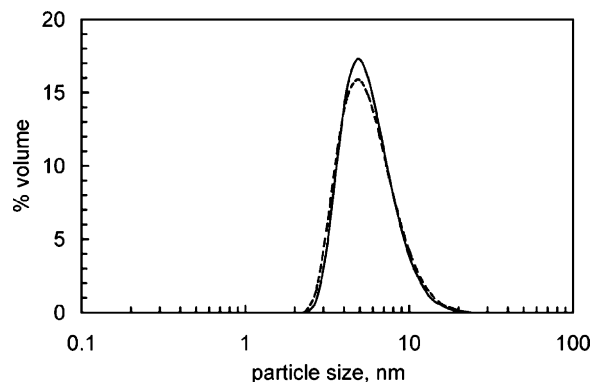


Fig. 4. Volume particle size distributions of titanium dioxide particles synthesized for $H = 0.5$, $W = 2$, $FR = 110$ ml/min, $c_{Ti} = 1$ mol/l as soon as synthesized (continuous line) and after four days or gentle stirring (dashed line).

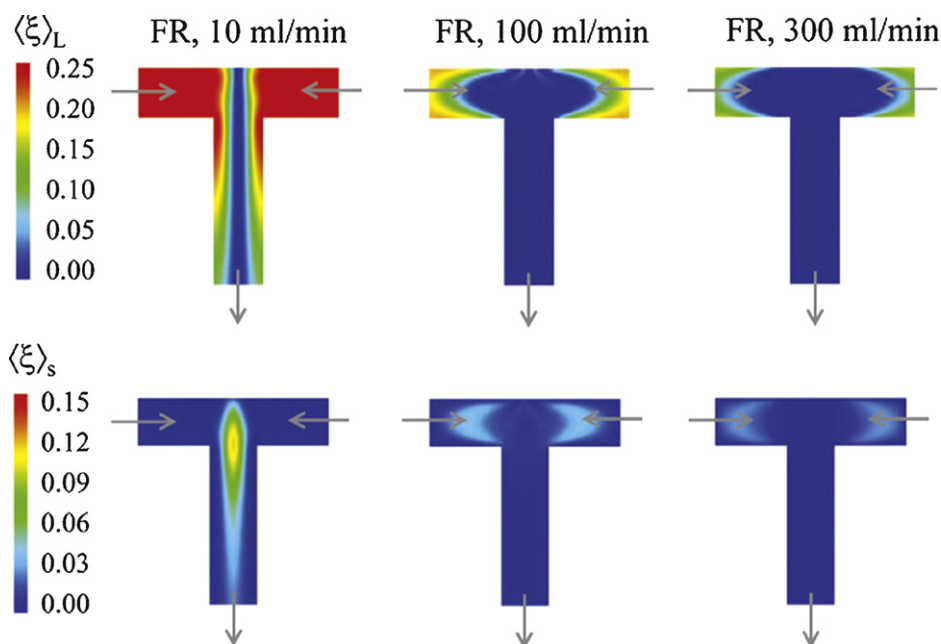


Fig. 5. Contour plots for the large-scale variance (top) and small-scale variance (bottom) at different FR values.

the PSD of titanium dioxide particles synthesized at high H values (e.g., $H = 0.5$) remains constant and after four days it was identical to what originally measured. When the H factor is lowered down to 0.25, and therefore less acid is available, aggregation becomes very important, and the mean particle size increases with time. The effect of the hydrochloric acid content is usually related to the ability of solid oxides to form in aqueous suspensions electrical charges. These charges are caused by the amphoteric dissociation of surface hydroxyl groups, the adsorption of protons and hydroxyl ions, or metal hydroxo compounds from the hydrolysis of solid material. The strong repulsive force among charged particles reduces the probability to aggregate and therefore more stable sols can be formed in acidic or alkaline media.

The effect of these operating parameters (i.e., c_{Ti} , W , H) during particle synthesis have been extensively investigated in the past and our results are consistent with similar works published and available in the specialized literature [44]. However, as already reported the effect of mixing has received little or no attention. For this reason it is particularly interesting to analyse the effect of this parameter on the final PSD of synthesized particles. Mixing can be quantitatively manipulated in the Vortex Reactor simply changing the flow rates of the inlet solutions.

As already reported in the previous section mixing can be quantified by the local value of the large- and small-scale variances. The contour plots of these quantities for the different flow rates investigated in this work are reported in Fig. 5. As expected the large-scale variance reaches its maximum value in the inlets and is then destroyed by turbulence. Due to the fact that mixing is a cascade process, the small-scale variance is generated in the regions where the large-scale variance is dissipated, and is instead dissipated afterwards due to molecular mixing. It is interesting to point out that the regions of the reactor presenting high values of large-scale variance are sensibly reduced as the flow rate is increased. Moreover, it is also clearly evident that at low flow rates at the outlet some macro-scale gradients are still present. The situation improves when the flow rate is increased, reducing the regions of the reactor characterized by macro- and micro-scale gradients.

This is confirmed by the calculations of the volume-averaged mixing times throughout the entire reactor reported in Fig. 6. In this

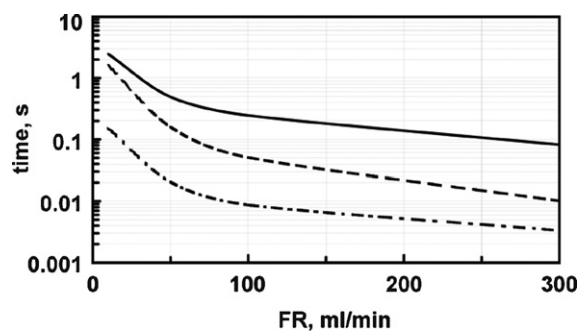


Fig. 6. Mean residence time (continuous line), macro-mixing time (dashed line) and micro-mixing time (dashed-dotted line) versus the reactor flow rate (FR).

figure for the different flow rates investigated, the relevant characteristic times are reported, namely, the mean residence time of the reactants in the reactor, and the macro- and micro-mixing times. As expected increasing the flow rate all these characteristic times are sensibly reduced. However, at low flow rates, the time required for the reactant solutions to mix down to the molecular level is quite large and very similar to the mean residence time of the reactor, resulting in very poor mixing and macro- and micro-scale segregation still characterizing the fluids leaving the reactor outlet. At higher flow rates the mixing time is much smaller than the residence time, and therefore when the fluid leaves the reactor it is completely mixed at the macro- and micro-scale levels.

Fig. 7 compares the PSD obtained at the minimum and the maximum flow rate investigated in this work. As it is possible to see the effect is quite important, since increasing the flow rate from 3 to 330 ml/min the resulting PSD is totally different. For the lowest flow rate the PSD is very broad, and particles as big as 70 nm are produced, whereas for the higher flow rate particles are much smaller, and the PSD has as higher bound 8 nm. As already mentioned the effect of these operating parameter has been carefully investigated, and a summary is reported in Fig. 8. As it is seen, there is a steady decrease of the mean particle size as the flow rate is increased (and as mixing becomes more and more efficient) until a constant value

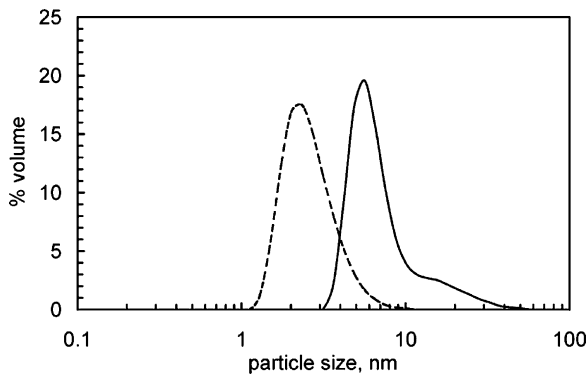


Fig. 7. Volume particle size distributions of titanium dioxide particles synthesized for $c_{Ti} = 1.0$ mol/l, $W = 2$, $H = 0.25$, and for FR = 3 ml/min (continuous line) and for FR = 330 ml/min (dashed line).

is reached. This decrease is caused by the fact that better mixing favours nucleation of new particles with respect to particle growth until a constant value is reached. In fact, as soon as the characteristic mixing time becomes smaller than the typical particle formation time, a further improvement in mixing does not affect any more the final PSD. For the operating conditions reported in Fig. 8 this characteristic particle formation time is about 0.03 s, corresponding to FR \approx 200 ml/min.

It is also interesting to point out that if the effect of mixing is significant on the PSD of titanium dioxide particles as soon as synthesized, its effect is even greater in terms of their time evolution. In Fig. 9 the time evolution of two different samples prepared under that same operating conditions but at different flow rates are reported. As it is possible to see when particles are synthesized at high flow rate, their initial particle size is very small, and their hydrolysed state is such that they tend to be stable and do not show any tendency to aggregate, whereas on the opposite when the flow rate is very small (and mixing is poor), particles are bigger and tend to aggregate forming bigger particles and eventually under some operating conditions form an aggregate of infinite size called gel.

SEM and FESEM observation supported the hypothesis that under these operating conditions two distinct steps exist. In the first step a burst of particles is produced by nucleation in a very short time. Then this sol evolves into different products through aggregation. In fact the filtered and dried powders observed at the microscope (see Fig. 10) showed a structure resembling that of large aggregates formed by very small primary particles, with about the same PSD of the particles analysed immediately after hydrolysis. This is also supported by specific surface area measurements not reported in this work for the sake of brevity.

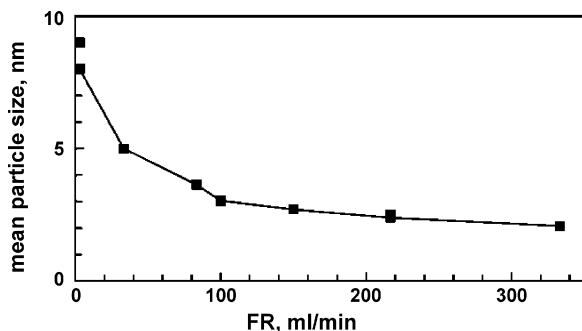


Fig. 8. Mean particle size for titanium dioxide particles synthesized for $H = 0.25$, $W = 2$, $c_{Ti} = 1.0$ mol/l at different FR values.

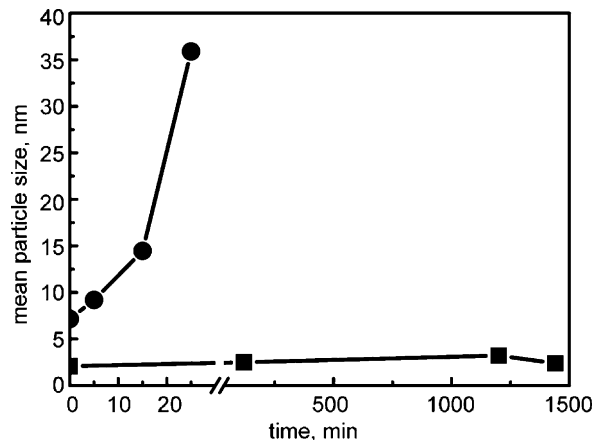


Fig. 9. Time evolution of the mean particle size of titanium dioxide particles synthesized for $c_{Ti} = 1$ mol/l, $W = 2$, $H = 0.25$ at FR = 3 ml/min (circles) and FR = 330 ml/min (squares).

If for the different cases investigated the total particle number density is plotted versus time (see for example Figs. 11 and 12) it is possible to observe the linear decay predicted by Eq. (11). As previously highlighted, the slope characterizing the decay of the total particle number density, is function of a kinetic constant k_0 , of the initial titanium concentration c_{Ti} and of the residual water concentration after hydrolysis c_W that can be easily calculated as follows:

$$c_W = c_W^0 - H_0 c_{Ti}, \quad (12)$$

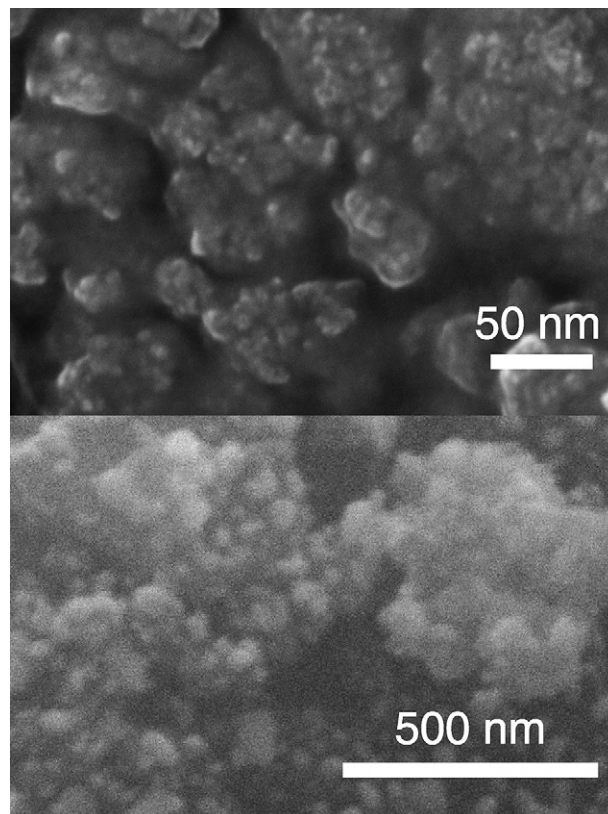


Fig. 10. Morphology of titanium dioxide aggregates synthesized for $c_{Ti} = 1$ mol/l, $W = 2$, FR = 110 ml/min and for $H = 0.25$ (top) and $H = 0.5$ (bottom).

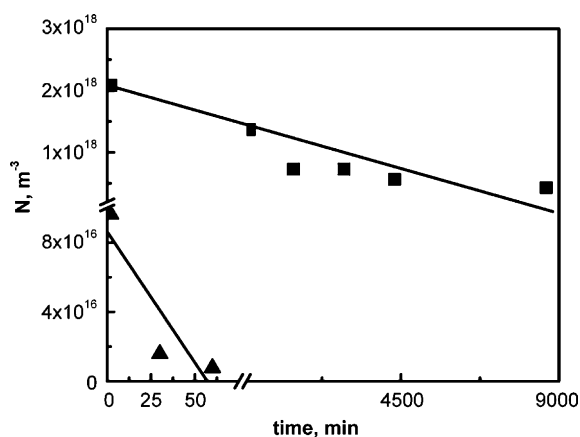


Fig. 11. Time evolution of the total particle number density (N) for $c_{Ti} = 0.5$ mol/l, $H = 0.5$, FR = 110 ml/min; $W = 4$ (triangles) and $W = 2$ (squares).

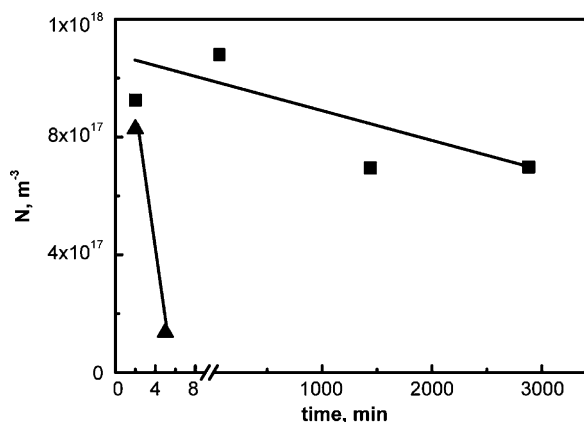


Fig. 12. Time evolution of the total particle number density (N) for $c_{Ti} = 0.5$ mol/l, $H = 0.25$, FR = 110 ml/min; $W = 4$ (triangles) and $W = 2$ (squares).

where c_W^0 is the initial water concentration, and $H_0 = 1.46$ is the average amount of water consumed immediately after hydrolysis in the first stages of particle formation; k_0 is therefore a kinetic constant that does not depend on titanium alkoxide and water concentrations, but only on the tendency of the primary particles to stick together and aggregate, namely for this particular case the hydrochloric acid content. If for $H = 0.5$ all the slopes from the different time evolutions are calculated a unique value

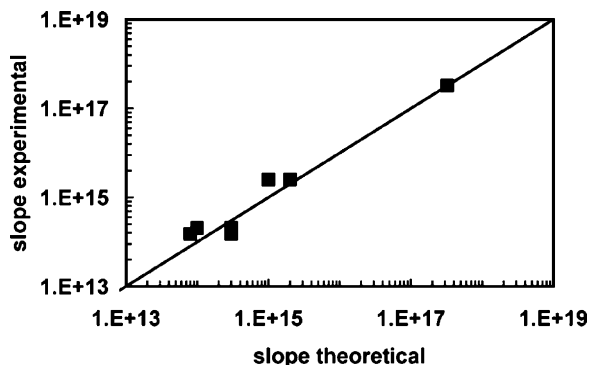


Fig. 13. Comparison between the experimental and calculated slope for the time evolution of total particle number density for all the investigated operating conditions and for $H = 0.5$.

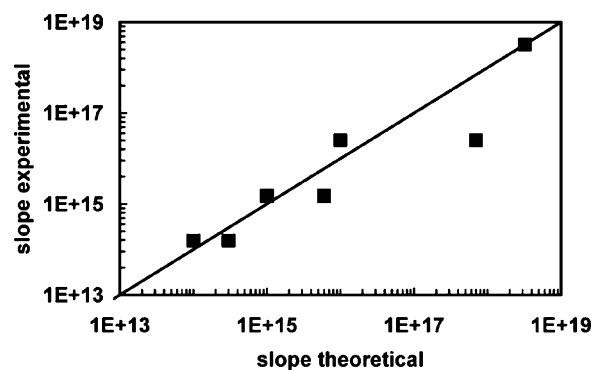


Fig. 14. Comparison between the experimental and calculated slope for the time evolution of total particle number density for all the investigated operating conditions and for $H = 0.25$.

of the kinetic constant that can fit all the experimental data is found. In Fig. 13 the comparison of the calculated and experimental slope for $k_0 = 6 \times 10^{15}$ and $p = 5$ is reported, and as it can be seen the agreement is satisfactory. In Fig. 14 the same comparison is reported for $H = 0.25$, resulting in this case in a bigger kinetic constant value $k_0 = 6 \times 10^{16}$ and $p = 5$; in fact, as previously observed the smaller is the acid content the faster is the aggregation process. It is also worth noticing that the value $p = 5$ is supported by other investigations [40], and can be obtained only if $n = 3$ and $k = 2$. In other words this result implies that adhesion between particles requires the condensation between three hydroxyl groups on each particle, with the second step being the kinetically limiting one (irreversible) and the others being at equilibrium.

These results confirm that during condensation particle aggregation is in the so-called reaction limited regime and therefore its rate is only affected by reactant concentrations as explained in Eq. (11). Nevertheless, it is worth reminding that the effect of mixing is still very important because it determines the initial particle size of the primary particles. Small differences in the primary particle size result in order of magnitudes of difference in the total particle number density, resulting therefore in very different time evolutions, but same kinetic constants.

5. Conclusions

In this work the production of titanium dioxide nanoparticles via the sol-gel route in a Vortex Reactor was considered. The main novelty of this work stands in the investigation of the effect of many operating parameters during synthesis including the mixing rate of the reactants. This investigation was carried out quantitatively by adopting a special passive mixer, whose characteristic mixing features can be easily tuned by manipulating the flow rate of the reactants. This analysis is supported by detailed CFD simulations of the velocity and turbulent fields in the reactor at the different operating conditions investigated.

The reported results clearly show that mixing plays a very important role: not only it determines the PSD of the particles formed immediately after mixing, but it affects also its subsequent evolution. In fact, as demonstrated by the theoretical analysis carried out in this work, after synthesis particles aggregate in the so-called reaction limited regime, but still since mixing determines the size, the number density and the hydrolysed state of the primary particles, it indirectly affects also the aggregation/condensation process.

The results seem to support that mixing can be actively used as one of the operating parameters during synthesis, rather than be passively accepted as a characteristic of the reactor adopted for particle synthesis. The use of adaptable mixing devices, such as the one described in this work, allows to tune the mixing rate in order to obtain the particulate product (e.g., sol or gel) with the desired particle size and morphology. Moreover, it should be highlighted that the CFD calculations, for the global mixing time-scale reported in this work, can be effectively used during process scale up. In fact, as showed in our previous work for precipitation and crystallization [36], a few selected experiments in one equipment (performed under different mixing rates) and CFD calculations of the characteristic time-scale of mixing, suffice to scale up the particle formation process. In fact, for the identical chemical recipe, the same particulate product is obtained in different reactors, if both reactors are operated under the same mixing conditions. The mixing conditions can be considered identical if the global mixing time, calculated with Eq. (7), is the same. Because, as showed with the experimental evidence reported in this work, the effect of mixing on this sol–gel process is very similar to that on standard precipitation, we can extend this scale up methodology to sol–gel processes.

Acknowledgement

This research project has been partially supported by the CRT foundation through the Lagrange project.

Appendix A. Supplementary data

Supplementary data associated with this article can be found, in the online version, at doi:10.1016/j.cej.2008.10.031.

Appendix B. Supplementary data

References

- [1] N.S. Allen, M. Edge, A. Ortega, C.M. Liauw, J. Stratton, R.B. McIntyre, Behaviour of nanoparticle (ultrafine) titanium dioxide pigments and stabilizers on the photooxidative stability of water based acrylic and isocyanate based acrylic coatings, *Polymer Degrad. Stab.* 78 (2002) 467–478.
- [2] K. Hasimoto, H. Irier, A. Fujishima, TiO₂ photocatalysis: a historical overview and future prospects, *Jpn. J. Appl. Phys.* 44 (2005) 8268–8301.
- [3] A. Fujishima, T.N. Rao, D.A. Tryk, Titanium dioxide photocatalysis, *J. Photochem. Photobiol. C* 1 (2000) 1–21.
- [4] G.-M. Zuo, Z.-X. Cheng, H. Chen, G.-W. Li, T. Miao, Study of photocatalytic degradation of several volatile organic compounds, *J. Hazard. Mater. B* 128 (2006) 158–163.
- [5] A.L. Linsebigler, G.Q. Lu, J.T. Yates, Photocatalysis on TiO₂ surfaces—Principles, mechanisms, and selected results, *Chem. Rev.* 95 (1995) 735–758.
- [6] S.S. Watson, D. Beydoun, J.A. Scott, R. Amal, The effect of preparation method on the photoactivity of crystalline titanium dioxide particles, *Chem. Eng. J.* 95 (2003) 213–220.
- [7] A. Mills, N. Elliott, G. Hill, D. Fallis, J.R. Durrant, R.L. Willis, Preparation and characterisation of novel thick sol–gel titania film photocatalysts, *Photochem. Photobiol. Sci.* 2 (2003) 591–596.
- [8] M.H. Habibi, H. Vosooghian, Photocatalytic degradation of some organic sulfides as environmental pollutants using titanium dioxide suspension, *J. Photochem. Photobiol. A* 174 (2005) 45–52.
- [9] R.R. Bacsa, J. Kiwi, Effect of rutile phase on the photocatalytic properties of nanocrystalline titania during the degradation of p-coumaric acid, *Appl. Catal. B* 16 (1998) 19–29.
- [10] J.M. Watson, A.T. Cooper, J.R.V. Flora, Nanoglued titanium dioxide aerogels for photocatalysis, *Env. Eng. Sci.* 22 (2005) 666–675.
- [11] M.C. Yan, F. Chen, J.L. Zhang, M. Anpo, Preparation of controllable crystalline titania and study on the photocatalytic properties, *J. Phys. Chem. B* 109 (2005) 8673–8678.
- [12] A. Testino, I.R. Bellobono, V. Buscaglia, C. Canevali, M. D'Arienzo, S. Polizzi, R. Scotti, F. Morazzoni, Optimizing the photocatalytic properties of hydrothermal TiO₂ by the control of phase composition and particle morphology. A systematic approach, *J. Am. Chem. Soc.* 129 (2007) 3564–3575.
- [13] R. Scotti, I.R. Bellobono, C. Canevali, C. Cannas, M. Catti, M. D'Arienzo, A. Musinu, S. Polizzi, M. Sommariva, A. Testino, F. Morazzoni, Sol–gel pure and mixed-phase titanium dioxide for photocatalytic purposes: relations between phase composition, catalytic activity, and charge-trapped Sites, *Chem. Mat.* 20 (2008) 4051–4061.
- [14] C. Su, B.-Y. Hong, C.-M. Tseng, Sol–gel preparation and photocatalysis of titanium dioxide, *Catal. Today* 96 (2006) 119–126.
- [15] M. Lackhoff, F. Prieto, N. Nestle, F. Dehn, R. Niessner, Photocatalytic activity of semiconductor-modified cement—Influence of semiconductor type and cement ageing, *Appl. Catal. B* 43 (2003) 205–216.
- [16] M. Keshmiri, T. Troczynski, M. Mohseni, Oxidation of gas phase trichloroethylene and toluene using composite sol–gel TiO₂ photocatalytic coatings, *J. Hazard. Mater. B* 128 (2006) 130–137.
- [17] A. Petrella, M. Tamborra, P.D. Cozzoli, M.L. Curri, M. Striccoli, P. Cosma, G.M. Farinola, F. Babudri, F. Naso, A. Agostiano, TiO₂ nanocrystals—MEHPPV composite thin films as photoactive material, *Thin Solid Films* 451–452 (2004) 64–68.
- [18] P.M. Ajayan, L.S. Schadler, P.V. Braun, *Nanocomposite Science and Technology*, Wiley-VCH, Weinheim, 2003.
- [19] S.E. Pratsinis, Flame aerosol synthesis of ceramic powders, *Prog. Energy Combust. Sci.* 24 (1998) 197–219.
- [20] Y.V. Kolen'ko, V.D. Maximov, A.A. Burukhin, V.A. Muhanov, B.R. Churagulov, Synthesis of ZrO₂ and TiO₂ nanocrystalline powders by hydrothermal process, *Mater. Sci. Eng. C* 23 (2003) 1003–1038.
- [21] Z. Li, B. Hou, Y. Xu, D. Wu, Y. Sun, W. Hu, F. Deng, Comparative study of sol–gel hydrothermal and sol–gel synthesis of titania–silica composite nanoparticles, *J. Solid State Chem.* 178 (2005) 1395–1405.
- [22] F. Sayilkan, M. Asilturk, S. Erdemoglu, M. Akarsu, H. Sayilkan, M. Erdemoglu, E. Arpac, Characterization and photocatalytic properties of TiO₂-nanosols synthesized by hydrothermal process at low temperature, *Mater. Lett.* 60 (2006) 230–235.
- [23] J. Yang, S. Mei, M.F. Ferreira, Hydrothermal processing of nanocrystalline anatase films from tetraethylammonium hydroxide peptized titania sols, *J. Eur. Ceram. Soc.* 24 (2004) 335–339.
- [24] X.-Z. Ding, X.-H. Liu, Synthesis and microstructure control of nanocrystalline titania powders via sol–gel process, *Mater. Sci. Eng. A* 224 (1997) 210–215.
- [25] C.W. Turner, Sol–gel process—principles and applications, *Ceram. Bull.* 70 (1998) 1487–1490.
- [26] M.T. Harris, H. Byers, Effect of solvent on the homogeneous precipitation of titania by titanium ethoxide hydrolysis, *J. Non-Cryst. Solids* 103 (1998) 49–64.
- [27] J. Blanchard, F. Ribot, C. Sanchez, P.-V. Bellot, A. Trokner, Structural characterization of titanium-oxo-polymers synthesized in the presence of protons or complexing ligands as inhibitors, *J. Non-Cryst. Solids* 265 (2000) 83–97.
- [28] C.J. Brinker, G.W. Scherer, *Sol–Gel Science—The Physics and Chemistry of Sol–Gel Processing*, Academic Press, San Diego, 1990.
- [29] K.Y. Jung, S.B. Park, M. Anpo, Photoluminescence and photoactivity of titania particles prepared by the sol–gel technique: the effect of the calcination temperature, *J. Photochem. Photobiol. A* 170 (2005) 247–252.
- [30] R.O. Fox, *Computational Models for Turbulent Reacting Flows*, Cambridge University Press, Cambridge, 2003.
- [31] B.K. Johnson, R.K. Prud'homme, Chemical processing and micromixing in confined impinging jets, *AIChE J.* 49 (2003) 2264–2282.
- [32] Y. Liu, R.O. Fox, CFD predictions for chemical processing in a confined impinging-jets reactor, *AIChE J.* 52 (2006) 731–744.
- [33] E. Gavi, D.L. Marchisio, A.A. Barresi, CFD modelling and scale-up of Confined Impinging Jet Reactors, *Chem. Eng. Sci.* 62 (2007) 2228–2241.
- [34] A. Soloviev, B. Ivanov, R. Tufeu, A.V. Kanaev, Nanoparticle growth during the induction period of the sol–gel process, *J. Mater. Sci. Lett.* 20 (2001) 905–906.
- [35] D.L. Marchisio, M. Soos, J. Sefcik, M. Morbidelli, Role of turbulent shear rate distribution in aggregation and breakage processes, *AIChE J.* 52 (2006) 158–173.
- [36] D.L. Marchisio, L. Rivautella, A.A. Barresi, Design and scale-up of chemical reactors for nanoparticle precipitation, *AIChE J.* 52 (2006) 1877–1887.
- [37] E. Gavi, D.L. Marchisio, A.A. Barresi, On the importance of mixing for the production of nano-particles, *J. Disp. Sci. Tech.* 29 (2008) 548–554.
- [38] F. Lince, D.L. Marchisio, A.A. Barresi, Strategies to control the particle size distribution of poly-caprolactone nanoparticles for pharmaceutical applications, *J. Coll. Int. Sci.* 332 (2008) 505–515.
- [39] E. Gavi, L. Rivautella, D.L. Marchisio, M. Vanni, A.A. Barresi, G. Baldi, CFD modelling of nano-particle precipitation in Confined Impinging Jet Reactors, *Chem. Eng. Res. Des.* 85 (A5) (2007) 735–744.
- [40] M. Rivallin, M. Benmami, A. Kanaev, A. Gaunand, Sol–gel reactor with rapid micromixing. Modelling and measurements of titanium dioxide nano-particle growth, *Chem. Eng. Res. Des.* 83 (A1) (2005) 67–74.
- [41] M.Z. Smoluchowski, Versuch Einer Mathematischen Theorie Der Koagulation-skinetik Kolloider Losunger, *Z. Phys. Chem.* 92 (1917) 129–145.
- [42] M. Soos, D.L. Marchisio, J. Sefcik, R.O. Fox, M. Morbidelli, Assessment of gel formation conditions in turbulent jets, in: *Proceedings of the Fifth World Congress on Particle Technology*, Orlando, FL, USA, April 23–27, 2006.
- [43] D.L. Marchisio, M. Soos, J. Sefcik, M. Morbidelli, A.A. Barresi, G. Baldi, Effect of fluid dynamics on particle size distribution in particulate processes, *Chem. Eng. Technol.* 29 (2006) 191–199.
- [44] D.L. Marchisio, F. Omegna, A.A. Barresi, P. Bowen, Effect of mixing and other operating parameters in sol–gel processes, *Ind. Eng. Chem. Res.* 47 (2008) 7202–7210.

- [45] Y. Liu, C.Y. Cheng, Y. Liu, R.K. Prud'homme, R.O. Fox, Mixing in a multi-inlet vortex mixer (MIVM) for flash nano-precipitation, *Chem. Eng. Sci.* 63 (2008) 2829–2842.
- [46] B.K. Johnson, Flash nanoprecipitation of organic actives via confined micromixing and block co-polymer stabilization, PhD Thesis, Princeton University, (2003).
- [47] S. Valerio, M. Vanni, A.A. Barresi, G. Baldi, Engineering modelling of turbulent flows in chemical engineering applications, *Trends Chem. Eng.* 5 (1998) 1–44.
- [48] A. Soloviev, R. Tufeu, C. Sanchez, A. Kanaev, Nucleation stage in the $\text{Ti}(\text{OPri})_4$ sol-gel process, *J. Phys. Chem. B* 105 (2001) 4175–4180.

Solvothermal Synthesis of Tungsten Oxide Nanorod/Nanowire/ Nanosheet

Hong Goo Choi, Young Hwa Jung, and Do Kyung Kim*[†]

Department of Materials Science and Engineering, Korea Advanced Institute of Science and Technology (KAIST),
Taejeon 305-701, Korea

A simple process enables to synthesize tungsten oxide with various nanomorphologies, i.e. nanorods, nanowires, and nanosheets. The tungsten hexachloride (WCl₆) was used as a raw material and the tungsten oxide nanoparticles were obtained by solvothermal treatment with solvents, i.e., ethanol, mixed solvent (ethanol+water), and water, at 200°C for 10 h. The various crystalline phases of tungsten oxide, such as monoclinic W₁₈O₄₉ nanorods, hexagonal WO₃ platelets, and monoclinic WO₃ nanosheets, were synthesized by simply changing the composition of the solvent. The oxygen, which was contained in water, played an important role in the final tungsten oxide phase. Especially, W₁₈O₄₉ nanorods grew to nanowires as the concentration of WCl₆ was decreased. Using this simple process, it will be possible to control the crystalline phase and morphologies of nanostructured tungsten oxide system.

NANOSIZED transition metal oxides, because of their high surface areas, are promising candidates for a vast range of applications including positive electrode materials for lithium-ion batteries, photoelectrochemical cells, electrochromic display, and sensors.^{1–4} Among various metal oxides, tungsten oxide has found useful application in electrochromic devices, semiconductor gas sensors, and photocatalysis.^{5–7} Sodium-doped WO₃ is also reported to be a high-temperature superconductor with $T_c = 90$ K.⁸ Especially, one-dimensional tungsten oxides have been of special interest due to their lower dimensionality and superior properties. Tungsten oxide nanowires or nanorods were synthesized by heat treatment of tungsten metal,^{9–11} such as, a tungsten wire partly wrapped with boron oxide in nitrogen atmosphere at 1600°C, an electrochemical etched tungsten tip at 700°C in an Ar atmosphere, and a tungsten foil, partly covered by a SiO₂ plate, in an Ar atmosphere at 1600°C. Recently, tungsten oxide nanorod and nanowire were synthesized by a wet chemical reaction^{12,13} that could control the particle shape and size, and make large-scale production possible.

Nanorods and nanowires with uniform sizes and aspect ratios have been synthesized by different techniques; for example, ZnO in the vapor–liquid–solid method, silver in capping reagent, and TiO₂ in the template method.^{14–16} Solvothermal synthesis, which utilizes a solvent under high pressures and temperatures to increase the solubility of solid and to enhance the reaction rate, is also one of the methodologies for generating a one-dimensional nanostructure. The advantage of this process is that most materials can be made soluble in a proper solvent by heating and pressurizing the system close to its critical point. Using solvo-

thermal synthesis, CdE (E = S, Se, Te), CdWO₄, and La₂O₂S nanocrystals (nanorods/nanowires/nanoparticles) have been successfully achieved.^{17–19}

In this work, we report a simple process for synthesizing tungsten oxide with various morphologies of nanostructures, i.e. nanorods, nanowires, and nanosheets. The process also enables to control the crystalline phase of tungsten oxide, such as monoclinic W₁₈O₄₉, hexagonal WO₃, and monoclinic WO₃, by simply changing the composition of solvent.

The starting solution was prepared by dissolving 8.1 g of tungsten hexachloride (98%, WCl₆, Aldrich, Milwaukee, WI) in 200 mL of ethanol (99.8%, Merck, Germany). For the solvothermal reaction, final solutions were prepared by mixing 60.0 mL of ethanol, 2.0–10.0 vol. % of distilled water with ethanol, and 100% distilled water with 10.0 mL of the starting solution. ([WCl₆] = 0.014M). The prepared solution was transferred to 100-mL Teflon-lined acid digestion bombs. Solvothermal synthesis was conducted at 200°C for 10 h in an electric oven. The reaction conditions of each sample are shown in Table I. After the reactions, particles were obtained by centrifugation and by washing with ethanol. The obtained particles were characterized with X-ray diffraction (XRD, CuK α radiation, RIGAKU D/max-IIIC, Tokyo, Japan), scanning electron microscopy (SEM, PHILIPS XL30, Eindhoven, The Netherlands), and transmission electron microscopy (TEM, JEOL JEM3010, Tokyo, Japan).

Figure 1 shows TEM micrograph of tungsten oxide particles that were synthesized by the solvothermal treatment at 200°C for 10 h in different solvent; (a) sample ES synthesized with ethanol as solvent, (c) sample MS with mixed solvent, and (e) sample WS with water. At increased water content in solvent, the particle shape was changed from nanorods or nanowires to hexagonal platelets, and finally to square nanosheets with water. On the basis of the TEM analysis with about 100 nanorods, the average diameter of these uniform nanorods was 6.2 ± 1.1 nm and the length of the nanorods was 116.4 ± 20 nm (aspect ratio ≈ 19) (Fig. 1(a)). Hexagonal platelets were about 2 μ m in size and 250 nm in thickness based on SEM micrographs. The final particles in water as solvent were agglomerates composed of square nanosheets; the nanosheets were easily separated and displayed edge cracking after sonification. The particle size of square nanosheets was 150 nm and their thickness was thin so that it was possible to observe the HRTEM image in the normal direction to the plane. When mixed solvent (ethanol+water) was used, the color of as-prepared tungsten oxide particles changed from dark blue to light blue with the change of water content from 0 to 10 vol%. Yellowish particles were obtained from the solvent of 100 vol% water. Tungsten oxide has various colors with different W/O molar ratio, such as brown WO₂ phase, blue sub oxide of W, and yellow WO₃. These color changes occurred due to the various valencies of the transition metal W. Therefore, the color change in our system implied that the tungsten oxide crystalline phase had changed with the composition of solvents. That is, as the amount of water in mixed solvent increases, the mole fraction of oxygen in the tungsten oxide system also increases because water is a source of oxygen in the solvo-

L. C. Klein—contributing editor

Manuscript No. 11040. Received May 18, 2004; approved January 6, 2005.
Supported by Center for Nanostructured Materials Technology (CNMT) of the 21st Century Frontier R&D program funded by Korean Ministry of Science and Technology.
^{*}Member, American Ceramic Society.
[†]Author to whom correspondence should be addressed. e-mail: dkkim@kaist.ac.kr

Table I. Reaction Conditions and Results for the Synthesis of Tungsten Oxide

Sample ID	Solvothermal condition and solvent	Morphology of tungsten oxide	Phase and composition
ES	200°C/10 h with ethanol	Nanorods/nanowires	Monoclinic—W ₁₈ O ₄₉
MS	200°C/10 h with water/ethanol (1:9) mixed solvent	Hexagonal platelets	Hexagonal—WO ₃
WS	200°C/10 h with water	Square nanosheets	Monoclinic—WO ₃

thermal synthesis. An HRTEM micrograph taken from one individual nanorod confirms that the nanorod grows along the [010] direction (indicated with an arrow). The 3.78 Å spacing corresponds to the {010} interplanar distance of monoclinic W₁₈O₄₉ (Fig. 1(b)). The HRTEM micrograph of tungsten oxide nanorod accorded with that of previous researches.^{12,13} Figure 1(d) shows the atomic-resolution micrograph of hexagonal platelets, with the electron beam parallel to the [0001] direction. The crystal planes are separated by 6.34 Å, which coincide with the {1000} plane of hexagonal WO₃ phase. The crystallographic angle was 90.9° and the interplanar spacings of nanosheets were 3.69 and 3.76 Å, which also correspond to {020} and {200} of monoclinic WO₃, respectively. On the report of W–O system, the presence of water vapor is important for the production and growth of W₁₈O₄₉; however, the existence of moisture is not a necessary condition for the growth of W₁₈O₄₉.²⁰ The tungsten suboxides have been prepared by controlled reduction of WO₃ in certain gas atmospheres such as CO/CO₂ mixtures or H₂/H₂O mixtures.^{21, 22} The result of this study shows that the solvent composition strongly affected the morphology and crystalline phase of tungsten oxide, i.e., nanorod W₁₈O₄₉, hexagonal platelet WO₃, and nanosheet WO₃. That is, various tungsten oxides were obtained by controlling oxygen percent of solvent as controlling oxygen potential of gas mixture in the previous literature.

Figure 2 shows XRD patterns of tungsten oxide prepared by the solvothermal treatment with different solvents. The XRD pattern of tungsten oxide nanorod matched with monoclinic W₁₈O₄₉ (JCPDS No. 05-0392). XRD peak intensity of the (010) plane was relatively higher than that of other planes. This implies that the nanorods grow along the [010] direction. Hexagonal platelets and square nanosheets were hexagonal WO₃ (JCPDS No. 33-1387) and monoclinic WO₃ (JCPDS No. 43-1035), respectively. These XRD results reconfirmed the crystalline phase of tungsten oxide and corresponded to the atomic image in HRTEM micrographs. From the XRD results, the crystalline phase of tungsten oxide could be controlled by the content of water in the solvent. Nanorods of W₁₈O₄₉ were sta-

ble in ethanol (without water), hexagonal WO₃ phase was obtained from the ethanol–water mixed solvent with a small amount of water (2–10 vol%), and finally monoclinic WO₃ phase was obtained from water. It was considered that the oxygen, which was contained in water, played an important role in the final tungsten oxide phase. The formation of hexagonal WO₃ phase in mixed solvent is worthy noting. Hexagonal WO₃ phase was usually achieved by dehydration of WO₃· $\frac{1}{3}$ H₂O²³ and was intensively investigated, especially as an intercalation host for obtaining hexagonal tungsten bronzes M_xWO₃ and a promising material for positive electrodes of rechargeable lithium batteries. In our research, hexagonal WO₃ phase was easily and directly obtained (no heat treatment) by solvothermal synthesis.

Figure 3 represents tungsten oxide nanowires, rather than nanorods, which were synthesized by solvothermal treatment with ethanol. Synthesis conditions were same as Fig. 1(a) except that the WCl₆ concentration decreased from 0.014M to 0.007M. The average diameter of tungsten oxide nanowires was similar to the nanorods. The measured mean diameter of nanowires on the basis of the TEM investigation was 5.2±1.4 nm, and the length of the nanowires was up to several microns. Therefore, the nanowires reached a high aspect ratio of more than 100. The tungsten oxide nanowires also showed the phase of monoclinic W₁₈O₄₉, which was confirmed by XRD results. Moon *et al.*²⁴ reported that the feedstock concentration greatly influences particle morphology of the hydrothermally derived oxides. At lower feedstock concentration, the particle shape was tabular, whereas cubic particles were produced at a higher concentration. The shape of a crystal is determined by the difference in the relative growth rates of the individual crystal planes, and the resulting particles are anisotropic in shape under a certain supersaturation. In our experiment, one-dimensional growth of tungsten oxide nanorod (W₁₈O₄₉) along the <010> direction was enhanced at a lower concentration. It was considered that the lower concentration of feedstock solution contributed to the lower supersaturation of tungsten source, which enhanced the growth of tungsten oxide nanorod.

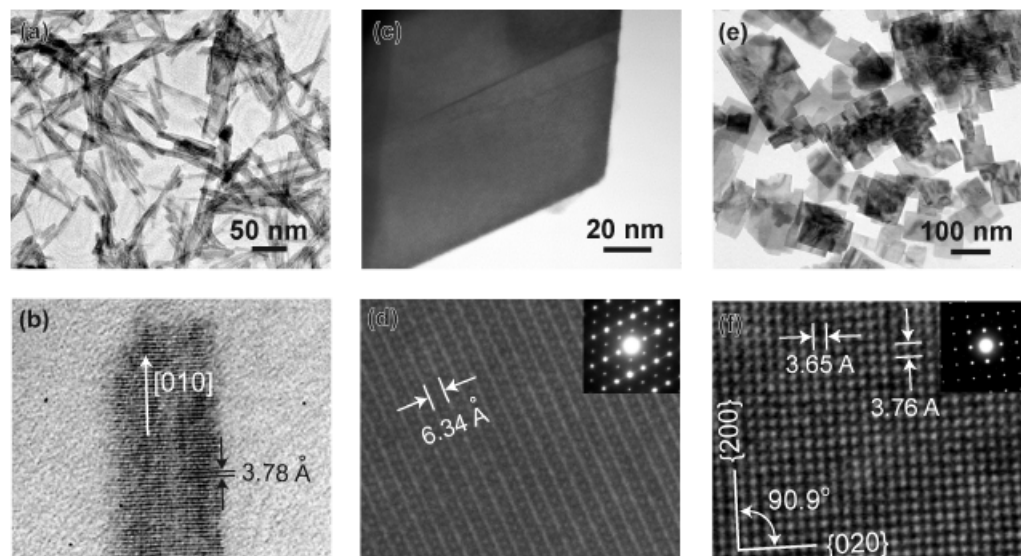


Fig. 1. TEM images (top) and corresponding high-resolution atomic images (bottom) of tungsten oxide particles: (a), (b) sample ES, monoclinic W₁₈O₄₉; (c), (d) sample MS, hexagonal WO₃; and (e), (f) sample WS, monoclinic WO₃.

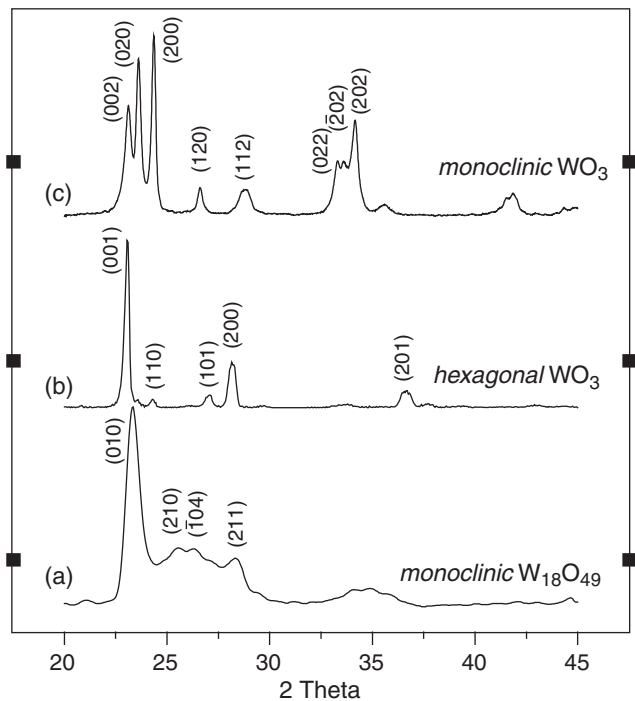


Fig. 2. X-ray diffraction patterns of tungsten oxide nanostructures synthesized by solvothermal treatment in different solvents; (a) monoclinic $W_{18}O_{49}$ nanorods (ES), (b) hexagonal WO_3 platelets (MS), and (c) monoclinic WO_3 nanosheets (WS).

In summary, we report a simple solvothermal process to synthesize tungsten oxide nanoparticles with different solvents. The composition and concentration of solvent played an im-

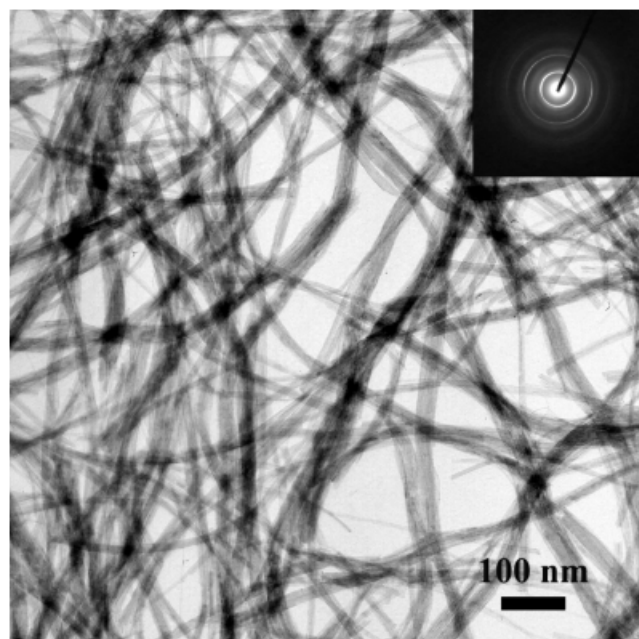


Fig. 3. TEM micrograph of tungsten oxide nanowires as the concentration of WCl_6 solution decreased from 0.014M to 0.007M.

portant role in controlling the shape and phase of tungsten oxide. Monoclinic $W_{18}O_{49}$ nanorods and nanowires were obtained in ethanol, hexagonal WO_3 in ethanol–water mixed solvents (2–10 vol% water), and monoclinic WO_3 in water. Using this simple approach, it will be possible to control the crystalline phase and morphologies of the nanostructured tungsten oxide system.

References

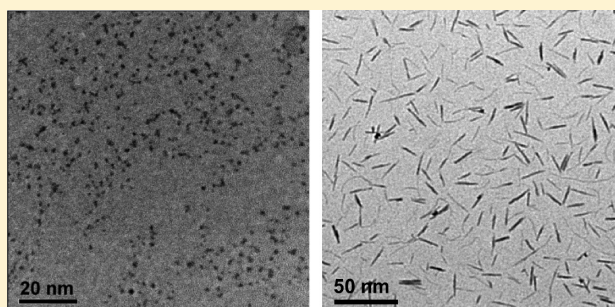
- P. Poizot, S. Laruelle, S. Grugeon, L. Dupont, and J.-M. Tarascon, "Nano-Sized Transition-Metal Oxides as Negative-Electrode Materials for Lithium-Ion Batteries," *Nature*, **407**, 496–9 (2000).
- P. Knauth and H. L. Tuller, "Solid-State Ionics: Roots, Status, and Future Prospects," *J. Am. Ceram. Soc.*, **85**, 1654–80 (2002).
- M. Sun, N. Xu, Y. W. Cao, J. N. Yao, and E. G. Wang, "Nanocrystalline Tungsten Oxide Thin Film: Preparation, Microstructure, and Photochromic Behavior," *J. Mater. Res.*, **15**, 927–33 (2000).
- J. L. Solis, A. Heel, L. B. Kish, C. G. Granqvist, S. Saukko, and V. Lantto, "Gas-Sensing Properties of Nanocrystalline WO_3 Films Made by Advanced Reactive Gas Deposition," *J. Am. Ceram. Soc.*, **84**, 1504–8 (2001).
- O. Lev, Z. Wu, S. Bharathi, V. Glezer, A. Modestov, J. Gun, L. Rabinovich, and S. Sampath, "Sol-Gel Materials in Electrochemistry," *Chem. Mater.*, **9**, 2354–75 (1997).
- M. Ferroni, V. Guidi, G. Martinelli, and G. Sberveglieri, "Microstructural Characterization of a Titanium–Tungsten Oxide Gas Sensor," *J. Mater. Res.*, **12**, 793–8 (1997).
- X. Z. Li, F. B. Li, C. L. Yang, and W. K. Ge, "Photocatalytic Activity of WO_3 - TiO_2 Under Visible Light Irradiation," *J. Photochem. Photobiol. A*, **141**, 209–17 (2001).
- S. Reich and Y. Tsabba, "Possible Nucleation of a 2D Superconducting Phase on WO_3 Single Crystals Surface Doped with Na^+ ," *Eur. Phys. J. B*, **9**, 1–4 (1999).
- Z. Liu, Y. Bando, and C. Tang, "Synthesis of Tungsten Oxide Nanowires," *Chem. Phys. Lett.*, **372**, 179–82 (2003).
- G. Gu, B. Zheng, W. Q. Han, S. Roth, and J. Liu, "Tungsten Oxide Nanowires on Tungsten Substrates," *Nano Lett.*, **2**, 849–51 (2002).
- Y. Q. Zhu, W. Hu, W. K. Hsu, M. Terrones, N. Grobert, J. P. Hare, H. W. Kroto, D. R. M. Walton, and H. Terrones, "Tungsten Oxide Tree-Like Structures," *Chem. Phys. Lett.*, **309**, 327–34 (1999).
- K. Lee, W. S. Seo, and J. T. Park, "Synthesis and Optical Properties of Colloidal Tungsten Oxide Nanorods," *J. Am. Chem. Soc.*, **125**, 3408–9 (2003).
- X. W. Lou and H. C. Zeng, "An Inorganic Route for Controlled Synthesis of $W_{18}O_{49}$ Nanorods and Nanofibers in Solution," *Inorg. Chem.*, **42**, 6169–71 (2003).
- M. H. Huang, Y. Wu, H. Feick, N. Tran, E. Weber, and P. Yang, "Catalytic Growth of Zinc Oxide Nanowires by Vapor Transport," *Adv. Mater.*, **13**, 113–6 (2001).
- Y. Sun, B. Gates, B. Mayers, and Y. Xia, "Crystalline Silver Nanowires by Soft Solution Processing," *Nano Lett.*, **2**, 165–8 (2002).
- P. Hoyer, "Formation of a Titanium Dioxide Nanotube Array," *Langmuir*, **12**, 1411–3 (1996).
- S.-H. Yu, Y.-S. Wu, J. Yang, Z.-H. Han, Y. Xie, Y.-T. Qian, and X.-M. Liu, "A Novel Solvothermal Synthetic Route to Nanocrystalline CdE (E = S, Se, Te) and Morphological Control," *Chem. Mater.*, **10**, 2309–12 (1998).
- H.-W. Liao, Y.-F. Wang, X.-M. Liu, Y.-D. Li, and Y.-T. Qian, "Hydrothermal Preparation and Characterization of Luminescent $CdWO_4$ Nanorods," *Chem. Mater.*, **12**, 2819–21 (2000).
- Y. Jiang, Y. Wu, Y. Xie, and Y. T. Qian, "Synthesis and Characterization of Nanocrystalline Lanthanide Oxysulfide via a $La(OH)_3$ Gel Solvothermal Route," *J. Am. Ceram. Soc.*, **83**, 2628–30 (2000).
- F. R. Sale, "Thermochemistry and Phase Equilibria in the W–O, W–C and Related W–Co-Containing Ternary Systems," *J. Less-Common Metals*, **100**, 277–97 (1984).
- G. R. S. Pierre, W. T. Ebihara, M. J. Pool, and R. Speiser, "The Tungsten-Oxygen System," *Trans. Metall. Soc. AIME*, **224**, 259–64 (1962).
- F. R. Sale, "Heat Capacities of the Tungsten Oxides WO_3 , $W_{20}O_{58}$, $W_{18}O_{49}$ and WO_2 ," *Thermochim. Acta*, **30**, 163–71 (1979).
- B. Gerand, G. Nowogrocki, J. Guenot, and M. Figlarz, "Structural Study of a new Hexagonal form of Tungsten Trioxide," *J. Solid State Chem.*, **29**, 429–34 (1979).
- J. Moon, M. L. Carasso, H. G. Krarup, J. A. Kerchner, and J. H. Adair, "Particle-Shape Control and Formation Mechanisms of Hydrothermally Derived Lead Titanate," *J. Mater. Res.*, **14**, 866–75 (1999). □

Solvothermal Synthesis of Ultrasmall Tungsten Oxide Nanoparticles

Nikolaos Soultanidis,^{†,⊥} Wu Zhou,^{‡,¶} Christopher J. Kiely,[‡] and Michael S. Wong^{*,†,§,||}[†]Department of Chemical and Biomolecular Engineering, Rice University, Houston, Texas 77005, United States[‡]Department of Materials Science & Engineering, Lehigh University, Bethlehem, Pennsylvania 18015, United States[§]Department of Chemistry, Rice University, Houston, Texas 77005, United States^{||}Department of Civil and Environmental Engineering, Rice University, Houston, Texas 77005, United States

Supporting Information

ABSTRACT: The synthesis of catalytically useful, ultrasmall oxide nanoparticles (NPs) of group 5 and 6 metals is not readily achievable through reported methods. In this work, we introduce a one-pot, two-precursor synthesis route to <2 nm MO_x NPs in which a polyoxometalate salt is decomposed thermally in a high-boiling organic solvent oleylamine. The use of ammonium metatungstate resulted in oleylamine-coated, crystalline WO_x NPs at consistently high yields of $92 \pm 5\%$. The semicrystalline NPs contained 20–36 WO_x structural units per particle, as determined from aberration-corrected high-resolution scanning transmission electron microscopy, and an organic coating of 16–20 oleylamine molecules, as determined by thermogravimetric analysis. The NPs had a mean size of 1.6 ± 0.3 nm, as estimated from atomic force microscopy and small-angle X-ray scattering measurements. Carrying out the synthesis in the presence of organic oxidant trimethylamine *N*-oxide led to smaller WO_x NPs (1.0 ± 0.4 nm), whereas the reductant 1,12-dodecanediol led to WO_x nanorods (4 ± 1 nm \times 20 ± 5 nm). These findings provide a new method to control the size and shape of transition metal oxide NPs, which will be especially useful in catalysis.



1. INTRODUCTION

Efficient structural control at the nanometer scale (<5 nm) is of increasing interest for the synthesis of metal oxide nanoparticles (MO_x NPs) that have exceptional physical and chemical properties with potential applications in the fields of energy storage^{1–4} and conversion,^{1,5} gas sensing,^{6–10} and catalysis.^{11–13} Thermodynamic limitations, as well as experimental considerations, lead to significant barriers in the controlled synthesis of ultrasmall MO_x NPs. This is especially true in the case for oxides of early transition metals such as W,^{14–18} Mo,^{19–23} and V^{24–29} where larger NPs, usually in the shape of rods or wires, are commonly produced.

WO_x NPs have been successfully synthesized via chemical vapor deposition,^{30,31} sonochemical,³² reverse microemulsion,³³ combustion,³⁴ and solvothermal techniques with a focus on generating 1-dimensional WO_x nanorods^{4,15,18,35–37} or nanowires^{10,14,30,38} and 2-dimensional films^{31,39–42} due to their interesting optical,^{15,31,40,41} semiconducting,^{34,39} and photocatalytic⁴² properties. Solvothermal synthesis involves the heating of solvents and metal coordination compounds in the presence of an organic capping agent at high temperatures. It is comprised usually of three stages: (1) heating of the solution or slurry suspension during which dissociation of the metal precursor occurs (usually above 523 K); (2) aging of the solution at the desired temperature for further particle nucleation and growth that determines the final size and

surface properties of the particles; and (3) particle separation and collection from the unreacted material and the solvent.

Supported tungsten oxide catalysts essentially comprise molecular WO_x species ranging in size, supported on a catalytically inert metal oxide. Such materials are typically prepared through impregnation of a metal oxide support with a tungstate salt solution and subsequent calcination to form a supported metal oxide catalyst. For many reactions, <2 nm WO_x NPs are responsible for high catalytic activity.^{43–46} These NP species have not previously been synthesized by colloidal methods or studied in an unsupported form.

In this study, we report the synthesis and characterization of 1.6 ± 0.3 nm WO_x NPs using a polyoxometalate salt (ammonium metatungstate hydrate) and a cationic organic amine (oleylamine). The effects of an oxidizing agent and a reducing agent on NP synthesis were studied using trimethylamine *N*-oxide and 1,12-dodecanediol, respectively. The nanostructures were studied in detail using a suite of characterization methods, which included aberration-corrected high-resolution scanning transmission electron microscopy, small-angle X-ray scattering, dynamic light scattering, atomic force microscopy, and thermogravimetric analysis. This method of decomposing polyanion salts in an oil was extended to the

Received: July 20, 2012

Revised: November 27, 2012

Published: December 11, 2012

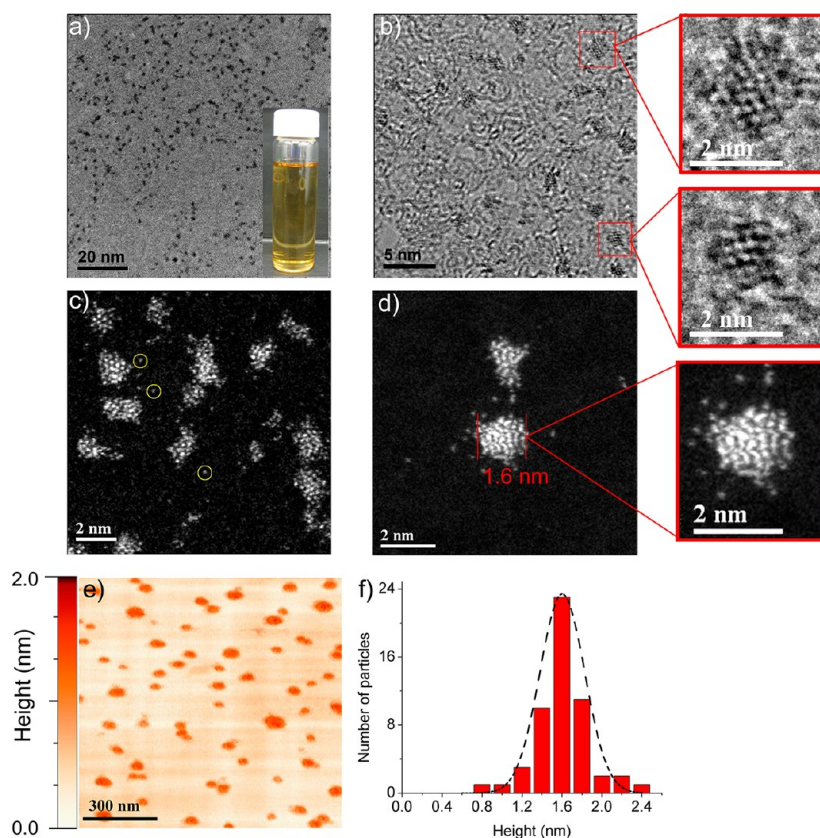


Figure 1. (a) BF-TEM, (b) HR-TEM, and (c, d) HAADF STEM images of WO_x NPs supported on continuous amorphous carbon film. (e) AFM image and (f) corresponding particle height distribution of WO_x NPs supported on HOPG. Insets to panels b and d: single WO_x NPs at higher magnification.

synthesis of molybdenum oxide (MoO_x) and vanadium oxide (VO_x) NPs.

2. EXPERIMENTAL SECTION

Chemicals. Ammonium metatungstate hydrate (AMT, $(\text{NH}_4)_6\text{H}_2\text{W}_{12}\text{O}_{40}\cdot x\text{H}_2\text{O}$), ammonium molybdate tetrahydrate (AMM, $(\text{NH}_4)_6\text{Mo}_7\text{O}_{24}\cdot 4\text{H}_2\text{O}$), ammonium metavanadate (AMV, NH_4VO_3), oleylamine (1-amino-9-octadecene) (70% purity, Sigma-Aldrich), acetone, toluene, trimethylamine *N*-oxide (TANO), and 1,2-dodecanediol were purchased from Sigma-Aldrich. All chemicals were used without further purification.

Synthesis of WO_x NPs. The synthetic procedure consists of three steps: synthesis, nanoparticle separation, and redispersion in an organic solvent. First, a slurry suspension of the ammonium salt (0.1 mmol) and 20 mL of oleylamine was introduced into a four-neck flask and slowly heated up to 523 K at a controlled rate of 2.0 K/min under continuous flowing argon ($10\text{ cm}^3/\text{min}$). A reflux condenser was used to prevent any loss of oleylamine due to evaporation. The suspension was then left to soak for 2 h and cooled down to room temperature. Particle collection consisted of washing with acetone (20 mL) and centrifuging at 4000 rpm for 2 h. After removing the supernatant (containing excess oleylamine and acetone), the acquired NPs were dried at room temperature and then redispersed in toluene. Finally, the toluene suspension of the NPs was centrifuged to remove any larger agglomerates.

To understand the effect of an oxidizing agent on NP synthesis, a series of experiments were performed by adding 5 mmol of TANO to the initial slurry suspension. To understand the effect of a reducing agent on NP synthesis, 5 mmol of 1,12-dodecanediol was added instead of TANO. MoO_x and VO_x nanoparticles were also synthesized by a similar procedure, whereby the AMT was substituted with AMM and AMV, respectively.

Characterization Methods. To determine the MO_x particle morphology and composition, the following characterization tools were employed.

Samples of the as-synthesized WO_x NPs were prepared for TEM/STEM analysis by pipetting a drop of toluene suspension of the WO_x NPs onto a continuous ultrathin carbon film supported on a copper mesh TEM grid. The TEM samples were left under ambient conditions until the solvent had completely evaporated. Bright field (BF) and high-resolution TEM (HRTEM) images of the samples were obtained using a JEOL 2100FX TEM operating at 200 kV.

Aberration-corrected high-angle annular dark field (HAADF) *Z*-contrast imaging experiments were performed on a 200 kV JEOL 2200FS (S)TEM equipped with a CEOS probe C_s -corrector. For STEM-HAADF imaging, typically a $\sim 1\text{ \AA}$ (fwhm) coherent electron beam with $\sim 30\text{ pA}$ probe current was used. Dwell times between 48 and $62\text{ }\mu\text{s}$ per pixel were typically employed. The TEM samples for the as-synthesized WO_x NPs were pretreated with an “electron beam shower” in order to reduce the carbon contamination during high-magnification STEM-HAADF image acquisition. This electron beam shower treatment entailed allowing a broad intense electron probe to illuminate a large area of the sample for a short time, which can in principle reduce the mobility of any adsorbed hydrocarbon molecules. The HAADF images presented were low-pass filtered to reduce background noise. During our experiments, the electron dose levels for the electron beam shower and subsequent imaging experiments were carefully chosen to minimize the electron-beam-induced knock-on damage to the samples, while still achieving the purpose of minimizing carbon contamination (Supporting Information, Figure S1). The particle size analysis was performed using the Image J software package.⁴⁷

Atomic force microscopy (AFM) measurements were performed on a digital instrument Nanoscope IIIA AFM using a PointProbe Plus Non-Contact tip in Tapping Mode-High Resonance Frequency (PPP-

NCH). The AFM resolution along the *x*- and *y*-axis is low due to (i) the AFM tip diameter (~20 nm) and (ii) the interaction between the tip and the NP ligands (oleylamine), but it is high along the *z*-axis (~0.3 nm). NPs dispersed in toluene were deposited and spin-coated onto a highly ordered pyrolytic graphite (HOPG) substrate for optimal imaging properties. The flat nature of the HOPG surface made it ideal for detecting the smallest of particles. Image analysis was performed using the WSM software package,⁴⁸ and particle size distributions were calculated using Origin (OriginLab, Northampton, MA).

Dynamic light scattering (DLS) studies were used to measure WO_x NP hydrodynamic diameter size when suspended in toluene using a ZetaPALS (Brookhaven Instruments Corporation) instrument equipped with a He–Ne laser ($I = 656$ nm), a detector set at 363 K, and a BI-9000AT digital autocorrelator that records scattered light. The NP suspension was transferred into 4 mL quartz cuvettes at room temperature and analyzed in triplicate over intervals of 3 min to ensure reproducibility. The laser was stabilized for 15 min prior to each measurement, and the instrument was calibrated using a polystyrene bead standard (diameter: 92 ± 3 nm). Non-negative least-squares (NNLS) and CONTIN fitting routines in the instrument software (9KDLSW) were used.⁴⁹ The particle hydrodynamic diameter was calculated using the Stokes–Einstein relation.

Small-angle X-ray scattering (SAXS) studies were performed on a Rigaku SmartLab X-ray diffractometer using a Cu $K\alpha$ radiation source ($\lambda = 1.54$ Å). A toluene suspension of WO_x NPs was sealed in a borosilicate glass capillary and analyzed in transmission mode at 40 kV and 44 mA. Average particle sizes were determined by simulating the peak widths from reflections with 2θ values in the 0.2° – 4.0° range using Nanosolver (Rigaku software).⁵⁰ A core/shell model was applied for the SAXS calculations, and the shell (oleylamine) thickness was set to 2 nm. Experimental and simulated (fitted) data were matched satisfactorily for $2\theta > 0.04^\circ$ (i.e., *R*-factor <2%).

Thermogravimetric analysis (TGA) was performed on a Q600 TA instrument in order to calculate the organic content of the particles. Samples that had previously been dried at room temperature overnight were heated up to 1073 K at a ramp rate of 3.0 K/min under flowing air (100 mL/min). Combined TGA-FTIR^{51–53} analysis was performed to study the decomposition of AMT in the presence of oleylamine. To simulate the synthesis conditions, the sample was heated under continuous flowing argon and the outgas line was passed into a Nicolet FTIR. The line between the TGA and the FTIR was heated at 393 K to prevent any condensation. In this case, sample preparation consisted of drying the sample at room temperature overnight and then heating up to 523 K at a ramp rate of 2.0 K/min under flowing argon (50 cm^3 /min).

X-ray diffraction (XRD) patterns were acquired on a Rigaku D/Max-2100PC using a continuous scanning mode with 0.02° step size⁴⁶ and a scan rate of 2.5 s/step. Ultraviolet–visible absorption spectra were collected using a Shimadzu UV-2401 PC spectrometer. Toluene suspensions of WO_x NPs, WO_x sNPs, and WO_x -NRs were placed into quartz cuvettes, and spectra were collected across the 400–900 nm wavelength range.

3. RESULTS AND DISCUSSION

WO_x Nanoparticle Structure. DLS analysis verified the formation of WO_x NPs; the NNLS and CONTIN routines consistently gave average hydrodynamic diameters of 1.1 ± 0.2 and 1.3 ± 0.2 nm, respectively. From SAXS analysis, the NP size was ~1.7 nm (Figure S2).

Representative BF-TEM and HRTEM images of the as-synthesized WO_x NPs are shown in Figures 1a and 1b, respectively. These WO_x NPs were found to have very small average size (1.6 nm) and a narrow size distribution (standard deviation of 0.2 nm). The HRTEM image presented in Figure 1b suggests that these WO_x NPs have irregular spherical shapes, and some of them (highlighted in red) are crystalline in nature as revealed by the presence of lattice fringes. XRD analysis of

WO_x NPs indicated the tungsten suboxide phase $W_{18}O_{49}$ ($WO_{2.72}$) (JCPDS 05-0392).

STEM-HAADF imaging, which provides *Z*-contrast information, was also applied in order to more clearly image the WO_x structures and estimate the number of WO_x structural units within each WO_x NP (Figures 1c and 1d). Structural deformation and aggregation of the WO_x NPs could in principle occur as the oleylamine molecules were disrupted or modified on the NP surface during the “electron beam shower” procedure. However, no significant particle size distribution difference was noticed from the HAADF images taken with and without an “electron beam shower” pretreatment, indicating that particle sintering was not induced by this process.

The atomic resolution HAADF images (Figures 1c and 1d) allowed us to estimate the number of WO_x structural units within each NP. Each atomic column can be clearly resolved, and the intensity variations between different atomic columns are directly related to the number of W atoms in the columns along the viewing direction. By quantifying the intensity variations to determine the number of W atoms in each atom column within a NP, we found that most WO_x NPs contained between 20 and 36 W atoms (or WO_x structural units). Stoichiometrically, ~2–3 AMT species (each having 12 W atoms) are required for each WO_x NP, which is an important clue in understanding the formation mechanism.

It can also be estimated from the HAADF images that about 80% of the W atoms are associated with the outer surface. The structure of the WO_x NPs as revealed by STEM-HAADF imaging was not highly crystalline (Figure 1c), which could be either due to (i) some inherent semicrystalline nature of the WO_x NPs or (ii) possibly due to some slight structural damage induced by the “electron beam shower” pretreatment. Single, isolated W atoms (highlighted by yellow circles in Figure 1c) were also observed, presumably in the form of isolated WO_x structural units. These could be due to severe reduction of the polyoxometalate species during solvothermal synthesis or to structural damage of the NPs induced by the incident electron beam.

The WO_x NP size was characterized as a particle height distribution using AFM (Figure 1e). The number-average particle height was 1.6 nm and the standard deviation was 0.3 nm, representing a relative standard deviation (RSD) of 19% (Figure 1f). The AFM image of oval-shaped particles may be the result of the WO_x NP ligands weakly interacting with the AFM tip.

Synthesis with Coaddition of an Oxidant. Several color transitions were observed during NP synthesis. The solution in the flask was clear during heating (ramp rate of 2.0 K/min). A clear, blue suspension formed when ~493 K was reached, which turned into a dark yellow/brown suspension once the soak temperature of ~523 K was reached; the color remained the same after 2 h at this temperature. The blue color was attributed to the reduction and decomposition of the AMT (by oleylamine and/or NH_3 decomposition byproduct), in accordance with previous reports on heteropoly blue chemistry^{54–58} and ammonium paratungstate gas-phase reduction.⁵⁹ The blue-to-yellow transition was attributed to the formation of the WO_x NPs.

When the synthesis took place in the presence of 5 mmol of TANO, the suspension did not turn blue during the heating stage. Instead, it remained clear and colorless until the soak temperature of ~523 K was reached, when it became yellow-colored and eventually turned to dark yellow/brown after 2 h.

The absence of the blue color could be attributed to a very low concentration of reduced tungsten oxo species, which required a higher temperature to result in formation of NPs (with an initially low concentration compared to the non-TANO case). HAADF imaging and AFM analysis indicated a mean particle size of 1.0 nm with a standard deviation of 0.4 nm, with nanoclusters comprising 18–24 WO_x units (Figure 2). As an oxidizing agent,^{60–62} TANO apparently prevented the reductive decomposition of AMT, favoring the formation of smaller NPs (generated from ~ 1.5 –2 AMT species).

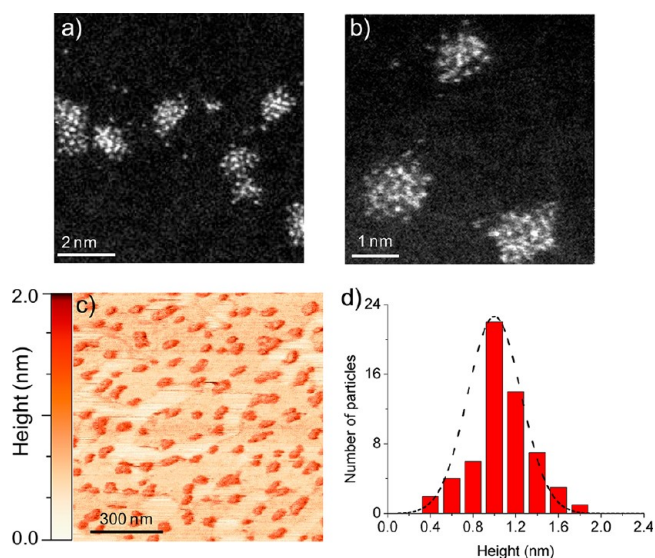


Figure 2. (a, b) HAADF STEM images of small WO_x nanoparticles (sNPs) supported on continuous amorphous carbon film. (c) AFM image and (d) corresponding particle height distribution of WO_x sNPs supported on HOPG.

On the basis of chemical safety, TANO is much preferred over air or O_2 as oxygen sources. No reaction occurred when the TANO precursor amount was doubled, indicating interference with AMT decomposition.

Synthesis with Coaddition of a Reductant. To test the hypothesis that AMT reduction is needed for particle formation and growth, we used 5 mmol of 1,12-dodecanediol as a reducing agent.⁶² In this case, the initially colorless suspension turned blue during the temperature ramp but at a lower temperature (at ~ 473 K) and remained blue upon completion of the reaction (after reaching ~ 523 K and soaking for 2 h). The resultant particles were found to have shapes of rods and needles (Figure 3a). These WO_x nanorods (NRs) measured 4.0 ± 1.0 nm in width and 20.0 ± 5.0 nm in length. XRD analysis indicated the $\text{W}_{18}\text{O}_{49}$ phase,¹⁵ with preferred crystal growth along the [010] direction (Figure 3b).

The contrasting color of the NR suspension (blue, Figure 3c) with that of the WO_x NP and sNP suspensions (yellow) can be analyzed through UV–vis spectroscopy. The WO_x NRs showed strong absorbance (Figure 3c) through the 400–900 wavelength range, with a minimum near ~ 510 nm. The color was attributed to the large presence of oxygen vacancies (and W^{5+} sites) at the WO_x NR surface, as proposed by others for WO_x NR^{15,18,36,37,63} and WO_3 colloidal suspensions.^{64–67} The W^{5+} species arises from W^{6+} reduction by 1,12-dodecanediol. Larger quantities of the reducing agent did not prevent particle

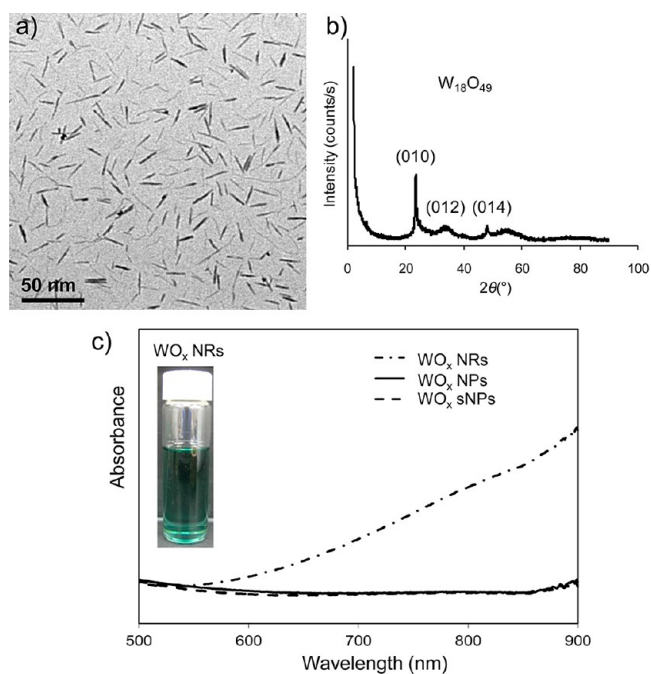


Figure 3. (a) TEM image and (b) XRD pattern of WO_x NRs and (c) UV–vis absorption spectra of toluene suspensions of WO_x NPs, sNPs, and NRs. Inset: toluene suspension of WO_x NRs.

formation (as in the case of TANO); rather, they resulted in the formation of bulk $\text{W}_{18}\text{O}_{49}$.

To gain insights into the NR growth process, we extracted a 1 mL aliquot of the synthesis medium at 513 K during the heating step and injected it into 10 mL of toluene to quench particle growth. HAADF STEM analysis showed partially formed, single-crystal NRs with an interplanar spacing of 0.378 nm and smaller WO_x clusters attached to the tips and sides of NRs (Figure 4). The images suggest NRs lengthened along the

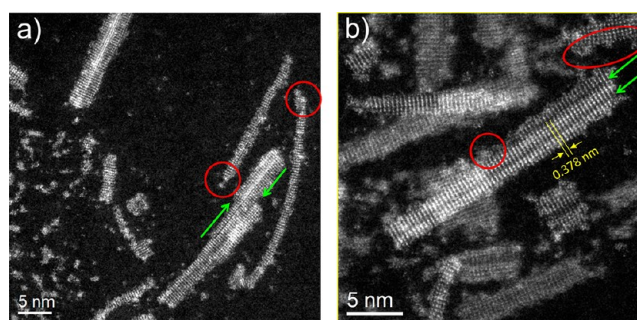


Figure 4. (a) Low- and (b) high-magnification HAADF STEM images of WO_x NRs recovered at 513 K during temperature ramp. Green arrows: interface between WO_x rods within a single particle. Red circles: locations of WO_x clusters adsorbed onto a NR.

[010] direction by “consuming” WO_x clusters at the rod tip, perhaps through an oriented attachment mechanism described by Banfield and co-workers.^{68,69} The local contrast variations indicated the presence of 2–3 thinner, epitaxially bound rods within some NRs, with an isolated thin rod observed with a width of ~ 0.5 –1.0 nm. Most of the crystalline NRs with widths of 2–5 nm have become disordered as a result of the electron-beam-induced structural damage (as shown by sequential imaging in Figure S2). Note that the width of these NRs is

larger than the diameter of the WO_x NPs. Considering that the small particles have been preprocessed with an “electron beam shower” under relatively high electron dose levels, which was required in order to avoid carbon contamination, the disordered character of these small oxide particles is most likely the result of a similar electron beam induced amorphization process.

Oleylamine Content of WO_x Particles. TGA was carried out on WO_x NPs, WO_x sNPs, WO_x NRs, oleylamine, and AMT (Figure 5). AMT lost $\sim 8\%$ of its initial weight when 1073 K

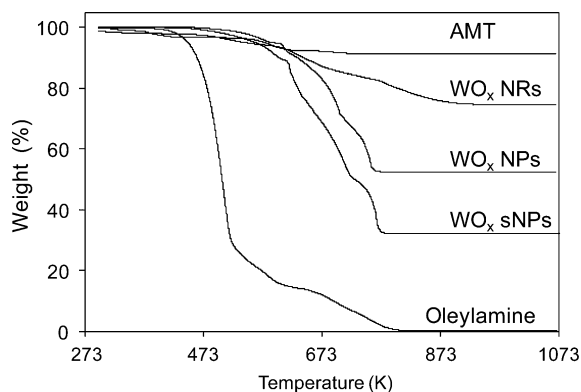


Figure 5. TGA profiles for the various WO_x particles and the oleylamine and AMT precursors.

was reached, with 2 wt % loss due to the liberation of 3.2 equiv of water of crystallization ($(\text{NH}_4)_6\text{H}_2\text{W}_{12}\text{O}_{40} \cdot x\text{H}_2\text{O}$, where $x = 3.2$) and 6 wt % loss due to H_2O and NH_3 formation from AMT decomposing into WO_3 . Pure oleylamine decomposed completely at ~ 773 K, the temperature at which WO_x NPs and WO_x sNPs experienced a significant weight loss. The WO_x NRs became free of organic species at 100 K higher (~ 873 K), pointing to a stronger interaction of oleylamine to the NR surface, and by inference, a weaker interaction to the NP/sNP surface.

Attributed to oleylamine bound to the particle as surface ligands, the organic content was ~ 27 wt % for the NRs, ~ 48 wt % for the NPs, and ~ 65 wt % for the sNPs. With the assumption that the remaining 73, 52, and 35 wt % corresponded to the respective WO_x content, the average nanoparticle yield based on 30 different sample batches was $95 \pm 3\%$ (where 3% is the relative standard deviation based on triplicate synthesis experiments, $n = 3$) for the NRs, $92 \pm 5\%$ ($n = 30$) for the NPs, and $89 \pm 4\%$ ($n = 15$) for the sNPs. The number of oleylamine molecules per W atom was calculated to be of 0.1, 0.7, and 0.9 for the WO_x NRs, NPs, and sNPs, respectively (Table 1). The small percentage of oleylamines per NR particle reflects the small surface-to-volume ratio of nonspherical particles of comparable diameters.

The ligand molecules can be removed through established methods such as plasma cleaning, washing with different organic solvents, or calcination. We are currently studying the preparation of WO_x/SiO_2 catalysts through the deposition of WO_x NPs on SiO_2 and removal of the oleylamine via controlled calcination.

Proposed Synthesis Mechanism. In our synthesis method, an excess of oleylamine was used to ensure stabilization and avoid aggregation of the formed WO_x NPs. The use of a high-boiling temperature solvent like 1-octadecene led to the formation of larger, rod-shaped structures (not

Table 1. Summary of Size, Composition, and NP Yield of WO_x NPs, sNPs, and NRs

	WO_x sNPs	WO_x NPs	WO_x NRs
AFM size (nm)	1.0 ± 0.4	1.6 ± 0.3	
TEM size (nm)	1.0 ± 0.3	1.6 ± 0.2	$4 \pm 1 \times 20 \pm 5$
hydrodynamic diam (nm)		1.3 ± 0.2	
organic content (%)	65	48	27
inorganic content (%)	35	52	73
nanoparticle yield (%)	89 ± 4	92 ± 5	95 ± 3
oleylamine molecules per W atom	0.9	0.7	0.1

shown), suggesting the importance of the amine functional group in controlling particle growth.

We carried out a TGA/FTIR decomposition experiment that mimicked the temperature ramp and soak of the synthesis procedure (Figure 6). A mixture of AMT and oleylamine was

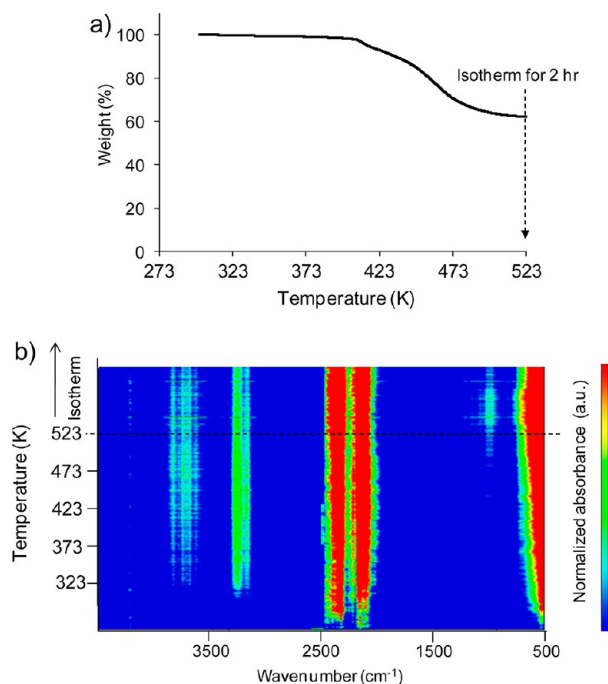


Figure 6. (a) TGA profile of an AMT/oleylamine mixture (same ratio used in synthesis method) and (b) FTIR spectra of the TGA effluent. A ramp rate of 2.0 K/min under flowing argon (50 mL/min) was employed.

heated under flowing argon to 523 K at a ramp rate of 2.0 K/min and kept at 523 K for 2 h. The weight loss between 373 and 473 K corresponded to absorption regions assigned to (i) the N–H stretching modes (~ 3000 – 3300 cm^{-1}) and (ii) the O–H stretching modes (~ 3600 – 3700 cm^{-1}) from the liberated NH_3 and H_2O , respectively (Figure 6b). The strong bands at ~ 2350 and ~ 540 cm^{-1} corresponded to the asymmetric stretching and the bending modes of CO_2 . A band at ~ 900 cm^{-1} appeared at ~ 493 K, the same temperature at which the synthesis suspension was previously observed to turn blue-colored due to the reduction and decomposition of AMT. This ~ 900 cm^{-1} band may be associated with an oleylamine decomposition gas-phase product containing a C–H group. The TGA/FTIR gives evidence for oleylamine as a reducing agent, as it oxidizes to form the detected gas-phase products.

The reduction reaction appears to be moderated by introducing the TANO oxidation agent that either (1) facilitates another reaction pathway that moderates the reduction step and/or (2) shifts the equilibrium of the reaction mechanism by increasing the concentration of oxygen atoms. When the concentration of TANO was doubled, no particle formation took place perhaps due to neutralization of the oleylamine, such that it failed to reduce the decomposed AMT WO_3 species to WO_{3-x} reactive species.

A plausible model for WO_x NPs formation involves (i) the reductive decomposition of the metatungstate by the oleylamine and (ii) the formation of the WO_x NPs from the aggregation of *in situ* generated reactive tungsten oxo species. TANO leads to smaller WO_x NPs by lessening the extent of reduction. In contrast, 1,12-dodecanediol leads to rod-shaped particles, probably by causing more reactive tungsten oxo-species to form, which then attach reactively to WO_x NPs in the growth process. The diol could also generate WO_x NPs with more reduced (and therefore more reactive) end groups, to which other NPs can attach in an oriented manner.

Other Oxide Nanoparticle Compositions. The synthesis method was extended to MoO_x and VO_x compositions. The hydrodynamic radii of MoO_x and VO_x NPs were 1.2 ± 0.2 and 2.0 ± 0.2 nm, respectively. MoO_x NPs were colloidally stable in toluene, but VO_x NPs were not; they precipitated out of toluene within 48 h of synthesis and particle recovery. SAXS analysis of the stable MoO_x NP suspension indicated a particle diameter of ~ 2.2 nm (Figure S3).

The HAADF images showed the MoO_x NPs to be irregularly shaped (Figure 7a,b). AFM analysis indicated the particles were

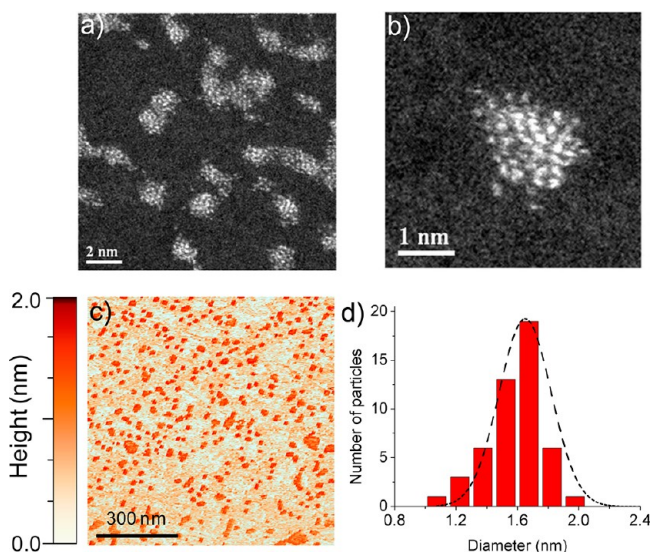


Figure 7. (a, b) HAADF STEM images of MoO_x NPs supported on continuous amorphous carbon film. (c) AFM image and (d) corresponding particle height distribution of MoO_x NPs supported on HOPG.

1.7 nm in size with a standard deviation of 0.4 nm (RSD = 20%) (Figure 7c,d). In contrast VO_x NPs are unstable and have a tendency to self-assemble into linear wire-like structures when deposited onto a continuous carbon TEM grid (Figure S4).

4. CONCLUSIONS

Presented is a synthesis method to produce ultrasmall metal oxide nanoparticles (<2 nm) based on the concept of thermal

decomposition of a polyoxometalate salt in a coordinating organic solvent. WO_x particles with a diameter of 1.6 nm were synthesized with minimal batch-to-match variations and with yields that exceeded 90%. Careful structural analysis indicated a $\text{WO}_{2.72}$ crystal phase with 20–36 WO_x structural units and 16–20 oleylamine molecules per particle. Used as the solvent and particle stabilizer, oleylamine appears to act as a reducing agent in converting the ammonium metatungstate precursor into a reactive intermediate species toward the nucleation and growth of WO_x NPs. Indicating the importance of the tungsten reducibility on the particle morphology, the use of an oxidizing agent leads to smaller, 1 nm particles, and the use of an additional reducing agent leads to rod-shaped nanoparticles. A formation mechanism is proposed, in which partially reduced polyoxometalate anions aggregate into ultrasmall NPs, and the extent of aggregation is affected by the presence of oxidizing and reducing agents.

■ ASSOCIATED CONTENT

Supporting Information

Notes about STEM-ADF imaging; Figure S1 (a series of sequentially obtained STEM-ADF images of WO_x particles supported on SiO_2); Figure S2 (electron-beam induced amorphization of the crystalline WO_x NRs); Figure S3 (experimental and simulated SAXS scattering profiles of WO_x NPs and MoO_x NPs); Figure S4 (HAADF STEM images of a single VO_x NP and an array of VO_x NPs). This material is available free of charge via the Internet at <http://pubs.acs.org>.

■ AUTHOR INFORMATION

Corresponding Author

*E-mail mswong@rice.edu.

Present Addresses

[†]ExxonMobil Chemical Company, Global Process Research, 4500 Bayway Drive, Baytown, TX 77575.

[#]Materials Science and Technology, Oak Ridge National Laboratory, Oak Ridge, TN 37831.

Notes

The authors declare no competing financial interest.

■ ACKNOWLEDGMENTS

We gratefully acknowledge Prof. A. R. Barron and Mr. E. Dillon for their help with AFM analysis, Dr. H. Bagaria, Dr. Gautam Kini, Ms. Sravani Gullapali, and Ms. L. Pretzer for their help with SAXS and DLS. Financial support for this work was provided by the National Science Foundation Nanoscale Interdisciplinary Research Team program (CBET-0609018), SABIC Americas, 3M (NTF Award), and the DCG Partnership. Research supported in part by ORNL's Shared Research Equipment (ShaRE) User Facility, which is sponsored by the Office of Basic Energy Sciences, U.S. Department of Energy.

■ REFERENCES

- (1) Arico, A. S.; Bruce, P.; Scrosati, B.; Tarascon, J.-M.; van Schalkwijk, W. *Nat. Mater.* **2005**, *4*, 366.
- (2) Lou, X. W.; Archer, L. A. *Adv. Mater.* **2008**, *20*, 1853.
- (3) Poizot, P.; Laruelle, S.; Grugeon, S.; Dupont, L.; Tarascon, J. M. *Nature* **2000**, *407*, 496.
- (4) Dillon, A. C.; Mahan, A. H.; Deshpande, R.; Parilla, P. A.; Jones, K. M.; Lee, S. H. *Thin Solid Films* **2008**, *516*, 794.
- (5) Wang, Y.; Zhang, Z.; Zhu, Y.; Li, Z.; Vajtai, R.; Ci, L.; Ajayan, P. M. *ACS Nano* **2008**, *2*, 1492.

- (6) Benkstein, K. D.; Raman, B.; Montgomery, C. B.; Martinez, C. J.; Semancik, S. *IEEE Sens. J.* **2010**, *10*, 137.
- (7) Franke, M. E.; Koplin, T. J.; Simon, U. *Small* **2006**, *2*, 36.
- (8) Eranna, G.; Joshi, B. C.; Runthala, D. P.; Gupta, R. P. *Crit. Rev. Solid State Mater. Sci.* **2004**, *29*, 111.
- (9) Li, X.-L.; Lou, T.-J.; Sun, X.-M.; Li, Y.-D. *Inorg. Chem.* **2004**, *43*, 5442.
- (10) Yan, A.; Xie, C.; Zeng, D.; Cai, S.; Hu, M. *Mater. Res. Bull.* **2010**, *45*, 1541.
- (11) Xie, X.; Li, Y.; Liu, Z.-Q.; Haruta, M.; Shen, W. *Nature* **2009**, *458*, 746.
- (12) Ryan, J. V.; Berry, A. D.; Anderson, M. L.; Long, J. W.; Stroud, R. M.; Cepak, V. M.; Browning, V. M.; Rolison, D. R.; Merzbacher, C. I. *Nature* **2000**, *406*, 169.
- (13) Rodriguez, J. A.; Ma, S.; Liu, P.; Hrbek, J.; Evans, J.; Perez, M. *Science* **2007**, *318*, 1757.
- (14) Gu, G.; Zheng, B.; Han, W. Q.; Roth, S.; Liu, J. *Nano Lett.* **2002**, *2*, 849.
- (15) Lee, K.; Seo, W. S.; Park, J. T. *J. Am. Chem. Soc.* **2003**, *125*, 3408.
- (16) Hudson, M. J.; Peckett, J. W.; Harris, P. J. F. *J. Mater. Chem.* **2003**, *13*, 445.
- (17) Zhang, H.; Feng, M.; Liu, F.; Liu, L.; Chen, H.; Gao, H.; Li, J. *Chem. Phys. Lett.* **2004**, *389*, 337.
- (18) Seo, J.-w.; Jun, Y.-w.; Ko, S. J.; Cheon, J. J. *Phys. Chem. B* **2005**, *109*, 5389.
- (19) Phuruangrat, A.; Ham, D. J.; Thongtem, S.; Lee, J. S. *Electrochem. Commun.* **2009**, *11*, 1740.
- (20) Zach, M.; Ng, K.; Penner, R. M. *Science* **2000**, *290*, 2120.
- (21) Zhou, J.; Xu, N. S.; Deng, S. Z.; Chen, J.; She, J. C.; Wang, Z. L. *Adv. Mater.* **2003**, *15*, 1835.
- (22) Du, K.; Fu, W.; Wei, R.; Yang, H.; Xu, J.; Chang, L.; Yu, Q.; Zou, G. *Ultrason. Sonochem.* **2008**, *15*, 233.
- (23) Niederberger, M.; Krumeich, F.; Muhr, H.-J.; Muller, M.; Nesper, R. *J. Mater. Chem.* **2001**, *11*, 1941.
- (24) Lutta, S. T.; Dong, H.; Zavalij, P. Y.; Whittingham, M. S. *Mater. Res. Bull.* **2005**, *40*, 383.
- (25) Viswanathamurthi, P.; Bhattarai, N.; Kim, H. Y.; Lee, D. R. *Scr. Mater.* **2003**, *49*, 577.
- (26) Spahr, M. E.; Bitterli, P.; Nesper, R.; Mueller, M.; F., K.; Nissen, H. U. *Angew. Chem., Int. Ed.* **1998**, *37*, 1263.
- (27) Spahr, M. E.; Stoschitzki-Bitterli, P.; Nesper, R.; Haas, O.; Novak, P. *J. Electrochem. Soc.* **1999**, *146*, 2780.
- (28) Muhr, H. J.; Krumeich, F.; Schönholzer, U. P.; Bieri, F.; Niederberger, M.; Gauckler, L. J.; Nesper, R. *Adv. Mater.* **2000**, *12*, 231.
- (29) Niederberger, M.; Muhr, H.-J.; Krumeich, F.; Bieri, F.; Gunther, D.; Nesper, R. *Chem. Mater.* **2000**, *12*, 1995.
- (30) Thangala, J.; Chen, Z.; Chin, A.; Ning, C.-Z.; Sunkara, M. K. *Cryst. Growth Des.* **2009**, *9*, 3177.
- (31) Blackman, C. S.; Parkin, I. P. *Chem. Mater.* **2005**, *17*, 1583.
- (32) Koltypin, Y.; Nikitenko, S. I.; Gedanken, A. *J. Mater. Chem.* **2002**, *12*, 1107.
- (33) Xiong, L.; He, T. *Chem. Mater.* **2006**, *18*, 2211.
- (34) Morales, W.; Cason, M.; Aina, O.; de Tacconi, N. R.; Rajeshwar, K. *J. Am. Chem. Soc.* **2008**, *130*, 6318.
- (35) Ham, D. J.; Phuruangrat, A.; Thongtem, S.; Lee, J. S. *Chem. Eng. J.* **2010**, *165*, 365.
- (36) Pol, S. V.; Pol, V. G.; Kessler, V. G.; Seisenbaeva, G. A.; Solovyov, L. A.; Gedanken, A. *Inorg. Chem.* **2005**, *44*, 9938.
- (37) Wang, J.; Khoo, E.; Lee, P. S.; Ma, J. *J. Phys. Chem. C* **2008**, *112*, 14306.
- (38) Li, X.-L.; Liu, J.-F.; Li, Y.-D. *Inorg. Chem.* **2003**, *42*, 921.
- (39) Solis, J. L.; Saukko, S.; Kish, L.; Granqvist, C. G.; Lantto, V. *Thin Solid Films* **2001**, *391*, 255.
- (40) Yang, B.; Zhang, Y.; Drabarek, E.; Barnes, P. R. F.; Luca, V. *Chem. Mater.* **2007**, *19*, 5664.
- (41) Santato, C.; Ulmann, M.; Augustynski, J. *J. Phys. Chem. B* **2001**, *105*, 936.
- (42) Watcharenwong, A.; Chanmanee, W.; de Tacconi, N. R.; Chenthamarakshan, C. R.; Kajitvichyanukul, P.; Rajeshwar, K. *J. Electroanal. Chem.* **2008**, *612*, 112.
- (43) Ross-Medgaarden, E. I.; Knowles, W. V.; Kim, T.; Wong, M. S.; Zhou, W.; Kiely, C. J.; Wachs, I. E. *J. Catal.* **2008**, *256*, 108.
- (44) Zhou, W.; Ross-Medgaarden, E.; Wachs, I. E.; Kiely, C. J. *Microsc. Microanal.* **2008**, *14*, 1350.
- (45) Zhou, W.; Ross-Medgaarden, E. I.; Knowles, W. V.; Wong, M. S.; Wachs, I. E.; Kiely, C. J. *Nat. Chem.* **2009**, *1*, 722.
- (46) Soultanidis, N.; Zhou, W.; Psarras, A. C.; Gonzalez, A. J.; Iliopoulou, E. F.; Kiely, C. J.; Wachs, I. E.; Wong, M. S. *J. Am. Chem. Soc.* **2010**, *132*, 13462.
- (47) Abramoff, M. D.; Magalhaes, P. J.; Ram, S. J. *Biophotonics Int.* **2004**, *11*, 36.
- (48) Horcas, I.; Fernandez, R.; Gomez-Rodriguez, J. M.; Colchero, J.; Gomez-Herrero, J.; Baro, A. M. *Rev. Sci. Instrum.* **2007**, *78*, 013705.
- (49) Murthy, V. S.; Cha, J. N.; Stucky, G. D.; Wong, M. S. *J. Am. Chem. Soc.* **2004**, *126*, 5292.
- (50) Pretzer, L. A.; Nguyen, Q. X.; Wong, M. S. *J. Phys. Chem. C* **2010**, *114*, 21226.
- (51) Wilkie, C. A. *Polym. Degrad. Stab.* **1999**, *66*, 301.
- (52) Li, B.; Gonzalez, R. D. *Appl. Catal., A* **1997**, *165*, 291.
- (53) Deng, Q.; Wilkie, C. A.; Moore, R. B.; Mauritz, K. A. *Polymer* **1998**, *39*, 5961.
- (54) Pope, M. T. *Heteropoly and Isopoly Oxometalates*; Springer-Verlag: New York, 1983.
- (55) Pope, M. T.; Varga, G. M. *Inorg. Chem.* **1966**, *5*, 1249.
- (56) Papaconstantinou, E.; Pope, M. T. *Inorg. Chem.* **1970**, *9*, 667.
- (57) Katsoulis, D. E.; Pope, M. T. *J. Am. Chem. Soc.* **1984**, *106*, 2737.
- (58) Pope, M. T.; Müller, A. *Angew. Chem., Int. Ed. Engl.* **1991**, *30*, 34.
- (59) Kirilenko, O.; Girgsdies, F.; Jentoft, R. E.; Ressler, T. *Eur. J. Inorg. Chem.* **2005**, *2005*, 2124.
- (60) Stichbury, J. C.; Mays, M. J.; Raithby, P. R.; Rennie, M.-A.; Fullalove, M. R. *J. Chem. Soc., Chem. Commun.* **1995**, 1269.
- (61) Soderquist, J. A.; Najafi, M. R. *J. Org. Chem.* **1986**, *51*, 1330.
- (62) Rotello, V. M. *Nanoparticles: Building Blocks for Nanotechnology*; Kluwer Academic: Dordrecht, 2004.
- (63) Chang, X.; Sun, S.; Li, Z.; Xu, X.; Qiu, Y. *Appl. Surf. Sci.* **2011**, *257*, 5726.
- (64) Bedja, I.; Hotchandani, S.; Kamat, P. V. *J. Phys. Chem.* **1993**, *97*, 11064.
- (65) Gomez-Romero, P.; Casan-Pastor, N. *J. Phys. Chem.* **1996**, *100*, 12448.
- (66) He, T.; Ma, Y.; Cao, Y.; Hu, X.; Liu, H.; Zhang, G.; Yang, W.; Yao, J. *J. Phys. Chem. B* **2002**, *106*, 12670.
- (67) Nenadovic, M. T.; Rajh, T.; Micic, O. I.; Nozik, A. J. *J. Phys. Chem.* **1984**, *88*, 5827.
- (68) Penn, R. L.; Banfield, J. F. *Science* **1998**, *281*, 969.
- (69) Penn, R. L.; Banfield, J. F. *Geochim. Cosmochim. Acta* **1999**, *63*, 1549.



US006710091B1

(12) **United States Patent**
Womelsdorf et al.

(10) **Patent No.:** **US 6,710,091 B1**
(45) **Date of Patent:** **Mar. 23, 2004**

(54) **NANOPARTICULATE, REDISPERSIBLE ZINC OXIDE GELS**

(75) Inventors: **Hermann-Jens Womelsdorf**,
Leverkusen (DE); **Werner Hoheisel**,
Köln (DE); **Gerd Passing**, Köln (DE)

(73) Assignee: **Bayer Aktiengesellschaft**, Leverkusen
(DE)

(*) Notice: Subject to any disclaimer, the term of this
patent is extended or adjusted under 35
U.S.C. 154(b) by 0 days.

(21) Appl. No.: **09/913,990**

(22) PCT Filed: **Feb. 11, 2000**

(86) PCT No.: **PCT/EP00/01116**

§ 371 (c)(1),

(2), (4) Date: **Aug. 21, 2001**

(87) PCT Pub. No.: **WO00/50503**

PCT Pub. Date: **Aug. 31, 2000**

(30) **Foreign Application Priority Data**

Feb. 23, 1999 (DE) 199 07 704

(51) **Int. Cl.**⁷ **B01F 3/12**; C01G 9/02

(52) **U.S. Cl.** **516/33**; 516/88; 516/98;
423/101; 423/102; 423/104; 423/622

(58) **Field of Search** 516/33, 88, 98;
423/101, 102, 104, 622

(56) **References Cited**

U.S. PATENT DOCUMENTS

5,089,248 A * 2/1992 Akhtar 423/604
5,391,354 A 2/1995 Petersen et al. 422/129
5,716,679 A * 2/1998 Krug et al. 427/515
6,200,680 B1 3/2001 Takeda et al. 428/402

FOREIGN PATENT DOCUMENTS

JP 4-164814 6/1992
JP 7-232919 9/1995
WO 97/24224 * 7/1997

OTHER PUBLICATIONS

Sakohara et al., "Visible Luminescence and Surface Properties of Nanosized ZnO Colloids Prepared by Hydrolyzing Zinc Acetate", *J. Phys. Chem. B.*, vol. 102, No. 50, Dec. 1998, pp. 1016910175.*

Hilgendorff et al., "From ZnO Colloids to Nanocrystalline Highly Conductive Films", *J. Electrochem. Soc.*, vol. 145, No. 10, Oct. 1998, pp. 3632-3637.*

Spanhel et al., "Semiconductor Clusters in the Sol-Gel Process: Quantized Aggregation, Gelation, and Crystal Growth in Concentrated ZnO Colloids", *J. Am. Chem. Soc.* 1991 (month unavailable) 113, pp. 2826-2833.*

Patent Abstracts of Japan, vol. 199, No. 605, corresponding to Jp 08 026823 A (Toshio Tsuchiya) Jan. 30, 1996.*

J. Phys. Chem., 92 (month unavailable) 1988, Month unknown pp. 482-487, "Photochemistry and Radiation Chemistry of Colloidal Semiconductors. 23. Electron Storage on ZnO Particles and Size Quantization", Markus Haase, Horst Weller and Arnim Henglein.

J. Phys. Chem., 90 (month unavailable) 1986, Month unknown pp. 2555-2560, "Electronic Wave Functions in Semiconductor Clusters: Experiment and Theory", Louis Brus.

Gmelins Handbuch, Vol 32, 8th ed. Supplementary vol. (month unavailable) 1956, Month unknown pp. 722-773 "Zinkoxyd".

* cited by examiner

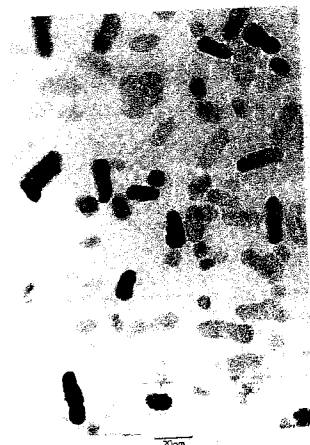
Primary Examiner—Daniel S. Metzmaier

(74) *Attorney, Agent, or Firm*—Joseph C. Gil; Gary Matz

(57) **ABSTRACT**

A method for the preparation of nano size zinc oxide particles having an average primary particle diameter of less than or equal to 15 nm, which are redispersible in organic solvents and/or water, by basic hydrolysis of at least one zinc compound in alcohol or an alcohol/water mixture. The hydrolysis is carried out with substoichiometric amounts of base, based on the zinc compound. The precipitate which originally forms during hydrolysis is left to mature until the zinc oxide has completely flocculated. This precipitate is then thickened to give a gel and separated off from the supernatant phase.

6 Claims, 2 Drawing Sheets



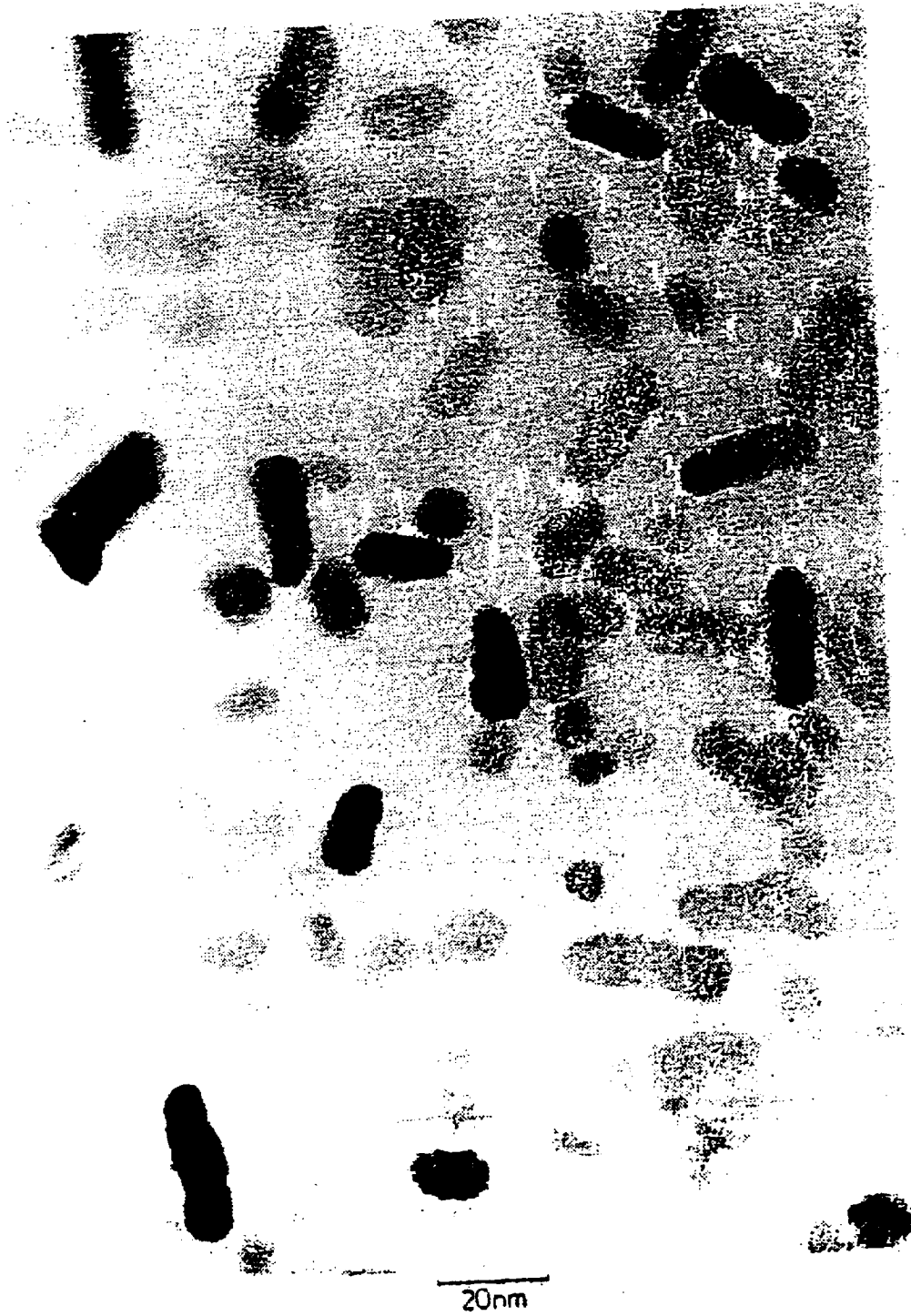


FIG. 1

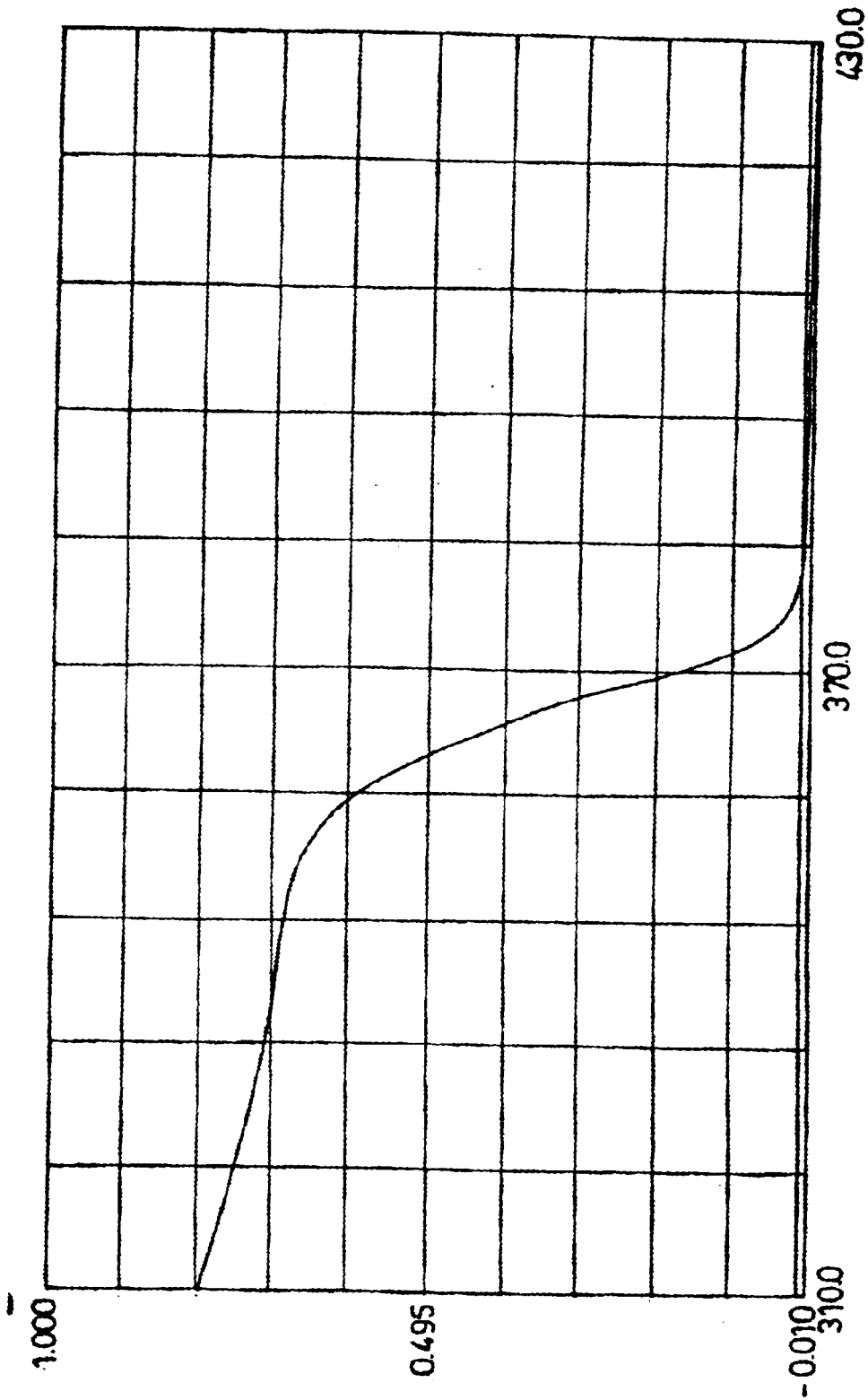


FIG. 2

NANOPARTICULATE, REDISPERSIBLE ZINC OXIDE GELS

FIELD OF THE INVENTION

The present invention relates to nanoparticulate, redispersible zinc oxide gels, to processes for their preparation and to their use.

BACKGROUND OF THE INVENTION

Zinc oxide is used for diverse purposes, such as, for example, as a white pigment, as a catalyst, as a constituent of antibacterial skin-protection ointment and as an activator for rubber vulcanization. Sunscreens and wood varnishes contain finely divided zinc oxide as UV-absorbing pigment.

The term "nanoparticle" is generally used to refer to particles having a diameter of less than about 100 nm.

Zinc oxide nanoparticles having particle sizes below about 30 nm are potentially suitable for use as UV absorbers in transparent organic-inorganic hybrid materials, plastics, paints and coatings. In addition, use for the protection of UV-sensitive organic pigments is also possible.

Particles, particle aggregates or particle agglomerates of zinc oxide which are greater than about 30 nm lead to scattered light effects and thus to an undesired decrease in transparency in the visible light region. For this reason, redispersibility, i.e. the convertibility of the prepared zinc oxide nanoparticles into a colloid-disperse state, is an important prerequisite for the abovementioned applications.

Zinc oxide nanoparticles having particle sizes below about 5 nm exhibit, because of the size quantization effect, a blue shift in the absorption edge (L. Brus, *J. Phys. Chem.* (1986), 90, 2555-2560) and are therefore less suitable for use as UV absorbers in the UV-A region.

The preparation of zinc oxide by dry and wet processes is known. The classical method of burning zinc, the dry process (e.g. *Gmelin vol. 32*, 8th edition, supplementary volume, p. 772 ff), generates aggregated particles having a broad size distribution. Although in principle it is possible to prepare stable dispersions by grinding procedures with the help of surface-active agents, because the shear forces which can be achieved are too low, it is not possible to obtain dispersions having average particle sizes below about 30 nm from such powders.

Particularly finely divided zinc oxide is prepared predominantly by wet chemical methods by precipitation processes. Precipitation in aqueous solution generally gives hydroxide- and/or carbonate-containing materials which have to be thermally converted to zinc oxide. The thermal post-treatment has a negative effect on the finely divided nature since the particles are subjected during this treatment to sintering processes which lead to the formation of μm -sized aggregates which can be broken down only incompletely to the primary particles by grinding.

JP-A-04 164 814 describes a process which leads, as a result of precipitation in aqueous medium at elevated temperature even without thermal post-treatment, to finely divided ZnO. The average particle size is given as 20-50 nm, with no information on the degree of agglomeration. These particles are relatively large. Even if agglomeration is minimal, this leads to scattering effects which are undesired in transparent applications.

JP-A-07 232 919 describes the preparation of ZnO particles which are 5-10,000 nm in size from zinc compounds by reaction with organic acids and other organic compounds

such as alcohols at elevated temperature. The hydrolysis is carried out here such that the by-products which form (esters of the acids used) can be distilled off. The process permits the preparation of ZnO powders which are redispersible as a result of surface modification which has been carried out beforehand. However, on the basis of the disclosure of this application it is not possible to prepare particles having an average diameter of <15 nm. Accordingly, in the examples given in the application, the smallest average primary particle diameter is given as 15 nm.

EP 0 893 409 A1 describes the preparation of zinc oxide nanoparticles as in JP-A-07 232 919, except that during the precipitation of the ZnO, another metal oxide, from the groups of the Periodic Table of the Elements named "IIIB" and "IVB" in the application, aluminum and indium being given in particular by name, is coprecipitated.

Furthermore, attempts have been made to obtain ZnO directly by hydrolysis of zinc salts in alcohols (Henglein et al., *J. Phys. Chem.* 1988, 92, 482-487). Using NaOH as base it was not possible to obtain stable and concentrated sols ($C_{\text{ZnO}} >> 10^{-3}$ mol/l).

The hydrolysis of zinc acetate with LiOH or tetramethylammonium hydroxide (Spanhel et al., *JACS* 1991, 113, No.8, 2826-2833) in alcoholic solution gave concentrated sols which, in addition to zinc oxide nanoparticles, also comprised lithium acetate or tetramethylammonium acetate, respectively, in stoichiometric amount. For this reason, firstly, cost-effective preparation is not possible since LiOH and tetramethylammonium hydroxide are relatively expensive, and, secondly, further use of the sols is severely limited since the by-products of the precipitation are not separated off. By concentrating these sols it was possible to obtain ZnO-containing gels which likewise still contained the by-products of the ZnO preparation in stoichiometric amount and were thus severely limited with regard to their further possible uses.

Other processes for the preparation of nanosize zinc oxide, such as that described in U.S. Pat. No. 5,391,354, which starts from zinc alkoxides, use expensive starting materials and are therefore uneconomical.

SUMMARY OF THE INVENTION

The object of the present invention was therefore to provide a nanosize zinc oxide which combines strong UV-absorption even in the UV-A region with excellent dispersion properties for minimal scattering. To this end, it was necessary to find a simple process which is suitable for preparing nanosize zinc oxide having an average primary particle diameter between 5 and 15 nm from commercially available, cost-effective starting materials on an industrial scale at low cost in a manner which permits the zinc oxide, following preparation, to be separated off from the by-products without the particles undergoing irreversible aggregation and, following redispersion, to be prepared for further use in the form of sols without laborious grinding.

Starting from the method for the hydrolysis of zinc acetate in alcoholic media described by Henglein et al., it has now surprisingly been found that by hydrolysing zinc compounds with bases in alcohol or alcohol/water mixtures, followed by removal of the supernatant solution charged with the by-products of the precipitation, it is possible to obtain zinc oxide gels comprising zinc oxide nanoparticles having average primary particle diameters of ≤ 15 nm which, simply by adding suitable solvents or solvent combinations—optionally together with suitable surface modifier—sand stirring, and dispensing with grinding stages or other labo-

rious mechanical comminution processes, can be redispersed completely to give largely primary-particle-disperse zinc oxide sols, without a significant loss in quality with regard to the monodispersity and size of the particles.

The invention therefore relates to zinc oxide gels comprising nanosize zinc oxide particles having an average primary particle diameter of ≤ 15 nm, water and alcohol, which are redispersible in at least one organic solvent and/or water, optionally with the addition of surface-modifying compounds, to give sols.

For the purposes of the invention, "average primary particle diameter" means the average circle-equivalent primary particle diameter of the zinc oxide particles which can be determined in a transmission electron micrograph.

The invention also relates to a process for the preparation of zinc oxide gels by basic hydrolysis of at least one zinc compound in alcohol or an alcohol/water mixture, characterized in that the precipitate which initially forms during hydrolysis is left to mature until the zinc oxide has completely flocculated, then this precipitate is thickened to a gel and separated off from the supernatant phase.

DESCRIPTION OF THE DRAWINGS

FIG. 1 is a transmission electron micrograph of a sample of the gel (A) diluted in an ethylene glycol/water mixture; and

FIG. 2 is an optical absorption spectrum of the sol of Example 7.

DESCRIPTION OF THE PREFERRED EMBODIMENT

The process according to the invention is preferably carried out such that at least one zinc compound is completely or partially dissolved in alcohol or an alcohol/water mixture and hydrolysed by adding at least one base at temperatures between the freezing point of the solution and its boiling point. This produces, depending on the temperature and concentration, and optionally after a time delay, a whitish precipitate.

As soon as zinc oxide is no longer or virtually no longer in colloidal disperse form, optionally after interspersed washing steps in which, after the precipitate has settled, the supernatant is exchanged for fresh solvent the precipitate can be thickened to give a gel and separated off from the supernatant phase. To test whether any zinc oxide is still in colloidal disperse form, it is possible to filter a sample of the reaction mixture through a filter having a pore size of $0.2 \mu\text{m}$ and test the filtrate for the Tyndall effect. The precipitate can be thickened to give a gel by settling and leaving to stand, or by centrifuging, the precipitate preferably being centrifuged.

The resulting zinc oxide gel can be redispersed to give largely primary-particle-disperse sols by adding organic solvents and/or water, optionally with the addition of surface-modifying compounds. The redispersion here is preferably effected by admixing the corresponding solvent or solvent mixture with stirring.

The zinc compound used in the process according to the invention is preferably a salt-like compound which is completely or partially soluble in the chosen alcohol or water/alcohol mixture, particular preference being given to zinc acetate, and very particular preference to its dihydrate.

The alcohol used is preferably a monoalcohol, very particularly preferably methanol.

The base can be an OH- or NH-group-containing basic compound, particularly one obtainable in concentrated form

and soluble in alcohol or alcohol/water mixtures. These include, in particular, sodium and potassium hydroxide and amine bases, the former being preferred. The base can either be used in solid form, for example as NaOH or KOH pellets, or in dissolved form in the process according to the invention. In a preferred embodiment of the invention, the base is added in dissolved form to the solution of the zinc salt. Here, the base is preferably dissolved in alcohol, water or alcohol/water mixtures, particularly preferably in methanol, water or methanol/water mixtures.

The hydrolysis is preferably carried out using nonstoichiometric amounts of base, particularly preferably substoichiometric amounts, very particularly preferably with a Zn to OH ratio of from 1:1.6 to 1:1.95.

The minimal water content of the reaction mixture is determined by the water content of the starting materials used and by the amount of zinc oxide which forms. Moreover, water can be added in order to achieve particular effects, e.g. to accelerate the formation of ZnO or to improve the solubility of the starting materials.

In a preferred embodiment of the invention, more zinc salt is used than corresponds to the solubility product in the solvent used. By adding a fraction of the amount of base intended for the hydrolysis, the solubility of the zinc salts is improved without zinc oxide already being formed.

In a further preferred embodiment of the invention, dissolution of the starting materials and hydrolysis are carried out with inert-gas blanketing.

In a further preferred embodiment, the zinc compound used is a commercially available, coarsely divided zinc oxide which is reacted in an up reaction to give a suitable zinc compound, preferably zinc acetate. In a particularly preferred embodiment of the invention, this is carried out by reacting zinc oxide with glacial acetic acid in a glacial acetic acid/acetic anhydride mixture or in an alcohol/water mixture.

In a preferred embodiment of the invention, the temperature during dissolution and reaction is between 0°C . and the boiling point of the solvent used. In a particularly preferred embodiment of the invention, the temperature is increased before and/or during and/or following precipitation to the boiling point of the mixture or a temperature below it.

To influence the morphology and/or the crystallinity of the zinc oxide particles, it is possible to add suitable compounds (foreign ions) before, during or after precipitation. Preference is given to compounds of the 2nd-4th main group and transition metal compounds. Particular preference is given to manganese, magnesium, silicon and aluminium compounds, very particular preference to aluminium and silicon alkoxides, aluminates and silicates. In a preferred embodiment of the process according to the invention, these compounds are added to the reaction mixture in dissolved form. Here, preferably from 0.01 to 3 mol %, based on zinc, are used.

The precipitate can be isolated, for example by decantation or by drawing off the supernatant with suction. In this connection, it is favourable to thicken the precipitate well, for example as a result of long settling times, since the redispersibility behaviour of the precipitate depends on the content of salt and solvent. If the settling time is relatively long, the precipitate thickens to give a high-viscosity gel. Particularly good thickening of the material and thus also particularly complete removal of the zinc oxide from the by-products of the precipitation is achieved by centrifugation. Here, a translucent, solid gel having a high solids content is obtained which is particularly readily redispersible.

In a further preferred embodiment, the salt content of the precipitate is, after settling, reduced by drawing off some of the supernatant with suction and adding fresh solvent. The salt content of the precipitate is particularly preferably reduced by drawing off some of the supernatant with suction and adding fresh solvent if the zinc oxide gel which forms is to be redispersible in water or alcohol/water mixtures, in particular diol and/or polyol/water mixtures, preferably with use of surface-modifying compounds, to give a sol.

The resulting zinc oxide gel can be converted into a colloid-disperse sol by suitable measures. In a preferred embodiment of the invention, this is effected by adding organic solvents, preferably polar aprotic solvents, very particularly preferably dichloromethane and/or chloroform. In a further preferred embodiment, the gel is redispersed in water. In a further preferred embodiment, the gel is redispersed in mixtures, in particular diol and/or polyol/water mixtures, preferably using surface-modifying compounds. The surface-modifying compounds are preferably nitrogen-containing compounds, particular preference being given to triethanolamine.

Grinding steps or other laborious mechanical comminution steps are not necessary.

The addition preferably takes place in a mass ratio of zinc oxide gel to solvent of from 1:0.4 to 1:10, particularly preferably in the ratio from 1:0.4 to 1:3, very particularly preferably in the ratio from 1:0.7 to 1:1.5. The mass ratios which are required to obtain a stable sol vary depending on the solvent used.

In a further preferred embodiment, the precipitate can, prior to thickening to give the gel, be converted, by adding dichloromethane and/or chloroform, into a zinc oxide sol in which the zinc oxide particles are in colloid-disperse form. This is preferably carried out after the salt content of the precipitate has previously been reduced by repeatedly settling and drawing off some of the supernatant with suction and adding fresh solvent.

The invention further relates to the use of the zinc oxide gel according to the invention or the sol produced therefrom in organic-inorganic hybrid materials, in particular for the UV protection of polymeric materials, paints and coatings, in particular for transparent applications. In addition, use for the protection of UV-sensitive organic pigments and dyes is also possible. In addition, the zinc oxide gels and zinc oxide sols according to the invention are also suitable for the matrix modification of polymers, paints and coatings and as an improved vulcanization activator for rubbers and latices.

EXAMPLES

The invention is described in more detail with reference to the examples below without being limited to these examples.

The centrifugation steps were carried out in a laboratory centrifuge from Heraeus (Variofuge RF) having a rotor with a radius of 20.4 cm.

Example 1

590 g of zinc acetate dihydrate were dissolved in 2000 g of methanol at 55° C. in a 6 l flask and a solution, conditioned at room temperature, of 302 g of potassium hydroxide pellets (84.7%) in 1000 g of methanol were added with stirring. A white, voluminous precipitate immediately formed, which was left to settle for 14 h. 3165 g were then drawn off from the supernatant with suction and replaced by 1000 g of methanol. The mixture was then stirred for about 20 min.

After a settling time of 75 min, a further 806 g of supernatant were drawn off with suction and replaced by 500 g of methanol. The mixture was stirred for a further 40 min, and then, after a settling time of 40 min, a further 786 g of supernatant were drawn off with suction and replaced by 500 g of methanol. After a stirring time of 30 min, the mixture was centrifuged (5500 rotations/min, 30 min). Following centrifugation, the mass of the resulting zinc oxide gel was 251 g.

The solids content of the gel was 75.3% (drying: 1 h at 130° C.). Elemental analysis revealed a zinc content of 75.7%, corresponding to 93.9% of ZnO. In addition, 0.25% of potassium, corresponding to about 0.63% of potassium acetate, were found.

An X-ray diffractogram of the dried sample indicated exclusively hexagonal zinc oxide. Evaluation of the reflections according to Scherrer revealed an average crystallite size of 6.9 nm (reflections: 100 and 002, 100 doubly weighted since identical to 010 in the hexagonal crystalline system).

Example 2

218.5 g of zinc oxide (99.8%) were introduced into a 6 litre 4-necked flask and mixed with 1200 g of methanol, 330 g of glacial acetic acid and 46.5 g of deionized water and heated to 60° C. with stirring. In parallel to this, a solution of 301.68 g of potassium hydroxide pellets (84.7%) and 700 g of methanol was prepared with cooling. After the mixture present in the flask had reached 60° C., approximately 80 ml of the prepared KOH/methanol solution was slowly metered in via a dropping funnel. The mixture clarified slowly and after about 30 min was clear. Then, at 60° C., the remainder of the KOH/methanol solution was metered in over the course of 30 seconds via a dropping funnel. Considerable white turbidity immediately formed, and the temperature of the mixture increased by about 2° C. After a few minutes the mixture clarified somewhat and then again turned milky white. The heating source was then removed and the mixture was cooled in an ice bath for 20 min. The stirrer was switched off at a temperature of 16° C. After about 2 hours a white sediment formed in the flask, and the supernatant was virtually clear. 2078 g were drawn off from the supernatant with suction and replaced by 750 g of methanol. The mixture was then stirred for about 60 min and then the reaction mixture was divided in the ratio 1:1. One half (A) was further processed as follows: after settling out for 14 h, the supernatant was decanted off and replaced by 375 g of methanol. The mixture was then stirred for about 50 min and then, after renewed settling out and decantation, 375 g of methanol was again added. The mixture was then stirred again for about 50 min, then centrifuged at 5500 rpm for 30 min, and the supernatant was decanted off. The gel weight was 130.6 g.

The solids content of the gel was 75.8% (drying: 1 h at 130° C.). Elemental analysis revealed a zinc content of 76%, corresponding to 94.6% of ZnO. In addition, 0.09% of potassium, corresponding to about 0.21% of potassium acetate, were found.

An X-ray diffractogram of the dried sample indicated exclusively hexagonal zinc oxide. Evaluation of the reflections according to Scherrer revealed an average crystallite size of 7.9 nm (reflections: 100 and 002, 100 doubly weighted since identical to 010 in the hexagonal crystalline system).

A transmission electron micrograph of a sample of the gel (A) diluted in an ethylene glycol/water mixture is shown in FIG. 1.

The other half of the reaction mixture was thickened by centrifugation at 5500 min^{-1} for 30 min to give a gel. The gel weight of the gel (B) was 134.1 g.

Example 3

218.5 g of zinc oxide (99.8%) were introduced into a 6 litre four-necked flask and mixed with 1200 g of methanol, 328.5 g of glacial acetic acid and 46.5 g of deionized water and heated to 60° C . with stirring. In parallel thereto, a solution of 308.1 g of potassium hydroxide pellets (84.7%) and 700 g of methanol was prepared with cooling. After the mixture in the flask had reached 60° C ., about 90 ml of the prepared KOH/methanol solution was slowly metered in via a dropping funnel. The solution clarified slowly and was clear after about 15 min. A solution of 2.8 g of aluminium tri-sec-isobutoxide in 20 g of 2-propanol were then added. The remaining KOH/methanol solution was then metered in over the course of 30 seconds by a dropping funnel. Considerable white turbidity immediately formed, and the temperature of the mixture increased by about 2° C . After a few minutes, the mixture clarified somewhat and then again turned milky white. The heating source was then removed and the mixture was cooled in an ice bath. The stirrer was switched off at a temperature of 23° C . After a settling out time of 14 h, a white sediment had formed. 1920.7 g were drawn off from the supernatant with suction and replaced by 700 g of methanol. The mixture was then stirred for about 45 min and was then divided in the ratio 1:1. One half was further processed as follows: after a settling out time of 3 hours, the supernatant was decanted off and replaced by 300 g of methanol. The mixture was then stirred for about 45 min. After renewed settling out for 14 hours and decantation, 300 g of methanol were again added. The mixture was then stirred again for about 60 min. The mixture was then centrifuged at 5500 rpm for 30 min, and the supernatant was decanted off. The gel weight was 133 g.

The solids content of the gel was 78.7% (drying: 1 h at 130° C .). Elemental analysis revealed a zinc content of 72%, corresponding to 89.6% of ZnO. In addition, 0.17% of potassium, corresponding to about 0.43% of potassium acetate, and 0.15% of aluminium, corresponding to 0.31% of Al_2O_3 , were found.

An X-ray diffractogram of the dried sample indicated exclusively hexagonal zinc oxide. Evaluation of the reflections according to Scherrer revealed an average crystallite size of 7.7 nm (reflections: 100 and 002, 100 doubly weighted since identical to 010 in the hexagonal crystalline system).

Example 4

770 ml of methanol were introduced into a 21 vessel having ground glass joints and fitted with a mechanical stirrer, condenser, thermometer and argon blanketing, and heated to 40° C . 284.91 g of zinc acetate dihydrate were then metered in and dissolved, and the solution was then heated to 60° C . The solution was slightly cloudy. After the addition of 4.60 g of sodium hydroxide pellets (98.8% strength), a clear solution was obtained. Then, over the course of 7 minutes, 173.29 g of aqueous sodium hydroxide solution (49.8% strength) were added, and the temperature increased to a maximum of 64° C . The solution immediately became cloudy, and a white precipitate formed, which was stirred for one hour at 60° C . The mixture was then cooled to room temperature. The volume of the mixture was 960 ml. After a settling out time of 14 h, the turbid supernatant was drawn off with suction, 750 ml of methanol were added to the

sediment and the mixture was stirred for 30 minutes. After 4 hours, the precipitate had settled again, the clear supernatant was drawn off with suction, 750 ml of methanol were added to the sediment and the mixture was stirred for 30 minutes. After a further settling time of 14 h and withdrawal of the clear supernatant with suction, 250 ml of methanol were added to the sediment and the mixture was centrifuged for 10 minutes at 5500 rpm . 129.14 g of gel were obtained.

The solids content of the gel was 79.1% (dry residue: 1 h, 130° C .). The elemental analysis of the dry residue revealed a zinc content of 77.0%, corresponding to 95.8% of ZnO. The sodium content was 0.22%, corresponding to 0.78% of sodium acetate. The X-ray diagram of the gel dry residue indicated exclusively hexagonal ZnO. Evaluation of the reflections according to Scherrer revealed an average crystallite size of 9.4 nm.

Example 5

770 ml of methanol was introduced into a 21 vessel having ground glass joints and fitted with a mechanical stirrer, condenser, thermometer and argon blanketing, 122.30 g of zinc oxide (99.8%) were introduced, and the mixture was heated to 50° C . A solution of 183 g of glacial acetic acid (100% strength) and 27 g of water was then metered in over the course of 10 minutes, and the mixture was then heated to 60° C . A slightly turbid solution was formed. After the addition of 7.56 g of sodium hydroxide pellets (98.8% strength), the solution became as clear as water. The mixture was then cooled to 21° C . and, over the course of 60 seconds, 200.91 g of aqueous sodium hydroxide solution (49.5% strength) were added, and the temperature increased briefly to 51° C . The solution immediately became turbid and a white precipitate formed, which was stirred for one hour at 60° C . The mixture was then cooled to room temperature in iced water. The volume of the mixture was 1100 ml. The mixture was centrifuged for 30 minutes at 500 min^{-1} without the precipitate thickening to give a gel. The supernatant was drawn off with suction, and the sediment was re ed with 750 ml of methanol by stirring for 15 min. The mixture was again centrifuged for 45 min at 500 min^{-1} , the clear supernatant was drawn off with suction and the sediment was again resuspended with 750 ml of methanol for 30 minutes. After centrifugation at 500 min^{-1} for a further 45 minutes and removal of the clear supernatant with suction, the sediment was resuspended with 250 ml of methanol and thickened to give a gel by centrifuging for 10 minutes at 5200 min^{-1} . 168.5 g of gel were obtained.

The solids content of the gel was 74.1% (1 h, 130° C .). The elemental analysis revealed a zinc content of 78%, corresponding to 97.1% of ZnO. The sodium content was 0.870%, corresponding to 3.1% of sodium acetate. The X-ray diagram of the gel dry residue indicated exclusively hexagonal ZnO. Evaluation of the reflections according to Scherrer revealed an average crystallite size of 10.2 nm.

Example 6

Preparation of a Zinc Oxide Sol

134.1 g of dichloromethane were added to 134.1 g of the zinc oxide gel (B) prepared in Example 2 and occasionally shaken. A translucent sol (244.4 g) formed. Elemental analysis revealed a zinc content of 31%, corresponding to 38.6% of ZnO. By evaluating transmission electron micrographs of a sample of the sol diluted in an ethylene glycol/water mixture (FIG. 1, magnification 1,000,000:1), the average, circle-equivalent primary particle diameter of the zinc oxide particles was determined as 13 nm (number-average, from 283 counted particles).

Example 7

Preparation of a Zinc Oxide Sol

300 g of a zinc oxide gel prepared as in Example 1 were stirred with 291 g of ethylene glycol, 145 g of water and 82 g of triethanolamine. The methanol content of the gel was stripped off at room temperature under reduced pressure. 683 g of a yellowish translucent sol were obtained. By evaluating transmission electron micrographs of a sample of the sol diluted in an ethylene glycol/water mixture, the average, circle equivalent primary particle diameter of the zinc oxide particles was defined as 10.2 nm (number-average from 584 counted particles). The optical absorption spectrum of a sample of this sol diluted in an ethylene glycol/water mixture is shown in FIG. 2 (1: absorbance, 2: wavelength [nm]).

After a standing time of 3 months, the sol was externally unchanged. Redetermination of the average, circle-equivalent primary particle diameter of the zinc oxide particles by evaluating a transmission electron micrograph of a sample of the sol diluted in an ethylene glycol/water mixture revealed a value of 9.4 nm (number-average from 803 counted particles).

What is claimed is:

1. Process for the preparation of nano size zinc oxide particles, which are redispersible in organic solvents and/or water, comprising

- a) carrying out basic hydrolysis of at least one zinc compound in alcohol or an alcohol/water mixture,

wherein the hydrolysis is carried out with substoichiometric amounts of base, based on the zinc compound, to form a precipitate;

b) leaving the precipitate which initially forms during hydrolysis to mature until the zinc oxide has completely flocculated,

c) thickening the precipitate to give a gel; and

d) separating the gel from the supernatant phase;

wherein the gel comprises nano sized zinc oxide particles having an average primary particle diameter of <15 nm, determined in a transmission electron micrograph.

2. The process of claim 1, wherein prior to, during or after precipitation, from 0.01 to 3 mol % of foreign ions, based on proportion of zinc, are added.

3. Process according to claim 1 wherein the zinc compound comprises at least one of zinc acetate and zinc acetate dihydrate.

4. Process according to claim 3, wherein the at least one of zinc acetate and zinc acetate dihydrate is prepared from zinc oxide in an upstream process.

5. The process of claim 1, wherein the gel is redispersed in organic solvents and/or water, optionally with the addition of surface-modifying compounds.

6. The process of claim 1, wherein the gel is redispersed by adding dichloromethane and/or chloroform.

* * * * *